

Vol. 18

2025

No. 01

GEOGRAPHY
ENVIRONMENT
SUSTAINABILITY

«The journal GEOGRAPHY, ENVIRONMENT, SUSTAINABILITY was founded in 2008 by Russian Geographical Society, the Lomonosov Moscow State University Geography Department, and the Russian Academy of Sciences Institute of Geography. Since that time the journal publishes **4 issues per year**, containing original research papers and reviews. The journal issues are open source and distributed through subscriptions, library exchanges of leading universities, and via the website through the world»

FOUNDERS OF THE JOURNAL: Russian Geographical Society, Faculty of Geography, Lomonosov Moscow State University and Institute of Geography of the Russian Academy of Sciences

The journal is published with financial support of the Russian Geographical Society.

The journal is registered in Federal service on supervision of observance of the legislation in sphere of mass communications and protection of a cultural heritage. The certificate of registration: ПИ № ФС77-67752, 2016, December 21.

PUBLISHER

Russian Geographical Society
Moscow, 109012 Russia
Novaya ploshchad, 10, korp. 2
Phone 8-800-700-18-45
E-mail: press@rgo.ru
www.rgo.ru/en

EDITORIAL OFFICE

Lomonosov Moscow State University
Moscow 119991 Russia
Leninskie Gory, 1,
Faculty of Geography, 1806a
Phone 7-495-9391552
Fax 7-495-9391552
E-mail: ges-journal@geogr.msu.ru
www.ges.rgo.ru

DESIGN

Layout designer: Tereshkin Anton
Moscow, 115088,
26 Simonovsky Val str., bldg. One
Phone: +7 (903) 108-04-44
E-mail: smile.tai@gmail.com

DOI prefix: 10.24057

Format A4 (210x297mm)

“GEOGRAPHY, ENVIRONMENT, SUSTAINABILITY” is the only original English-language journal in the field of geography and environmental sciences published in Russia. It is supposed to be an outlet from the Russian-speaking countries to Europe and an inlet from Europe to the Russian-speaking countries regarding environmental and Earth sciences, geography and sustainability. The main sections of the journal are the theory of geography and ecology, the theory of sustainable development, use of natural resources, natural resources assessment, global and regional changes of environment and climate, social-economical geography, ecological regional planning, sustainable regional development, applied aspects of geography and ecology, geoinformatics and ecological cartography, ecological problems of oil and gas sector, nature conservations, health and environment, and education for sustainable development.

OPEN ACCESS POLICY. “GEOGRAPHY, ENVIRONMENT, SUSTAINABILITY” is an open access journal. All articles are made freely available to readers immediately upon publication. Our open access policy is in accordance with the Budapest Open Access Initiative (BOAI) definition - it means that articles have free availability on the public internet, permitting any users to read, download, copy, distribute, print, search, or link to the full texts of these articles, crawl them for indexing, pass them as data to software, or use them for any other lawful purpose, without financial, legal, or technical barriers other than those inseparable from gaining access to the internet itself.

Date of publication: March 31st, 2025.

EDITORIAL BOARD

EDITORS-IN-CHIEF:

Kasimov Nikolay S.

Lomonosov Moscow State University,
Faculty of Geography, Russia

DEPUTY EDITORS-IN-CHIEF:

Solomina Olga N. - Russian Academy of Sciences,
Institute of Geography, Russia

Tikunov Vladimir S. - Lomonosov Moscow State
University, Faculty of Geography, Russia

Alexeeva Nina N. - Lomonosov Moscow State University,
Faculty of Geography, Russia

Baklanov Alexander - World Meteorological Organization,
Switzerland

Chubarova Natalya E. - Lomonosov Moscow State
University, Faculty of Geography, Russia

De Maeyer Philippe - Ghent University, Department of
Geography, Belgium

Dobrolubov Sergey A. - Lomonosov Moscow State
University, Faculty of Geography, Russia

Ferjan J. Ormeling - University of Amsterdam, Amsterdam,
Netherlands

Sven Fuchs - University of Natural Resources and Life
Sciences

Haigh Martin - Oxford Brookes University, Department of
Social Sciences, UK

Golosov Valentin N. - Lomonosov Moscow State
University, Faculty of Geography, Russia

Golubeva Elena I. - Lomonosov Moscow State University,
Faculty of Geography, Russia.

Gulev Sergey K. - Russian Academy of Sciences, Institute
of Oceanology, Russia

Guo Huadong - Chinese Academy of Sciences, Institute of
Remote Sensing and Digital Earth, China

Jarsjö Jerker - Stockholm University, Department of
Physical Geography and Quaternary Geography, Sweden

Jeffrey A. Nittrouer - Rice University, Houston, USA

Ivanov Vladimir V. - Arctic and Antarctic Research
Institute, Russia

Karthe Daniel - German-Mongolian Institute for Resources
and Technology, Germany

Kolosov Vladimir A. - Russian Academy of Sciences,
Institute of Geography, Russia

Kosheleva Natalia E. - Lomonosov Moscow State
University, Faculty of Geography, Russia

Konečný Milan - Masaryk University, Faculty of Science,
Czech Republic

Kotlyakov Vladimir M.

Russian Academy of Sciences
Institute of Geography, Russia

Vandermotten Christian - Université Libre de Bruxelles
Belgium

Chalov Sergei R. - (Secretary-General) Lomonosov
Moscow State University, Faculty of Geography, Russia

Kroonenberg Salomon - Delft University of Technology,
Department of Applied Earth Sciences, The Netherlands

Kulmala Markku - University of Helsinki, Division of
Atmospheric Sciences, Finland

Olchev Alexander V. - Lomonosov Moscow State
University, Faculty of Geography, Russia

Malkhazova Svetlana M. - Lomonosov Moscow State
University, Faculty of Geography, Russia

Maslakov Alexey A. - Lomonosov Moscow State
University, Faculty of Geography, Russia

Minkina Tatiana M. - Southern Federal University, Russian
Federation

Moreido Vsevolod M. - Russian Academy of Sciences,
Water Problems Institute, Russia

Meadows Michael E. - University of Cape Town,
Department of Environmental and Geographical Sciences
South Africa

O'Loughlin John - University of Colorado at Boulder,
Institute of Behavioral Sciences, USA

Paula Santana - University of Coimbra, Portugal

Pedroli Bas - Wageningen University, The Netherlands

Pilyasov Alexander N. - Institute of Regional Consulting,
Moscow, Russia

Radovanovic Milan - Serbian Academy of Sciences and
Arts, Geographical Institute "Jovan Cvijić", Serbia

Samsonov Timofey E. - Lomonosov Moscow State
University, Faculty of Geography, Russia

Sebentsov Alexander B. - Russian Academy of Sciences,
Institute of Geography, Russia

Sokratov Sergei A. - Lomonosov Moscow State University,
Faculty of Geography, Russia

Tishkov Arkady A. - Russian Academy of Sciences,
Institute of Geography, Russia

Wuyi Wang - Chinese Academy of Sciences, Institute of
Geographical Sciences and Natural Resources Research,
China

EDITORIAL OFFICE

ASSOCIATE EDITOR

Maslakov Alexey A.

Lomonosov Moscow State University,
Faculty of Geography, Russia

ASSISTANT EDITOR

Komova Nina N.

Lomonosov Moscow State University,
Faculty of Geography, Russia

ASSISTANT EDITOR

Mozolevskaya Irina V.

Lomonosov Moscow State University,
Faculty of Geography, Russia

PROOF-READER

Denisova Irina S.

Lomonosov Moscow State University,
Faculty of Geography, Russia

CONTENTS

Elena M. Baglaeva, Aleksandr P. Sergeev, Andrey V. Shichkin, Alexander G. Buevich

INDIVIDUAL AND PAIRWISE REPRESENTATIVENESS OF SAMPLING POINTS
IN INTERPOLATION TASKS OF HEAVY METALS DISTRIBUTION IN THE TOPSOIL6

Munazza Fatima, Ibtisam Butt, Neda Firouraghi, Behzad Kiani

EXPLORING GEOSPATIAL CLUSTERS OF FIVE PRIMARY RESPIRATORY DISEASES
IN SOUTH PUNJAB, PAKISTAN: AN EPIDEMIOLOGICAL EXAMINATION 14

Anastasia A. Lisina, Natalia L. Frolova, Andrey S. Kalugin, Inna N. Krylenko, Yuri G. Motovilov

ASSESSMENT OF THE KOLYMA RIVER HYDROLOGICAL REGIME DYNAMICS
IN THE 21ST CENTURY BASED ON RUNOFF FORMATION MODEL23

Maria Tereshina, Oxana Erina, Dmitriy Sokolov, Kristina Pilipenko, Timur Labutin

LAKE PHYSICS IN CHANGING CLIMATE: CASE STUDY
OF KOSINO LAKES (MOSCOW, RUSSIA) IN 1984-202335

Mir Najaf Mousavi, Safdar Ali Shirazi, Muhammad Nasar-u-Minallah, Nima Bayramzadeh

INTRODUCING THE MOUSAVI PRIMATE CITY INDEX FOR IRAN'S URBAN SYSTEM ASSESSMENT.....44

Abdul Hadi Z., Che Dom N., Ishak A.R., Salleh S.A., Abdullah S., Precha N.

GEOSPATIAL DYNAMICS OF DENGUE FEVER DENSITY IN KUANTAN,
MALAYSIA: GIS-BASED APPROACH54

Sapelko T.V., Lapenkov A.E., Guzivaty V.V., Karetnikov S.G., Gazizova T.V., Ignatyeva N.V., Kuznetsov D.D., Rusanov A.G.

FEATURES OF UNIQUE LAKES DEVELOPMENT ON THE KURGALSKY PENINSULA
IN THE SOUTHEAST BALTIC SEA BASED ON THE RESULTS
OF INTERDISCIPLINARY RESEARCH.....65

Andrey N. Shikhov, Yulia I. Yarinich, Alexander V. Chernokulsky

ASSOCIATION OF SPATIAL AND TEMPORAL WINDTHROW DISTRIBUTION WITH
CONVECTIVE PARAMETERS AND LIGHTNING DENSITY IN RUSSIA75

Mikhail V. Uzhegov, Andrey L. Entin

A REVIEW OF UPSCALING ALGORITHMS FOR FLOW DIRECTION RASTERS89

Wahyu Adi, Agus Hartoko, Pujiono W. Purnomo, Okto Supratman, Udhi E. Hernawan

SEAGRASS CARBON STOCKS AND SEQUESTRATION IN HABITAT IMPACTED BY TIN MINING
ACTIVITIES IN BANGKA BELITUNG, INDONESIA97

Andrey G. Purekhovskiy, Alexey N. Gunya, Evgeniy Yu. Kolbowski, Alexei A. Aleinikov METHODS OF STUDYING THE ALPINE TREELINE: A SYSTEMATIC REVIEW	105
Ekaterina V. Romanova, Evgeny I. Vdovkin CO-LOCATION OF INNOVATORS AND FINAL PRODUCTS: CASE OF WIND ENERGY OF GERMANY	117
Dedi Irawadi, Tuga Mauritsius, Dony Kushardono, Syarif Budhiman, Karunika Diwyacitta, Bayu S. Adhitama, Fauzan A. Ayubi, Olivia Maftukhaturrizqoh, Ika S. Supriyani SMART DETECTION OF ILLICIT CANNABIS PLANTATIONS USING REMOTE SENSING TECHNOLOGY AND MACHINE LEARNING	130
Mikhail M. Lobanov, Jelena Zvezdanović Lobanova, Miroljub Milinčić, Milan Zvezdanović IMPACT OF COAL-BASED ELECTRICITY GENERATION, LAND USE CHANGE, STEEL AND CEMENT PRODUCTION ON CO2 EMISSIONS: EVIDENCE FROM EASTERN EUROPEAN AND CENTRAL ASIAN COUNTRIES.....	139

Disclaimer:

The information and opinions presented in the Journal reflect the views of the authors and not of the Journal or its Editorial Board or the Publisher. The GES Journal has used its best endeavors to ensure that the information is correct and current at the time of publication.

INDIVIDUAL AND PAIRWISE REPRESENTATIVENESS OF SAMPLING POINTS IN INTERPOLATION TASKS OF HEAVY METALS DISTRIBUTION IN THE TOPSOIL

Elena M. Baglaeva*, Aleksandr P. Sergeev, Andrey V. Shichkin, Alexander G. Buevich

Institute of Industrial Ecology UB RAS, S. Kovalevskaya str., 20, Ekaterinburg, 620990, Russia

*Corresponding author: elenbaglaeva@gmail.com

Received: February 8th 2024 / Accepted: November 27th 2024 / Published: March 31st 2025

<https://doi.org/10.24057/2071-9388-2025-3240>

ABSTRACT. The optimization of environmental soil monitoring based on representative selection of a training subset for an artificial neural network is an unresolved problem in the tasks of interpolation of the distribution of metals in the topsoil. The soil survey data, often used as input for artificial neural network modeling, are datasets at irregular points. Usually, the division of the input data into training and test subsets is carried out randomly in a ratio of 70% to 30% points, respectively. The question of the individual and collective representativeness of local sampling points on the element content in the soil in a given area for a training subset remains beyond the scope of interpolation problems. In this work, the representativeness of the sampling points plays a crucial role in reducing the ANN error and enhancing the correlation between the results of model calculations on the test subset and natural measurements when the points are part of the training subset. When evaluating the pairwise representativeness, we found two types of effects: synergy and anti-synergy. The synergy was achieved with an increase in model accuracy when the pair entered the training subset. The anti-synergy manifested in a decrease informativeness of the point pair for modeling. The various sampling locations have different information and unequal meaning for feature interpolation. The scale-free network structures were found to have pairwise representativeness by *RMSE*.

KEYWORDS: representativeness, sampling, heavy metals, artificial neural networks, training subset

CITATION: Baglaeva E. M., Sergeev A. P., Shichkin A. V., Buevich A. G. (2025). Individual And Pairwise Representativeness Of Sampling Points In Interpolation Tasks Of Heavy Metals Distribution In The Topsoil. *Geography, Environment, Sustainability*, 6-13

<https://doi.org/10.24057/2071-9388-2025-3240>

Conflict of interests: The authors reported no potential conflict of interest.

INTRODUCTION

The environmental soil monitoring methods often require preliminary data to be sufficient to represent soil-environment relationships throughout the study area (Zhu 2015). A limited quantity of soil sample data to represent the study area is still an issue to predict soil properties and estimate prediction uncertainty. A large number of publications are devoted to the issues of representative sampling of the components of the environment (Malof 2018; Liu 2022). The task of assessing representativeness and constructing a representative set arises when organizing sampling to assess the quality of environmental components, when statistically processing environmental monitoring data, and when choosing a training subset for artificial neural networks (ANNs) that model the spatial distribution of a feature (Nath 2018; Demyanov 2020; Mello 2022). The existing rules for choosing a training subset do not reflect the picture of pollution (Baglaeva 2020; Malof 2018). The formal structure of the training subset must be determined by the rules governing the origin and maintenance of ecological topologies in order to correctly interpret ecological patterns (Prager 2009).

Insufficient attention is paid to the interpretation of the results of a modeling. Often behind the scenes is the

connection between the features of environmental data and landscapes (Boussange 2022). The key challenge is understanding how the connectivity and heterogeneity of the model results relate to environmental characteristics. To characterize environmental connectivity, these tasks are proposed to be solved by spatial graph theory methods (O'Brien 2006, Urban 2009). We are interested in how graph topology is combined with the spatial distribution of element contents in topsoil. The graph topology properties demonstrate landscape complexity and allow us to determine a finite size of local basic landscape diversity. Using graph topology, we evaluate a representativeness training subset to build the element content distribution in the topsoil. Our study suggests a formalization of assessment of individual and collective representativeness for sampling points to explain the connected landscape pattern. If there are individual sampling points that are important at some scale but not at another one, then there can be doublets, triplets, or *n*-lets of the sample that are important for modeling at some scale but not at another one (Dale 2010; Shu 2015).

Monitoring of environmental parameters in the conditions of urban development is not able to provide complete spatial and temporal characteristics of pollution (O'Hare 2020; Pesch 2008; Zhong 2021). For a comprehensive assessment of the levels of environmental pollution in cities

(Wang 2020; Xu 2023), monitoring is often combined with other methods of obtaining data, including models based on ANN. In the scientific literature, works have been published when the selection of points in the training subset occurs using information about the distribution of the feature under study, but the gain in the accuracy of the model turns out to be small (Kramm 2020; Fernandez Jaramillo 2018; Gutierrez-Velez 2020). The prediction accuracy of ANN models is greatly influenced by the choice of points used to train the ANN. Random sampling points should only be used on a homogeneous experimental site (Legendre 2004; Prager 2009). As demonstrated by (Wang 2021; Ziggah 2019; Baglaeva 2021), various sampling points make contribute differently to the ANN forecast error, i.e., have different representativeness for the purposes of the forecast.

Previously, some authors presented a definition of representativeness. Zhu (2018) uses the representativeness of a single sampling point and a sampling point set to other points as the similarity of these points to the sampling point set. The representativeness is a similarity in geographic configuration between sample point k and prediction point i , which is then used as the weight in the prediction of the value of the target variable at prediction point i , together with the other involved sample points whose weights are determined similarly. And this similarity is also used to measure the uncertainty associated with the prediction (Levin 2002; Zhu 2018). By representativeness, we understand the characteristics of points of the studied statistical population to adequately reflect the characteristics of the trait under study. Representative sampling or a representative selection of points in the training subset provides, within a given accuracy, reliable data on the content of a pollutant in an environmental component (air, water, soil etc.) in a selected area at a given point in time.

We assume that not only points distinguish in different representativeness for the evaluation of a feature, but also sets of points (doublet, triplets, ..., n -lets) have different

representativeness. In the present work, it is proposed to consider the comparison of individual and collective representativeness when points are included in the training subset. Under the individual representativeness of the sampling point, we mean the frequency of its hits in the training subset, training on which provides the smallest model error. Collective representativeness is the frequency of hits of a collection of points (pairs, triples, quadruples, etc.) in the training subset, training on which provides the smallest model error. To build a representative training subset, it is necessary to 1) determine which n -lets are the most representative (n -lets size and representativeness level); 2) reveal the relationship between individual and collective representativeness. Determination of the volume of all representative n -lets requires large computing power of the computer, so the collective representativeness in this work was evaluated by pair.

MATERIALS AND METHODS

Sampling location

200 soil samples were collected in the residential part of Noyabrsk city (N 63.2°, E 75.5°), Russia. The industry of the city is hydrocarbon energy. The climatic zone is subarctic, or Dfc, by Köppen climate classification. The predominant soil type is gley taiga (Gd 23-1ab) on the FAO-UNESCO soil map¹.

The sampling point map was designed so that a given number of samples (200 in the residential area of Noyabrsk) on average evenly filled the study area. The average distance between sampling points was about 300 m. This distance varied depending on the density of buildings, the location of roads, etc. in order to ensure sampling in undisturbed areas of the open soil surface. The sampling depth was 0.05 m, since we were interested in the top layer of soil. The sampling was carried out with a cylindrical sampler with a diameter of 0.05 m. The soil sampling procedure schema was shown in Fig. 1.

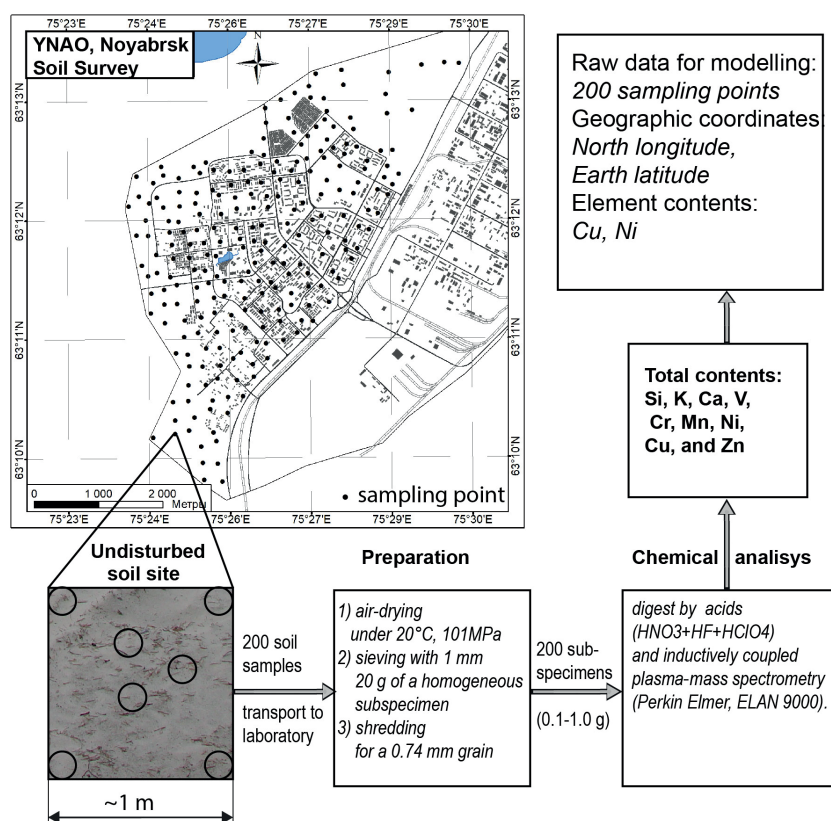


Fig. 1. The soil sampling procedure schema

¹HWSD (Harmonized World Soil Database), 2009. Soil Units in the Revised Legend of the Soil Map of the World. <https://www.fao.org/soils-portal/soil-survey/soil-maps-and-databases/harmonized-world-soil-database-v12/en/> (accessed 15 May 2023).

The raw data preparation

The soil sampling procedure was previously described in detail for Noyabrsk (Baglaeva 2020). Fig. 1 shows the schema of this procedure. The raw data preparation consisted of sampling 200 specimens from undisturbed soil sites, sample preparation, and chemical analysis using inductively coupled plasma-mass spectrometry.

Preparation of soil samples and chemical analysis were conducted in compliance with actual standard requirements. For quality control, standard reference samples were used, certified for the content of determined elements, similar in composition to the samples under study.

The same total element contents were determined in the topsoil. Further modeling involved the total content of *Cuprum* and *Niccolum* in topsoil.

Multilayer perceptron

The input data are the geographic coordinates for the simulation. The output data are the element's contents.

The multilayer perceptron (MLP) with Levenberg-Marquardt learning algorithm was used to demonstrate the possibilities of the method as the easy-to-understand model ANN for modeling the spatial distribution of the element contents in the topsoil. The construction of the MLP model based on the number of neurons inside the hidden layer was chosen after several training cycles and error estimation for the test subset. We used the tangential activation function, which is best suited for predicting the features of the spatial distribution of element content in the topsoil (Baglaeva 2021). The MLP structure had one input layer consisting of two neurons (spatial coordinates x and y), one hidden layer with 9 neurons, and one output layer with one neuron (element content).

Representativeness assessment

Let the representativeness of the sampling point be an ability of this point to provide: 1) a small root-mean-square error $RMSE$ (Eq. 1) for estimating accuracy; 2) a high correlation coefficient $Corr$ (Eq. 2) to check the synchronism of changes between predicted and observed values with the participation of this point in training.

$$RMSE = \sqrt{\frac{\sum_{i=1}^n (p(i) - o(i))^2}{n}} \quad (1)$$

where $p(i)$ is predicted data; $o(i)$ is observed data; n is the number of subset points. $RMSE$ (1) tests the accuracy between predicted and observed data.

$$Corr = \frac{\sum_{i=1}^n (p(i) - \bar{p})(o(i) - \bar{o})}{\sqrt{\sum_{i=1}^n (p(i) - \bar{p})^2 \sum_{i=1}^n (o(i) - \bar{o})^2}} \quad (2)$$

where \bar{p} is predicted average; \bar{o} is observed average. The correlation coefficient $Corr$ shows the linear statistical relationship between the predicted values and the observed ones, how much the changes in the predicted values repeat the systematic changes in the observed ones.

The individual representativeness for each point considers the set of the best (small $RMSE$ (Eq. 1) and high $Corr$ (Eq. 2)) networks in which the point participated in training. Collective representativeness is the representativeness of the sampling

points, which support connections with the neighbors, which makes it possible to provide a small $RMSE$ and a high $Corr$ when participating in the training of a group of sampling points. Collective representativeness considers the various combinations of training sampling points, such as doublets, triplets, and so on.

Individual representativeness

A four-step (4-step) algorithm was used for individual representativeness assessment of the sampling points involved in the training subset (Fig. 2). The raw data were repeatedly divided randomly into training and test subsets in the ratio of 75%/25%, respectively. 200 points were randomly divided into 150 training and 50 test points. The number of divisions was 100,000.

1. The total raw data set was randomly divided 100,000 times into two non-overlapping sets, training and test subsets, in the ratio of 75%/25%, respectively. Thus, we got 100,000 training and 100,000 test subsets.

2. For each random division, 5 MLP networks were built additionally (500,000 MLP networks in total). For each trained network, the root-mean-square errors ($RMSE$) of the forecast of the training and test subsets were determined. The network with the minimum $RMSE$ was chosen.

3. $RMSE$ and $Corr$ for the training, test, and general subsets were calculated for 100,000 better networks.

4. Each sample point was assigned a set of the best networks in which it participated in training. For each sample point, we calculated the basic statistics of $RMSE$ and $Corr$ for the training, test, and general subsets for the networks in which the point participated in training.

Individual representativeness was assessed by comparing mean $RMSE$ and $Corr$ values. The best representative point is the one whose inclusion in the training subset provides a lower mean $RMSE$ and a higher mean correlation coefficient with the observed values.

Collective representativeness

To assess the collective representativeness of the sampling points of the training subset, a four-step (4-step) algorithm was also used (Fig. 2). We divided the training and test subsets into 75% and 25%, respectively, used the training results as a set of the best networks for each point, and calculated the corresponding distributions of $RMSE$ and correlation coefficients for the training, test, and general subsets.

Collective (paired) representativeness was assessed using samples of two points out of two hundred. For each pair of sampling points, the basic statistics of $RMSE$ for the training, test, and total subsets were calculated for networks in which both points participated in training. 1000 pairs from these pairs were selected with the lowest mean $RMSE$ for the pair that fell into the training set, which corresponded to the 0.051 quantile. The collective representativeness of the sampling points was assessed by the number of its connections with other points within the 0.051 quantile (1000 point pairs) according to the average $RMSE$ or within the $1 - 0.051 = 0.949$ quantile (1000 point pairs) according to the average correlation coefficient. We built graphs for a cutoff threshold of 10 connections with other sampling points.

In this work, due to computational difficulties, we limited ourselves to pairs of sampling points. The hypothesis that the synergy effect exists was tested by comparing individual and paired representativeness to predict element content. For verification, we used the conditional distribution of the correlation coefficients and $RMSE$ means (provided that a pair of sampling points fell into the best training subset).

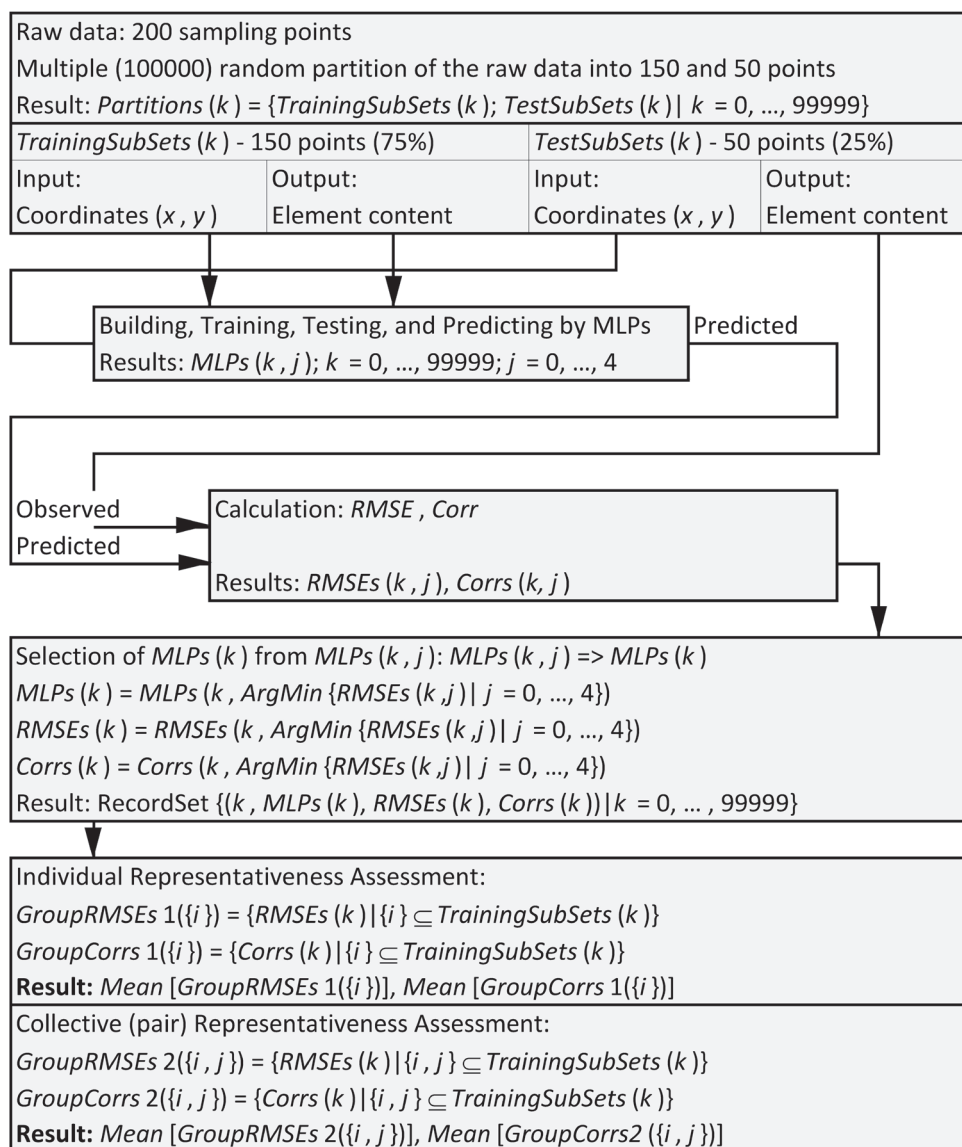


Fig. 2. The representativeness assessment algorithm

RESULTS

Table 1 presents the characteristics of *Cuprum* and *Niccolum* distributions in the study area. The total Cuprum content is in the range from 5.89 to 69.59 mg/kg, *Niccolum* from 3.58 to 41.94 mg/kg, which does not exceed Clarke in the urban soil (Shichkin 2018).

For each data split, MLP models were built, and representativeness characteristics were calculated: *RMSE* and correlation coefficients. Table 2 presents the statistical characteristics of the representativeness assessment. Fig. 3 shows the *RMSE* means and correlation coefficients obtained for 19,900 models.

Table 1. Element statistics in Noyabrsk topsoil

Element	Element Content, mg/kg					CV, %	Skewness	Excess Kurtosis
	Minimum	Maximum	Mean	SD*)	Median			
Cu	5.89	69.59	16.12	7.64	14.67	47	2.69	13
Ni	3.58	41.94	11.67	4.50	11.15	39	2.16	11

*) SD – standard deviation; **) CV – coefficient of variation.

Table 2. Representativeness characteristic statistics

Element	Characteristic	Mean	Median	Minimum	Maximum	SD	CV, %	Skewness	Excess Kurtosis
Cu	<i>RMSE</i> , mg/kg	3.325	3.336	2.771	3.395	0.059	2	-5.5	39
	<i>Corr</i>	0.256	0.256	0.236	0.271	0.003	1	-0.3	2
Ni	<i>RMSE</i> , mg/kg	4.312	4.322	3.720	4.340	0.049	1	-7.2	58
	<i>Corr</i>	0.285	0.285	0.271	0.302	0.004	1	0.2	1

As can be seen from Fig. 3, the *RMSE* distribution is split into two clusters: *Cuprum* and *Niccolum*. The lower *RMSE* cluster is associated with the inclusion in the training subset of a single point 129 for *Niccolum* (the point with the highest *Niccolum* content) and 134 for *Cuprum* (the point with the highest *Cuprum* content).

Pair representativeness was visualized as *RMSE* and correlation coefficient graphs for *Niccolum* and *Cuprum* contents (Fig. 4). The sampling points are graph vertices. The graph edges were the best links between pairs of sampling the points named by doublet.

Pair representativeness graphs were built by the least *RMSE* doublets and the largest *Corr* doublets for Ni and Cu (Fig. 4). When constructing the graphs, we were limited to about 20 doublets. That is, the correlation graphs included the doublets with correlation coefficients greater than 0.2667 for Cu and 0.2983 for Ni. The *RMSE* graphs consisted of the doublets with *RMSE*s less than 2.83 for Cu and 3.868 for Ni. Both *Niccolum* and *Cuprum* *RMSE* graphs seem to have a scale-free network structure. The edges of the

correlation coefficient graphs are stitching through the area for each element. *RMSE* as the representativeness indicator define the most “polluted” points, and the correlation coefficient adds “important” points for description of the element distributions in the topsoil. Individual and pairwise representativeness comparisons were shown for *Niccolum* and *Cuprum* contents in Table 3.

DISCUSSION

Individual representativeness is not enough to determine the best training subset. A point with low individual representativeness in pairs may be “good” for learning. By analogy with individual characteristics, there can be “good” pairs for training (these are all 199 pairs with 129 points for *Niccolum*, and 134 points for *Cuprum*), there can be “bad” ones, which increase the model error when included in pairs in the training subset. The results are shown in Table 3. 9 points were selected: 8, 12, 14, 63, 67, 116, 165, 168, 199 for *Cuprum* and 49, 52, 84, 102, 103, 104,

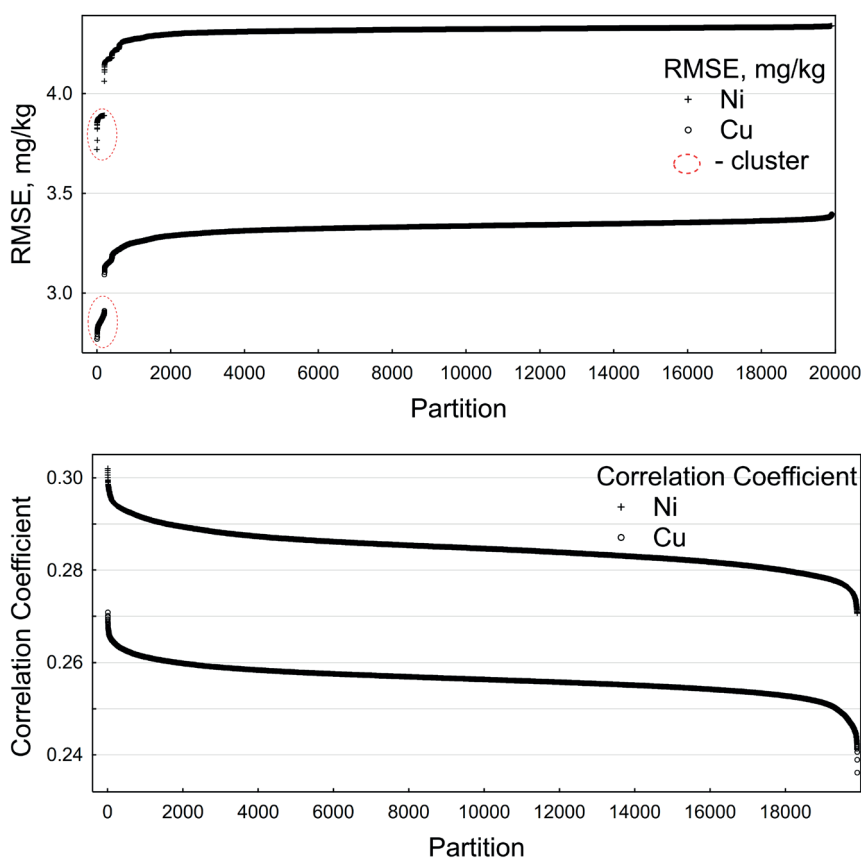


Fig. 3. *RMSE* mean and correlation coefficients mean

Table 3. Individual and pairwise representativeness comparison

Characteristic	«Best» <i>RMSE</i> doublet			«Bad» <i>RMSE</i> doublet			«Best» <i>Corr</i> doublet			«Bad» <i>Corr</i> doublet		
Element	Ni (<i>Niccolum</i>)											
n	{94;129}	{94}	{129}	{19;56}	{19}	{56}	{13;25}	{13}	{25}	{88;145}	{88}	{145}
<i>RMSE</i> , mg/kg	3.720	4.167	3.880	4.340	4.325	4.326	4.234	4.266	4.281	4.155	4.166	4.304
<i>Corr</i>	0.281	0.278	0.287	0.284	0.284	0.284	0.302	0.294	0.293	0.271	0.278	0.278
Element	Cu (<i>Cuprum</i>)											
n	{134;135}	{134}	{135}	{139;165}	{139}	{165}	{22;135}	{22}	{135}	{126;127}	{126}	{127}
<i>RMSE</i> , mg/kg	2.771	2.859	3.319	3.395	3.354	3.358	3.226	3.253	3.319	3.152	3.284	3.148
<i>Corr</i>	0.27	0.259	0.264	0.254	0.258	0.253	0.271	0.263	0.264	0.236	0.248	0.246

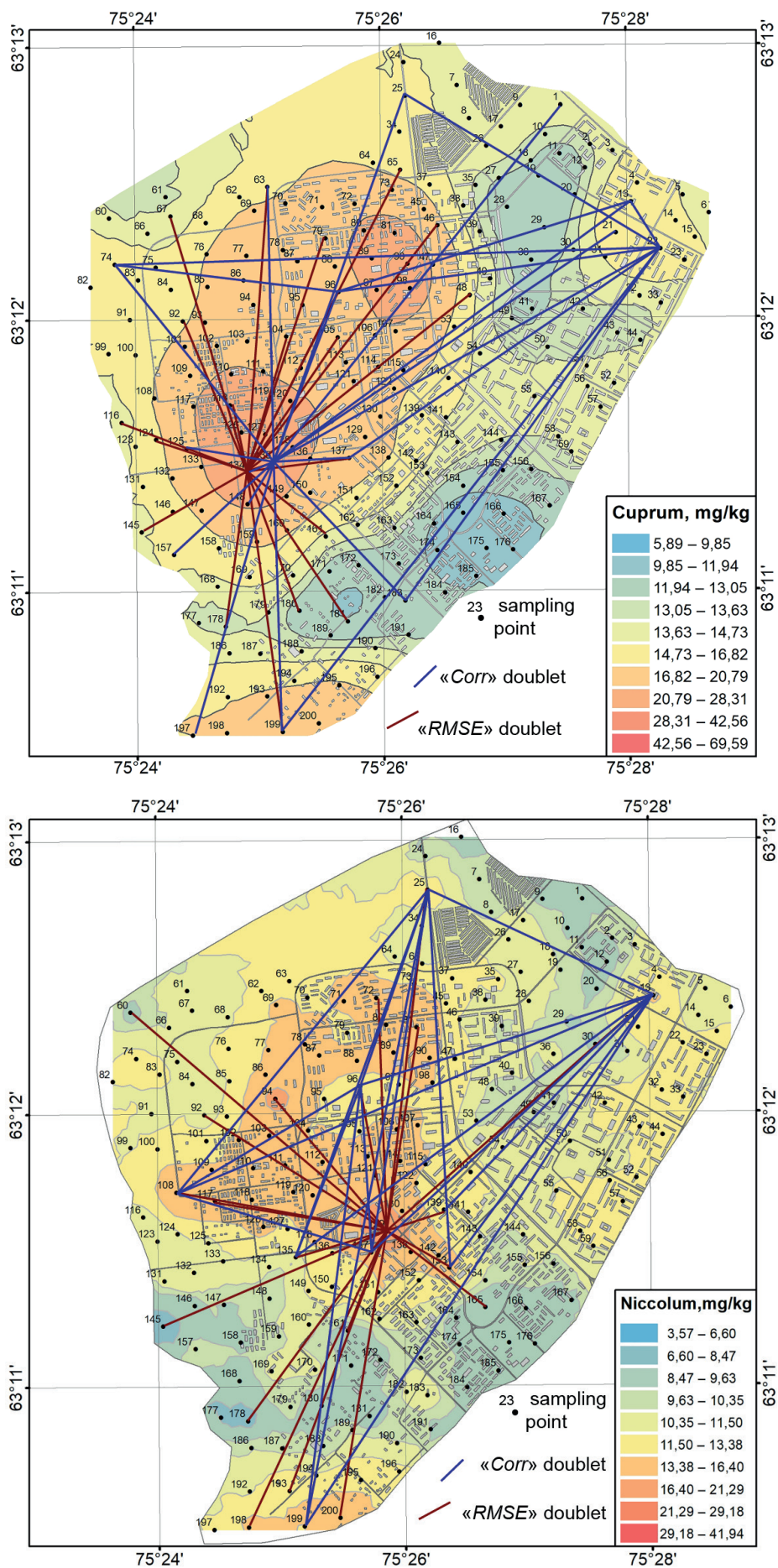


Fig. 4. RMSE and correlation coefficient graphs of the pair representativeness

118, 146, 192 for *Niccolum*. The elemental content at these points is below or close to the average.

Pair representativeness is not always limited to individual. There is a synergy effect, i.e., taking into account the collective (n -let) representativeness makes it possible to reduce the model error. Paired (collective) representativeness characterizes the interaction of pairs of points, i.e., the ability of pairs of points, when included in the training subset, to provide *RMSE* and correlation coefficient characteristics that exceed the best individual characteristics. The value added by the pair {94; 129} for *Niccolum* and a pair of {134; 135} for *Cuprum* is higher than the value contributed by individual points {94} and {129} for *Niccolum* and {134} and {135} for *Cuprum*. This synergy effect is created through the mutual influence between the points. Table 3 shows the best pairs with the lowest *RMSE* and the highest correlation coefficient and the worst pairs with the highest *RMSE* and the lowest correlation coefficient for Cu and Ni. Along with the synergy effect, there are relationships that reduce the value of the model. In this case, pairs of points provide less information to describe the element content distribution than individual points included in a pair as the effect of antisynergy. This may be due to the redundant use of points to describe the distribution of the feature.

As can be seen from Table 3, for example, this is {19; 56} for Ni and {139; 165} for Cu. *RMSE* pair {19; 56} for *Niccolum* and {139; 165} for *Cuprum* is greater than the *RMSE* of individual points {19} and {56} for *Niccolum* and {139} and {165} for *Cuprum*. Conversely, the correlation coefficients of a pair {88; 145} for Ni and {126; 127} for Cu are smaller than the correlation coefficients of individual points {88} and {145} for Ni and {126} and {127} for Cu.

The effects found here (synergy and anti-synergy) seem to be useful for predicting spatial variability and predicting the content of elements in the topsoil in areas with complex geographical conditions. This benefit may be expressed as a reduction in the uncertainty of the results of future field studies when they are planned.

The scale-free network structures *RMSE* graphs of the pair's representativeness are the same for both *Niccolum*

and *Cuprum* (Fig. 4), and the central points of these graphs are territorial characteristics. For each pair of the points, the best graph topology characteristic of the territory is identified. This topology can be explained by man-made activity.

The obtained results do not contradict the hypothesis that different locations (geolocations) carry different information and an unequal value for the interpolation of the feature distribution. Evaluation of the representativeness of the points will allow you to choose the most representative points for the areas.

CONCLUSIONS

Comparison of individual and pair (collective) representativeness when points were included in the training subset showed their unequal value for interpolating the distribution of heavy metals in the topsoil. The most representative in terms of individual representativeness were the points with the maximum element content in the selected area. Including these points in the ANN training subset reduces the error and increases the correlation between the results of model calculations and field measurements on the test subset. The graph topology of the best collective representativeness (it looks like a constellation) can be used as territory characteristics associated with man-made activity. The volume of the n -let can be analogous to the dimension of the phase space. Although it is impossible to predict every detail of the evolution of such a system, it is possible to develop statistical mechanics with heterogeneous ensembles of interacting agents (Levin 2002), similar to the description of statistical ensembles in gas dynamics.

In this work, we have limited ourselves to pair representativeness; determining the volume of all representative n -s requires huge computational costs and remains a task for future research. Complex adaptive systems are limited in their predictability because multiscale interactions and evolutionary processes are linked through non-linear interactions. ■

REFERENCES

- Baglaeva E.M., Sergeev A.P., Shichkin A.V., Buevich A. G. (2020). The Effect of Splitting of Raw Data into Training and Test Subsets on the Accuracy of Predicting Spatial Distribution by a Multilayer Perceptron. *Math. Geosci.*, 52, 111–121.
- Baglaeva E.M., Sergeev A.P., Shichkin A.V., Buevich A.G. (2021). The Extraction of the training subset for the spatial distribution modelling of the heavy metal in topsoil. *Catena*, 207, 105699. <https://doi.org/10.1016/j.catena.2021.105699>
- Boussange V., Pellissier L. (2022). Eco-evolutionary model on spatial graphs reveals how habitat structure affects phenotypic differentiation. *Communications Biology*, 5, 668. <https://doi.org/10.1038/s42003-022-03595-3>
- Dale M.R. and Fortin M. (2010). From graphs to spatial graphs. *Annu. Rev. Ecol. Evol. Syst.*, 41, 21–38.
- Demyanov V., Gloaguen E., Kanevski M. (2020). A special issue on data science for geosciences. *Math. Geosci.*, 52, 1–3.
- Fernandez Jaramillo J.M. and Mayerle R. (2018). Sample selection via angular distance in the space of the arguments of an artificial neural network. *Computers and Geosciences*, 114, 98–106.
- Gutierrez-Velez V.H. and Wiese D. (2020). Sampling bias mitigation for species occurrence modeling using machine learning methods. *Ecological Informatics*, 58, 101091. <https://doi.org/10.1016/j.ecoinf.2020.101091>.
- Kramm T. and Hoffmeister D. (2020). Assessing the influence of environmental factors and datasets on soil type prediction with two machine learning algorithms in a heterogeneous area in the Rur catchment, Germany. *Geoderma Regional*, 22, e00316. <https://doi.org/10.1016/j.geodrs.2020.e00316>.
- Legendre P., Dale M.R.T., Fortin M.J., et. al. (2004). Effects of spatial structures on the results of field experiments. *Ecology*, 85(12), 3202–3214.
- Levin S.A. (2002). Complex adaptive systems: Exploring the known, the unknown and the unknowable. *Bull. Am. Math. Soc.*, 40, 3–20.
- Liu Q., Li H., Guo L., et.al. (2022). Digital mapping of soil organic carbon density using newly developed bare soil spectral indices and deep neural network. *Catena*, 219, 106603. <https://doi.org/10.1016/j.catena.2022.106603>.
- Malof J.M., Reichman D., Collins L.M. (2018). How do we choose the best model? The impact of cross-validation design on model evaluation for buried threat detection in ground penetrating radar. *Proceedings. 10628, Detection and Sensing of Mines, Explosive Objects, and Obscured Targets XXIII*, 106280C. <https://doi.org/10.1117/12.2305793>
- de Mello D.C., Ferreira T.O., Veloso G.V., et. al. (2022). Pedogenetic processes operating at different intensities inferred by geophysical sensors and machine learning algorithms. *Catena*, 216, Part A, 106370, ISSN 0341-8162. <https://doi.org/10.1016/j.catena.2022.106370>.

Nath A. and Subbiah K. (2018). The role of pertinently diversified and balanced training as well as testing data sets in achieving the true performance of classifiers in predicting the antifreeze proteins. *Neurocomputing*, 272, 294–305.

O'Brien D., Manseau M., Fall A., Fortin M.-J. (2006). Testing the importance of spatial configuration of winter habitat for woodland caribou: An application of graph theory. *Biological Conservation*, 130, 70–83.

O'Hare M.T., Gunn I.D.M., Critchlow-Watton N., et. al. (2020). Fewer sites but better data? Optimising the representativeness and statistical power of a national monitoring network. *Ecological Indicators*, 114, 106321. <https://doi.org/10.1016/j.ecolind.2020.106321>.

Pesch R., Schröder W., Dieffenbach-Fries H., et. al. (2008). Improving the design of environmental monitoring networks. Case study on the heavy metals in mosses survey in Germany. *Ecological Informatics*, 3(1), 111–121. <https://doi.org/10.1016/j.ecoinf.2007.11.001>.

Prager S.D. and Reiners W.A. (2009). Historical and emerging practices in ecological topology. *Ecological complexity*, 6, 160–171. doi:10.1016/j.ecocom.2008.11.001

Shichkin A.V., Buevich A.G., Sergeev A.P., et. al. (2018). Prediction of the content of anomalously distributed chromium in the soil by hybrid models based on artificial neural networks. *Geoecology. Engineering geology. Hydrogeology. Geocryology*, 3, 86–96. [in Russian]

Urban D.L., Minor E.S., Trembl E.A., Schick R.S. (2009). Graph models of habitat mosaics. *Ecology Letters*, 12, 260–73.

Wang I.J. and Bradburd G.S. (2014). Isolation by environment. *Molecular Ecology*, <https://doi.org/10.1111/mec.12938>

Wang X., An Sh., Xu Y., et. al. (2020). A back propagation neural network model optimized by mind evolutionary algorithm for estimating Cd, Cr, and Pb concentrations in soils using Vis-NIR diffuse reflectance spectroscopy. *Applied Sciences*, 10(51), 1–17. <https://doi.org/10.3390/app10010051>

Wang Y., Ma H., Wang J., et. al. (2021). Hyperspectral monitor of soil chromium contaminant based on deep learning network model in the Eastern Junggar coalfield. *Spectrochimica Acta Part A: Molecular and Biomolecular Spectroscopy*, 257, 119739. <https://doi.org/10.1016/j.saa.2021.119739>.

Xu Q., Zhu A.-X., Liu J. (2023). Land-use change modeling with cellular automata using land natural evolution unit. *Catena*, 224, 106998. <https://doi.org/10.1016/j.catena.2023.106998>.

Zhu A.X., Liu J., Du F., et.al. (2015). Predictive soil mapping with limited sample data. *European Journal of Soil Science*. 66, 535–547. doi: 10.1111/ejss.12244

Zhu A.X., Lu G., Liu J., et.al. (2018). Spatial prediction based on Third Law of Geography. *Annals of GIS*, 24 (4), 225–240. <https://doi.org/10.1080/19475683.2018.1534890>

Zhu A.X., Lv G.N., Zhou C.H., et al. (2020). Geographic similarity: Third Law of Geography? *Journal of Geoinformation Science*, 22(4), 673–679. <https://doi.org/10.12082/dqxxkx.2020.200069>.

Zhong L., Guo X., Xu Zh., Ding M. (2021). Soil properties: Their prediction and feature extraction from the LUCAS spectral library using deep convolutional neural networks. *Geoderma*, 402, 115366.

Ziggah Y.Y., Youjian H., Tierra A.R., Laari P.B. (2019). Coordinate Transformation between Global and Local Data Based on Artificial Neural Network with K-Fold Cross-Validation in Ghana. *Earth Sciences Research Journal*, 23(1), 67–77. <https://doi.org/10.15446/esrj.v23n1.63860>.

EXPLORING GEOSPATIAL CLUSTERS OF FIVE PRIMARY RESPIRATORY DISEASES IN SOUTH PUNJAB, PAKISTAN: AN EPIDEMIOLOGICAL EXAMINATION

Munazza Fatima^{1*}, Ibtisam Butt², Neda Firouraghi³, Behzad Kiani⁴

¹ Department of Geography, The Islamia University of Bahawalpur, Bahawalpur, Punjab Pakistan

² Institute of Geography, University of the Punjab Lahore, Pakistan

³ Centre de Recherche en Santé Publique (CRéSP), Département de Médecine Sociale et Préventive, École de Santé Publique, Université de Montréal, Montreal, Quebec, Canada

⁴ University of Queensland Centre for Clinical Research, The University of Queensland, Brisbane, Australia

*Corresponding author: munazza.fatima@iub.edu.pk

Received: August 22nd 2024 / Accepted: November 27th 2024 / Published: March 31st 2025

<https://doi.org/10.24057/2071-9388-2025-3568>

ABSTRACT. Respiratory diseases constitute a significant burden of morbidity and mortality in developing nations such as Pakistan. This study aims to analyze five prevalent respiratory ailments - acute respiratory infections (ARI), tuberculosis (TB), pneumonia, asthma, and chronic obstructive pulmonary diseases (COPD) - within South Punjab, Pakistan. Utilizing the tehsil level (the administrative sub unit of district), case data spanning five years (2016-2020) were collected from 1,487 government health centers across the study area. Spatial analysis techniques including Local Moran's I and Getis Ord Gi* statistics were employed to identify clusters and outliers. The results revealed spatial heterogeneity in respiratory disease prevalence, delineating both high-intensity (hotspots) and low-intensity (cold spots) clusters across the region. Specifically, ARI hotspots were observed in northeastern and central regions, asthma hotspots in central and north-central areas, COPD hotspot areas in the north and northeast, pneumonia hotspots in the central region, and TB hotspots predominantly in the central region. These findings offer critical insights for targeted public health interventions, facilitating resource allocation for disease prevention and control efforts. Additionally, this study presents recommendations addressing local environmental and socio-economic factors to mitigate respiratory disease incidence through administrative environmental management and community engagement strategies.

KEYWORDS: respiratory diseases, spatial analysis, hotspots, public health interventions, South Punjab

CITATION: Fatima M., Butt I., Firouraghi N., Kiani B. (2025). Exploring Geospatial Clusters of Five Primary Respiratory Diseases in South Punjab, Pakistan: An Epidemiological Examination. *Geography, Environment, Sustainability*, 14-22
<https://doi.org/10.24057/2071-9388-2025-3568>

Conflict of interests: The authors reported no potential conflict of interest.

INTRODUCTION

Respiratory diseases profoundly influence public health and contribute significantly to global morbidity and mortality rates. Whether they manifest acutely or chronically and exhibit communicable or non-communicable characteristics, respiratory diseases impose a substantial global burden, affecting millions of individuals (ERS 2021). The spectrum of respiratory diseases includes a range of conditions, each with distinct characteristics and impacts on pulmonary health (John Hansen-Flaschen et al., 2023). ARI, a transient affliction lasting less than 30 days, may affect various respiratory components, including the lungs, trachea, bronchioles, or nasal cavity (Jolliffe et al., 2013). Pneumonia, a more severe lower respiratory infection, not only shares the respiratory domain with ARI but also poses a threat to lung functionality by filling alveoli with pus and fluid, resulting in breathing difficulties (EPI 2018). COPD, an incurable yet manageable condition, introduces a chronic

dimension to respiratory health, impacting airways and lung structures with persistent airflow blockage and associated breathing challenges (CDC 2022a). The chronicity of COPD contrasts with the transient nature of ARI and the severity of pneumonia. However, asthma, characterized by airway inflammation and muscle constriction, contributes to the complexity of respiratory diseases, affecting individuals of all age groups with symptoms such as coughing, wheezing, shortness of breath, and chest tightness (WHO 2021). While asthma and COPD share certain symptoms, the underlying mechanisms and triggers often differ. TB, caused by mycobacterium tuberculosis, presents another facet of respiratory health, primarily targeting the lungs but also capable of affecting organs beyond the respiratory system, such as the kidneys, spine, and brain (CDC 2016). TB introduces an infectious dimension, distinct from the acute and chronic respiratory conditions previously discussed. Each respiratory disease has its own set of factors.

Lung cancer, asthma, acute respiratory infections, tuberculosis (TB), and chronic obstructive pulmonary disease (COPD) are the five main respiratory diseases that place a significant burden on society (Marciniuk et al., 2014; Wisnivesky & De-Torres, 2019). It is estimated that globally around a billion people suffer from seasonal influenza annually (WHO, 2023b), 488.9 million people from lower respiratory infections (Safiri et al., 2022), 454.6 million people from COPD (Momtazmanesh et al., 2023), 262 million people from asthma (WHO, 2023a), and 10.6 million from TB (WHO 2020b). In addition, on a global scale, four million individuals experience premature mortality due to chronic respiratory diseases (Ferkol & Schraufnagel, 2014; WHO, 2007; Wisnivesky & De-Torres, 2019). A recent study stated that during the year 2019 there were approximately 454.6 million reported cases of chronic respiratory diseases worldwide (Momtazmanesh et al., 2023). Young children and infants are particularly vulnerable. Nearly three million children, the majority of whom were under five, lost their lives to lower respiratory tract infections and pneumonia, particularly in developing and underdeveloped regions (Lim et al., 2012).

Respiratory diseases also contribute significant disease burden in Pakistan. In 2019, the country reported over 200 million cases of upper respiratory infections (Liu et al., 2022) and annually witnesses around half a million new TB cases, with approximately 15 thousand evolving into drug-resistant strains (WHO 2022). Pneumonia, claiming the lives of over one million children each year, stands as the leading cause of death among children in Pakistan (EPI 2018). COPD ranks as the seventh major cause of death in the country, contributing to nearly 5% of total mortality (CDC 2022b). Moreover, there is a growing concern that this percentage may rise in the coming years (Amir Khan et al., 2019). Also, asthma has a substantial impact on the population in Pakistan, with an estimated fifteen million children and 7.5 million adults living with the condition (Khan; Noman et al., 2016). As per the District Health Information System (DHIS), ARI stands as the primary contributor to morbidity in the Punjab Province. The calculated mean index of the top ten diseases spanning the years 2015 to 2018 revealed that ARI, with a prevalence of 12.67%, ranks as the foremost ailment within the province (DHIS 2019). Likewise, in South Punjab, Pakistan, acute respiratory infections constitute a substantial burden, comprising 24% of all reported diseases and a staggering 77% of all respiratory diseases within the region. (DHIS 2019). Some factors responsible for these high respiratory diseases rates are indoor (Rabbani et al., 2022) and ambient air pollution (Fatima et al., 2023a), smoking (Cinar & Dede 2010), adult crowding, increased family size, poor ventilation and use of biofuels, illiteracy, and unawareness of the disease (Khaliq et al., 2015).

Numerous investigations conducted in Pakistan have employed spatial clustering techniques to explain the distribution patterns of diverse diseases. Notable examples include studies on polio (Ahmad et al. 2015), malaria (Fatima, Butt, et al., 2022; Umer et al. 2018), dengue (Khaliq et al., 2023; Naqvi et al. 2021) and cutaneous leishmaniasis (Zeb et al. 2021). However, the existing literature reveals a scarcity of studies focusing on the spatial cluster analysis of respiratory diseases. Only few studies has been identified such as those on TB (I. Fatima et al. 2021; Fatima et al. 2024; Miandad et al. 2014), asthma (Khan et al. 2020) and ARI (Fatima, Khattak, et al. 2022). These studies focused either on one disease at a time or covered a small region. Hence, against this backdrop, we set out to investigate clusters and hotspots of all major respiratory diseases in South Punjab at the tehsil level as the finest geographical scale to identify high-risk areas and provide a foundation for more scientific investigation into the etiology of each respiratory disease.

Literature review

The global prevalence of respiratory disease varies regionally. The WHO estimates that respiratory infections cause 6% of all diseases in the world. Throughout the globe, 6.6 million children under the age of five die every year because of respiratory infections out of which 95% are from low-income nations (Ghimire et al. 2022). Similarly, South Asia exhibited the most elevated mortality rates associated with chronic respiratory disease, whereas sub-Saharan Africa recorded the lowest (Labaki & Han 2020). In 2021, TB caused 1.6 million deaths, making it the second leading cause of death after COVID-19 (WHO 2020b). Asthma has been associated with one in every 250 deaths globally, ranking 26th among causes contributing to years of life lost in South Asia (Burney et al., 2015; Masoli et al. 2004). Based on the most recent data from the WHO published in 2020, the incidence of lung disease-related fatalities in Pakistan escalated to 86,968 constituting 5.96% of the total mortality rate (WHO 2020a). The age-adjusted death rate stands at 77.79 per 100,000 individuals, positioning Pakistan at the eighth rank globally in this regard (WHO 2020a). Hence, there is a multifactorial difference in the mortality rate of respiratory diseases globally that is linked to various etiological agents, available therapeutics, exposure frequencies, and host immunity (Ho et al., 2018).

Spatial analysis of respiratory diseases involves using geographic information system (GIS) and spatial analytic techniques to study the distribution and patterns of respiratory diseases in specific regions (Rex et al. 2020). When it comes to geographical surveillance for geographically dispersed diseases, the main obstacles are identifying areas with markedly higher prevalence rates, carrying out statistical analyses to determine their importance, and explaining the factors that contribute to the higher disease prevalence in these areas (Tiwari et al., 2006). Spatial clustering and hotspot detection techniques using the Anselin Local Moran's I statistic and the Getis-Ord G_i^* statistic play a vital role in ensuring accurate examination of such areas (M. Fatima et al. 2021; Kiani et al. 2023; Laohasirwong et al. 2017). This spatial clustering technique has been employed to only Bahawalpur district of South Punjab in analyzing ARI during 2010-2015 (Fatima, Khattak et al. 2022). However, the current study appears to be the first of its type in that it provides fine-grained spatial patterns of all the main respiratory diseases across 11 districts in South Punjab, especially at the tehsil level. This degree of detail may provide insightful information on the distribution and incidence of respiratory diseases in the area, which might help better guide public health initiatives and the distribution of resources. The study's coverage of several districts may also make it possible to compare and identify regional differences in the frequency and distribution of respiratory diseases. All things considered, this kind of research has the potential to greatly advance our knowledge of respiratory health in the concerned region and support the creation of focused preventative and management plans.

METHODS

Study area

The focus of this research is an area called South Punjab, which is the most populous province in Pakistan. It is situated in the southern part of the larger Punjab region. South Punjab spans across a total area of 99,579 square kilometers and is located between coordinates 69.5–74°E and 27.6–31.4°N. It shares borders with India to the east, Sindh Province to the south, a portion of Baluchistan Province to the west, and North Punjab to the north. South Punjab is made up of three divisions: Bahawalpur, Dera Khazi Khan (D.G. Khan), and Multan. These

divisions are further divided into 11 districts and 46 Tehsils, as shown in Fig. 1. For this study, all tehsils within South Punjab have been included for spatial analysis.

The environmental risk factors, including indoor and outdoor air pollution and frequent dust storms in summer, which are coupled with high density and low socio-economic conditions could increase vulnerability to respiratory diseases. The climate in South Punjab is characterized by intense heat and aridity during the summer months and dust storms are common throughout the season (GOP 2021). High values of particulate matter (30 - 70PM_{2.5} µg/m³) making this region's air quality unhealthy and sometimes very unhealthy according to the WHO air quality standards (Fatima et al. 2023b). In addition, almost 87.6% population rely on solid fuel for cooking and heating (Sajid Rasul et al. 2021).

This region is one of the poor regions of Pakistan with multi-fold environmental and socio-economic issues. The prevalence of multi-dimensional poverty significantly surpasses that observed in other regions of the province, characterized by high rates of stunting growth, extensive undernourishment, incomplete access to clean water and hygiene, and a great number of out-of-school children (UNDP 2022). The literacy

rate in the region is notably deficient, averaging at 46.2% across the entire population (Sajid Rasul et al. 2021; UNP 2022). Additionally, the area exhibits a substantial dependency ratio of 79.6%, highlighting a considerable portion of the population dependent on adults for support (GOP 2018). All of these make South Punjab a good choice for this study.

Disease Data

The respiratory disease data was spatially aggregated at the tehsil level, while temporally it spanned monthly records as reported cases from January 2016 to December 2020. Primary disease data collection was conducted through the District Health Information System (DHIS) of respective districts, utilizing consolidated reports of cases from each health facility within the district. A comprehensive network of healthcare facilities in the South Punjab region, comprising 102 hospitals, 383 dispensaries, 110 rural health centers, 762 basic health centers, 6 TB centers, 56 sub-health centers, and 68 maternity health centers, facilitated the acquisition of disease data. Fig. 2 represents the steps of methods and results.

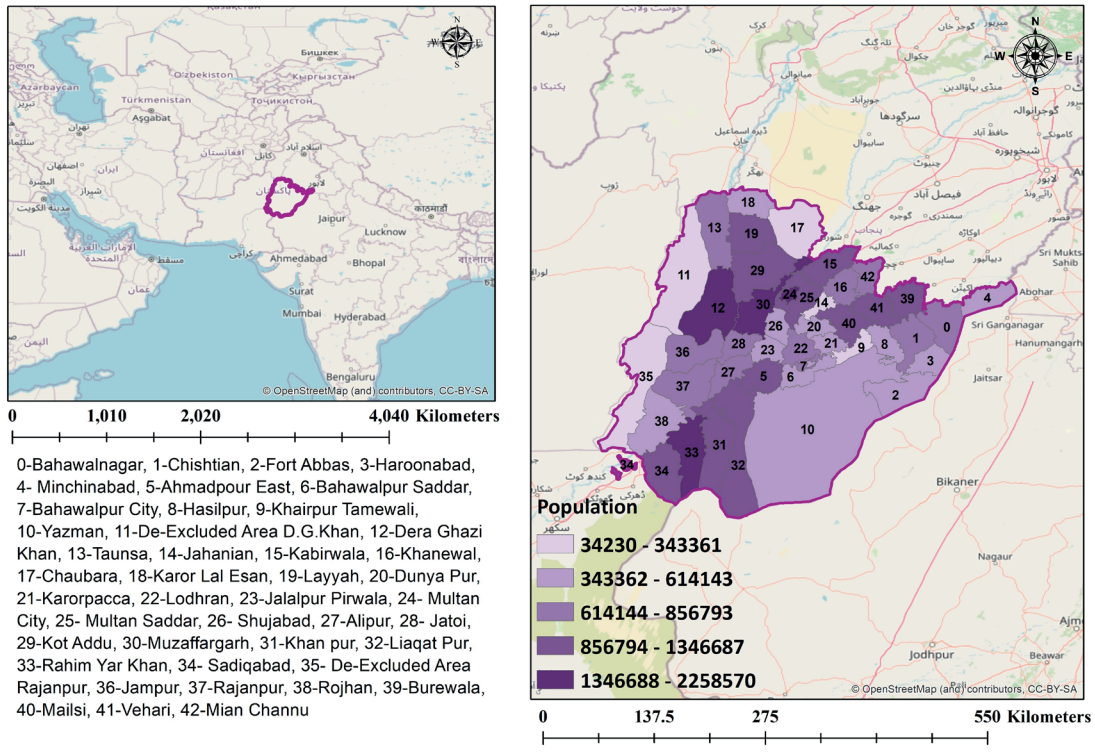


Fig. 1. Map of the study area including the population at the Tehsil level in South Punjab

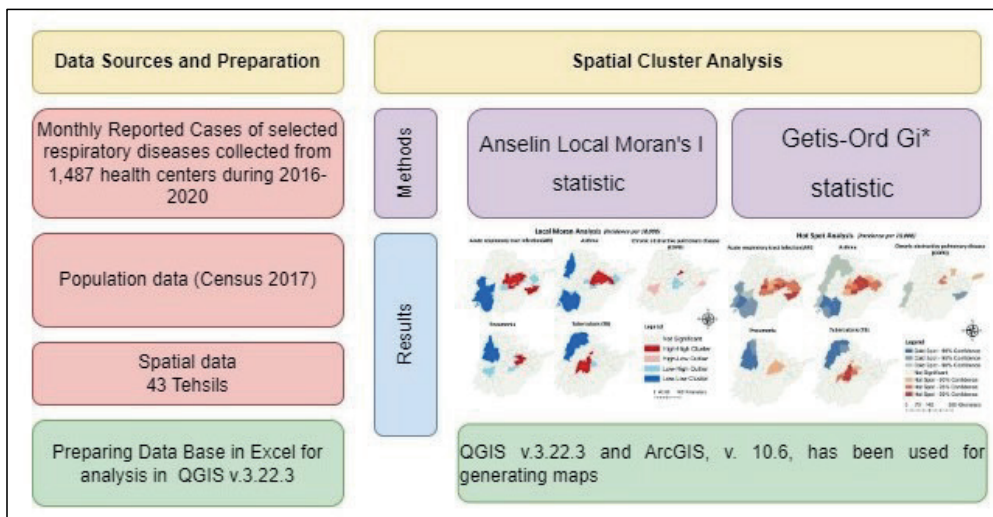


Fig. 2. Methodological Steps

Spatial analysis

This study incorporated two local spatial methods, specifically Local Moran's I and Getis-Ord G_i^* . Both the Anselin Local Moran's I statistic and the Getis-Ord G_i^* statistic were employed to analyze the clustering patterns of respiratory disease incidence and identify areas with high incidence (hotspots) (Anselin, 1995; Getis & Ord 1992; Ord & Getis 1995). The primary aim was to assess the spatial patterns in the observed data values for each location. In both instances, the null hypothesis assumed the absence of spatial clustering or patterns in the distribution of the observed data values. Essentially, it signifies that the data values are randomly dispersed across the study area without any significant clustering or spatial interrelation.

Spatial autocorrelation and cluster outlier analysis Global and local Moran's I statistics is applied on incidence rates of respiratory diseases. Global Moran's I provide an overall measure of spatial autocorrelation for an entire dataset, indicating whether there is a general clustering or dispersion of similar values across the study area. In this study, we employed the Euclidean distance method to calculate spatial relationships. However, Local Moran I, also known as Local Indicators of Spatial Association (LISA), is a spatial method extensively used for assessing spatial autocorrelation in geospatial data sets. It plays a key role in spatial analysis. The Local Moran I calculation involves comparing the value of each observation with the values of its neighboring observations. This analysis aims to determine if there is a relationship between the value of a specific location and its neighboring values. The spatial association is measured by employing a standardized z-score formula. Positive values indicate positive spatial autocorrelation, which signifies the presence of clusters with similar values. Conversely, negative values indicate negative spatial autocorrelation or spatial outliers. Clusters and outliers offer a deeper understanding of how certain areas or locations relate to their surrounding neighbors (Anselin, 1995). The clusters indicate that similar values tend to be spatially clustered together. There are two types of local Moran clusters (Anselin, 1995):

- High-High (HH): High-High clusters represent areas with high respiratory disease incidence that are surrounded by other high-value areas. These clusters indicate the presence of spatially concentrated regions of high values.
- Low-Low (LL): Low-Low clusters represent areas with low disease incidence that are surrounded by other low-value areas. These clusters indicate the presence of spatially concentrated regions of low values.

Local Moran outliers, also known as spatial outliers, are locations that exhibit values significantly different from their neighboring areas. They represent locations with values that do not conform to the spatial pattern observed in the surrounding regions. There are two types of local Moran outliers:

- High-Low (HL): High-Low outliers represent areas with high values that are surrounded by low-value areas. These outliers indicate the presence of areas with unusually high values in regions where low values are predominant.
- Low-High (LH): Low-High outliers represent areas with low values that are surrounded by high-value areas. These outliers indicate the presence of areas with unusually low values in regions where high values are predominant.

Local Moran I statistic is calculated using equation 1:

$$I_i = \frac{\sum_{j=1}^n w_{ij} (x_i - \bar{x})(x_j - \bar{x})}{\frac{1}{n} \sum_{i=1}^n (x_i - \bar{x})^2}, \quad i \neq j \quad (1)$$

In this formula, " x_i " and " x_j " represent observed values at two different locations i and j , " \bar{x} " is the average of these observed values, " n " is the total number of assessed locations, and " w_{ij} " represents the spatial weight associated with observations (Anselin, 1995).

Hot-spot analysis (Getis-Ord G_i^* statistic)

Another spatial approach is hot-spot analysis, which calculates the Getis-Ord G_i^* statistic, as a spatial measure that is used to identify local clusters of high or low values for a specific phenomenon within a geographical dataset (Getis & Ord 1992). It utilizes spatial weights to define the neighborhood relationships between spatial units. The spatial weights matrix defines the proximity and strength of interaction between neighboring units. The Getis-Ord G_i^* statistic calculates a z-score, p-value, and confidence level (CI) bin for each individual location in a study area, indicating the degree of spatial clustering and the significance of that clustering. Statistical significance can be determined by comparing the z-scores to critical values obtained from a normal distribution or through permutation methods. In this study, permutation methods were used in conjunction with the Getis-Ord G_i^* statistic (Anselin, 1995; Ord & Getis, 1995). The number of permutations was 499, which indicates that 499 random shuffling of attribute values were performed to establish the reference distribution.

Eq. 2 is used to calculate the Getis-Ord G_i^* statistic:

$$G_i^* = \frac{\sum_{j=1}^n w_{i,j} x_j - \bar{x} \sum_{j=1}^n w_{i,j}}{\sqrt{s \left(n \sum_{j=1}^n w_{i,j}^2 - \left(\sum_{j=1}^n w_{i,j} \right)^2 \right)}} \quad (2)$$

The given expression suggests that x_j represents the observed value for a specific region j . w_{ij} indicates the spatial weight between two regions, i and j . The total number of regions is represented by n . \bar{x} denotes the average value of the observed values, and s represents the standard deviation (Getis & Ord, 1992).

RESULTS

Global Moran's I

Global Moran's I was employed to assess the spatial autocorrelation for each disease, determining whether similar values were clustered, randomly distributed, or dispersed across the study area. The Euclidean distance method was used to compute spatial relationships between geographic units. The results revealed varying patterns of spatial distribution (Fig 3). For pneumonia, the Moran's I value (0.0073) indicated no significant clustering, suggesting a random spatial pattern ($p = 0.599$). In contrast, ARI displayed a strongly clustered pattern, with a Moran's I of 0.2652 and a z-score of 3.7268, meaning there is less than a 1% likelihood that the clustering occurred by random chance ($p = 0.0001$). Similarly, asthma showed significant clustering (Moran's I = 0.1057), with a z-score of 2.2861, indicating less than a 5% probability of this pattern arising randomly ($p = 0.022$). However, for COPD, the Moran's I value of -0.1106 suggested no significant departure from randomness ($p = 0.227$). Lastly, tuberculosis exhibited the strongest clustering, with a Moran's I of 0.3054 and a z-score of 4.1643, indicating a less than 1% likelihood that the clustering is due to chance ($p = 0.000031$) (Table 1).

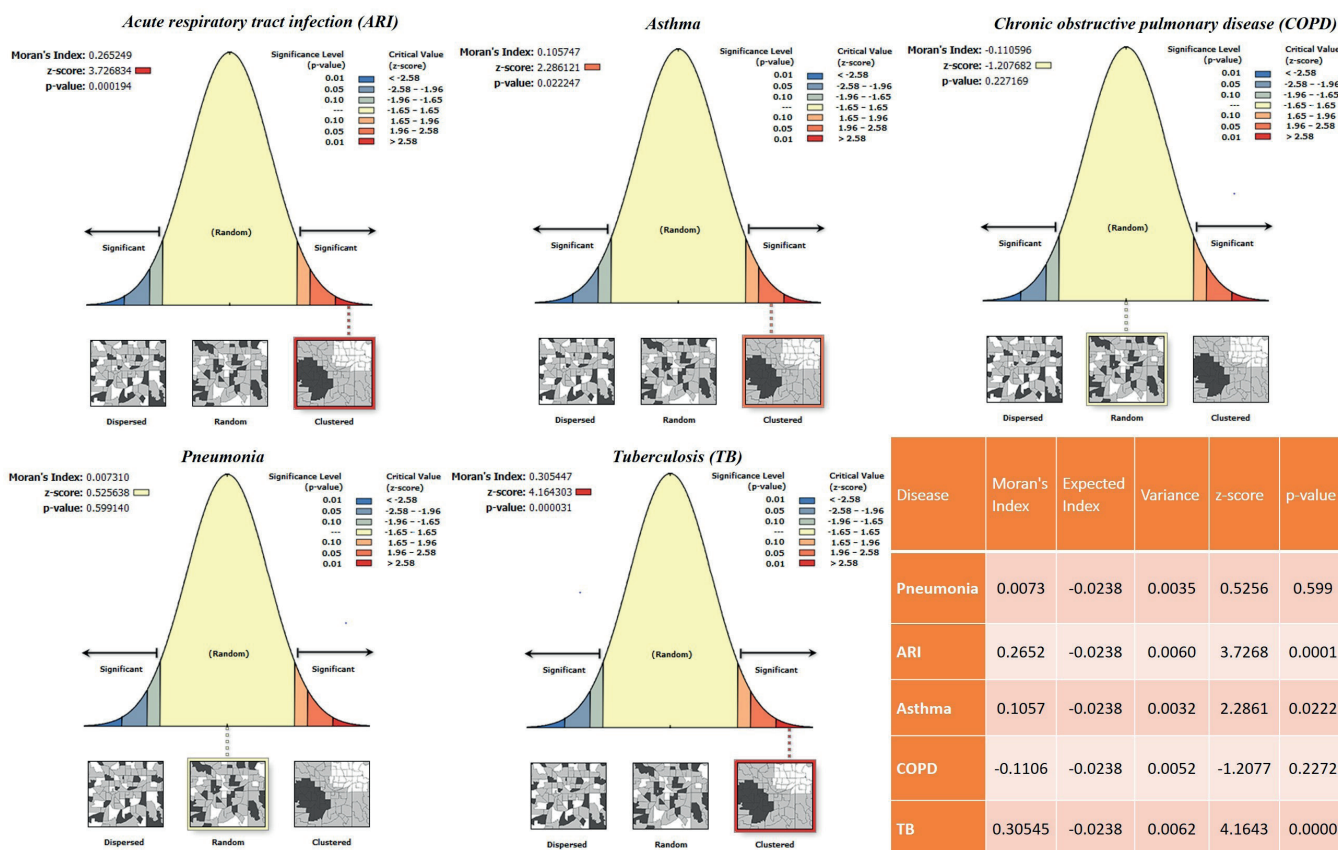


Fig. 3. Global Moran's I result for respiratory diseases incidence rates in South Punjab during 2016-2020

Table 1. Global Moran's I Summary by Disease

Disease	Moran's Index	Expected Index	Variance	z-score	p-value
Pneumonia	0.0073	-0.0238	0.0035	0.5256	0.599
ARI	0.2652	-0.0238	0.0060	3.7268	0.0001
Asthma	0.1057	-0.0238	0.0032	2.2861	0.0222
COPD	-0.1106	-0.0238	0.0052	-1.2077	0.2272
Tuberculosis	0.30545	-0.0238	0.0062	4.1643	0.0000

Anselin Local Moran I

Clusters and outliers identified by Anselin local Moran's I are detected and presented in Fig. 4. These results reveal the spatial variation patterns of common respiratory diseases.

Acute respiratory infection (ARI)

For ARI, the HH clusters were located in Fort Abbas, Bahawalpur Saddar, Dunya Pur, Karorpacca, Lodhran, Jalalpur Pirwala, Shujabad, Mailsi and the southwest part of South Punjab displayed LL cluster. According to Moran I statistics, Chishtian, Ahmadpour East, and Khairpur Tamewali were LH areas that were surrounded by areas with high ARI incidence.

Asthma

In terms of asthma, Bahawalpur City, Hasilpur, Khairpur Tamewali, Jahanian, Dunya Pur, Karorpacca, Lodhran, and Mailsi exhibited high-high clusters. Conversely, De-excluded areas D.G.Khan, Khan pur, Rahim Yar Khan, Sadiqabad, Rojhan were concentrated in low-low clusters. Chishtian, Bahawalpur Saddar, and Jalalpur Pirwala had a lower incidence of asthma but were surrounded by areas with higher incidence rates.

Chronic obstructive pulmonary disease

COPD is predominantly associated with a high-risk cluster in Jahanian, low-high areas in Bahawalpur Saddar and Lodhran, as well as high-low clusters in Haroonabad and Rajanpur.

Pneumonia

In terms of Pneumonia, Karorpacca and Mailsi were identified as high-risk clusters, while the areas of De-excluded, D.G.Khan and Dera Ghazi Khan, were found to be low-risk clusters. Additionally, Bahawalpur Saddar, Jahanian, and Rajanpur displayed characteristics of low-high areas in relation to Pneumonia.

Tuberculosis

When it comes to tuberculosis, there is a high-risk cluster that encompasses Ahmadpur East, Jalalpur Pirwala, Multan City, Shujabad, Alipur, and Jatoi. However, De-Excluded Area D.G.Khan, Taunsa, Karor Lal Esan, and Layyah have been identified as low-risk clusters. Although Lodhran itself is a low-risk area, with an increased risk of the disease in the surrounding regions.

Hot-spot analysis (Getis-Ord G_i^* statistic)

The utilization of hotspot analysis allows us to identify locations where there is a statistically significant incidence of diseases and create maps highlighting these hotspots and cold spots. This is accomplished through the calculation of z-scores, with negative values indicating cold spots and positive values indicating hotspots (Fig 5).

Acute respiratory tract infection

The current study revealed the existence of distinct spatial clusters in certain locations, suggesting the presence of hotspots for ARI in the northeastern and central regions of the study area. Conversely, the southwestern area was identified as a cold spot, indicating a lower incidence of ARI cases in that specific region.

Asthma

The figure displays the spatial distribution of asthma hotspots, which are primarily situated in the central and north-central regions. Conversely, cold spots, where the

incidence of asthma is relatively lower, are concentrated in the southern and southwestern areas.

Chronic obstructive pulmonary disease

Regarding COPD, the high-risk areas are primarily located in the north and northeast, whereas the cold spot with a 95% confidence interval is situated in the eastern part of the study area.

Pneumonia

The map demonstrates that when it comes to pneumonia, the central part of the study area has hotspots, while the cold spots are mainly located in the northwestern region.

Tuberculosis

In terms of TB, the map illustrates that the central part exhibits a greater number of hotspots with high z-score values, while the cold spots are concentrated in the northwestern region.

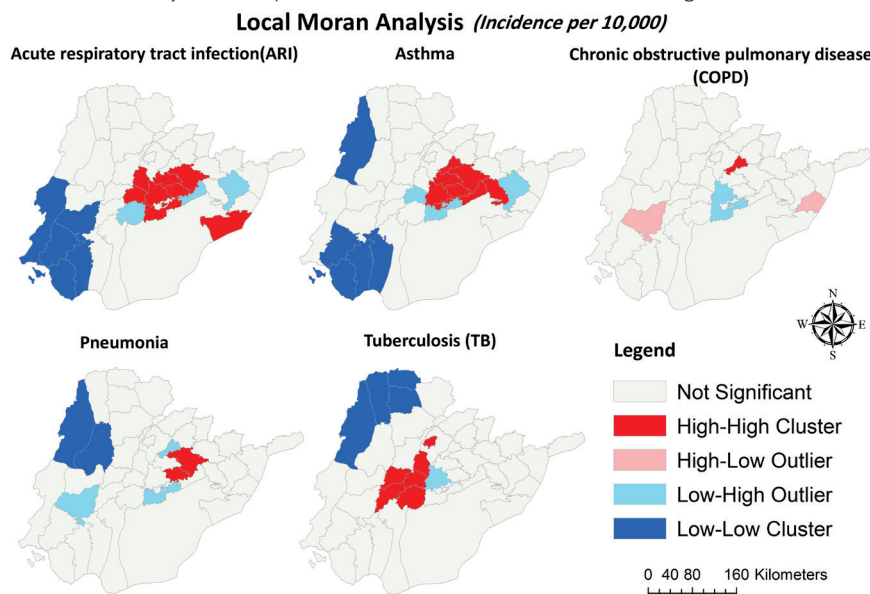


Fig. 4. Spatial clusters and outliers of respiratory diseases incidence rates, using local Moran I statistics, in South Punjab during 2016-2020

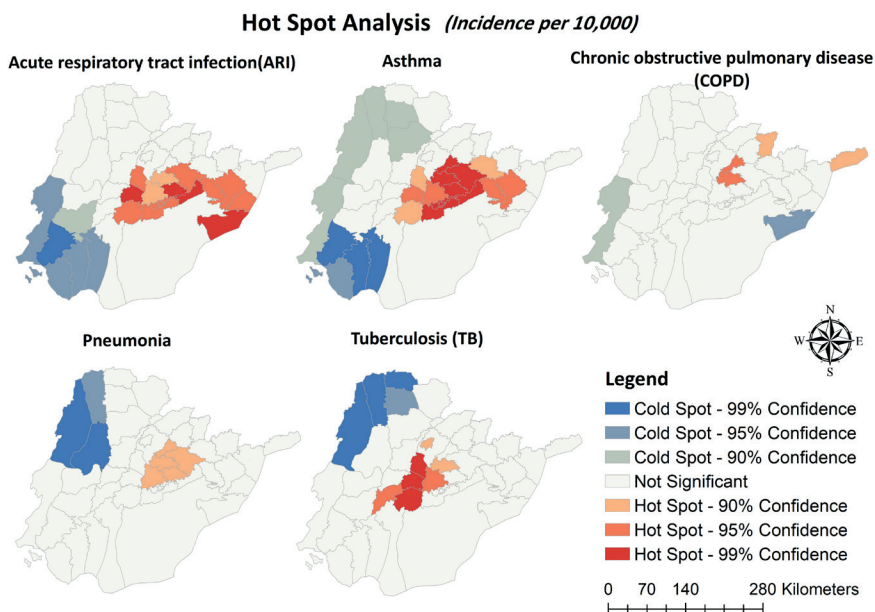


Fig. 5. Spatial hotspots and cold spots of respiratory diseases incidence rates, using Getis-ord G_i^* statistics, in South Punjab during 2016-2020

DISCUSSION

The geospatial epidemiological analysis conducted in South Punjab, Pakistan, revealed complex patterns in the spatial distribution of five major respiratory diseases. Using Anselin Local Moran's I and hotspot analysis (Getis-Ord G_i^* statistic), the study identified distinct clusters and hotspots, offering valuable insights into the epidemiological dynamics of these diseases within the region. Specifically, the analysis highlighted significant clustering patterns for ARI, asthma, COPD, pneumonia, and tuberculosis.

The findings indicated the prevalence of HH clusters across multiple tehsils, alongside the presence of LL clusters in specific regions. Moreover, areas exhibiting LH characteristics were surrounded by elevated disease rates, suggesting localized factors influencing disease transmission. Hotspot analysis further validated these clusters, identifying statistically significant disease incidence areas.

The environmental and socio-economic conditions prevalent in South Punjab create an environment that is highly favorable for the occurrence of respiratory diseases. While each respiratory disease may have its unique risk factors, there are shared elements that impact the respiratory health of individuals in the region.

The climate of this region is of extreme type with January and December being the coldest months in the region with temperatures usually lower than 15°C (PMD, 2020). Influenza as the most prevalent infection among the Pakistan population is found to be high in the spring and winter seasons (Naz et al., 2019). A previous study by Fatima et al. (2022) also supports the fact that during 2010-2012 ARIs were widely reported during winter seasons in the Bahawalpur district. Fog similarly promotes influenza transmission and causes respiratory problems. In foggy weather, aerosol inhalation, as noted by Song et al. (2022), is frequent, particularly during the winter season in South Punjab (Song et al. 2022). The number of foggy days increased up to an average of 7 days/month during December and January in this region (PMD 2020). Furthermore, it is proved through literature that dust storms affect respiratory health by direct inhalation of particles (Sadeghimoghaddam et al. 2021). In this context, South Punjab is an arid and semi-arid region, with frequent dust storms with an average of 10 to 20 dust storms from April to August (PMD 2020). While these dust storms are prevalent across the entirety of South Punjab, they are particularly pronounced in the southeastern area, which comprises the Cholistan Desert (Britannica 2010).

Ambient air pollution is one of the prime factors affecting the respiratory health of the population of this region, as South Punjab exhibits, high values of particulate matter ($30 - 70\text{PM}_{2.5} \mu\text{g}/\text{m}^3$) making this region's air quality unhealthy and sometimes very unhealthy according to the WHO air quality standards (Fatima et al. 2023a). Similarly, 87.6% of households rely on solid fuel for cooking and heating making the indoor air quality bad and making respiratory health vulnerable (Sajid Rasul et al. 2021). Pakistan is one of the most polluted countries in the world, and COPD has the highest mortality and morbidity burden attributed to air pollution. In 2019, COPD represented the greatest burden, accounting for 57% of total deaths attributed to air pollution (Fatima et al. 2023a). Apart from air pollution, smoking is recognized as a primary risk factor for COPD (Leberl et al. 2013; Liu et al. 2015). In this region, nearly 24% of males and 3.3% of females are reported to be tobacco smokers (UNICEF 2019) making them vulnerable to respiratory diseases.

The spatial patterns of respiratory diseases showed that the central part of South Punjab is a hotspot of almost all respiratory diseases. Therefore, multiple factors can be related to these respiratory diseases. For instance, the tehsils showing hotspots of respiratory diseases include mainly high-density such as Multan city (7903 persons per km^2) and Bahawalpur city (2773 persons per km^2) (Sajid Rasul et al., 2021). Lai et al. (2013) explored that high-density residential structures increase the risk of TB. The same is the case with South Punjab where on average, there are 6.6 persons per household, with a room density of 3.9 persons per room (UNICEF 2019). Besides, the poor structure of the house also contributes to the risk of respiratory disease (Fakunle et al., 2018), this region is characterized by 32% of households having mud as their primary building material, indicative of the region's low socioeconomic status (Nawab et al. 2022). Illiteracy was found to be positively related to respiratory infections such as COVID-19 (Mohammadi et al. 2023), thus, the literacy rate is as low as 46.6% in South Punjab (GOP 2018) increasing the risk of respiratory infections such as ARI, TB, and pneumonia.

Hence, a multitude of environmental factors including severe weather conditions, frequent dust storms, and ambient air pollution, alongside socioeconomic determinants such as low literacy rates, substandard living conditions, increased transmission risk due to overcrowding, reliance on solid fuels for cooking, smoking habits, elevated levels of ambient air pollution, and constrained access to healthcare services may collectively contribute to the prevalence of respiratory diseases in the region.

The primary strength of this study lies in its comprehensive analysis of the spatial clustering of respiratory diseases within South Punjab, employing commonly utilized methods in epidemiological research. These findings offer potential insights for further exploration of these respiratory disease dynamics concerning additional variables. However, this study also possesses certain limitations. It relied solely on disease data and did not incorporate other relevant factors such as environmental, socio-economic, and behavioral variables in the context of these diseases. Consequently, building upon our results, we suggest future investigations employing spatial regression modeling to investigate deeper into the patterns of each disease within South Punjab, Pakistan.

CONCLUSION

In conclusion, the geospatial epidemiological analysis conducted in South Punjab, Pakistan, has unveiled intricate patterns in the spatial distribution of five major respiratory diseases, shedding light on the epidemiological dynamics within the region. These findings highlight the multifaceted nature of respiratory disease prevalence in South Punjab, which may be influenced by a multitude of environmental and socio-economic factors. Among the studied diseases, asthma is more likely to spread in the region due to its association with air pollution and other environmental factors prevalent in South Punjab. Furthermore, there is a notable interdependence among the diseases, with areas showing high cases of COPD also experiencing increased rates of bronchitis, indicating shared environmental and socio-economic vulnerabilities. While this study provides valuable insights into the spatial epidemiology of respiratory diseases, future research endeavors should consider integrating additional variables and employing spatial regression modeling to further explain the complex dynamics and inform targeted interventions aimed at mitigating the burden of respiratory diseases in South Punjab, Pakistan. ■

REFERENCES

- Ahmad, U., Ahmad, S. R., & Luqman, M. (2015). A study of polio disease in Pakistan using GIS approach. *International Journal of Scientific Technology Research*, 4, 315-322.
- Amir Khan, M., Ahmar Khan, M., Walley, J. D., Khan, N., Imtiaz Sheikh, F., Ali, S., Salahuddin, E., King, R., Ellahi Khan, S., Manzoor, F., & Jehangir Khan, H. (2019). Feasibility of delivering integrated COPD-asthma care at primary and secondary level public healthcare facilities in Pakistan: a process evaluation. *BJGP Open*, 3(1), bjgpopen18X101632. <https://doi.org/10.3399/bjgpopen18X101632>
- Anselin, L. (1995). Local indicators of spatial association—LISA. *Geographical analysis*, 27(2), 93-115.
- Britannica. (2010). Punjab. In N. Tesch (Ed.), *Encyclopedia Britannica: Britannica*.
- Burney, P., Jarvis, D., & Perez-Padilla, R. (2015). The global burden of chronic respiratory disease in adults. *The International Journal of Tuberculosis Lung Disease*, 19(1), 10-20.
- CDC. (2016). Tuberculosis (TB). Centre for Disease Control and Preventions. Retrieved 4.7.2021 from <https://www.cdc.gov/tb/topic/basics/risk.htm>
- CDC. (2022a). Chronic Obstructive Pulmonary Disease (COPD). Centre of Disease Control and Prevention Retrieved 11-11-2022 from <https://www.cdc.gov/copd/index.html>
- CDC. (2022b). Global Health Pakistan. Centre for Disease Control and Prevention. Retrieved 11-11-2022 from <https://www.cdc.gov/globalhealth/countries/pakistan/default.htm>
- Cinar, N. D., & Dede, C. (2010). Effects of environmental tobacco smoke on the respiratory health of children. *Pakistan journal of medical sciences*, 26(1).
- EPI. (2018). Pneumonia. Expanded Programme on Immunisation (EPI). Retrieved 7.11.2022 from <http://www.epi.gov.pk/vaccine-preventable-diseases/pneumonia/>
- ERS. (2021). European Lung White Book. European Respiratory Society <https://www.erswhitebook.org/about/>
- Fakunle, A., Ogundare, J., Olayinka-Alli, L., Aridegbe, M., Bello, T., Elujulo, O., & Saliu, I. J. H. (2018). Housing quality and risk factors associated with respiratory health conditions in Nigeria. 19, 20.
- Fatima, I., Shaikh, W. A., Shaikh, A., Shaikh, A. A., & Abro, S. (2021). The Spatial-Temporal Epidemiology Analysis of Tuberculosis Disease in Pakistan. *Quaid-E-Awam University Research Journal of Engineering, Science Technology, Nawabshah*, 19(2), 60-67.
- Fatima, M., Butt, I., & Arshad, S. (2022). Geospatial clustering and hot spot detection of malaria incidence in Bahawalpur district of Pakistan. *GeoJournal*, 87(6), 4791-4806.
- Fatima, M., Butt, I., Firouraghi, N., Khalil, M., & Kiani, B. (2024). Space-time analysis of tuberculosis (2016–2020) in South Punjab, Pakistan. *GeoJournal*, 89(1), 1-13.
- Fatima, M., Butt, I., Nasar-u-Minallah, M., Atta, A., & Cheng, G. (2023a). Assessment of air pollution and its association with population health: Geo-statistical evidence from Pakistan. *Geography, Environment, Sustainability*, 16(2), 93-101.
- Fatima, M., Butt, I., Nasar-u-Minallah, M., Atta, A., & Cheng, G. J. G., Environment, Sustainability. (2023b). Assessment of air pollution and its association with population health: Geo-statistical evidence from Pakistan. 16(2), 93-101.
- Fatima, M., Khattak, R. M., Grady, S. C., Butt, I., Arshad, S., Ittermann, T., & Volzke, H. (2022). Spatial and temporal analysis of acute respiratory infections (Aris) in southern Punjab, Pakistan. *Spatial Information Research*, 30(4), 477-487.
- Fatima, M., O'Keefe, K. J., Wei, W., Arshad, S., & Gruebner, O. (2021). Geospatial Analysis of COVID-19: A Scoping Review. *International Journal of Environmental Research and Public Health*, 18(5), 2336.
- Ferkol, T., & Schraufnagel, D. (2014). The global burden of respiratory disease. *Annals of the American Thoracic Society*, 11(3), 404-406.
- Getis, A., & Ord, J. K. (1992). The analysis of spatial association by use of distance statistics. *Geographical analysis*, 24(3), 189-206.
- Ghimire, P., Gachhadar, R., Piya, N., Shrestha, K., & Shrestha, K. (2022). Prevalence and factors associated with acute respiratory infection among under-five children in selected tertiary hospitals of Kathmandu Valley. *PLOS ONE*, 17(4), e0265933. <https://doi.org/10.1371/journal.pone.0265933>
- GOP. (2018). Multiple Indicator Cluster Survey Punjab (MICS). Bureau of Statistics Punjab Retrieved from <https://www.bos.gop.pk/mics>
- GOP. (2021). District at a Glance: Rahim Yar Khan. Government of the Punjab Pakistan. Retrieved 19.6.2021 from https://rykhan.punjab.gov.pk/district_at_glance
- Ho, N. T., Thompson, C., Van, H. M. T., Dung, N. T., My, P. T., Quang, V. M., Minh, N. N. Q., Tuan, T. A., Hung, N. T., & Tuan, H. M. (2018). Retrospective analysis assessing the spatial and temporal distribution of paediatric acute respiratory tract infections in Ho Chi Minh City, Vietnam. *BMJ open*, 8(1), e016349.
- John Hansen-Flaschen, Letricia Dixon, Emily Rodriguez, Kara Rogers, Veenu Setia, & Young, G. (2023). Respiratory disease. In *Encyclopedia Britannica*. <https://www.britannica.com/science/respiratory-disease>
- Jolliffe, D. A., Griffiths, C. J., & Martineau, A. R. (2013). Vitamin D in the prevention of acute respiratory infection: Systematic review of clinical studies. *The Journal of Steroid Biochemistry and Molecular Biology*, 136, 321-329. <https://doi.org/https://doi.org/10.1016/j.jsbmb.2012.11.017>
- Khaliq, A., Ashraf, U., Chaudhry, M. N., Shahid, S., Sajid, M. A., & Javed, M. (2023). Spatial distribution and computational modeling for mapping of tuberculosis in Pakistan. *Journal of Public Health*, 45(2), 338-346.
- Khaliq, A., Khan, I., Akhtar, M., & Chaudhry, M. (2015). Environmental risk factors and social determinants of pulmonary tuberculosis in Pakistan. *Epidemiology*, 5(3), 201.
- Khan, I. A., Arsalan, M. H., Mehdi, M. R., Kazmi, J. H., Seong, J. C., & Han, D. (2020). Assessment of asthma-prone environment in Karachi, Pakistan using GIS modeling. *Journal of Pakistan Medical Association*, 70(4), 636-649.
- Khan, M. A. Monthly and seasonal prevalence of asthma and chronic obstructive pulmonary disease in the District Dera Ismail Khan, Khyber Pakhtunkhwa, Pakistan. *Egypt J Bronchol*. 2022;16(1):63. doi: 10.1186/s43168-022-00166-2. Epub 2022 Dec 3.
- Kiani, B., Fatima, M., Amin, N. H., & Hesami, A. (2023). Comparing geospatial clustering methods to study spatial patterns of lung cancer rates in urban areas: A case study in Mashhad, Iran. *GeoJournal*, 88(2), 1659-1669. <https://doi.org/10.1007/s10708-022-10707-3>
- Labaki, W. W., & Han, M. K. (2020). Chronic respiratory diseases: a global view. *The Lancet Respiratory Medicine*, 8(6), 531-533.
- Lai, P.-C., Low, C.-T., Tse, W.-S. C., Tsui, C.-K., Lee, H., & Hui, P.-K. (2013). Risk of tuberculosis in high-rise and high density dwellings: An exploratory spatial analysis. *Environmental Pollution*, 183, 40-45. <https://doi.org/https://doi.org/10.1016/j.envpol.2012.11.025>
- Laohasiriwong, W., Puttanapong, N., & Luenam, A. (2017). A comparison of spatial heterogeneity with local cluster detection methods for chronic respiratory diseases in Thailand. *F1000Res*, 6, 1819. <https://doi.org/10.12688/f1000research.12128.2>
- Leberl, M., Kratzer, A., & Taraseviciene-Stewart, L. J. F. i. p. (2013). Tobacco smoke induced COPD/emphysema in the animal model—are we all on the same page? , 4, 91.

- Lim, S. S., Vos, T., Flaxman, A. D., Danaei, G., Shibuya, K., Adair-Rohani, H., AlMazroa, M. A., Amann, M., Anderson, H. R., & Andrews, K. G. (2012). A comparative risk assessment of burden of disease and injury attributable to 67 risk factors and risk factor clusters in 21 regions, 1990–2010: a systematic analysis for the Global Burden of Disease Study 2010. *The Lancet Respiratory Medicine*, 380(9859), 2224–2260.
- Liu, Q., Qin, C., Du, M., Wang, Y., Yan, W., Liu, M., & Liu, J. (2022). Incidence and Mortality Trends of Upper Respiratory Infections in China and Other Asian Countries from 1990 to 2019. *Viruses*, 14(11), 2550. <https://www.mdpi.com/1999-4915/14/11/2550>
- Liu, Y., Pleasants, R. A., Croft, J. B., Wheaton, A. G., Heidari, K., Malarcher, A. M., Ohar, J. A., Kraft, M., Mannino, D. M., & Strange, C. J. I. j. o. c. o. p. d. (2015). Smoking duration, respiratory symptoms, and COPD in adults aged ≥ 45 years with a smoking history. 1409–1416.
- Marciniuk, D., Ferkol, T., Nana, A., de Oca, M. M., Rabe, K., Billo, N., & Zar, H. (2014). Respiratory diseases in the world: realities of today, opportunities for tomorrow. *African Journal of Respiratory Medicine*, 9(1).
- Masoli, M., Fabian, D., Holt, S., Beasley, R., & Program, G. I. f. A. (2004). The global burden of asthma: executive summary of the GINA Dissemination Committee report. *Allergy*, 59(5), 469–478.
- Miandad, M., Burke, F., Nawaz-ul-Huda, S., & Azam, M. (2014). Tuberculosis incidence in Karachi: A spatio-temporal analysis. *Geografia*, 10(5).
- Mohammadi, A., Pishgar, E., Fatima, M., Lotfata, A., Fanni, Z., Bergquist, R., & Kiani, B. (2023). The COVID-19 Mortality Rate Is Associated with Illiteracy, Age, and Air Pollution in Urban Neighborhoods: A Spatiotemporal Cross-Sectional Analysis. *Tropical Medicine and Infectious Disease*, 8(2), 85. <https://www.mdpi.com/2414-6366/8/2/85>
- Momtazmanesh, S., Moghaddam, S. S., Ghamari, S.-H., Rad, E. M., Rezaei, N., Shobeiri, P., Aali, A., Abbasi-Kangevari, M., Abbasi-Kangevari, Z., & Abdelmasseh, M. (2023). Global burden of chronic respiratory diseases and risk factors, 1990–2019: an update from the Global Burden of Disease Study 2019. *Eclinical Medicine*, 59.
- Naqvi, S. A. A., Sajjad, M., Waseem, L. A., Khalid, S., Shaikh, S., & Kazmi, S. J. H. (2021). Integrating spatial modelling and space–time pattern mining analytics for vector disease-related health perspectives: a case of dengue fever in Pakistan. *International Journal of Environmental Research and Public Health*, 18(22), 12018.
- Nawab, T., Raza, S., Shabbir, M. S., Yahya Khan, G., & Bashir, S. (2022). Multidimensional poverty index across districts in Punjab, Pakistan: estimation and rationale to consolidate with SDGs. *Environment, Development Sustainability*, 1–25.
- Naz, R., Gul, A., Javed, U., Urooj, A., Amin, S., & Fatima, Z. (2019). Etiology of acute viral respiratory infections common in Pakistan: A review. *Rev Med Virol*, 29(2), e2024. <https://doi.org/10.1002/rmv.2024>
- Noman, N., Ahmad, I., Marwat, M., & Zaffar, T. (2016). Pattern of adult asthma in district Dera Ismail Khan. *Gomal Journal of Medical Sciences*, 14(2).
- Ord, J. K., & Getis, A. (1995). Local spatial autocorrelation statistics: distributional issues and an application. *Geographical analysis*, 27(4), 286–306.
- PMD. (2020). Meteorological Data of South Punjab.
- Rabbani, U., Razaq, S., Irfan, M., Semple, S., & Nafees, A. A. (2022). Indoor air pollution and respiratory health in a metropolitan city of Pakistan. *Journal of Occupational and Environmental Medicine*, 64(9), 761–765.
- Rex, F. E., Borges, C. A. d. S., & Käfer, P. S. (2020). Spatial analysis of the COVID-19 distribution pattern in São Paulo State, Brazil. *Ciência & Saúde Coletiva*, 25, 3377–3384.
- Sadeghimoghaddam, A., Khankeh, H., Norozi, M., Fateh, S., & Farrokhi, M. (2021). Investigating the effects of dust storms on morbidity and mortality due to cardiovascular and respiratory diseases: A systematic review. *J Educ Health Promot*, 10(1), 191. https://doi.org/10.4103/jehp.jehp_1272_20
- Safiri, S., Mahmoodpoor, A., Kolahi, A. A., Nejadghaderi, S. A., Sullman, M. J. M., Mansournia, M. A., Ansarin, K., Collins, G. S., Kaufman, J. S., & Abdollahi, M. (2022). Global burden of lower respiratory infections during the last three decades. *Front Public Health*, 10, 1028525. <https://doi.org/10.3389/fpubh.2022.1028525>
- Sajid Rasul, Muhammad Mumtaz Ahmad, Syed Wasim Abbas, Sana Gull, Maryam Pervez, & Fiaz Ahmad. (2021). South Punjab Developmental Statistics 2020. B. O. STATISTICS.
- Song, H., Jin, Z., Shan, C., & Chang, L. (2022). The spatial and temporal effects of Fog–Haze pollution on the influenza transmission. *International Journal of Biomathematics*, 2250096.
- Tiwari, N., Adhikari, C. M. S., Tewari, A., & Kandpal, V. (2006). Investigation of geo-spatial hotspots for the occurrence of tuberculosis in Almora district, India, using GIS and spatial scan statistic. *International Journal of Health Geographics*, 5(1), 33. <https://doi.org/10.1186/1476-072X-5-33>
- Umer, M. F., Zofeen, S., Majeed, A., Hu, W., Qi, X., & Zhuang, G. (2018). Spatiotemporal clustering analysis of malaria infection in Pakistan. *International journal of environmental research public health*, 15(6), 1202.
- UNDP. (2022). High-Level Deep Dive On South Punjab. https://pakistan.un.org/sites/default/files/2022-04/South%20Punjab%20Deep%20Dive%20Report_Final.pdf
- UNICEF. (2019). Punjab: Multiple Indicator Cluster Survey 2017–18. U. N. C. s. F. (UNICEF).
- UNP. (2022). HIGH-LEVEL DEEP DIVE ON SOUTH PUNJAB. U. N. Pakistan. https://pakistan.un.org/sites/default/files/2022-04/South%20Punjab%20Deep%20Dive%20Report_Final.pdf
- WHO. (2007). Global surveillance, prevention and control of chronic respiratory diseases: a comprehensive approach. In *Global surveillance, prevention and control of chronic respiratory diseases: a comprehensive approach* (pp. vii. 146–vii. 146). World Health Organization.
- WHO. (2020a). Health Profile: Pakistan. Retrieved 7th February from <https://www.worldlifeexpectancy.com/pakistan-lung-disease>
- WHO. (2020b). Tuberculosis: Key Facts. World Health Organization. Retrieved 22.6.2021 from <https://www.who.int/news-room/fact-sheets/detail/tuberculosis>
- WHO. (2021). Asthma. World Health Organization. Retrieved 24.7.2021 from <https://www.who.int/news-room/fact-sheets/detail/asthma>
- WHO. (2022). Tuberculosis. World Health Organization: Pakistan. Retrieved 9-1-2023 from <https://www.emro.who.int/pak/programmes/stop-tuberculosis.html>
- WHO. (2023a). Asthma. World Health Organization. Retrieved 17-10-2023 from <https://www.who.int/news-room/fact-sheets/detail/asthma#:~:text=Asthma%20is%20a%20chronic%20lung,come%20and%20go%20over%20time>.
- WHO. (2023b). Influenza (Seasonal). World Health Organization Retrieved 17-10-2023 from [https://www.who.int/news-room/fact-sheets/detail/influenza-\(seasonal\)](https://www.who.int/news-room/fact-sheets/detail/influenza-(seasonal))
- Wisnivesky, J., & De-Torres, J. P. (2019). The Global Burden of Pulmonary Diseases: Most Prevalent Problems and Opportunities for Improvement. *Ann Glob Health*, 85(1). <https://doi.org/10.5334/aogh.2411>
- Zeb, I., Qureshi, N. A., Shaheen, N., Zafar, M. I., Ali, A., Hamid, A., Shah, S. A. A., & Ashraf, A. (2021). Spatiotemporal patterns of cutaneous leishmaniasis in the district upper and lower Dir, Khyber Pakhtunkhwa, Pakistan: A GIS-based spatial approaches. *Acta Tropica*, 217, 105861.

ASSESSMENT OF THE KOLYMA RIVER HYDROLOGICAL REGIME DYNAMICS IN THE 21ST CENTURY BASED ON RUNOFF FORMATION MODEL

Anastasia A. Lisina^{1,2*}, Natalia L. Frolova¹, Andrey S. Kalugin², Inna N. Krylenko^{1,2}, Yuri G. Motovilov²

¹ Lomonosov Moscow State University, Department of Land Hydrology, GSP-1, Leninskie Gory, 119991, Moscow, Russia

² Water Problems Institute of the Russian Academy of Sciences, ul. Gubkina 3, 119333, Moscow, Russia

*Corresponding author: lisanastya99@mail.ru

Received: July 1st 2024 / Accepted: November 22nd 2024 / Published: March 31st 2025

<https://doi.org/10.24057/2071-9388-2025-3482>

ABSTRACT. Using the physically-based model of runoff formation ECOMAG (ECOLOGical Model for Applied Geophysics), the response of the Kolyma River's water regime to ongoing and projected climate changes has been investigated. To operate the ECOMAG model, which calculates daily water discharges for control sections, information was gathered on the characteristics of the land surface and watershed relief, as well as archives of daily observations from meteorological stations within the basin. The calibration and validation of the model, performed for two sections on the Kolyma River and two sections on its tributaries – the Bolshoy Anyuy and Yasachnaya rivers – demonstrated strong agreement between the modelled and observed water discharges for the Kolyma River. Moreover, the analysis of observed water discharges and those calculated by the ECOMAG model reveals similar changes in the water regime that occurred from 1979 to 2020, such as an increase in annual and summer-autumn runoff, and a decrease in the duration of the winter low-flow period. To assess potential changes in the Kolyma River's runoff in the 21st century, numerical experiments were conducted using the ECOMAG hydrological model and an ensemble of four global climate models. Calculations were performed for the periods 2020–2039, 2040–2059, 2060–2079, and 2080–2099 for four different Representative Concentration Pathway (RCP) scenarios. Anomalies in annual runoff, peak water discharges, flood volumes, winter low-flow periods, and summer-autumn periods were considered. Under all scenarios, the calculations indicate an increase in the annual and summer-autumn runoff of the Kolyma River.

KEYWORDS: river runoff, model of runoff formation, Kolyma, ECOMAG, CMIP5, climate change

CITATION: Lisina A. A., Frolova N. L., Kalugin A. S., Krylenko I. N., Motovilov Y. G. (2025). Assessment Of The Kolyma River Hydrological Regime Dynamics In The 21st Century Based On Runoff Formation Model. *Geography, Environment, Sustainability*, 23-34

<https://doi.org/10.24057/2071-9388-2025-3482>

ACKNOWLEDGEMENTS: The results of section on calibration and verification of the runoff formation model were obtained with the support of the Russian Science Foundation, Project 24-17-00084 – Hydrological outcomes of climate change and anthropogenic impact in the cryolithozone. The results on the application of calculation of global climate models were obtained with the support of the Russian Science Foundation, Project 23-77-01097 – Assessing Future Runoff Variations.

Conflict of interests: The authors reported no potential conflict of interest.

INTRODUCTION

Global climate changes inevitably lead to responses in the hydrological system of river basins. According to the latest report by the Intergovernmental Panel on Climate Change (IPCC 2013), greenhouse gas emissions will cause further warming and changes in other climate characteristics, with particularly intense effects in polar regions. Changes in the key factors of runoff formation – air temperature and precipitation – are most pronounced in polar areas compared to other regions of the planet. According to the Third Assessment Report by Roshydromet, by the end of the 21st century, a temperature increase of 2–7°C is expected in Russia, depending on the scenario (Roshydromet 2022).

Future changes in river runoff can be assessed, firstly, by modeling hydrological processes using climate models, and secondly, by calculations based on hydrological models that use climate model outputs as inputs. The use of hydrological models allows for a more comprehensive consideration of the mechanisms of hydrological regime response to climate impacts. Authors such as Krysanova et al. (2018) and Kundzewicz et al. (2018) agree that the use of regional hydrological models provides more reliable estimates of water regime characteristics than using a climate model ensemble. Furthermore, calculations with climate models provide more accurate results on a global scale, while for practical tasks related to the organization of safe water use, the regional scale is often of particular interest.

In this study, the spatially distributed model ECOMAG (ECOLOGical Model for Applied Geophysics) is used to assess possible changes in the hydrological regime. This model has proven effective in calculating daily runoff values in watersheds of various sizes and different climate zones. Additionally, the ECOMAG model has demonstrated correct operation in non-stationary climate conditions, making it suitable for calculations under different climatic conditions than those used for model calibration and verification (Moreido and Kalugin 2017; Gelfan et al. 2015).

Meteorological data for the period 2020–2100 were obtained from model results within the CMIP5 project (IPCC 2013) under four different RCP (Representative Concentration Pathways) scenarios: RCP 2.6, RCP 4.5, RCP 6.0, RCP 8.5. The numbers in the scenario names indicate the level of radiative forcing in 2100 compared to pre-industrial values (RCP 2.6 corresponds to +2.6 W/m², etc.). Scenario RCP 2.6 implies a constant reduction in greenhouse gas emissions until 2100, while scenario RCP 8.5 assumes that greenhouse gas emissions will continue to rise (IPCC 2013).

The study focuses on the Kolyma River, the largest river whose basin is entirely located in the zone of continuous permafrost. Using the ECOMAG model of runoff formation and an ensemble of four climate models (GFDL-ESM2M, HadGEM2-ES, IPSL-CM5A-LR, MIROC5), estimates of the possible dynamics of the Kolyma River runoff in the 21st century were obtained under four radiative forcing scenarios: RCP 2.6, RCP 4.5, RCP 6.0, and RCP 8.5.

MATERIALS AND METHODS

Study area

The Kolyma River is one of the largest rivers in the Arctic zone of the Russian Federation. Its basin, covering an area of 647,000 km², is located in the subarctic and arctic climatic zones within the region of continuous permafrost. The river is 2,129 km long, originates in the Okhotsk-Kolyma highlands, and flows into the East Siberian Sea. The upper and middle reaches of the Kolyma are situated in mountainous terrain, while the lower reaches lie in the Kolyma Lowland, encompassing taiga and tundra zones (Water of Russia 2022). More than half of the Kolyma basin is forested, with lakes covering a total area of up to 10%, and swamps comprising around 8%.

The hydrological regime of the Kolyma River is typical for rivers in Eastern Siberia. The spring flood usually occurs from late May to June, followed by a summer-autumn period with rain floods continuing until October. Winter runoff is mainly sustained by riverbank taliks and decreases during the winter low-water period (Lebedeva et al. 2019). The Kolyma has a mixed water supply: snowmelt contributes 47%, rain 42%, and groundwater 11% (Water of Russia 2022).

The Kolyma River's flow is regulated by the Kolyma Hydroelectric Cascade, which is for seasonal regulation. The upper stage, the Kolymaskaya hydroelectric power plant (Kolymaskaya HPP) (1894 km from the river mouth), began regulation in the 1980s. The lower stage, the Ust-Srednekanskaya hydroelectric power plant (Ust-Srednekanskaya HPP) (1678 km from the river mouth), saw its first two of four units commissioned in 2013 (Rushydro.ru 2024). The hydrological impacts of flow regulation have been extensively studied (Magritsky et al. 2018). The authors found that the operation of the HPPs reduced the volume of the spring flood by 30–50%, while winter runoff almost doubled in the downstream sections of the river.

Anthropogenic changes in the Kolyma's flow are compounded by climatic changes (Magritsky et al. 2019;

Ushakov 2013). An increase in air temperature by 2–4°C (AMAP 2017) and an increase in precipitation (Lebedeva et al. 2019) have led to an 8.7 mm rise in annual runoff at Srednekolymsk (Magritsky et al. 2018). Studies focusing on the unregulated part of the basin (Lebedeva et al. 2019; Ushakov 2013; Majhi, Yang 2008) have shown a 14% increase in annual inflow to the reservoir, particularly noting a more than 30% increase in inflow in May, August, and September (Ushakov, Lebedeva 2016). Nasonova et al. (2018) provided estimates of possible changes in the Kolyma's runoff using the SWAP land surface model and climate model outputs. They assessed potential anomalies in annual runoff as 16% and 28% for the periods 2026–2045 and 2081–2100, respectively, compared to 1978–1998.

Input Data for the Model of runoff formation

The information-modelling complex ECOMAG (Motovilov et al. 1999) is a spatially-distributed physically based model of runoff formation. The hydrological block describes the main processes in the watershed: infiltration, evaporation, freezing and thawing, snow cover formation and melting, and the formation of surface, subsurface, groundwater, and river runoff. To schematize the watershed in ECOMAG, elementary watersheds are created, forming an irregular grid of relatively homogeneous landscape units (Motovilov, Gelfan 2018).

For the development of the Kolyma River basin model, information on the characteristics of the underlying surface and relief was collected. Data on landscape, soil type, and vegetation cover were determined from the landscape map of the former USSR and the soil map of Russia, developed by the Soil Institute of the Russian Academy of Sciences. The source of the digital elevation model is the GLOBE (Global Land One-kilometer Base Elevation) project by the Defense Mapping Agency (DMA).

Currently, there are 35 hydrological posts operating in the Kolyma basin, with 14 of them measuring water discharge. Data on water discharge for the Kolyma River are published for two gauging stations: the town of Srednekolymsk (641 km from the mouth) and the village of Ust-Srednekan, the lower reaches of the Ust-Srednekanskaya HPP (1623 km from the mouth). A long-term series of daily water discharges is also available for the Kolymskoye-I gauging station, located 283 km from the mouth and a few kilometers downstream from the confluence of the largest tributary, the Omolon River. Water levels are measured at the gauging station in the village of Kolymskoye, located 10 km upstream from the Kolymskoye-I gauging station, and thus upstream from the confluence of the Omolon. Since 1998, at the Kolymskoye-I gauging station (downstream from the confluence of the Omolon), flow velocities have not been measured, water discharges have been reconstructed using the $Q = f(H)$ curves, depending on the water level at the Kolymskoye village station (upstream from the confluence of the Omolon), resulting in a decrease in the quality of discharge calculations published in the annual reports of the Federal Department of Hydrometeorological and Environmental Monitoring (FDHEM).

Calibration and verification of the ECOMAG model of runoff formation were carried out by comparing the model's calculated daily water discharges with observed data from 1979–2020 published in the FDHEM annual reports and on the AIS GMVO system website (AIS GMVO 2024). Observation archives were used from two gauging stations on the Kolyma River – Kolymskoye-I (283 km from the mouth) and Srednekolymsk (641 km from the mouth),

as well as from major tributaries with long-term water discharge series – Bolshoy Anyuy River at Konstantinovskaya station and Yasachnaya River at Nelemnoye village. Since the Kolyma River’s flow is regulated, data on the volumes of water discharge through the Kolymanskaya HPP dam from 1979–2020 were also used (Fig. 1).

The necessary daily values of air temperature, precipitation, and humidity deficit for the model were taken from observation archives at 37 meteorological stations (Fig. 1).

After calibration and verification of the model, a version of the ECOMAG model was launched in which it is not necessary to specify the air humidity deficit as input information. The deficit is calculated using an approximate formula based on air temperature and precipitation in accordance with Motovilov et al. 2022:

$$d = 2 \cdot e^{(0.08t - 0.1p)}$$

where d is a daily air humidity deficit, hPa; t is a daily air temperature, °C; p is a daily precipitation, mm.

This version of the model was used for 2014–2020, for which there was no data on the air humidity deficit.

RESULTS AND DISCUSSION

Application of the Model of runoff formation for the Kolyma River Basin

Calibration of the ECOMAG model parameters was conducted using average daily water discharge data from 1979–1999 for two gauging stations on the Kolyma River (Srednekolymsk and Kolymskoye-I), as well as for the Bolshoy Anyuy River (Konstantinovskaya) and the Yasachnaya River (Nelemnoye). The calibration was

performed simultaneously for all stations, ensuring the model contains a consistent set of parameters.

For verification, independent data – water discharges at the studied posts from 2000–2020 – were used. To evaluate the quality of the ECOMAG model calculations, the Nash and Sutcliffe criterion NSE (Nash, Sutcliffe 1970), a commonly used efficiency coefficient for assessing model performance, and the bias ($BIAS$) were applied. The formulas for these calculations are as follows:

$$NSE = 1 - \frac{\sum (Q_{obs} - Q_{sim})^2}{\sum (Q_{obs} - Q_{obs}^-)^2}$$

$$BIAS = \frac{Q_{sim}^- - Q_{obs}^-}{Q_{obs}^-} \cdot 100\%$$

where Q_{obs} and Q_{sim} are the observed and simulated daily water discharges, respectively.

In addition to the Nash and Sutcliffe criterion and bias, the coefficients of determination R^2 for the relationship between observed and simulated monthly runoff volumes were also calculated (Table 1, Fig. 2, Fig. 3).

The obtained criteria values were compared with those accepted in practice: thus, when the NSE values exceed the practical threshold of 0.75 and $BIAS$, the quality of model calculations is considered good. Values with NSE ranging from 0.5 to 0.75 and $BIAS$ from 10% to 15% are deemed satisfactory (Motovilov, Gelfan, 2018). During the calibration of the model parameters, the above quality criteria were calculated for four cross-sections and averaged proportionally to the basin area for each cross-section.

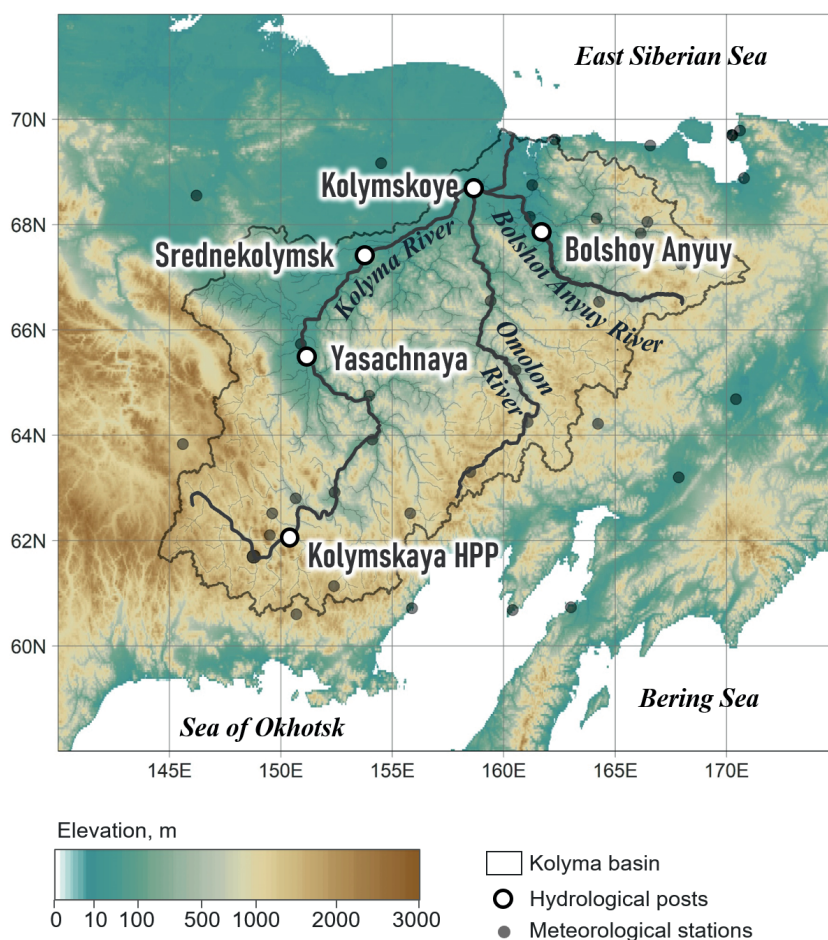
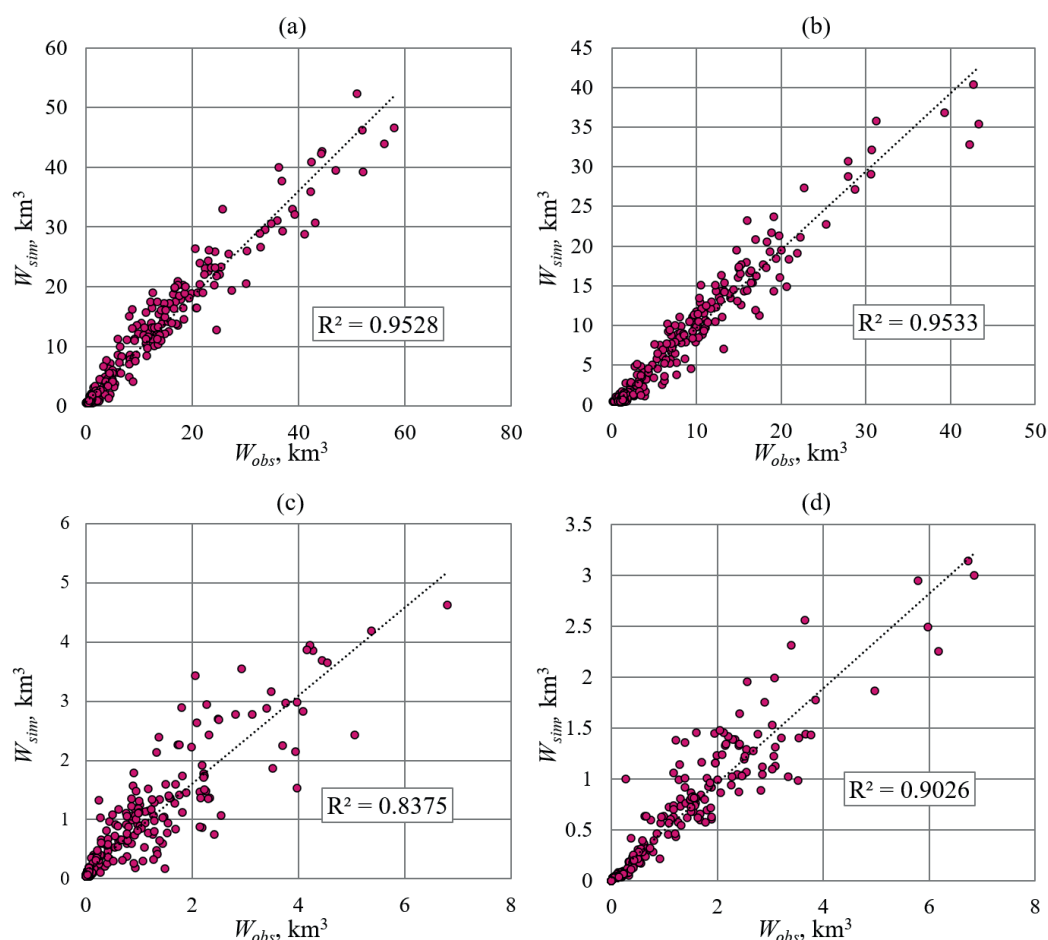


Fig. 1. The Kolyma River basin with the locations of hydrological (gauging) stations whose archives were used for the calibration and verification of the model of runoff formation

Table 1. Values of the performance criteria for daily and monthly runoff calculations in the Kolyma River basin for the calibration and verification periods

Hydrological Station	Basin area, ths. km ²	Distance from Mouth/ Source, km	Calibration Period 1979–1999				Verification Period 2000–2020			
			daily		monthly		daily		monthly	
			<i>NSE</i>	<i>BIAS</i> , %	<i>NSE</i>	<i>R</i> ²	<i>NSE</i>	<i>BIAS</i> , %	<i>NSE</i>	<i>R</i> ²
Kolyma – Kolymskoye-I	526	283/1846	0.90	1.6	0.95	0.95	0.82	1.9	0.94	0.96
Kolyma – Srednekolymsk	361	641/1488	0.87	5.1	0.95	0.94	0.84	-1.3	0.95	0.96
Bolshoy Anyuy – Konstantinovskaya	49.6	67/626	0.51	5.2	0.87	0.87	0.51	7.3	0.75	0.79
Yasachnaya – Nelemnoye	32	80/410	0.57	4.1	0.63	0.91	0.53	6.8	0.58	0.89

**Fig. 2. The relationship between observed and simulated monthly runoff volumes for the calibration and verification period: (a) for the Kolyma River at the Kolymskoye-I; (b) for the Kolyma River at Srednekolymsk; (c) for the Bolshoy Anyuy River at Konstantinovskaya station; (d) for the Yasachnaya River at Nelemnoye village**

The calculations demonstrated (Table 1) that the ECOMAG model shows good fit of observed water discharges for both cross-sections on the Kolyma River (at Srednekolymsk and the Kolymskoye-I hydrological post). For these cross-sections, the Nash-Sutcliffe efficiency during the verification period was 0.84 and 0.82, respectively, with bias of -1.3% and 1.9%, respectively. The quality of calculations for tributaries with smaller catchment areas (the Bolshoy Anyuy River at Konstantinovskaya station and the Yasachnaya River at Nelemnoye village) was worse, being satisfactory according to the accepted gradations.

In the figure below (Fig. 4), typical hydrographs are presented, the ordinates of which are obtained as the average water discharge for each date for the periods 1979–1999 and 2000–2020. The hydrographs illustrate the ECOMAG model's good

reproduction of intra-annual runoff changes observed in recent decades: shifts in the flood wave to earlier dates, later onset of winter low flow, and increased flow in the second half of August to October. However, the calculated changes in maximum water discharges do not coincide with the observation data: for Srednekolymsk, maximum discharges according to observed data practically did not change, while the model shows an increase of 7%; for Kolymskoye-I, observed maximum discharges increased by 15%, while simulated ones increased by 10%.

The annual runoff volumes of the ECOMAG model are best reproduced for Srednekolymsk, which is explained by the large watershed area for this station, exceeding the watershed areas of the Bolshoy Anyuy and Yasachnaya rivers, as well as the fact that at the Srednekolymsk station, unlike the Kolymskoye-I hydro

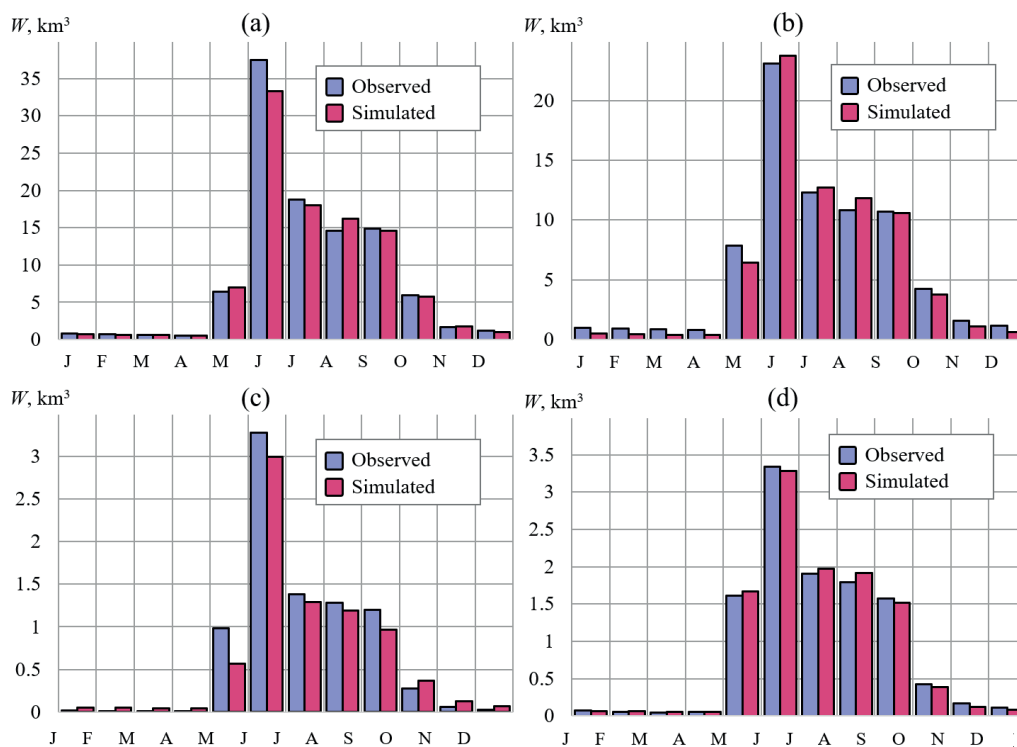


Fig. 3. Observed and simulated mean monthly runoff volumes for the verification period: (a) for the Kolyma River - Kolymskoye-I, (b) for the Kolyma River - Srednekolymsk, (c) for the Bolshoy Anyuy River – Konstantinovskaya station, (d) for the Yasachnaya River – Nelemnoye village

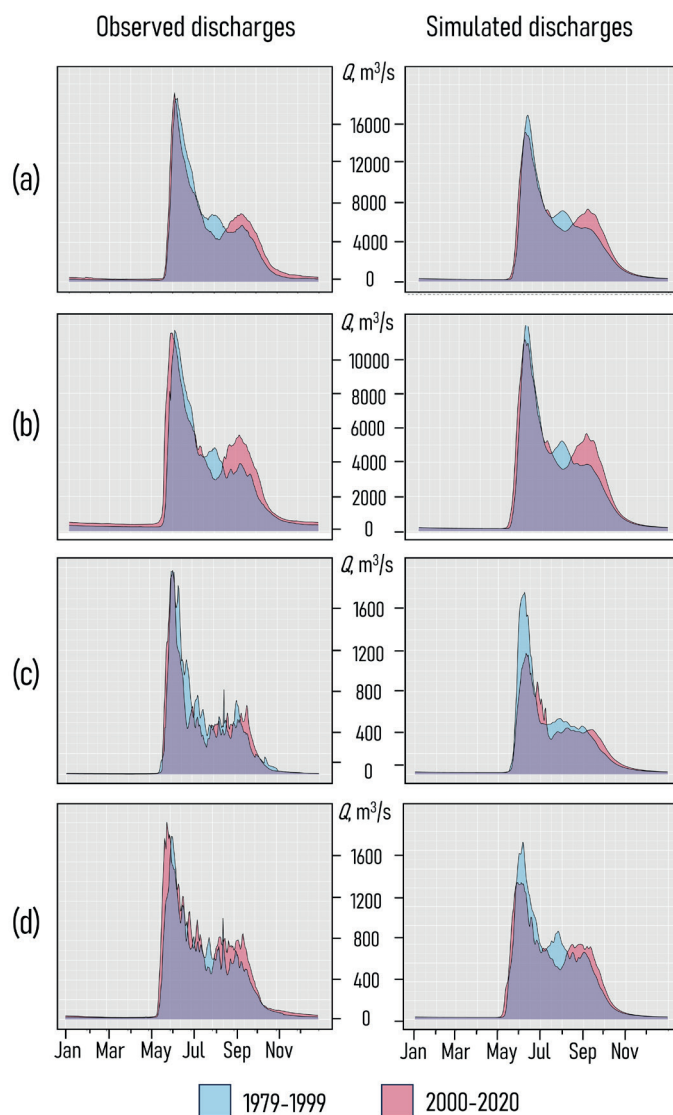


Fig. 4. Observed and simulated typical hydrographs for the periods 1979-1999 and 2000-2020 for studied stations

station, water discharges are calculated based on flow velocity measurements rather than being reconstructed based on the relationship $Q=f(H)$.

The results of the model calculation in the absence of data on air humidity deficit

When running the model with the calculation of the air humidity deficit, the quality of the calculations decreased but remained at a satisfactory level. For the Kolyma station – Kolymskoye, the Nash-Sutcliffe criterion decreased from 0.87 to 0.77, and the bias decreased from 1.9% to -16.3%. For the Kolyma River – Srednekolymsk station, the Nash-Sutcliffe criterion decreased more significantly, from 0.85 to 0.67, and the bias reached -17.9%. However, for the Bolshoy Anyuy River – Konstantinovskaya station, the calculation without using observed air humidity deficit did not decrease accuracy: the Nash and Sutcliffe criterion remained unchanged, and the BIAS changed from 5.5% to -2.7% (Table 2). The model with the calculation of the air humidity deficit was used for 2014–2020, as there was no data on the air humidity deficit.

Thus, despite the systematic underestimation of results, the application of the model version that calculates air humidity deficit allows obtaining satisfactory quality results. This indicates the feasibility of using this version of the ECOMAG model in the absence of observed data on humidity deficit.

Assessment of changes in the Kolyma River discharge based on global climate models

Historical simulations

To evaluate the hydrological consequences of climate change in the Kolyma River basin, the results of an ensemble of four global climate models (GCMs) were used: GFDL-ESM2M, HadGEM2-ES, IPSL-CM5A-LR, MIROC5, which are part of the CMIP5 project (Coupled Model Intercomparison Project Phase 5) (IPCC 2013).

To confirm the reliability of future climate scenario calculations by global models, a comparison was made between GCMs results for the historical period and observational data. Since the ensemble data for most climate models contain information up to 2006, the historical period considered was 1975–2004.

The GCMs data slightly smooth the annual temperature cycle. According to meteorological station data, the annual amplitude of monthly temperatures reaches 46.8°C (+14.1°C in July and -32.7°C in January), while according to climate models, the amplitude is 36.9°C (+10.2°C in July, -26.7°C in January). However, the annual mean values differ insignificantly. Climate models overestimate annual precipitation, most notably in November, October, and April (Table 3).

Table 2. Nash and Sutcliffe criterion and bias for daily streamflow calculation in the Kolyma River basin in various versions of the ECOMAG model from 1979–2013

Hydrological Stations	Air Humidity Deficit from Meteorological Stations Data		Calculated Air Humidity Deficit	
	<i>NSE</i>	<i>BIAS, %</i>	<i>NSE</i>	<i>BIAS, %</i>
The Kolyma River – Kolymskoye	0.87	1.9	0.77	-16.3
The Kolyma River – Srednekolymsk	0.85	-1.3	0.67	-17.9
The Bolshoy Anyuy River – Konstantinovskaya	0.51	5.5	0.51	-2.7
The Yasachnaya River – Neleynoie	0.55	5.5	0.50	-4.8

Table 3. Monthly and annual air temperature and precipitation observed at meteorological stations and calculated from the ensemble of GCMs (average values for 1975–2004)

Month	Air temperature, °C		Precipitation, mm	
	Meteorological stations	Climate models	Meteorological stations	Climate models
January	-32.7	-26.7	17.3	19.2
February	-32.1	-25	15.3	17.2
March	-23.8	-19.0	14.9	17.8
April	-12.2	-9.9	13.3	24.3
May	1.7	-0.3	20.0	32.3
June	11.2	6.9	43.0	49.7
July	14.1	10.2	63.6	70.8
August	10.4	9.5	61.2	85.6
September	3.1	4.0	40.1	61.4
October	-10.4	-7.0	27.8	66.2
November	-24.7	-18.5	28.4	53.8
December	-32.8	-24.9	19.6	24.6
Annual	-10.7	-8.4	364	523

These differences result in a delayed onset of spring floods and a slightly higher maximum discharge according to GCMs compared to observed data. The table 4 presents the bias between observed water discharges (1) and those modelled by ECOMAG using two versions of forcing data: measured at meteorological stations (2) and simulated by GCMs (3). For data simulated by GCMs the most significant errors in May (see bias between (1) and (3)) are associated with inaccuracies in reproducing the timing of spring floods by ECOMAG model using forcing data from global climate models. When calculating from the observed meteorological data, the errors are less (see bias between (1) and (2)). Despite such differences in calendar terms, the flood volume is calculated with significantly smaller errors. The error in calculating the annual discharge volume is within 10% (Table 4). To avoid errors associated with inaccurate calculations of interannual discharge variability by GCMs, multi-year average values of hydrological characteristics were considered to assess the general trend in discharge changes in the 21st century.

Projections

For possible variations in meteorological characteristics in the 21st century, four greenhouse gas emission scenarios were considered – RCP 2.6, RCP 4.5, RCP 6.0, RCP 8.5. Daily air temperature and precipitation values for each model from the GCMs ensemble were used as input data for the runoff formation model for the Kolyma River. Then the series of runoff values calculated for each model were averaged. When analyzing anomalies in meteorological variables and hydrological characteristics, mean values were calculated for four twenty-year periods (2020–2039, 2040–2059, 2060–2079, 2080–2099) and compared with calculations for the historical period (1975–2004).

To illustrate possible climate changes, average air temperature and precipitation for the Kolyma River basin were calculated, and then the deviation of average meteorological values for twenty-year periods of the

21st century from the historical period (1975–2004) was determined. For example, with an average air temperature of -13.6°C in 1975–2004, by the end of the 21st century, models predict a temperature rise of 3.5–8.4°C depending on the scenario. According to GCMs, the amount of precipitation relative to 334 mm for the historical period will decrease slightly in 2020–2039 and increase by 0.4–28.9% by the end of the century (Table A1).

To assess the hydrological response to climate change, the ECOMAG model of runoff formation was launched using meteorological data series for the 21st century from GCMs. For the four studied stations (on the Kolyma River, as well as tributaries of the Bolshoy Anyuy and Yasachnaya rivers), anomalies of annual discharge (Fig. 5), maximum water discharge (Fig. 6), and volumes of discharge in the summer-autumn period, summer, and winter low-flow periods (Table A2) were calculated for twenty-year periods of the 21st century (2020–2039, 2040–2059, 2060–2079, 2080–2099).

Under any greenhouse gas emission scenarios, an increase in the annual discharge volumes of the studied rivers was obtained, more pronounced for the Kolyma and Yasachnaya, and less noticeable for the Bolshoy Anyuy (Fig. 6). For example, under the RCP 2.6 scenario during the 21st century (from 1975–2004 to 2080–2099), the Kolyma discharge at the Kolymskoe-I demonstrates an increase of 13.5%, and at the Srednekolymsk station – 15.0%. On the Yasachnaya River, the increase is 16.5%, and on the Bolshoy Anyuy River – 9.0%. Under the RCP 8.5 scenario, the annual discharge by the end of the century will increase by 47.2% for the Kolyma, 54.3% for Srednekolymsk, 26.0% for Bolshoy Anyuy, and 62.2% for Yasachnaya.

When considering mean values for twenty-year periods, a nonlinear trend in hydrological regime changes is observed. For example, under the RCP 4.5 and RCP 6.0 scenarios, the most rapid changes occur between 2040–2059 and 2060–2079.

Expected changes in summer-autumn discharge for the studied rivers correlate well with the dynamics of

Table 4. Monthly and annual water discharges observed at the Kolymskoye gauging station and calculated with forcing data from the ensemble of GCMs and meteorological stations (average values for 1975-2004)

Month	Observed water discharge (1), m ³ /s	Calculated water discharge according to meteorological stations (2), m ³ /s	Calculated water discharge according to climate models (3), m ³ /s	Bias between (1) and (2), %	Bias between (1) and (3), %
January	269	266	298	-1.12	10.8
February	225	233	249	3.56	10.7
March	214	216	223	0.93	4.2
April	189	206	210	8.99	11.1
May	2040	2060	678	0.98	-66.7
June	15100	12800	17800	-15.2	17.7
July	7410	6760	8670	-8.77	17.0
August	5450	5770	6410	5.87	17.6
September	4940	4890	4890	-1.01	-1.01
October	1830	1920	1830	4.92	0.0
November	487	627	634	28.7	30.2
December	356	349	367	-1.97	3.1
Annual	3200	3090	3510	-3.44	9.7

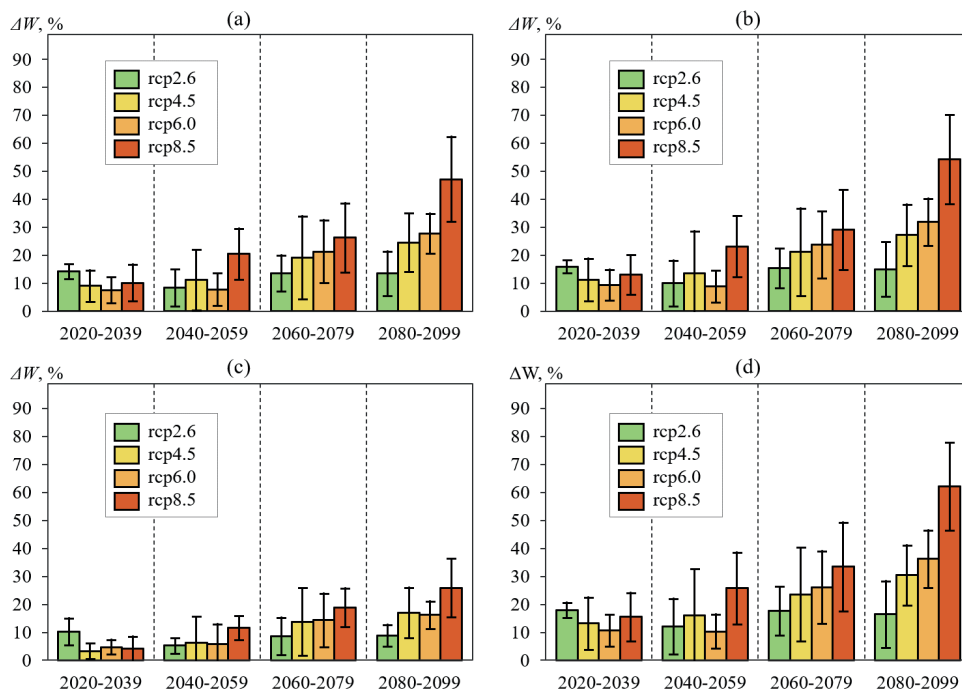


Fig. 5. Changes in the annual discharge volume for the 21st century periods under various greenhouse gas emission scenarios relative to the historical period: (a) for the Kolyma River – Kolymskoe-I; (b) for the Kolyma River – Srednekolymsk town; (c) for the Bolshoy Anyuy River – Konstantinovskaya station; (d) for the Yasachnaya River – Nelemnoye village

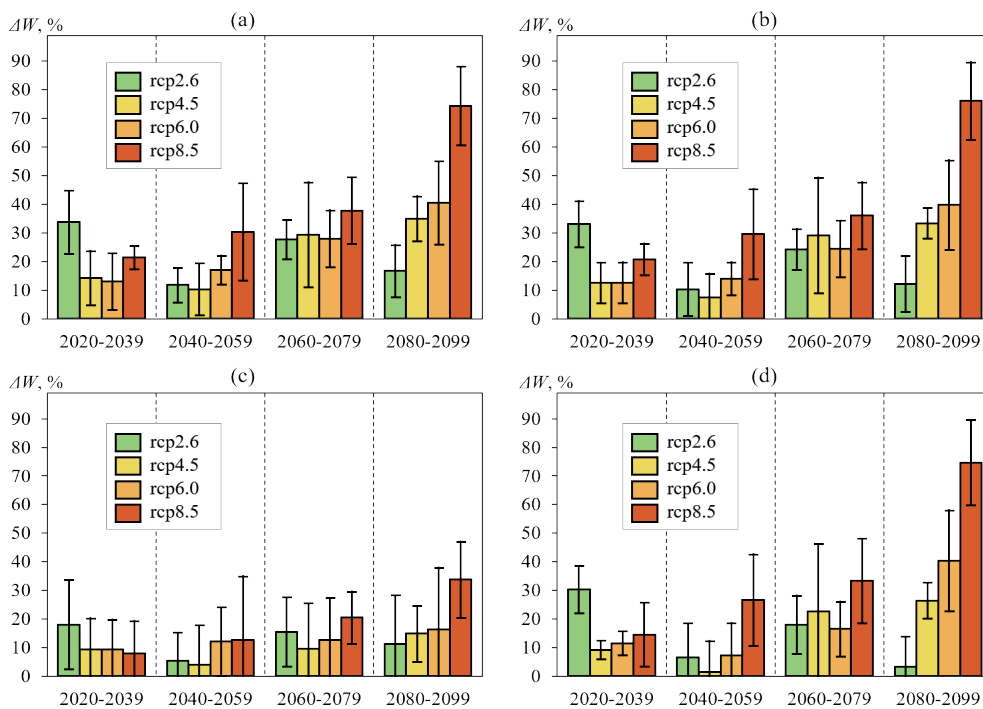


Fig. 6. Changes in maximum water discharge for the 21st century periods under various greenhouse gas emission scenarios relative to the historical period: (a) for the Kolyma River – Kolymskoe-I; (b) for the Kolyma River – Srednekolymsk town; (c) for the Bolshoy Anyuy River – Konstantinovskaya station; (d) for the Yasachnaya River – Nelemnoye village

annual discharge, although the summer-autumn discharge changes are less pronounced. Winter low-flow volumes are most affected by climate changes for the Bolshoy Anyuy River: by the end of the 21st century, calculations show an increase of 2.2% to 71.9% for the RCP 2.6 and RCP 8.5 scenarios, respectively. Maximum water discharges during the 21st century exceed values for the historical period. Under the RCP 2.6 scenario, the highest discharges are typical for 2020–2039, followed by a decrease.

Considering the RCP 4.5 scenario as the most likely (van Vuuren D.P. et al. 2011), the annual discharge of the studied rivers will steadily increase throughout the 21st

century, and by 2080–2099, an increase of approximately a quarter can be expected for the Kolyma, 17% for the Bolshoy Anyuy, and 31% for Yasachnaya. Full results of the expected discharge changes calculation are presented in Table A1.

CONCLUSIONS

Physically based models of river runoff formation allow the study of river regime responses to ongoing and projected climate changes. The ECOMAG model was calibrated for the Kolyma River basin, the largest Russian

river in the zone of continuous permafrost and the fourth largest by catchment area among the rivers of the Arctic Ocean basin.

Calibration and validation of the model demonstrated good fit of observed data for two sites on the Kolyma River and sites on its tributaries (Bolshoy Anyuy River and Yasachnaya River). In particular, the model accurately reproduces intra-annual runoff variations since 1979. This enabled the use of the model to assess possible changes in the runoff of the Kolyma River and its tributaries in the 21st century.

Air temperature and precipitation values for the 21st century were obtained for the Kolyma basin from an ensemble of four global climate models. By the end of the century, an increase in temperature of 3.5–8.4 °C and an increase in

precipitation of 0.4–28.9% can be expected, depending on the RCP radiation forcing scenario. Calculations were made for anomalies of annual runoff, maximum water discharge, and the volume of runoff during the winter low-water period and summer-autumn period under such changes in climatic characteristics in the Kolyma basin. It is shown that under any scenario, an increase in the annual runoff of the studied rivers can be expected: for the Kolyma River the increase is estimated at 13.5–47.2%, depending on the scenario, for the Bolshoy Anyuy – at 9.0–26.0% and for the the Yasachnaya River – at 16.5–62.2%. At the same time, an increase in summer-autumn flows, maximum discharges and winter low-flow volumes on the Kolyma River and its tributaries is expected in the 21st century, most noticeable under RCP 8.5 scenario. ■

REFERENCES

- AIS GMVO 2024: Automated Information System for State Monitoring of Water Bodies (AIS GMVO). [online] Available at: <https://gmvo.sknivh.ru> [Accessed on 1 Apr. 2024], (In Russian).
- Rushydro.ru 2024: Ust-Srednekanskaya HPP named after A.F. Dyakov. [online] Available at: <http://www.usges.rushydro.ru/> [Accessed on 1 Apr. 2024], (In Russian)
- Water of Russia 2022: Scientific-Popular Encyclopedia «Water of Russia». [online] Available at: https://water-ru.ru/Водные_объекты/434/Колыма [Accessed on 1 Jul. 2022], (In Russian)
- Magritskiy D.V., Povalishnikova E.S., Frolova N.L. (2019). History of the study of water discharge and water regime of rivers of the Arctic zone of Russia in the XX and early XXI centuries. *Arctic and Antarctic*, 3, 61–96, (In Russian), DOI: 10.7256/2453-8922.2019.3.29939.
- Moreydo V.M., Kalugin A.S. (2017). Assessing possible changes in Selenga R. water regime in the XXI century based on a runoff formation model. *Water Resources*, 44(3), 275–284, DOI:10.1134/S0097807817030149.
- Motovilov Yu.G. and Gelfan A.N. (2018) Models of runoff formation in the problems of hydrology of river basins. Moscow: Russian Academy of Sciences, 296, (In Russian).
- Roshydromet, 2022: Katzov V.M. (2022). Third assessment report on climate change and its consequences on the territory of the Russian Federation. Knowledge-intensive technologies. St. Petersburg: Roshydromet, 676. (In Russian)
- Ushakov M.V. (2013). Influence of the Kolyma HPP and climate change on the hydrological regime of the Kolyma River. *Bulletin of the Northeastern Scientific Center of the Russian Academy of Sciences*, 2, 20–24, (In Russian).
- Ushakov M.V., Lebedeva L.S. (2016). Climatic changes in the regime of water inflow formation into the Kolyma reservoir. *Scientific Notes of BelSU, Ser. Natural sciences*, 25(246), 120–127, (In Russian).
- AMAP 2017: Snow, Water, Ice and Permafrost in the Arctic (SWIPA). (2017). Arctic Monitoring and Assessment Programme (AMAP). Oslo, Norway.
- Gelfan A., Motovilov Y., Krylenko I. et al. (2015). Testing the robustness of the physically-based ECOMAG model with respect to changing conditions, *Hydrological Sciences Journal*, 60(7–8), 1266–1285, DOI: 10.1080/02626667.2014.935780.
- IPCC, 2013: Stocker T.F., Qin D., Plattner G.K., Tignor M. et al. Cambridge; N.Y. (2013). The Physical Science Basis. Contribution of Working Group I to the Fifth Assessment Report of the Intergovernmental Panel on Climate Change. Cambridge Univ. Press, 1535.
- Krysanova V. et al. (2018). How the performance of hydrological models relates to credibility of projections under climate change. *Hydrological Sciences Journal*, 63(5), 696–720.
- Kundzewicz Z. W., Krysanova V., Benestad R.E., Hov O. (2018). Uncertainty in climate change impacts on water resources. *Environmental Science & Policy*, 79, 1–8, DOI: 10.1016/j.envsci.2017.10.008
- Lebedeva L., Makarieva O., Vinogradova T. (2019). Analysis of spatial variability of river streamflow at the catchment area of the Kolyma reservoir, *IOP Conference Series: Earth and Environmental Science*, 321(1), 012022, DOI: 10.1088/1755-1315/321/1/012022.
- Magritskiy D.V., Frolova N.L., Evstigneev V.M. et al. (2018). Long-term changes of river water inflow into the seas of the Russian Arctic sector. *Polarforschung*, 87(2), 177–194, DOI: 10.2312/polarforschung.87.2.177.
- Motovilov Yu.G., Moreydo V.M., Millionshchikova T.D. (2022). An approximate formula for the vapor pressure deficit calculation to estimate the evaporation in runoff formation models of Russian rivers. *Water Resources*, 49(6), 1070–1081, DOI: 10.1134/S0097807822060094.
- Motovilov Y., Gottschalk L., Engeland K., Rodhe A. (1999). Validation of a distributed hydrological model against spatial observations. *Agric. For. Meteorol.*, 98–99, 257–277, DOI: 10.1016/S0168-1923(99)00102-1.
- Majhi I., Yang D. (2008). Streamflow characteristics and changes in Kolyma basin in Siberia. *Journal of Hydrometeorology*, 9(2), 267–279, DOI: 10.1175/2007jhm845.1.
- Nash J.E., Sutcliffe J.V. (1970). River flow forecasting through conceptual models. Part I – A discussion of principles. *Journal of Hydrology*, 10 (3), 282–290.
- Nasonova O.N., Gusev Ye.M., Volodin E.M., Kovalev E.E. (2018). Application of the land surface model SWAP and global climate model INMCM4.0 for projecting runoff of northern Russian rivers. 1. Historical simulations. *Water resources*, 45, 73–84, DOI:10.1134/S009780781806026X.
- van Vuuren D.P., Edmonds J., Kainuma M. et al. (2011). The representative concentration pathways: an overview. *Climatic Change*, 109(5), 5–31, DOI: 10.1007/s10584-011-0148-z.

APPENDICES

Table A.1. Changes in hydrological regime characteristics of the Kolymskoe station for the 21st century periods under various greenhouse gas emission scenarios.

Period	RCP	Air temperature anomalies (°C)	Precipitation Anomalies (%)	Annual discharge anomalies (%)	Maximum water flow anomalies (%)	Summer-autumn discharge volume anomalies (%)	Winter low-flow discharge volume anomalies (%)
Kolyma - Kolymskoe							
Relative to 1975-2004 Norm		-13.6 °C	344 mm	109 km ³	23200 m ³ /s	45.3 km ³	6.27 km ³
2020-2039	2.6	3.1	-0.2	14.2	19.8	15.7	2.3
	4.5	2.8	-4.3	9.0	11.8	11.8	-0.3
	6.0	2.9	-3.5	7.6	7.2	7.6	0.0
	8.5	3.3	-2.2	10.1	8.5	9.2	0.9
2040-2059	2.6	3.6	-0.7	8.3	6.1	9.7	9.9
	4.5	3.9	1.7	11.2	4.7	13.0	11.6
	6.0	3.3	-1.6	7.8	4.4	8.2	7.9
	8.5	4.8	8.0	20.4	16.1	19.8	15.7
2060-2079	2.6	3.3	0.6	13.6	14.5	11.2	0.5
	4.5	4.6	7.3	19.1	17.2	16.2	4.7
	6.0	4.6	7.8	21.3	17.8	21.9	8.4
	8.5	6.4	14.1	26.3	21.2	20.1	12.8
2080-2099	2.6	3.5	0.4	13.5	7.2	12.2	0.8
	4.5	4.7	9.0	24.6	20.1	25.1	6.9
	6.0	5.8	11.9	27.8	17.7	23.3	8.6
	8.5	8.4	28.9	47.2	35.7	34.2	31.4

Table A.2 (continued). Changes in hydrological regime characteristics of studied stations for the 21st century periods under various greenhouse gas emission scenarios

Period	RCP	Annual discharge anomalies (%)	Maximum water flow anomalies (%)	Summer-autumn discharge volume anomalies (%)	Winter low-flow discharge volume anomalies (%)
Kolyma - Srednekolymsk					
Relative to 1975-2004 norm		69.1 km ³	15500 m ³ /s	26.0 km ³	4.07 km ³
2020-2039	2.6	16.0	16.5	19.0	1.7
	4.5	11.3	8.7	16.1	-0.4
	6.0	9.3	1.9	11.0	-0.2
	8.5	13.0	8.9	13.5	0.5
2040-2059	2.6	10.0	3.3	12.6	10.0
	4.5	13.6	0.9	17.7	11.7
	6.0	8.9	0.4	10.6	8.1
	8.5	23.2	13.2	23.0	15.0
2060-2079	2.6	15.4	10.3	13.8	0.2
	4.5	21.2	17.0	18.6	4.2
	6.0	23.7	17.2	25.2	7.1
	8.5	29.2	21.3	23.4	10.9
2080-2099	2.6	15.0	3.3	15.2	0.2
	4.5	27.3	19.5	28.7	5.9
	6.0	31.9	14.5	28.5	7.8
	8.5	54.3	39.1	41.0	30.5
Bolshoy Anyuy - Konstantinovskaya					
Relative to 1975-2004 norm		15.8 km ³	3140 m ³ /s	6.51 km ³	0.647 km ³
2020-2039	2.6	10.4	8.7	9.7	3.7
	4.5	3.4	4.0	3.0	-0.3
	6.0	4.8	2.9	3.5	1.3
	8.5	4.3	-1.5	2.2	4.5
2040-2059	2.6	5.3	2.4	4.1	10.6
	4.5	6.3	-0.5	4.2	16.4
	6.0	5.9	0.8	2.4	12.0
	8.5	11.7	-0.1	12.5	23.8
2060-2079	2.6	8.7	5.1	6.2	1.5
	4.5	13.9	-2.2	12.7	9.2
	6.0	14.4	-1.5	15.9	12.2
	8.5	19.0	1.9	16.2	36.7
2080-2099	2.6	9.0	-2.8	8.3	2.2
	4.5	17.1	2.4	18.5	16.8
	6.0	16.4	4.9	12.7	27.6
	8.5	26.0	-0.5	21.5	71.9

Table A.2 (continued). Changes in hydrological regime characteristics of studied stations for the 21st century periods under various greenhouse gas emission scenarios.

Yasachnaya - Nelemnoye					
Relative to 1975-2004 norm		5.05 km ³	1190 m ³ /s	1.74 km ³	0.272 km ³
2020-2039	2.6	18.0	14.0	23.7	-3.7
	4.5	13.2	7.2	20.8	-5.3
	6.0	10.7	-2.0	14.6	-5.4
	8.5	15.5	5.9	18.4	-4.7
2040-2059	2.6	12.2	-0.1	15.5	8.2
	4.5	16.1	-3.6	23.6	11.2
	6.0	10.4	-6.5	13.0	6.8
	8.5	25.8	9.9	25.7	11.4
2060-2079	2.6	17.7	1.9	17.2	-4.4
	4.5	23.6	16.2	22.4	0.5
	6.0	26.2	12.6	29.8	-0.2
	8.5	33.4	16.4	29.2	5.6
2080-2099	2.6	16.5	-5.4	20.4	-4.3
	4.5	30.5	13.0	33.8	0.3
	6.0	36.3	10.5	35.1	6.4
	8.5	62.2	41.8	51.5	26.5

LAKE PHYSICS IN CHANGING CLIMATE: CASE STUDY OF KOSINO LAKES (MOSCOW, RUSSIA) IN 1984-2023

Maria Tereshina^{1*}, Oxana Erina^{1,2}, Dmitriy Sokolov¹, Kristina Pilipenko¹, Timur Labutin¹

¹ Lomonosov Moscow State University, Leninskie Gory 1, Moscow, 119234, Russia

² Shenzhen MSU-BIT University, Shenzhen, 518172, China

*Corresponding author: martereshina@yandex.ru

Received: July 22nd 2024 / Accepted: December 5th 2024 / Published: March 31st 2025

<https://doi.org/10.24057/2071-9388-2025-3505>

ABSTRACT. The one-dimensional lake model GLM was used to simulate the ice and stratification dynamics of two small lakes within Moscow City, Russia – lakes Beloe and Svyatoe of the Kosino Lake group. The model was calibrated on observation data from 2021–2023, and the significant trends of the lakes' thermal and mixing regime were calculated based on the model run for the period of 1983–2023. Some of the most distinct changes are associated with ice phenology, as both lakes lose ice cover at 4.4–5.0 days/decade. The length of the stratified period does not significantly change, but the stability of stratification in dimictic Lake Beloe is increasing. Both lakes have experienced an increase in mean surface water temperature over the year between 0.22–0.26 °C/decade, which is two times lower than the observed trend in the local air temperature. In polymictic Lake Svyatoe, bottom water temperature also increases at a maximum of 0.65 °C/decade. The fastest changes in ice phenology, water temperature and stratification occurred before 2013, while in the last decade most parameters have stabilized, despite the growing intensity of climate warming. This might demonstrate how the lakes are compensating for some of the climate signal.

KEYWORDS: lake modeling, thermal stratification, Schmidt stability, lake ice, climate change

CITATION: Tereshina M., Erina O., Sokolov D., Pilipenko K., Labutin T. (2025). Lake Physics In Changing Climate: Case Study Of Kosino Lakes (Moscow, Russia) In 1984-2023. *Geography, Environment, Sustainability*, 35-43
<https://doi.org/10.24057/2071-9388-2025-3505>

ACKNOWLEDGEMENTS: Field campaigns on Beloe and Svyatoe lakes were carried out with financial support from the Lomonosov Moscow State University (LMSU) research school framework (project no. 23-Sh07-67). Lake modeling and interpretation of results were supported by the state research assignment of the Department of Hydrology of the LMSU Faculty of Geography (project no. 121051400038-1).

Conflict of interests: The authors reported no potential conflict of interest.

INTRODUCTION

The physical aspects of lakes – their water temperature, density, and hydrodynamics – are the features that affect all the processes within their ecosystems. As lake hydrodynamics are closely interconnected with climate via changes in water and energy budget, lakes often act as good indicators of climate change (Williamson et al. 2008; Adrian et al. 2009), rapidly reacting to shifts in solar radiation, air temperature, available wind energy, precipitation, and other climate-related factors (Woolway et al. 2020).

Some of the most widely observed changes in lakes attributed to climate change include reduced ice cover (Sharma et al. 2021), rising water temperature in surface layers (O'Reilly et al. 2015; Dokulil et al. 2021), and some shifts in the water balance (Zhang et al. 2020; Yao et al. 2023). Prolonged ice-free periods with higher water temperatures can lead to an increase in biological productivity and the occurrence of harmful algal blooms (Ho et al. 2019; Woolway et al. 2021), the accumulation of nutrients and organic matter in the bottom layer (Schwefel et al. 2019), a worsening of the oxygen regime (Schwefel et al. 2016), and a restructuring of trophic webs (Jeppesen et al. 2014). Other changes are less detectable but can also pose a

threat to the stability of lake ecosystems. Hypolimnetic water temperature is shown to have both decreasing and increasing trends in various lakes around the world (Oleksy and Richardson 2021; Winslow et al. 2015), which can affect lake metabolism. Uneven heating at different depths and changing weather conditions during spring and fall can also cause the intensification of stratification (Magee and Wu 2017).

Many lake-specific characteristics, such as lake morphometry, water clarity, the structure of external water balance, and the surrounding landscape, significantly influence the thermal and mixing regime of lakes. Individual features of lakes can cause high variation in stratification and ice phenology even between lakes in very similar climatic conditions (Read et al. 2014; Higgins et al. 2021). The biogeochemistry of a specific lake can provide reliable feedback to climate signals, as dissolved substances and microorganisms also play a part in a lake's mixing regime (Mesman et al. 2021; Pilla et al. 2018). Due to this, the observed changes in water temperature, stratification, and ice phenology vary in intensity – and sometimes direction – in lakes around the world, as some of them effectively compensate for effects of climate change (Woolway et al. 2020). That means that climate change mitigation and

adaptation strategies in lake management have to be developed locally, taking into consideration the observed and expected changes in lake hydrodynamics and ecology. Studies on regional lakes are also necessary to assess the possible range of changes in a specific area.

A large number of European lakes are well monitored and thoroughly studied in terms of dynamics of water temperature, ice, and mixing regimes (Blenckner et al. 2007). However, a large part of Eastern Europe, including European Russia, remains relatively underinvestigated. At the same time, the effects of climate change are expected to be more dramatic in areas with a continental climate (Dokulil et al. 2010), making it possible to underestimate the possible consequences of climate change in more landlocked areas based on data from lakes located in milder climates.

The Kosino Lakes are three natural small lakes located on the eastern edge of Moscow City. In the first half of the 20th century, pioneering research on water physics, water chemistry, and hydrobiology was conducted at the Kosino biological station, although after 1941 only occasional short-term observations were made (Shirokova and Ozerova 2019). In 2021, a regular year-round monitoring campaign was started on the Kosino Lakes, and combined with a hydrodynamic lake model, this data allows us to describe their modern regime and emerging climate-related trends. These results can be used to make general assessments of the effects of climate change on small stratified and polymictic lakes in areas with continental European climates.

MATERIALS AND METHODS

Study sites

Lake Beloe is the largest of the three Kosino lakes, with a surface area of 0.3 km² and a maximum depth of 17 m (Fig. 1). A thin channel connects Lake Beloe to the smaller and shallower Lake Chernoe (maximum depth about 3 m). Occasional flow of water occurs between the two lakes through the channel; during winter and summer, the channel typically remains frozen or nearly dry, and during periods of higher water levels, its depth does not exceed 0.5 m. Lake Chernoe itself was not considered within the bounds of this study due to insufficient data on its thermal regime and its more complicated morphometry (the

presence of a large shallow zone with limited water exchange with the deeper part). There is also a small drainage outlet located at the south-western shore of Lake Beloe, where free flow into the municipal drainage system occurs when the water level reaches the outlet. Lake Svyatoe is the smallest of the three lakes, with a surface area of only 0.08 km² and a maximum depth of ~3 m. It is mostly surrounded by a 70–200 m wide strip of peat bog and does not have significant water exchange with any other water bodies.

The Kosino lakes historically had poor water quality due to eutrophication caused by their old age and exacerbated by anthropogenic pressure. Lake Beloe is dimictic, has a Secchi depth of 0.5–1.7 m (based on data of 2021–2024), and all water below 3–5 m depths is anoxic almost year-round (except for spring and autumn mixing periods) and contains hydrogen sulphide. Lake Svyatoe has a Secchi depth of 0.35–2.3 m; it is polymictic and has a lower dissolved salt and nutrient content; therefore, its oxygen regime is more favorable, but anoxic conditions may still spread for up to 1.5 m from the bottom in the summertime and take up almost all of the water mass in winter.

According to year-round manual observations on staff gauges maintained on the shores of both lakes throughout 2020–2023, Lake Beloe has an annual water level variation of 0.3–0.6 m, and Lake Svyatoe – about 0.2–0.5 m. In both lakes, the maximum water level is observed after snowmelt and is followed by a generally stable decline throughout the ice-free period.

Data collection

The data on the water temperature of lakes Beloe and Svyatoe was collected during the period of July 2021–December 2023. Monthly manual measurements of water temperature were taken at their deepest points with 1 m vertical resolution using a YSI Pro30 water temperature and conductivity meter. Buoys were also set up at the deepest point of each lake in ice-free months, with a chain of several HOBO Pendant water temperature loggers attached. On Lake Beloe, the loggers functioned in July–November 2021 and May–October 2023 at 0.5, 2, 4, 6, 10 and 15 m depths. On Lake Svyatoe, a buoy functioned during the same periods, and additionally, we set temperature loggers at 0.5, 1 and 2.5 m depths in late April–August 2022.

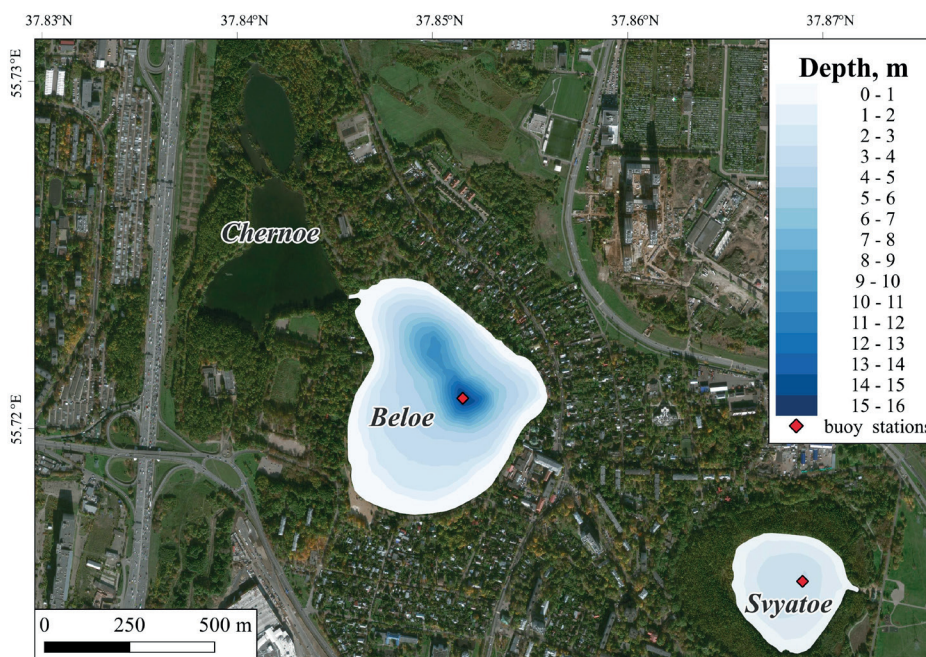


Fig. 1. Location and bathymetry of the Kosino Lakes

For lake bathymetry, a depth-area curve was approximated for each lake from the data of depth sounding made in the summer of 2020. As meteorological forcing, time series from ERA5 global reanalysis were used (Hersbach et al. 2020), and linearly interpolated to the lakes' coordinates between the nearest grid points.

There was no reliable data on surface and groundwater runoff for the lakes. Moreover, a large portion of the surrounding area drains into the municipal storm sewage system, and the high degree of urbanization in their watersheds limits the ability to model runoff. For the purpose of this study, the water balance of the lakes was only represented by surface mass fluxes (precipitation and evaporation) as calculated in the model based on meteorological data.

Model description and setup

The General Lake Model (GLM) is a one-dimensional model used for simulating lake hydrodynamics on seasonal and annual timescales. It utilizes a Lagrangian layer structure to simulate a lake's external water balance, heat budget, vertical mixing, and ice formation on a daily time step. External water balance includes surface mass fluxes, inflows, and outflows. The heat budget of the surface layer consists of shortwave and longwave radiation fluxes and sensible and latent heat fluxes. Mixing is simulated based on the balance of potential (PE) (Eq. 2) and available kinetic (TKE) energy (Eq. 1):

$$TKE = \left\{ 0.5C_K w_*^3 \Delta t \right\}_{conv} + \left\{ 0.5C_K C_w u_*^3 \Delta t \right\}_{wind} + \left\{ 0.5C_S \left(u_b^2 + \frac{u_b^2}{6} \frac{d\xi}{dz_{sml}} + \frac{u_b \xi}{3} \frac{du_b}{dz_{sml}} \right) \right\}_{shear} \Delta z_{k-1} \quad (1)$$

$$PE = \left[\left\{ 0.5C_T (w_*^3 + C_w u_*^3)^{2/3} \right\}_{accel} + \left\{ \frac{\Delta p}{\rho_0} g z_{sml} \right\}_{lift} + \left\{ \frac{g \xi^2}{24 \rho_0} \frac{d(\Delta \rho)}{dz_{sml}} + \frac{g \xi \Delta \rho}{12 \rho_0} \frac{d\xi}{dz_{sml}} \right\}_{K-H} \right] \Delta z_{k-1} \quad (2)$$

In model equations, TKE is made up of surface wind stress (*wind*), convective mixing (*conv*), shear production between layers, and Kelvin-Helmholtz billowing (*shear*). PE, on the other hand, is the amount of energy needed to lift water at the bottom of the mixed layer (*lift*), speed it up to the speed of the mixed layer (*accel*), and consume the energy that comes from making waves inside the layer (*K-H*). Internal heat balance also accounts for deep mixing based on constant or variable turbulent diffusivity in hypolimnion. A detailed description of model parameterization of hydrodynamic processes is provided in (Hipsey et al. 2019). A number of multi-lake studies (Read et al. 2014; Bruce et al. 2018; Prats et al. 2018) and cross-model comparisons (Golub et al. 2022; Ishikawa et al. 2022; Man et al. 2021) show that GLM is very good at simulating of the thermal regime of natural and man-made lakes in many places around the world.

In this study, we used GLM version 3.0.5 executed via the R package *GLM3r* and processed the output data with functions from the package *glmtools*. The required meteorological input data include daily shortwave and longwave radiation, air temperature, relative humidity, wind speed, and precipitation.

Model calibration was conducted via the random search function from the *FME R* package. It included adjusting model parameters to reach the minimal RMSE of water temperature, as well as a good representation of the water level and the timing of freezing and thawing of lakes. The model was calibrated on data from 2022–2023 and then its performance was validated based on data from 2021; data for a period of over two years of continuous water temperature measurements is considered sufficient in multi-model intercomparison studies, e.g., in works supporting the ISIMIP protocol (Mesman et al., 2020; Golub et al., 2022). The final values of the model parameters as well as the resulting model errors are presented in Table 1. Final RMSE values for the validation period were 1.45 °C for Lake Beloe and 1.19 °C for Lake Svyatloe.

The non-parametric Mann-Kendall trend test (Kendall 1975) as implemented in the *Kendall R* package was used to assess the statistical significance of the simulated trends on ice-on and ice-off dates and the parameters of summer stratification.

RESULTS

Freeze-up and ice-break dates

Lakes Beloe and Svyatloe show a high variation in freezing dates (Fig. 2). In the period from 1984–2023 the earliest ice-on date on Lake Beloe was November 10th, 1988, and the latest – December 26th, 2006. In 18 out of 40 simulated winters, the lake froze in the last ten days of November.

Table 1. Calibrated model parameters and model errors for calibration, validation, and whole simulation period

Parameter name	Parameter meaning	Lake Beloe	Lake Svyatloe
Kw	Light extinction coefficient	0.76	1.66
coef_wind_stir	Mixing efficiency – wind stirring	0.43	0.10
wind_factor	Scaling factor for wind speed	0.75	0.98
lw_factor	Scaling factor for longwave radiation	0.96	1.02
at_factor	Scaling factor for air temperature	1.02	0.98
snow_albedo_factor	Scaling factor for snow albedo	0.35	0.45
RMSE	– calibration (2022–2023)	0.90 (n=1026)	1.15 (n=809)
	– validation (2021)	1.45 (n=500)	1.19 (n=230)
	– whole period (2021–2023)	1.10 (n=1526)	1.55 (n=1039)

Lake Svyatoye, on average, freezes 2 days earlier than Lake Beloe and generally has the same long-term pattern of freeze-up dates with overall variation between November 4th and December 25th. In 1987, 1995 and 2021 ice cover on Lake Svyatoye appeared 10–16 days before Lake Beloe, but in all other cases, the difference between ice-on dates of the two lakes did not exceed one week. Although generally Lake Svyatoye freezes earlier, in 9 out of 40 simulated winters it froze 1–7 days later than Lake Beloe. This occurred in years where, following a fall cold period with negative air temperatures, as both lakes approached the freezing point, the daily air temperature rose by several degrees. In those years, the mean air temperature over the 10 days before freezing of Lake Beloe was on average $-1.6\text{ }^{\circ}\text{C}$ (-1.9 – $+0.8\text{ }^{\circ}\text{C}$), while in other years it averaged $-4.0\text{ }^{\circ}\text{C}$ (-9.0 – $-0.1\text{ }^{\circ}\text{C}$). While both lakes likely accumulated heat, the smaller Lake Svyatoye apparently heated more efficiently, which might also be aided by its lower transparency (light extinction coefficient of 1.66 versus 0.76 in Lake Beloe).

The ice-off dates of the two lakes showed much less variation: on Lake Beloe, break of ice cover occurred between March 28th and April 23rd; on Lake Svyatoye – between March 19th and April 19th. For Lake Beloe, in 29 out of 40 years, the ice-off occurred in the second ten days of April. For Lake Svyatoye, in 20 of the years it occurred in the first ten days of April, and for 19 of the years – in the second ten days of April. Lake Svyatoye lost ice cover 1–10 days before Lake Beloe (average 5 days).

For ice-on dates, despite the high variation, statistically significant (at $p < 0.05$) trends of $+2.4$ and $+3.1$ days/decade were detected for lakes Beloe and Svyatoye. However, only Lake Beloe showed a significant trend of -1.5 days/decade for ice-off dates. Between 1982–2002 and 2003–2023, the total duration of ice cover decreased from 122–160 days to 99–151 days on Lake Beloe and from 118–157 days to 95–153 days on Lake Svyatoye. The mean trend of ice cover loss was -4.4 days/decade for Lake Beloe and -5.0 days/decade for Lake Svyatoye ($p < 0.05$ in both cases). Changes in ice cover are also reflected in reduced ice thickness: while for the whole period maximum ice thickness varied between 23 and 67 cm, it is found to be declining at approximately 2 cm/decade, but these trends are not statistically significant.

Stratification duration

In this study, we classified a lake as stratified if the difference between the surface and bottom temperatures exceeded $1\text{ }^{\circ}\text{C}$, and defined the start of the stratified period as the date when this difference persisted for a minimum of 7 consecutive days. Over the simulation period, the stratified period on Lake Beloe began 1–22 days after ice melt – between April 11th (2008) and May 8th (1986). On Lake Svyatoye, periods of stratification over a week long did not occur before late April–May, or as late as 80 days after the ice-off date. The earliest onset of stratification on Lake Svyatoye was on March 31st (2007) and the latest – on June 13th (2021). On average, stratified period on Lake Beloe starts 7 days after ice melt, and on Lake Svyatoye – 22 days after ice melt.

Stratification on dimictic Lake Beloe remained unbroken for several months after its onset (Fig. 3), with fall mixing occurring normally from middle to late October. The earliest disruption of summer stratification occurred on September 28th in 1986, and the latest occurred on November 2nd in 2019. The uninterrupted stratified period lasted 143–198 days (183 days on average). It was followed by a mixing period of 18 to 65 days that ends with the formation of ice cover.

Lake Svyatoye is polymictic, and in 1983–2023 was characterized by 3 to 14 separate events of stratification onset and break per year (including periods when the lake became stratified for less than 7 days). The longest periods of uninterrupted stratification lasted for almost as long as on Lake Beloe: in various years they were 16 to 132 days long. Only in 5 out of 41 years did the longest period of stratification on Lake Svyatoye not reach 30 days; in most of the years, one stratified period of 50–90 days or two periods of 30–50 days occurred. Mixing between stratified periods lasted between 1 and 20 days. In total, Lake Svyatoye remained stratified for 66 to 143 days each year. After August, only shorter periods of stratification occurred (< 20 days long), and in October they only lasted for up to 5 days. For the remaining 32 to 118 days in fall until the freezing of the lake, it remained in a nearly mixed state as it cooled off.

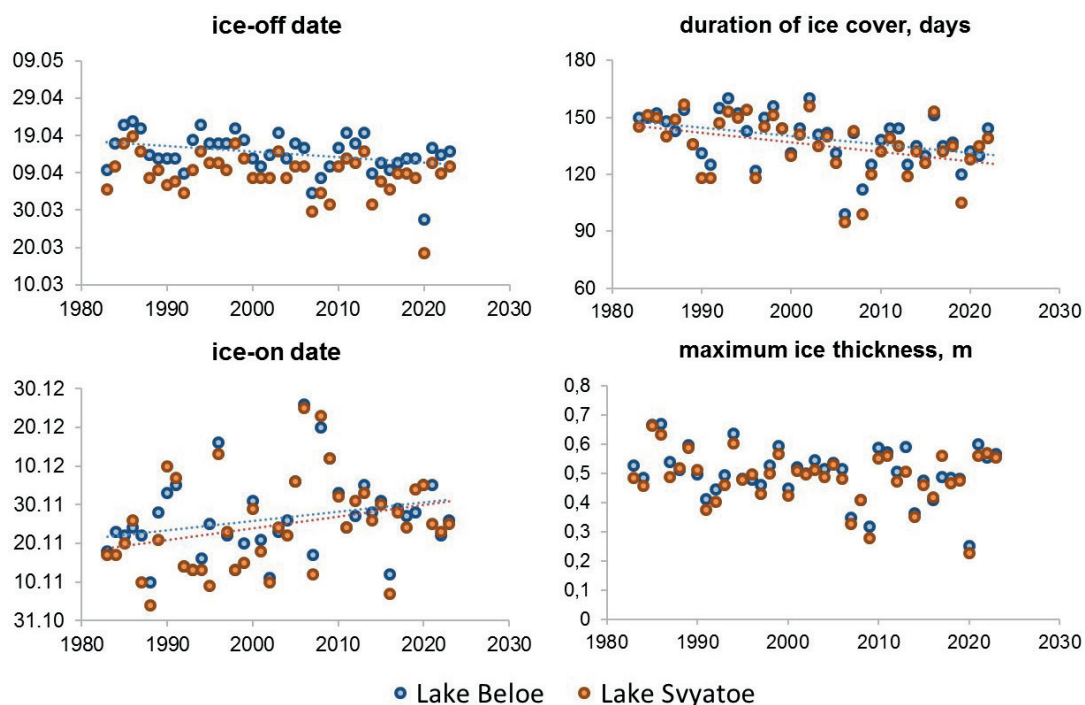


Fig. 2. Ice-off and ice-on dates, duration of ice cover, and maximum ice thickness on lakes Beloe and Svyatoye in 1983–2023. Dotted lines show statistically significant trends in time series

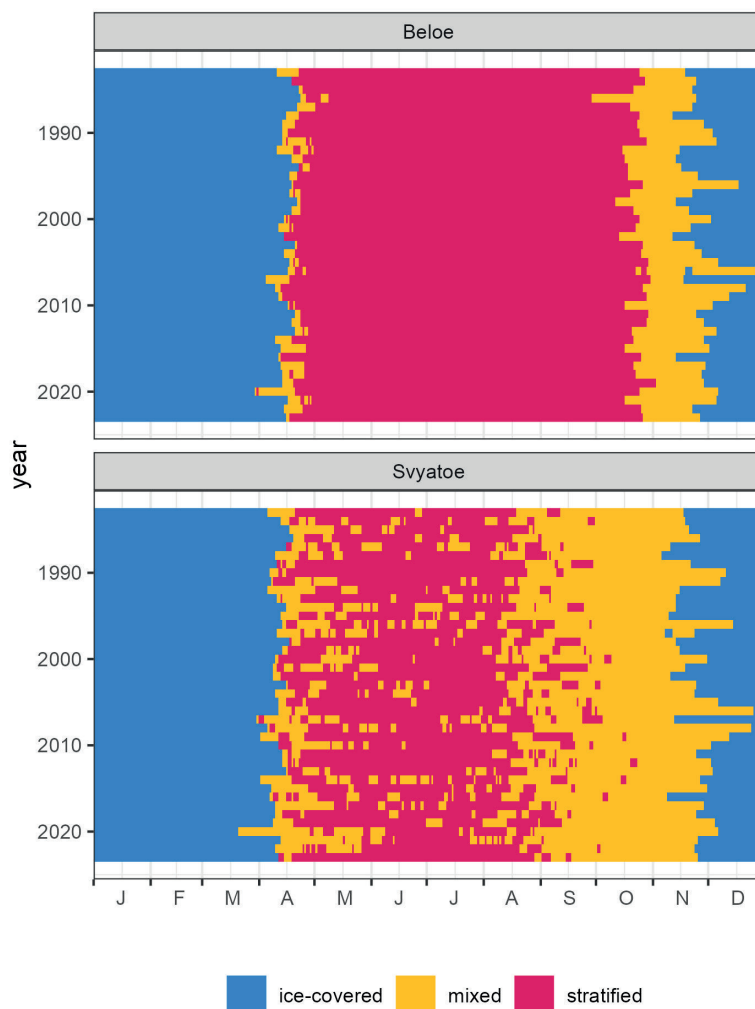


Fig. 3. Duration of ice-covered, mixed and stratified periods on lakes Beloe and Svyatooe based on simulations for 1983-2023

No statistically significant trends were detected for stratification onset, break, or duration for either of the lakes.

Water temperature

At the moment of stratification onset, the bottom temperature of Lake Beloe (at 0.5 m above lake bottom at the deepest point) varied between 4.2 and 7.9 °C. In general, higher bottom temperatures correspond to later stratification onset dates, but even in years with relatively fast stratification onset, the bottom layer can be relatively warm depending on wind conditions. For example, in 2008 the ice-off occurred on April 7th, but over the next 5 days, average air temperature of 12.8 °C and wind speed of 4.5 m/s caused the water temperature to reach 7.1 °C in the entire water column before the density gradient was enough to resist wind stirring. In most of the years, the bottom water temperature in Lake Beloe remained nearly constant (within 0.3 °C from starting temperature) during the whole period of summer stratification. There was a significant heat transfer into bottom layers only in 1997, 2009, 2017, and 2020. This was likely because heat moved slowly through the thermocline and into deeper layers during very warm times with little wind. This happened when the water temperature at the surface was high, which increased the vertical temperature gradient and, in turn, the vertical heat diffusion coefficient (Hondzo et al. 1991). Heating from the bottom sediments of the littoral zone or heat transport with dissipation of internal waves can also act as mechanisms of hypolimnion warming throughout the summer (Nishri et al. 2015). During the fall mixing, bottom water temperature rose by 1–3 °C

from summer value; the maximum water temperature at the bottom of the lake at fall overturn reached 5.1–8.2 °C. The mean value of the bottom temperature for the stratified period was 7.2–7.7 °C.

In Lake Svyatooe, the bottom temperature during the summer is much more variable and follows the dynamics of air temperature and temperature of the surface layer more closely than in seasonally stratified Lake Beloe. At the first occurrence of prolonged (>7 days) summer stratification, the bottom water temperature of the lake varied between 4.3 and 19.3 °C, on average equaling 10.1 °C. At the moment of maximum heat storage, which normally occurred in August, the bottom water temperature reached 16.9–25.9 °C, and mean values for the summer period of intermittent stratification varied between 11.8 and 21.2 °C.

The surface temperatures of both lakes have been found to be almost synchronous (fig. 4). Maximum surface temperature mostly occurred in the second half of July and was within 22.8–31.9 °C for Lake Beloe and 24.3–33.6 °C for Lake Svyatooe. Mean surface water temperatures over the stratified period were 15.6–19.9 °C and 18.0–26.1 °C, respectively.

No statistically significant trends were detected for the start and mean bottom water temperature over the stratified period, but the maximum bottom temperature of Lake Svyatooe increased by 0.65 °C/decade. The mean summer surface temperature of Lake Beloe increased by 0.27 °C/decade, and the yearly mean water temperature increased by 0.26 and 0.22 °C/decade for lakes Beloe and Svyatooe, which corresponds to an increase of the mean annual heat storage by 1.21 and 0.17 J/m² per decade.

Simulated parameters of ice phenology, stratification, and thermal regime of both lakes in a more detailed form are presented in supplementary materials.

DISCUSSION

Ice-on and ice-off dates, as well as the water temperature of the Kosino Lakes, changed significantly between 1922–1929 (as published in reports of the Kosino biological station) and 2021–2023 (as observed during field work for this study). Our results and calculated trends allow to explore those changes in the recent decades in more detail. Based on our simulations, we calculated linear trend values for ice phenology, thermal regime, and stratification intensity for both lakes over different time periods (table 2). The obtained trends in surface water temperature over the first 20 years of simulation are close to the world average lake surface water warming rate of $+0.34$ °C/decade between 1985–2009 as summarized by O'Reilly et al. (2015) and mean warming rate of Central European lakes of $+0.25$ °C/decade (Dokulil et al. 2010). The increase in maximum surface water temperature at $+0.42$ – 0.44 °C/decade is also coherent with the average trend for European lakes of $+0.58$ °C/decade (Dokulil et al. 2021). The changes in water temperature are non-linear: the sharpest increase in water temperature occurred before 2013, which coincided with the steepest trend in air temperature over the summer period, while in the last decade the intensity of those changes decreased. Our data does not show a significant slowdown of water temperature rise in response to the “warming hiatus” of 1998–2012 as was found for many lakes of the Northern hemisphere (Winslow et al. 2018), but shows similar correlation between air and water warming rate at different aggregation periods and proves the necessity of using multiple decades of data for evaluating the intensity of climate change in lakes.

Both lakes are warming significantly slower than the ambient air: over the period of 1983–2023 the average air temperature warming trend was $+0.53$ °C/decade, while the surface water temperature of lakes only increased

by 0.22 – 0.26 °C/decade. At the same time, a positive relationship between mean surface water temperatures over the whole year and the stratified period with air temperature is maintained with determination coefficients (r^2) of up to 0.40 – 0.81 . On average, lakes of the world are warming faster than the air, but this varies regionally, and cases such as the Kosino Lakes are not rare (O'Reilly et al. 2015, Dokulil et al. 2021). Reduced intensity of lake surface warming can be caused by various feedback mechanisms, such as increased evaporation contributing to larger heat loss (Woolway et al. 2020). Adding wind speed to the regression model insignificantly enhances its predictive ability, as evidenced by an increase in r^2 of less than 0.05 . This suggests that wind plays a minor role in the lakes' thermal regime during the current period.

Maximum bottom water temperature over the summer period has changed insignificantly for Lake Beloe, but for Lake Svyatloe it is increasing at a faster pace than mean surface temperature. Deep lakes around the world can show increasing or decreasing trends in bottom water temperature (Gerten and Adrian 2001), and for shallow polymictic lakes, the direction of its change depends on whether or not a lake is shifting into a dimictic regime. Lake Svyatloe does not show a statistically significant increase in duration or intensity of stratification, and its main tendency is currently towards a rise in bottom water temperature, which may negatively affect its water chemistry and biota.

The shift in ice phenology is one of the most prominent features of ongoing changes in temperate and high-latitude lakes (Sharma et al. 2021). Like many of the researched European and North American lakes, the Kosino Lakes experience a gradual decrease in ice cover period length at -4.4 – 5.0 days/decade, as well as increasingly frequent years with extreme ice phenology, such as multiple freezing and thawing events. For the Kosino Lakes and many other mesotrophic and eutrophic lakes in European Russia, the mixing regime and duration of ice cover are a defining trait for the entire ecological state. A decrease in the duration of the ice-covered period may have a positive impact on their

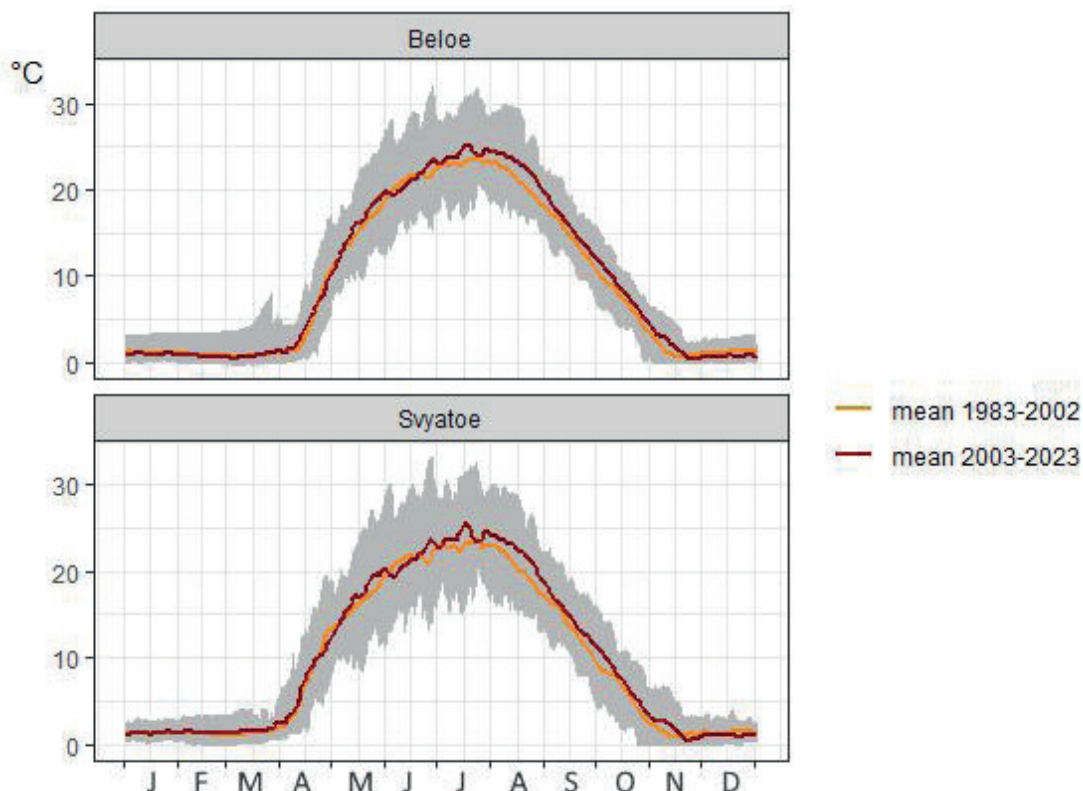


Fig. 4. Variation of surface water temperature of lakes Beloe and Svyatloe (grey) and mean daily surface water temperatures for periods of 1983–2002 and 2003–2023

Table 2. Mean linear trend coefficients for characteristics of climate, ice phenology and thermal regime of lakes Beloe and Svyatooe over various aggregation periods

parameter	unit (per decade)	Beloe			Svyatooe		
		1983-2003	1983-2013	1983-2023	1983-2003	1983-2013	1983-2023
mean air temperature (year)	°C	+0.50	+0.53**	+0.53***	+0.50	+0.53	+0.53
mean air temperature (April–November)	°C	+0.32	+0.70***	+0.48***	+0.32	+0.70***	+0.48***
mean wind speed (April–November)	m/s	−0.09*	−0.08**	−0.02	−0.09*	−0.08**	−0.02
ice-off date	days	−0.2	−0.7	−1.5*	−0.05	−0.8	−1.4
ice-on date	days	−0.2	+4.9*	+2.4*	+0.6	+6.1*	+3.1*
duration of ice cover	days	−1.3	−6.4*	−4.4**	−1.9	−7.8**	−5.0**
duration of stratification ¹	days	+3.6	+4.3	+2.4	+12.3	+10.4	+2.0
mean surface water temperature (year)	°C	+0.32	+0.40***	+0.26***	+0.24	+0.39***	+0.22***
mean surface water temperature (stratified period)	°C	+0.28	+0.39*	+0.27*	−0.08	+0.26	+0.32
max. surface water temperature (stratified period)	°C	+1.23	+0.96*	+0.44	+1.27	+0.97*	+0.42
maximum bottom water temperature (stratified period)	°C	−0.15	−0.09	+0.03	+0.69	+0.75	+0.65*
mean heat storage (year)	J/m ²	+2.7*	+1.7**	+1.2***	+0.22	+0.28***	+0.17**
maximum heat storage (stratified period)	J/m ²	+6.1*	+3.9**	+2.2*	+1.0	+0.7*	+0.3
mean Schmidt stability (stratified period)	J/m ²	+2.5	+4.7*	+2.9	+0.1	+0.2	+0.04

¹ duration of stratification for Lake Svyatooe given as the sum of days with difference between surface and bottom water temperature >1 °C. Significance levels: * $p < 0.05$ ** $p < 0.01$ *** $p < 0.001$

ecosystems, significantly improving oxygen availability in deeper layers and reducing the risk of winter fish-kills and the accumulation of dissolved nutrient elements during winter (Woolway et al. 2020). However, increasing availability of light might lead to a rise in phytoplankton production.

The absence of significant changes in the duration of the stratified period and bottom water temperature in stratified Lake Beloe suggests that ecological conditions in its hypolimnion during summer remain nearly unchanged, although this can change with future warming. For shallow Lake Svyatooe, patterns of summer mixing do not seem to have changed significantly, but enhanced heating has caused higher water temperature in all of the layers, which may affect aquatic organisms and biogeochemical processes, causing faster eutrophication than in deeper lakes.

CONCLUSIONS

Our simulations show noticeable and statistically significant changes in the ice and thermal regime of the Kosino Lakes. Some of the most dramatic changes are found in the loss of ice cover at 4–5 days/decade. Later ice-on dates contribute more to this change than earlier ice break-up dates, much like in other lakes of the Northern Hemisphere (Sharma et al. 2021). In 1984–2023, mean surface water increases at 0.2–0.3 °C/decade for both lakes. The strongest changes occurred in 1983–2013 at 0.4 °C/decade, which is close to the global average trend for 1985–2009 of 0.34 °C/decade, but slightly less than was found for European lakes (O'Reilly et al., 2015). Maximum surface water temperature increases at +0.42–0.44 °C/decade, which is also coherent with the average trend for European lakes of +0.58 °C/decade (Dokulil et al. 2021).

Over the period of 1983–2023 no statistically significant changes in stratification duration have occurred for either the dimictic Lake Beloe or polymictic Lake Svyatooe, and water column stability in Lake Beloe only increased significantly in 1983–2013 and not in a larger aggregation period of 1983–2023. Maximum bottom water temperature in the polymictic Lake Svyatooe also increases at +0.65 °C/decade. These findings show that there is no significant trend towards strengthening of stratification in either the polymictic or dimictic lake. Changes in mixing regime are some of the most irregular, as opposing trends are found throughout global lakes (Woolway et al., 2020).

The lake surface water has warmed up almost two times slower than the atmospheric air (0.22–0.26 °C/decade vs 0.53 °C/decade, respectively), but surface water temperature is closely correlated with air temperature. This relationship suggests that the thermal feedback of increased evaporation is more significant in the Kosino Lakes than in many lakes globally (Dokulil et al. 2021; Woolway et al. 2020). Aggregations over different time periods show a large variation in trend estimations, which underlines the importance of long-term data availability for reliable estimates of climate-related changes in lakes. Wind speed plays only a small part in determining changes in lake water temperature or stratification.

The case study of Kosino Lakes shows that ice regime and water temperature are currently among the most affected physical characteristics of lakes in this region, while the duration and intensity of thermal stratification are more stable. This implies that the winter regime of lakes in Central Russia and their extreme thermal conditions require close attention in environmental research and planning. ■

REFERENCES

- Adrian R., O'Reilly C.M., Zagarese H., Baines S.B., Hessen D.O., Keller W., Livingstone D.M., Sommaruga R., Straile D., Donk E., Weyhenmeyer G.A., and Winder M. (2009). Lakes as sentinels of climate change. *Limnology and oceanography*, 54(6), 2283–2297, DOI: 10.4319/lo.2009.54.6_part_2.2283.
- Blenckner T., Adrian R., Livingstone D.M., Jennings E., Weyhenmeyer G.A., George D.G., Jankowski T., Järvinen M., Aonghusa C.N., Nöges T., Straile D., and Teubner K. (2007) Large-scale climatic signatures in lakes across Europe: a meta-analysis. *Global Change Biology*, 13, 1–13, DOI: 10.1111/j.1365-2486.2007.01364.x.
- Bruce L.C., Frassl M.A., Arhonditsis G.B., Gal G., Hamilton D.P., Hanson P.C., Hetherington A.L., Melack J.M., Read J.S., Rinke K., Rigosi A., Trolle D., Winslow L., Busch R.D., Copetti D., Cortés A., de Eyto E., Elliott J.A., Gallina N., Gilboa Y., Guyennon N., Huang L., Kerimoglu O., Lenters J.D., MacIntyre S., Makler-Pick V., McBride C.G., Moreira S., Özkundakci D., Pilotti M., Rueda F.J., Rusak J.A., Samal N.R., Schmid M., Shatwell T., Snorthheim C., Soulignac F., Valerio G., van der Linden L., Vetter M., Vinçon-Leite B., Wang J., Weber M., Wickramaratne C., Woolway R.I., Yao H., and Hipsey M.R. (2018). A multi-lake comparative analysis of the General Lake Model (GLM): Stress-testing across a global observatory network. *Environmental Modelling & Software*, 102, 274–291, DOI: 10.1016/j.envsoft.2017.11.016.
- Dokulil M. T., Teubner K., Jagsch A., Nickus U., Adrian R., Straile D., Jankowski T., Herzig A., and Padišák J. (2010). The impact of climate change on lakes in Central Europe. In: G. George, ed., *The Impact of Climate Change on European Lakes*. Aquatic Ecology Series, vol 4. Dordrecht: Springer, 387–409, DOI: 10.1007/978-90-481-2945-4_20.
- Dokulil M.T., de Eyto E., Maberly S.C., May L., Weyhenmeyer G.A., and Woolway R.I. (2021). Increasing maximum lake surface temperature under climate change. *Climatic Change*, 165, 56, DOI: 10.1007/s10584-021-03085-1.
- Gerten D. and Adrian R. (2001). Differences in the persistency of the North Atlantic Oscillation signal among lakes. *Limnology and Oceanography*, 46, 448–455, DOI: 10.4319/lo.2001.46.2.0448, 2001.
- Golub M., Thiery W., Marcé R., Pierson D., Vanderkelen I., Mercado D., Woolway R., Grant L., Jennings E., Kraemer B., Schewe J., Zhao F., Frieler K., Mengel M., Bogomolov V., Bouffard D., Côté M., Couture R.-M., Debolskiy A., and Zdrovennova G. (2022). A framework for ensemble modelling of climate change impacts on lakes worldwide: the ISIMIP Lake Sector. *Geoscientific Model Development Discussions*, 15(11), 4597–4623, DOI: 10.5194/gmd-15-4597-2022.
- Hersbach H., Bell B., Berrisford P., Hirahara S., Horányi A., Muñoz-Sabater J., Nicolas J., Peubey C., Radu R., Schepers D., Simmons A., Soci C., Abdalla S., Abellana X., Balsamo G., Bechtold P., Biavati G., Bidlot J., Bonavita M., and Thépaut J.N. (2020). The ERA5 global reanalysis. *Quarterly Journal of the Royal Meteorological Society*, 146(730), 1999–2049, DOI: 10.1002/qj.3803.
- Higgins S.N., Desjardins C.M., Drouin H., Hrenchuk L.E., and van der Sanden J.J. (2021). The role of climate and lake size in regulating the ice phenology of boreal lakes. *Journal of Geophysical Research: Biogeosciences*, 126(3), e2020JG005898, DOI: 10.1029/2020JG005898.
- Hipsey M.R., Bruce L.C., Boon C., Busch B., Carey C.C., Hamilton D.P., Hanson P., Read J., Sousa E., Weber M., and Winslow L.A. (2019). A General Lake Model (GLM 3.0) for linking with high-frequency sensor data from the Global Lake Ecological Observatory Network (GLEON). *Geoscientific Model Development*, 12(1), 473–523, DOI: 10.5194/gmd-12-473-2019.
- Ho J.C., Michalak A.M., and Pahlevan N. (2019). Widespread global increase in intense lake phytoplankton blooms since the 1980s. *Nature*, 574(7780), 667–670, DOI: 10.1038/s41586-019-1648-7.
- Hondzo M., Ellis C.R., Stefan H.G. (1991) Vertical diffusion in small stratified lake: Data and error analysis. *Journal of hydraulic engineering*, 117(10), 1352–1369, DOI: 10.1061/(ASCE)0733-9429(1991)117:10(1352)
- Ishikawa M., Gonzalez W., Golyjeswski O., Sales G., Rigotti J.A., Bleninger T., Mannich M., and Lorke A. (2022). Effects of dimensionality on the performance of hydrodynamic models for stratified lakes and reservoirs. *Geoscientific Model Development*, 15(5), 2197–2220, DOI: 10.5194/gmd-15-2197-2022.
- Jeppesen E., Meerhoff M., Davidson T.A., Trolle D., Søndergaard M., Lauridsen T.L., Beklioglu M., Brucet S., Volta P., Gonzalez-Bergonzoni I., and Nielsen A. (2014). Climate change impacts on lakes: An integrated ecological perspective based on a multi-faceted approach, with special focus on shallow lakes. *Journal of Limnology*, 73, 88–111, DOI: 10.4081/jlimnol.2014.844.
- Kendall M.G. (1976). *Rank Correlation Methods*. New York: Oxford University Press.
- Magee M.R. and Wu C.H. (2017). Response of water temperatures and stratification to changing climate in three lakes with different morphometry. *Hydrology and Earth System Sciences*, 21(12), 6253–6274, DOI: 10.5194/hess-2016-262.
- Man X., Lei C., Carey C.C., and Little J.C. (2021) Relative Performance of 1-D Versus 3-D Hydrodynamic, Water-Quality Models for Predicting Water Temperature and Oxygen in a Shallow, Eutrophic, Managed Reservoir. *Water*, 13, 88, DOI: 10.3390/w13010088.
- Mesman J.P., Ayala A.I., Adrian R., De Eyto E., Frassl M.A., Goyette S., Kasparian J., Perroud M., Stelzer J.A.A., Pierson D.C., and Ibelings B.W. (2020). Performance of one-dimensional hydrodynamic lake models during short-term extreme weather events. *Environmental Modelling & Software*, 133, 104852, DOI: 10.1016/j.envsoft.2020.104852.
- Mesman J.P., Stelzer J.A.A., Dakos V., Goyette S., Jones I., Kasparian J., McGinnis D., and Ibelings B. (2021). The role of internal feedbacks in shifting deep lake mixing regimes under a warming climate. *Freshwater Biology*, 66, 1021–1035, DOI: 10.1111/fwb.13704.
- Nishri A., Rimmer A., Lechinsky Y. (2015). The mechanism of hypolimnion warming induced by internal waves. *Limnology and Oceanography*, 60, 1462–1476, DOI: 10/1002/lo.10109
- O'Reilly C.M., Sharma S., Gray D., Hampton S., Read J., Rowley R., Schneider P., Lenters J., McIntyre P., Kraemer B., Weyhenmeyer G., Straile D., Dong B., Adrian R., Allan M., Anneville O., Arvola L., Austin J., Bailey J., and Zhang G. (2015). Rapid and highly variable warming of lake surface waters around the globe. *Geophysical Research Letters*, 42(24), 10.773–10.781, DOI: 10.1002/2015GL066235.
- Oleksy I.A. and Richardson D.C. (2021). Climate change and teleconnections amplify lake stratification with differential local controls of surface water warming and deep water cooling. *Geophysical Research Letters*, 48(5), e2020GL090959, DOI: 10.1029/2020GL090959.
- Pilla R.M., Williamson C.E., Zhang J., Smyth R.L., Lenters J.D., Brentrup J.A., Knoll L., and Fisher T.J. (2018). Browning-related decreases in water transparency lead to long-term increases in surface water temperature and thermal stratification in two small lakes. *Journal of Geophysical Research: Biogeosciences*, 123(5), 1651–1665, DOI: 10.1029/2017JG004321.
- Prats J., Reynaud N., Danis P.A. (2018). Application of the General Lake Model (GLM) to a large set of French water bodies. 5th IAHR Europe Congress "New Challenges in Hydraulic Research and Engineering", Jun 2018, Trente, Italy. 337–338.
- Read J.S., Winslow L.A., Hansen G.J., Van Den Hoek J., Hanson P.C., Bruce L.C., and Markfort C.D. (2014). Simulating 2368 temperate lakes reveals weak coherence in stratification phenology. *Ecological modelling*, 291, 142–150, DOI: 10.1016/j.ecolmodel.2014.07.029.
- Schwefel R., Gaudard A., Wüest A., and Bouffard D. (2016). Effects of climate change on deepwater oxygen and winter mixing in a deep lake (Lake Geneva): Comparing observational findings and modeling. *Water Resources Research*, 52(11), 8811–8826, DOI: 10.1002/2016WR019194.
- Schwefel R., Müller B., Boisgontier H., and Wüest A. (2019). Global warming affects nutrient upwelling in deep lakes. *Aquatic Sciences*, 81(3), 50, DOI: 10.1007/s00027-019-0637-0.

Sharma S., Richardson D.C., Woolway R.I., Imrit M.A., Bouffard D., Blagrove K., Daly J., Filazzola A., Granin N., Korhonen J., Magnuson J., Marszelewski W., Matsuzaki S., Perry W., Robertson D., Rudstam L., Weyhenmeyer G., and Yao H. (2021). Loss of ice cover, shifting phenology, and more extreme events in Northern Hemisphere lakes. *Journal of Geophysical Research: Biogeosciences*, 126(10), e2021JG006348, DOI: 10.1029/2021JG006348.

Shirokova V. and Ozerova N. (2019). Kosino lakes as a cradle of Russian limnology: The history of the Kosino Biological Station and Kosino Nature Reserve. *Voprosy istorii estestvoznaniia i tekhniki*, 40(2), 233-253 (in Russian with English summary). DOI: 10.31857/S020596060004936-1.

Williamson C.E., Dodds W., Kratz T.K., and Palmer M. (2008). Lakes and streams as sentinels of environmental change in terrestrial and atmospheric processes. *Frontiers in Ecology and the Environment*, 6(5), 247-254, DOI: 10.1890/070140.

Winslow L.A., Leach T.H., and Rose K.C. (2018). Global lake response to the recent warming hiatus. *Environmental Research Letters*, 13, 054005, DOI: 10.1088/1748-9326/aab9d7.

Winslow L.A., Read J.S., Hansen G.J., and Hanson P.C. (2015). Small lakes show muted climate change signal in deepwater temperatures. *Geophysical Research Letters*, 42(2), 355-361, DOI: 10.1002/2014GL062325.

Woolway R.I., Kraemer B.M., Lenters J.D., Merchant C.J., O'Reilly C.M., and Sharma S. (2020). Global lake responses to climate change. *Nature Reviews Earth & Environment*, 1(8), 388-403, DOI: 10.1038/s43017-020-0067-5.

Woolway R.I., Kraemer B.M., Zscheischler J., and Albergel C. (2021). Compound hot temperature and high chlorophyll extreme events in global lakes. *Environmental Research Letters*, 16(12), 124066, DOI: 10.1088/1748-9326/ac3d5a.

Yao F., Livneh B., Rajagopalan B., Wang J., Crétau J.F., Wada Y., and Berge-Nguyen M. (2023). Satellites reveal widespread decline in global lake water storage. *Science*, 380(6646), 743-749, DOI: 10.1126/science.abo2812.

Zhang G., Yao T., Xie H., Yang K., Zhu L., Shum C.K., Bolch T., Yi S., Allen S., Jiang L., Chen W., and Ke C. (2020). Response of Tibetan Plateau lakes to climate change - Trends, patterns, and mechanisms. *Earth-Science Reviews*, 208, 103269, DOI: 10.1016/j.earscirev.2020.103269.

INTRODUCING THE MOUSAVI PRIMATE CITY INDEX FOR IRAN'S URBAN SYSTEM ASSESSMENT

Mir Najaf Mousavi¹, Safdar Ali Shirazi², Muhammad Nasar-u-Minallah^{2*}, Nima Bayramzadeh³

¹ Department of Geography, Geography and Urban Planning, Urmia University, Urmia, Iran

² Institute of Geography, University of the Punjab, Lahore, 54000, Pakistan

³ Ph.D. Student in Spatial Planning, Department of Geography, Urmia University, Urmia, Iran.

*Corresponding author: Nasarbhali@gmail.com

Received: January 21st 2024 / Accepted: December 26th 2024 / Published: March 31st 2025

<https://doi.org/10.24057/2071-9388-2025-3218>

ABSTRACT. The main goal of this research study is to analyze the urban system of Iran during the years 1956 to 2021 to propose a new model. This is done by examining the primate city index of the urban settlement system based on previous models. The study employs a descriptive-analytical approach. Initially, it investigates the population trends and the number of cities in Iran over the specified period, comparing the growth rates of the total population and the urban population to assess changes in population distribution across the country. Additionally, spatial analysis of population distribution is conducted using Hot Spot Analysis and Directional Distribution methods. This article evaluates the advantages and disadvantages of various primate city indices, ultimately leading to the formulation of a new index for measuring the degree of urban primacy. The findings reveal that the percentage of the urban population in Iran surged from 31.41% in 1956 to 75.99% in 2021. According to the Mousavi primate city index, urban primacy in Iran exhibited an upward trend from 1956 to 1986, followed by a decline from 1986 to 1996. However, this trend reversed upwards in 2016, attributed to the rising number of cities and migration to newly established urban areas due to drought and relative stagnation in agriculture. The rank-size pattern further validates the outcomes of the new index.

KEYWORDS: primate city, population, rank – size, urban system, Iran

CITATION: Mousavi M. N., Shirazi S. A., Nasar-u-Minallah M., Bayramzadeh N. (2025). Introducing the Mousavi Primate City Index for Iran's Urban System assessment. *Geography, Environment, Sustainability*, 44-53

<https://doi.org/10.24057/2071-9388-2025-3218>

Conflict of interests: The authors reported no potential conflict of interest.

INTRODUCTION

The rapid urbanization process around the world has brought renewed interest to the question of the size distribution of cities (Düben and Krause 2020). Studies show that all over the world, a growing proportion of the population lives in cities. Ten years ago, 51.1 percent lived in urban areas. By 2019, the share of the urban population increased to 55.7 percent. It is generally higher in the developed world (80.5 percent in 2019) in comparison to the developing world (51.1 percent), with transition economies in between the two (65.4 percent) (UNCTAD 2020). This trend shows that urbanization is occurring so rapidly in many areas that it has become difficult to distinguish between cities, suburbs, and towns (Decker et al. 2007). In general, the rate of growth in large cities is much faster than the total population growth (Ding et al. 2022). Metropolitan areas with over one million inhabitants grew half a percentage point faster per year than smaller ones (OECD 2020). Although cities tend to grow over time, they do not grow uniformly at the same rate (Duranton and Puga 2013). Much of the existing research on city size distributions has primarily focused on the largest urban centers, overlooking smaller cities, towns, and settlements (Decker et al. 2007). In essence, attention has mainly been given to large cities and metropolitan areas, while small and medium-sized cities (SMSC) have received little consideration (Wagner and Growe 2021).

The expansion of the largest cities appears to happen at an accelerated pace, leading to a trend of "region-based urbanization" rather than "city-based." Consequently, addressing regional developmental imbalances should be a key focus in future planning efforts (Wilson and Yudho et al. 2017). As a result, a greater focus should be on the development of small towns. Small towns are essential, as they play a key role as regional service centres in rural hinterland development through direct production linkages, as well as "spread" and "trickling down" effects. Reinforcement of small-town production and institutional structures not only contributes directly to rural and regional development but can also be considered a necessary condition (Abou-Korin 2014). An undeniable feature of contemporary urban population growth is how the largest cities appear to grow at increasingly rapid rates. This phenomenon has given rise to the concept of urban primacy which is the demographic, economic, social and political dominance of one city over all others within an urban system (Smith 2000). Present-day usage of the term "primacy" and "primate city" stems directly from the 1939 article, "The Law of the Primate City," by Mark Jefferson (1863-1949), a professor of geography at the U.S. Michigan Normal School (Meyer, 2019). In concept, primacy is a ratio of the characteristics of a country's dominant city (e.g. population, economic activity, and political influence), relative to smaller cities (Hartley 2015).

The irregularity begins to surface when metropolitan populations are examined, rather than those within city limits. Studies further demonstrate geographers have backed away from the use of the rank-size rule in favour of the primate city law. For instance, London and Paris are not twice the size of their second-ranked cities (Birmingham and Marseilles) but seven times larger. Bangkok, meanwhile, has twenty-two times the population of Nonthaburi (Campanella 2015). This means that urban primacy (i.e., the concentration of the urban population in only one or two centres), is a characteristic of many developing countries, and is viewed by many social scientists as detrimental to the balanced development of the country as a whole (Sokona, 1985). Over the past several decades, many studies about city size distribution have been launched, with most of them concentrating on only the largest cities while ignoring smaller cities, towns, and settlements. This is mainly due to the lack of accurate data for small cities. However, despite this, as much as 70% of the population may reside in these smaller areas, and omitting such a large majority of the population may lead to biased characterizations of city size distributions (Decker et al. 2007; Bhalli and Ghaffar 2015; Li et al. 2016; Nasar-u-Minallah et al. 2017; Riaz et al. 2017; Nasar-u-Minallah et al., 2021). Furthermore, political power is often concentrated in these large urban agglomerations (Sokona, 1985). Large differences across countries in the size and structure of local administrative units seriously affect cross-country comparisons and represent an obstacle to compiling robust worldwide evidence on the features of urbanization and its consequences (Nasar-u-Minallah et al. 2016; Parveen et al. 2019; Naem et al. 2021; Moreno-Monroy et al. 2021; Zia et al. 2022).

Given these considerations, examining the urban system to achieve the distribution and arrangement of the population and cities in the territorial structure is necessary and inevitable. This is largely because the optimal distribution of population and cities in the spatial organization of the land will lead to a balanced distribution of facilities and services. In this regard, the investigation of the structure of the urban system of Iran using the rank-size model shows the unbalanced distribution of the population in the urban hierarchy (Feizpour & Asayesh 2022). In general, the city size distribution can be categorized into rank-size and primate distributions, which include lognormal, primate, and intermediate types. Zipf's law, particularly its exponent of one, has been a focal point for understanding optimal city size distribution and is supported by empirical studies that also examine the implications of Gibrat's law. These studies explore how various factors, including geographical scale and developmental levels, influence Zipf's exponent (Li et al. 2016; Moreno-Monroy et al. 2021).

Rank size and primate distributions are two primary models of city size distribution, which can be categorized into three types: lognormal, primate, and intermediate. Zipf's law has long attracted significant attention for its compelling explanation of optimal city size distribution, grounded in the criterion of Pareto optimality (Li et al. 2016). In this paper, we question whether there is an optimal method to fully identify the "primate city" phenomenon. Many methods have already been proposed since Jefferson's initial idea. These proposals include six indicators which are suggested to determine the prime city. However, they fail to discuss two critical points. One is the lack of attention of this index to all cities of the urban system, considering their rank. Second, most of these indexes do not lead to a single basis. This has caused these indicators to not correspond to the results of the rank-size of cities in some cases. This shows that the phenomenon of "primate city" cannot be accurately expressed only by examining the

first few cities. Rather, it must consider the ratio of the first city to all cities in the urban system. This problem occurs when the researcher encounters many cities. Therefore, the negative effects of the growth of the first urban phenomenon are obvious in the urban system of any country. Identifying this phenomenon can help development planners to select policies and measures to solve this problem.

By accepting Jefferson's definition of a "primate city", the primacy of Tehran during the 2020s becomes readily apparent. In 2020, Tehran had 2.8 times more people than the next largest city, Mashhad (Iranian Statistics Center 2021). Important reasons accounting for such a high growth rate are the natural increase in the population, urban and rural immigration, as well as an expansion of the city limits (Feizpour & Asayesh 2022). This issue has led to doubts about the concept and theoretical basis of the prime city. The main goal of this research is to analyze Iran's urban system from 1956 to 2021, to develop a new model by evaluating the primate city index of various cities based on prior frameworks. It highlights the strengths and weaknesses of existing primate city methodologies and suggests a more effective approach to address their limitations. However, while the study presents data and trends, a more concise explanation of the findings from 1956 to 2021 would enhance the analysis, particularly in terms of how these results relate to the gaps identified in earlier research.

Material and Methods

Study area

In terms of geographical location, Iran is in the southwest of Asia and the Middle East region and is the eighteenth in the world in terms of size (Fig. 1). Iran is divided into thirty-one provinces. According to the statistical yearbook of the country 2021 (Iranian Statistics Center 2021), it has an area of 1.6 million square kilometres and a population of 84 million people, it is situated in the geographical coordinates of 25 to 40 degrees North latitude and 44 to 63 degrees East longitude, which has 8640 kilometres of border lines with neighbouring countries. The number of cities in Iran has increased to 1428 cities in 2021. Tehran, Mashhad, Isfahan, Tabriz, Shiraz, Ahvaz and Qom are among the biggest cities in Iran (Iranian Statistics Center 2021).

Data Sources

The main data used in this study are aggregate population data in the cities of Iran from 1956 to 2022 (www.amar.org.ir/english). Additionally, the point data of Iranian cities during the years 1956 to 2021, based on the latest census in Iran, has been entered into the GIS software.

Data Analysis Methods

The study method is descriptive-analytical. First, the situation of the population and the number of cities in Iran in the years 1956 to 2021 has been investigated, and in this regard, the data of the Iranian Statistics Center has been used. Eq. No. 1 was used to check the population growth rate and Eq. No. 2 was used to check the urban growth rate.

$$r = \left(\sqrt[n]{\frac{P_n}{P_0}} - 1 \right) \times 100 \quad (1)$$

$$r = \frac{b - a}{a} \times 100 \quad (2)$$

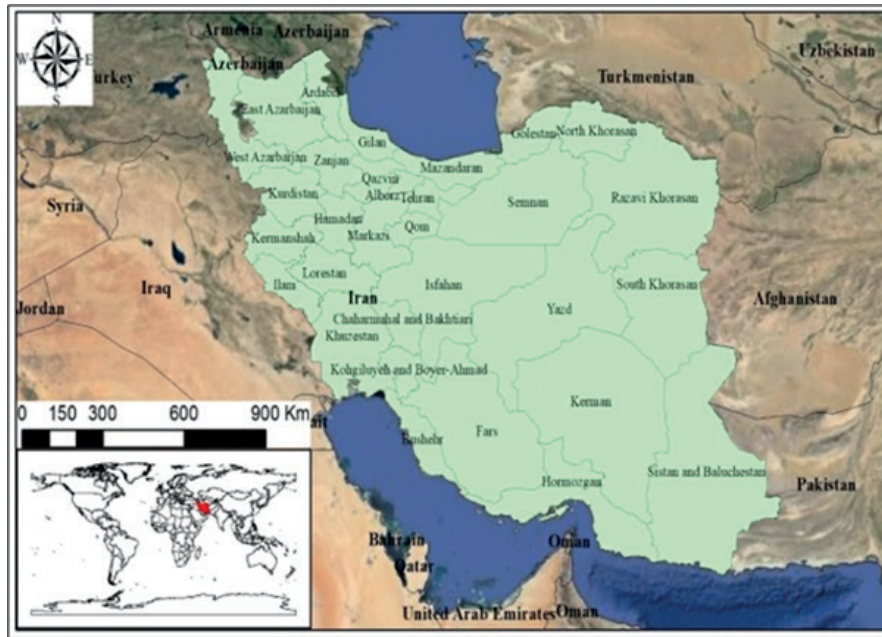


Fig. 1. Geographical location of the study area (Iran)

In the following analysis, the growth rate of the total population and the growth rate of the urban population have been compared to determine the changes in population distribution in the country. Furthermore, in this research study, the methods of Hot Spot Analysis and Directional Distribution were used for the spatial analysis of the population distribution. The Directional Distribution, represented by the Standard Deviational Ellipse, was used for the spatial analysis of population distribution, as it delineates the geographical distribution trend by summarizing both the dispersion and orientation of the observed samples (Wang et al. 2015). Hot Spot Analysis (Getis–Ord (Gi*)) spatial statistics were used for the spatial analysis of the population distribution, as they jointly evaluate the spatial dependency effect of both frequency and attribute values within the framework of the conceptualized spatial relationship (Songchitruksa & Zeng 2010).

Moreover, the first urban indicators, two cities, four cities, Mahta’s four cities, Herfindal concentration, and Momoa Al-Wasabi have been studied. This article examines the strengths and weaknesses of prime urban indicators. The results of these studies have led to the presentation of a new index to determine the degree of primacy.

Primate City Index

The degree of the primacy of the largest can be measured by the ratio of its population to that of the second largest city or those of some other ranks of cities combined. Primacy is the superlative lead of the largest or primate city over the smaller cities and towns. This could be expressed as a ratio:

$$\text{Index of primacy} = p1/p2$$

Where P1 and P2 are the populations of the first and second largest settlements respectively, or Primary Index (2) = P1/P3, where P1 and P3 are the populations of the first and third settlements respectively. It is necessary under the rank-size rule that the primacy index for P1 and P2 settlements be 2; for P1 and P3 it must be 3 and so on. When the second largest city has less than half the population of the largest city, then the degree or level of primacy is said to be high and vice versa (Dolui 2017).

Two City Index: One of the most common methods of determining the “primate city” is the index of two cities, which has been used by urban and regional planners due to its simplicity on a larger scale. This index is related to the Zipf law (rank size) and has a definite basis that is obtained by calculating the population ratio of the first city to the second city.

$$TCI = \frac{P1}{p2}$$

If the numerical yield concluded is 2, it is determined to have balance, and urban primacy is not dominant. However, if it is greater than 2, the urban primacy index is dominant (Henderson, 2003). The primary issue with this method is that the rest of the cities of the urban system are not considered. This is due to the consideration that it is possible the prime city would not be dominant over the second city in an urban system but has urban primacy toward other cities. In other words, this index does not calculate urban primacy toward the total cities of the urban system. Hence, it may raise criticism or questions regarding the urban system and urban primacy concept theoretically.

Four City Index: This index like the city index is based on urban Rank-Size distribution and includes the ratio of the prime city toward the total population of second, third and fourth cities obtained by this formula (Henderson, 2003):

$$FCI = \frac{P1}{P2 + P3 + P4}$$

This index numerical base is 0/923 which mostly shows urban primacy domination. The primary issue with this method is there is a lack of focus on the other cities’ urban systems as a city index. It can lead to misunderstanding about existing urban systems, and their abundance of cities.

Mahta’s Four City Index: Mahta (1964) proposed the best method to study urban primacy according to primate city size toward the first 4 cities by revising the four cities formula:

$$\frac{p1}{p1 + p2 + p3 + p4}$$

Richardson then adapted the four-city index to the criteria of the rank-size rule. If the desirable sizes of cities in an urban system according to the urban rank-size rule are apparent, then the prime city size will be twofold the second city, threefold the third city, and fourfold the fourth city. As a result, the ratio of the prime city toward the total urban system of prime four cities can be determined to be 0/48. A major caveat and consideration for this method, like other methods, is the need to focus on other cities' urban systems.

Herfindal Concentration Index: This index studies the degree of concentration in the urban system which is obtained by the below equation (Zebardast 2007):

$$Hi = \sum_{i=1}^n \left(\frac{p_i}{P} \right)^2$$

Where (pi) is the population of the studying city (i), and P is the total urban population. The issues with other methods do not particularly apply to this method. It studies the ratio of every city to the total urban population. However, it does not conclude. Moreover, the ratio of cities to total urban population cause cities' rank and rank-size rule to lack a role or necessity.

Moomav & Alwosabi Index: This index obtains from the fraction of the sum of the first and second population toward the sum of the 3rd & 4th cities:

$$Moomay \& Alwosasavi = \frac{p1 + p2}{p3 + p4}$$

The greater this numerical index is, the more urban primacy can be characterized as part of the urban system. This index, such as the Herfindal Concentration & Urban Primacy indexes, does not conclude with a unique base. On the other hand, it ignores the other cities' urban systems and does not conform to the Rank-Size Rule.

Providing a new primate city index

Providing a New Index for Assigning Primate City: The type of index that is to be provided will not have the existing problems of the other indexes from the author's point of view. The four-city index is provided as (1) Eq. containing the total urban system cities:

$$\frac{P1}{P1 + P2 + P3 + \dots + Pn} = \frac{P1}{P} \tag{1}$$

Although the (1) equation contains all the cities, the rank-size rule does not have any role. In other words, the city rank is not considered. In these circumstances, it has been decided to combine the Rank-Size Rule with the (1) Eq. in this study, to design a new urban primacy index in which the cities' rank will be considered. The general structure for the Rank-Size Model is as follows (Guerin 1995):

$$Pr = \frac{P1}{rq} \tag{2}$$

where, "Pr" is the population of the city that is ranked "r", "P1" is the prime city population and "q" is the line slope. The desired size of cities in equation (2) is obtained when "q" is equal to 1 or -1. In that case, the second city can be determined to be 1/2 of the prime city, the third city is 1/3 of the prime city and the n city is 1/n of the prime city. If "q"

is greater than 1, the prime city is dominant. If it is smaller than 1, the domination of cities is meant little (Hekmatnia & Moosavi, 2006). Therefore, providing the index will conclude to 1 according to the Rank-Size Rule. The number is considered when it is dominant to Rank-Size. It means that the indexes will be concluded to a unique base to compare different urban systems together. So, we will have:

$$P1 = \frac{p1}{R1} \gg P1 = P1R1 \tag{3}$$

For a city that is nth rank:

$$Pn = \frac{P1}{Rn} \gg P1 = PnRn \tag{4}$$

(4) Eq. is equal to the below equation:

$$\frac{Pn}{P1} = \frac{1}{Rn} \tag{5}$$

On the other words, it is equal to equation (6):

$$\frac{P1}{Pn} = Rn \tag{6}$$

To bring the base to number one, we combine the first and second parts of Equations 5 and 6. In this case, we will have:

$$\frac{Pn}{P1} \times Rn = \frac{P1}{Pn} \times \frac{1}{Rn} = 1 \tag{7}$$

If we consider the above relation, for each of the cities, the obtained number will be equal to one. However, if we consider the above relation for all cities (i.e. if the city system according to the rule of Rank-Size slope of the line is equal to 1), the number obtained will be equal to the number of cities.

$$\left(\frac{P1}{P1} \times \frac{1}{R1} \right) + \left(\frac{P1}{P2} \times \frac{1}{R2} \right) + \dots + \left(\frac{P1}{Pn} \times \frac{1}{Rn} \right) \tag{8}$$

In Eq. (8), the number of cities is equal to:

$$1 + 1 + 1 + \dots + 1 = N \tag{9}$$

Therefore, to conclude the designed indexes to 1, according to the Rank-Size Rule, we should necessarily divide Eq. (8) by Eq. (9) means the number of cities, to conclude to 1. If it is greater than 1, it shows urban primacy domination and less than 1 shows the middle & small cities domination. Therefore, the urban primacy index is as below (10):

$$P.C = \frac{\left(\frac{P1}{P1} \times \frac{1}{R1} \right) + \left(\frac{P1}{P2} \times \frac{1}{R1} \right) + \dots + \left(\frac{P1}{Pn} \times \frac{1}{Rn} \right)}{N} \tag{10}$$

As a result, According to Eq. (10) Mousavi primate city index is presented as follows (Mousavi and Taghvaei, 2009) (11):

$$P.C = \frac{\sum_{i=1}^n \left(\frac{P1}{Pi} \times \frac{1}{Ri} \right)}{N} \tag{11}$$

The basic capability of this index is that it can show the prime city domination over the total urban system cities on their rank base. This differs from the previous indexes which only show the prime city domination over some cities. It is possible that the prime city does not have as much domination over some cities in an urban system. However, it is also possible to have high domination over the next-rank cities, and this index can assist in calculating and assigning that domination.

RESULTS

Urbanizing Trends and Dynamics in Iran

Urbanization, as driven by higher population growth in urban than in rural areas, constitutes one of the most important transformations in contemporary population geography (Lerch 2017). In this regard, migration can play an important role in determining population growth in an area (Liu and Yamauchi 2014). Migration to cities in recent decades has led to an increase in population density as well as the level of large cities in Iran. Often after each general population and housing census, the data obtained can show the status of changes in population distribution. In this regard, the situation of urbanization trend in Iran during the years 1956 to 2021 has been investigated in Table 1.

According to Table 1, During the years 1956 to 2016, the urban population as well as the number of cities has increased in Iran. In this regard, the number of cities in Iran has increased from 199 cities in 1956, to 1428 cities in 2021. This has in turn led to an increase in the percentage of urbanization in the urban system from 31.41 to 75.99. Additionally, the geographical location of Iranian cities using GIS during the years 1956 and 2021 is shown in Fig. 2.

The trend of urban development and urbanization in Iran's urban system, according to Table 1 and Fig. 2, is that the number of cities in Iran has increased from 199 cities

in 1956 to 1428 cities in 2021. One of the main reasons for the increase in the number of cities in Iran has been the conversion of large villages into cities to prevent the migration of villagers to cities. Furthermore, the percentage of the urban population in Iran has reached 75.99% from 31.41% in these years; over 65 years, the percentage of the urban population has increased by 44.58% (i.e. by 57,922,437 people). While from 1956 to 2021, the total number of people added to the population of Iran was 65,100,296 people.

Moreover, according to Table 1, the growth rate of the total population and the urban population of Iran shows that the urban population has faced greater growth than the total population. As such, the main cause of this issue is the centralized policies of the government in big cities and the concentration of industries mines and major economic activities in cities. Finally, the phenomenon of industrialization of cities in Iran simultaneously with lifestyle changes and the transition from tradition to modernity, is another factor that has increased the trend of urbanization in Iran.

Spatial Analysis of the Urbanization Process

In this section, the spatial analysis of the distribution of Iranian cities in the years 1956 and 2021 has been investigated, so that the hot spots (densely populated

Table 1. Urbanizing Trend and dynamics in Iran

Year	number of cities	total population	Urban population	Urban population (%)	The growth rate of the number of cities	Population growth rate	Urban population growth rate
1956	199	18954704	5953563	31.41	-	-	-
1966	272	25788722	9794246	37.98	36.68	3.13	5.1
1976	373	33708744	15854680	47.03	37.13	2.71	4.93
1986	487	49445010	26844561	54.29	30.56	3.91	5.41
1996	612	60055488	36817789	61.31	25.67	1.96	3.21
2006	1015	70495782	48259964	68.46	65.85	1.62	2.74
2016	1242	79926270	59146847	74.00	22.36	1.26	2.06
2021	1428	84055000	63876000	75.99	14.98	1.01	0.77

Source: Statistics Center of Iran, 1956-2022

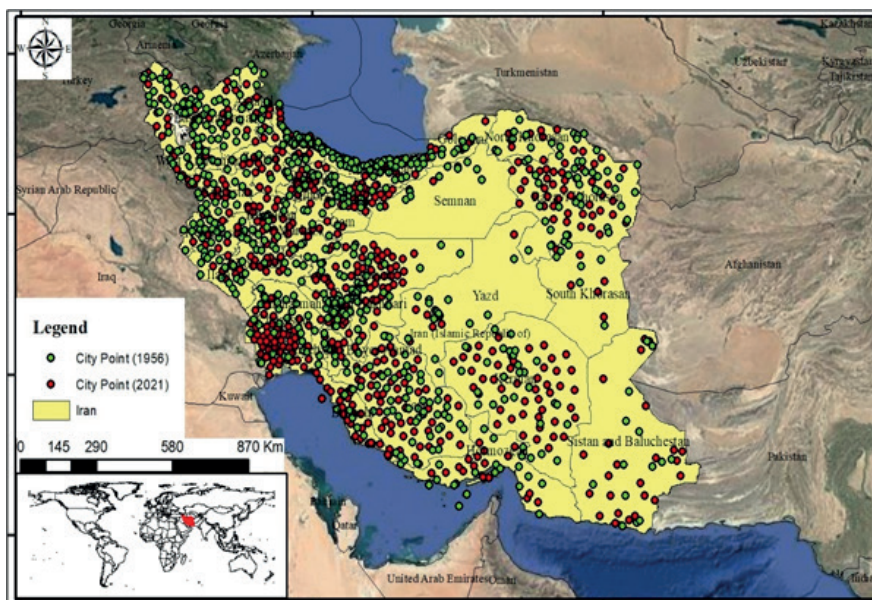


Fig. 2. Distribution of Iranian cities in 1956 and 2021

cities) in Fig. 3 have been examined first, and the changes in the concentration of cities have been investigated in Fig. 4.

The results of Fig. 3 show that in 1956, the population was more concentrated in the north of the country, while in 2021, the population of the country was more concentrated in Tehran and Khorasan-e-Razavi. Investigating the urbanization development process in Iran between 1956 and 2021 using hot spots in the ARC GIS environment shows a variety of considerations, for instance, the increasing number of cities and shift of the population to the central and southeastern regions of Iran was aimed at balancing the distribution and dispersion of the population, according to the purpose of the territorial land use planning. Most of the cities in the north and west of Iran have been able to have a better population due to their location on the slopes of the Alborz and Zagros mountains, and having favourable water, soil, and better climatic conditions. This issue was further corroborated by the study conducted by Seifoldini et al. (2014) and

Zebardast (2007), which revealed a concentration of densely populated cities in the central region of the country and close to Tehran.

Fig. 4 also shows that the concentration of Iranian cities has been from the northwestern side of the country to the centre of the country, and the main reason for this is the better living conditions, security and proximity to the country's capital. Additionally, Bayramzadeh & Mousavi (2024) highlight that the development and emergence of new cities have occurred primarily in the more developed regions of the country, further reinforcing the findings of this analysis. According to the Spatial analysis of the urbanization process in Iran, the results show that in 1956, the population was more concentrated in the north of the country, while in 2021, the population of the country was more concentrated in Tehran and Khorasan-e-Razavi. Additionally, the concentration of Iranian cities has been from the northwestern side of the country to the centre of the country. The main reason for this is the better living conditions, security, and proximity to the country's capital.

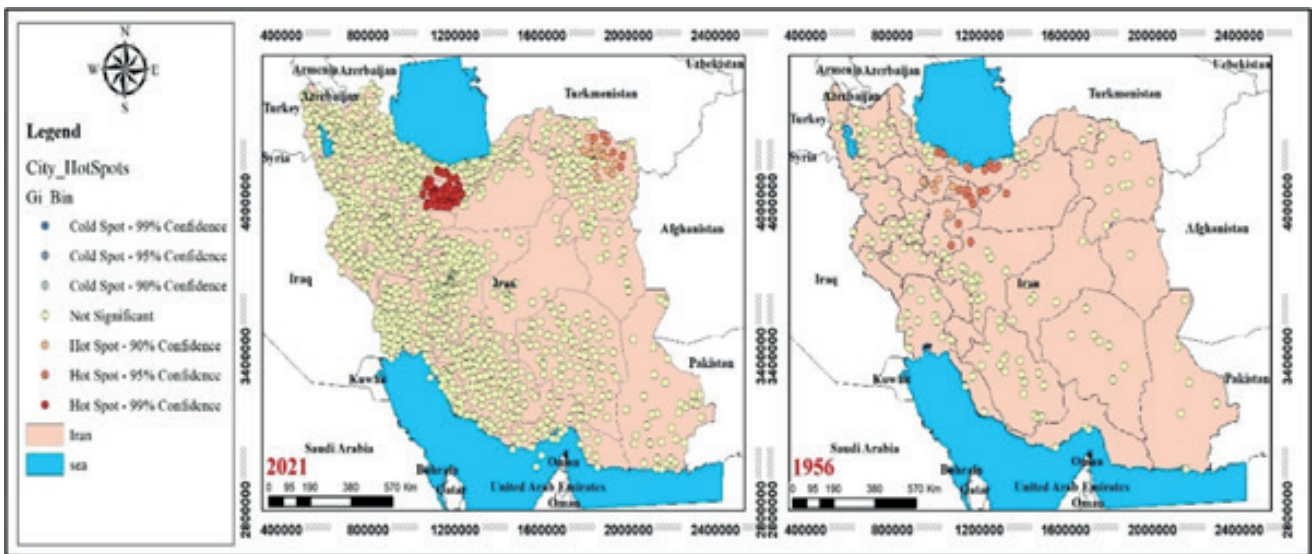


Fig. 3. Hot Spot Analysis in 1956 and 2021

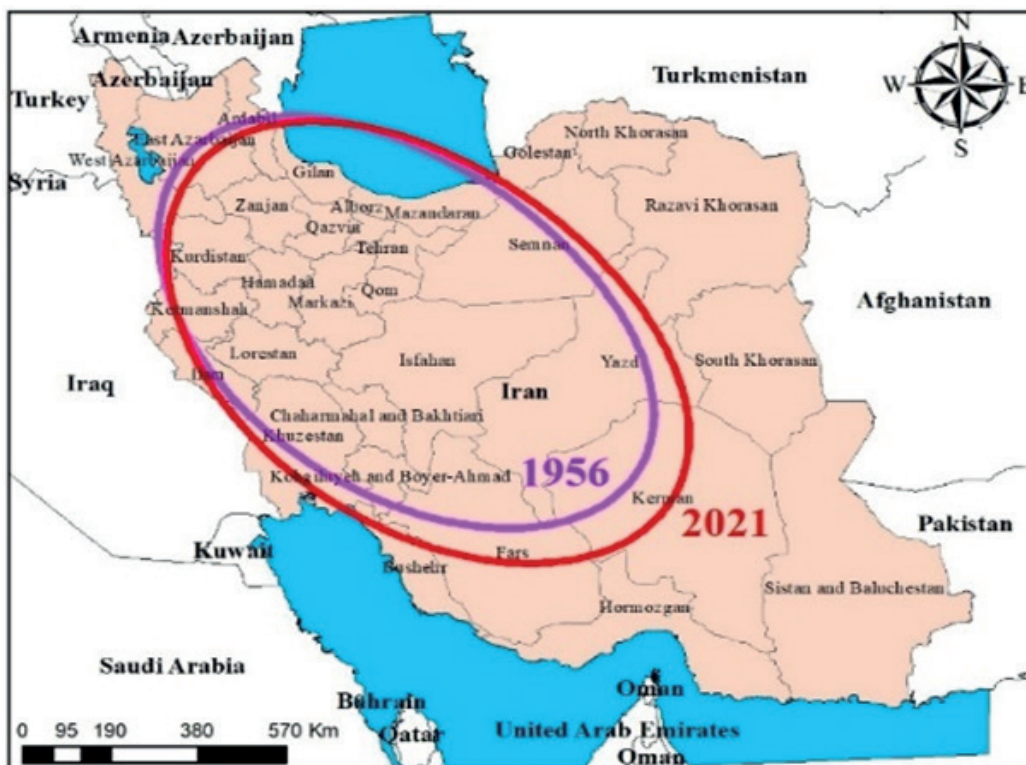


Fig. 4. The trend of concentration of Iranian cities in 1956 and 2021

Analysis of Rank-Size Rule in Iran

In the following, the status of the rank-size rule in the years 1956 to 2021 has been investigated, and the results of this investigation are shown in Fig. 5 and Tab. 2.

The results of the analysis of Fig. 5 and Table 2 indicate the urban primacy in Iran in all the years investigated. The main reason for this is the accumulation of capital and activities in Tehran, the country's capital. These results indicate the increase of the urban primacy from 1956 to 2016. This amount has decreased slightly in 2021, which

is the main reason for this issue was the government's attention to the border areas and deprivation.

Viewing Urban Primacy Changes in Iran

To view urban primacy changes in Iran, six previous indexes have been used, in addition to a proposed index. Undoubtedly, the purpose of this study is more to acquire the accuracy and falseness of the proposed index results and its superiority over the previous indexes. The results of this study are shown in Table 3.

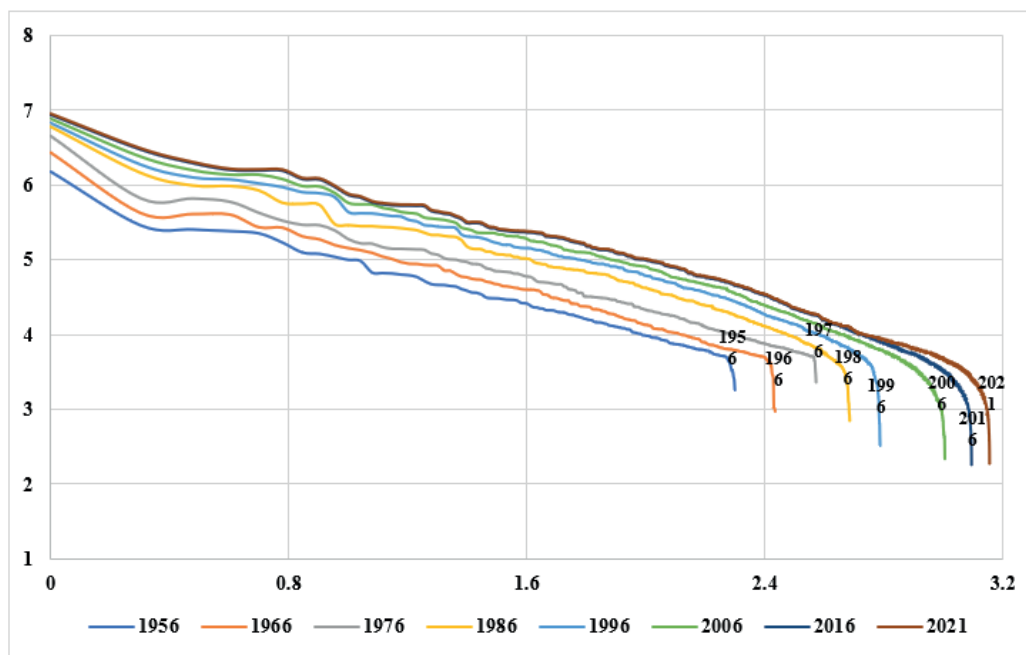


Fig. 5. Rank-Size rule trend in Iran

Table 2. Rank-size rule trend in Iran

Year	y	R ²
1956	$y = -1.0294x + 6.0319$	0.9837
1966	$y = -1.1107x + 6.3305$	0.9653
1976	$y = -1.0694x + 6.4521$	0.9928
1986	$y = -1.2359x + 7.0064$	0.9398
1996	$y = -1.2786x + 7.2538$	0.9265
2006	$y = -1.4125x + 7.6566$	0.9209
2016	$y = -1.4145x + 7.7765$	0.9342
2021	$y = -1.3555x + 7.6797$	0.9441

Table 3. Iran Urban Primacy indexes during 1956-2021

Index / year	1956	1966	1976	1986	1996	2006	2011	2016	2021
Urban primacy index	0.252	0.278	0.289	0.225	0.184	0.162	0.151	0.146	0.131
Two city indexes	5.21	6.41	6.78	4.13	3.58	3.2	2.947	2.89	2.54
Four city indexes	1.922	2.198	2.351	1.766	1.556	1.44	1.222	1.32	1.28
Mahtas index	0.657	0.687	0.701	0.638	0.608	0.589	0.550	0.570	0.567
Herfindal Concentration index	0.057	0.087	0.092	0.061	0.043	0.355	0.033	0.030	0.032
Moomav & Alvosabi index	3.37	3.78	4.31	2.38	3.25	3.42	2.797	3.29	2.08
Mousavi Primate City Index	1.161	2.2	2.27	2.35	2	2.85	2.327	2.24	2.26

According to Table 3, The study of Urban Primacy in the spatial structure of Iran shows that during the years 1956 to 2006 in all the studied periods and based on all the indicators, the urban primacy phenomenon has been dominant. The results of the six indexes in Table 3 show that the urban primacy scale has been increased from 1956 to 1976 and it has the highest degree in 1976. The first six indexes had a descent trend from 1986 to 2021, but the proposed index had an ascent trend in 1986, and it had a descent trend from 1986 to 1996. However, this index had an ascent trend in 2006.

An analytical observation of the developments and the formation of the urban order shows that Iran's industrialization, following land reforms and government investment in large urban centres, has led to the emigration of the villagers to the city and the rapid growth of urbanization. This resulted in an increase in the number of cities from 199 cities in 1956, to 373 cities in 1976. After the Islamic Revolution, the government pursued spatial organization and population adjustment policy by investing heavily in deprived and rural areas of the country. However, factors such as the migration of population from the border areas to central Iran the increase in the natural rate of population growth and the intense migration of villagers to the city led to increased inequality and imbalance in the urban system of Iran. This inequality and imbalance in the urban system of Iran reached its peak in 1986. Accordingly, among the Urban Primacy indexes, only the Mousavi primate city index shows the reality of the current situation of Iran's spatial structure, while previous indexes do not have this capability.

Based on the results of the proposed index, the phenomenon of "Urban Primacy" in Iran increased in 2016, while other indexes do not show this phenomenon. The study of the model of the urban system based on rank size also clearly shows the inequality in the urban system in Iran in 2016. It can be said that since the rankings of other cities in the urban system are ignored in the previous indicators, as a result, they are not able to express reality, and their weakness is obvious, while the proposed index is fully compatible with the rank-size model. Accordingly, if

we draw the draw $\left(\frac{1}{R_i}\right)$ logarithm & $\left(\frac{P_i}{P_i}\right)$ logarithm on the diagram, we will get the same result as in the Zipf pattern.

However, in the case of the Urban Primacy phenomenon in Iran, it can be inferred that the transformation of large and small villages into cities, great distance from the first city based on the rank of any city is the main cause of disorder and imbalance in the spatial structure of the country. These issues have led to the formation of the Urban Primacy phenomenon in the urban system of Iran. Given that this research has resulted in the development of a practical model that has yielded positive outcomes in the context of Iran, which is more reflective of real-world conditions, it is recommended to apply this model (Mousavi primate city index) in various geographical settings. Additionally, comparing its results with those of this study would facilitate a more thorough investigation.

DISCUSSION

The law of the primate city is one of the most basic generalizations regarding the size distribution of cities introduced by M. Jefferson. The law is established on the agglomeration effect by which a city repeatedly the capital city grows inexplicably to outshine the rest (Bajpai Tewari, 2024). The provided indexes' weaknesses are revealed when the various methods are exposed to case studies.

The objective is to compare the results of the obtained indexes to gain a more informed understanding of each of their strengths and weaknesses. Of course, however, it is important to consider that critics often focus on the weaknesses, while investigators insist more on the strengths. From Jefferson's era until now, many methods have been provided to assign urban primacy according to his idea. The two main points were not referred to in those indexes, however. It can be concluded that the provided indexes cannot state the urban primacy main concept based on the urban system (Moshfegh 2023- Lotfi et al. 2013- Mousavi & Tagvaei 2009).

- This is due to the lack of focus on the total urban system cities. If their ranks have a role in the calculation, the Rank-Size Rule principles will not be observed in urban primacy calculations.

- According to Table 3, some of the provided indexes have not been concluded to a unique base, this problem mainly manifests when we are deciding to compare different cities together.

Finally, as it is obvious from urban definition and concept, its assigning means the superiority of primate cities toward the total urban system cities. Hence, the theoretical basement of the provided methods is doubtful. This is due to the provided indexes only highlighting the prime city and or the total urban population as being of importance. In comparison, Rank-Size order may have been considered in the first cities, but urban primacy would be dominant over the down-ranked cities, or some down-ranked cities would be dominant over the prime city.

In this case, the provided methods are not able to acquire urban primacy superiority on the space structure related to an urban system. Therefore, the authors are trying to give a better index toward the provided ones to solve this problem. In this regard, researchers and planners can use Formula No. 11 (provided in the material and methods section) to evaluate the Urban Primacy Index. This index fundamentally enhances our understanding of urban dominance by allowing us to assess how the leading city compares, not only to a select few cities but to all cities within the urban system, while taking their ranks into account. While the top city might not exert significant influence over certain districts, it often wields considerable dominance over cities in the subsequent ranks. This index effectively captures and quantifies that relationship.

RESEARCH LIMITATION

One of the possible limitations of this research could be the lack of access to new data so the latest data published about the population by the Iranian Statistics Center is for 2021, which may change the results of the research with the presentation of new population statistics. Additionally, the lack of the existence of a government institution to provide population statistics is another factor. As a result of this, the validity of population data cannot be controlled and presents limitations.

CONCLUSION

This article has reviewed the strengths and weaknesses of the index's prime city, two-city index, four city indexes, Hrefindal Concentration index and Moomav & alosabi index. To solve the problems and inadequacies caused by these indicators, it has presented a new index called the Mousavi primate city index. The authors reviewed and analyzed Iran's urban primacy status according to the previous and new indexes from 1956 to 2021, to examine

the new index. However, according to the new index, urban primacy status in Iran had an upward trend from 1956 to 1986 and a downward trend from 1986 to 1996. This trend has taken an upward trend in 2016 due to the increase in the number of cities and migration to new cities due to drought and relative agricultural stagnation. The status of the rank-size pattern confirms the results of the new index. The results show that since Mark Jefferson's initial idea, six indicators have been proposed to determine the prime city, in which, two main points are not discussed. One is the lack of attention of this index to all cities of the urban system, considering their rank. Second, is that most of these indexes do not lead to a single basis. This has caused these indicators to not correspond in some cases to the results of the rank-size of cities. This issue has led to doubts about the concept and theoretical basis of the prime city. Therefore, this demonstrates that the introduction of mathematical models and formulas into geography is a critical turning point and is referred to as a quantitative revolution.

However, it is important to note that the weakness of this index points out to researchers and geographers that most models and methods are inconsistent with the theoretical and philosophical basis of geographical phenomena. Moreover, relying solely on these methods will deter geographers from the facts and realities of geographical and spatial phenomena. Of course, it is also noteworthy that these methods and models, as lawful tools, have a great impact on the understanding of geographical phenomena. Due to the inclusion of the rank-size rule and the potential to compare several cities, the presented model can help researchers in future research to evaluate urban primacy and this issue can provide better results than other models. This can be useful for planners to create a vision for the development path and plans. Finally, to thoroughly assess the model's efficiency, it is recommended that this model be utilized in various geographical locations and compared with the findings of this research. ■

REFERENCES

- Abou-Korin A.A. (2014). Small-size urban settlements: Proposed approach for managing urban future in developing countries of increasing technological capabilities, the case of Egypt, *Ain Shams Engineering Journal*, 5(2), 377-390. <https://doi.org/10.1016/j.jasej.2013.12.001>
- Bayramzadeh, N., Mousavi, M. N. (2024). Investigating the Relationship Between Development and Resource Allocation in the Creation of New Human Settlements During the Years 2011 to 2021 (Case Study: Iran). *Journal of Geography and Environmental Studies*, 13(49), 120-139. <https://sanad.iau.ir/Journal/ges/Article/1107624>
- Bhali, M. N. and Ghaffar, A. (2015). Use of Geospatial Techniques in Monitoring Urban Expansion and Land Use Change Analysis: A Case of Lahore, Pakistan. *Journal of Basic & Applied Sciences*, 11, 265-273.
- Bajpai Tewari, D. (2024). Urban Hierarchy, Primate city and Rank size rule. retrieved from: <https://nowgonggirlscollege.co.in/attendance/classnotes/files/1622105089.pdf>
- Campanella, R. (2015). Louisiana cities and the rank-size rule, *Geographers space*, https://richcampanella.com/wp-content/uploads/2020/02/article_Campanella_LCV_Spring2015_Rank-Size-Rule.pdf.
- Decker, E.H., Kerkhoff, A.J., Moses, M.E. (2007). Global Patterns of City Size Distributions and Their Fundamental Drivers, *PLOS One*, 2(9), 934. <https://doi.org/10.1371/journal.pone.0000934>
- Ding, C., He, X., & Zhu, Y. (2022). Megacity Growth, City System and Urban Strategy. *Chn. J. Urb. Environ.Stud.*, 10(01), 2250005. doi: 10.1142/S2345748122500051
- Dolui, S. (2017). Rank-Size Distribution and Primate City Characteristics in India and its Relationship with Economic Development: A Spatio – Temporal analysis of four Indian states (West Bengal, Andhra Pradesh, Kerala, Uttar Pradesh). *Scholars Journal of Arts, Humanities and Social Sciences*. 5(9B), 1234 – 1249. DOI: 10.21276/sjahss.2017.5.9.20
- Düben, Ch., and Krause, M. (2020). Population, light, and the size distribution of cities, *Journal of Regional Science (JRS)*. 61(1), 1-293. <https://doi.org/10.1111/jors.12507>.
- Duranton, G., and Puga, D. (2013). The growth of cities, CEPR Discussion, No DP9590, <https://ssrn.com/abstract=2309234>, https://www.oecd.org/economy/growth/Growth_of_cities_Duranton.pdf
- Feizpour, M. A., & asayesh, F. (2022). Regional Differences in The Primate City Changes of Iran: 1976-2016. *Journal of economics and regional development*, 28(22), 79-109. doi: 10.22067/erd.2022.70612.1047
- Hartley, K., (2015). Elephants in the room: urban primacy and economic growth in Africa, <https://blogs.lse.ac.uk/africaatlse/2015/06/15/elephants-in-the-room-urban-primacy-and-economic-growth-in-africa/>.
- Hekmatnia, H., and Mousavi, M.N. (2006). Application of the model in geography with emphasis on urban and regional planning, *New Science Publications*, Yazd https://opac.nlai.ir/opac-prod/search/briefListSearch.do?command=FULL_VIEW&id=3294178&pageStatus=0&sortKeyValue1=sortkey_title&sortKeyValue2=sortkey_author#
- Henderson, V. (2003). The Urbanization Process and Economic Growth: The So-What Question, *Journal of Economic Growth*. 8(1), 47-71, <https://www.jstor.org/stable/40215937>
- Lerch, M. (2017). International migration and city growth, UN Population Division, Technical Paper No. 10. New York: United Nations. <https://www.researchgate.net>.
- Li, H., Wei, Y. D., & Ning, Y. (2016). Spatial and Temporal Evolution of Urban Systems in China during Rapid Urbanization. *Sustainability*, 8(7), 651. doi: 10.3390/su8070651
- Liu, Y., and Yamauchi, F. (2014). Population Pressures, Migration, and the Returns to Human Capital and Land Insights from Indonesia, the World Bank, Development Research Group Agriculture and Rural, Development Team, Policy Research Working Paper 6790, <https://openknowledge.worldbank.org/bitstream/handle/10986/17338/WPS6790.pdf?sequence=1>
- Lotfi, S., Irandoost, Q., & Babakhanzadeh, E. (2013). Evaluating Changes of Primate City and Urban System in Zagros Region (1976–2006). *Geographical Planning of Space*, 3(8), 23-45. https://gps.gu.ac.ir/article_5663.html?lang=en
- Meyer, W.B. (2019). Urban Primacy before Mark Jefferson. *Geographical Review*, 109(1), 131-145. <https://doi.org/10.1111/gere.12308>.
- Moreno-Monroy, A. I., Schiavina, M., & Veneri, P. (2021). Metropolitan areas in the world. Delineation and population trends. *Journal of Urban Economics*, 125, 103242. doi: 10.1016/j.jue.2020.103242
- Mousavi, M. N., and Taghvaei, M. (2009). Critique of the indicators of Primate City determination and presentation of a new index (With an analytical look at the Primate City indicators in Iran), *Geography and environmental studies*, 1(1), 25-34, <http://ges.iaun.ac.ir/?lang=en>, <https://www.sid.ir/fa/journal/ViewPaper.aspx?ID=125609>
- Mousavi, M. N., & Tagvaei, M. (2009). A critique on the indicators of determining the primate city and presenting a new index (with an analytical view on the primate city indicators in Iran). *Geography and Environmental Studies*, 1(1), 25-34. SID. <https://sid.ir/paper/186424/fa>

- Moshfegh, M. (2023). Examining Shifts in Spatial Population Concentration Indices across Iran's First to Fifth Development Plans (1989-2015). *Quarterly Journals of Urban and Regional Development Planning*, 8(26), 1-41. doi: 10.22054/urdp.2023.72952.1537
- Nasar-u-Minallah, M., Ghaffar, A., Rafique, M., and Mohsin, M. (2016). Urban Growth and Socio-Economic Development in Gujranwala, Pakistan. *Pakistan Journal of Science*, 68(2), 176-183.
- Nasar-u-Minallah, M., Rafique, M., Anwar, M. M. and Mohsin, M. (2016). Assessing the Urban Growth and Morphological Patterns of Gojra City, Pakistan. *Sindh University Research Journal (Science Series)*, 48(2), 393-398.
- Naeem, M., Nasar-U-Minallah, M., Tariq, B., Tariq, N. and Mushtaq, K. (2021) Monitoring Land-use Change and Assessment of Urban Expansion of Faisalabad, Pakistan using Remote Sensing and GIS. *Pakistan Geographical Review*, 76(1), 174-190.
- Nasar-u-Minallah, M., Zia, S., Rahman, A., Riaz, O. (2021). Spatio-temporal analysis of Urban Expansion and Future Growth Patterns of Lahore, Pakistan. *Geography, Environment, Sustainability*. 14(3):41-53. <https://doi.org/10.24057/2071-9388-2020-215>.
- OECD (2020), Highlights Cities in the World A new perspective on urbanization, <https://www.oecd.org/cfe/cities/Cities-in-the-World-Policy-Highlights.pdf>.
- Parveen, N., Ghaffar, A., Nasar-u-Minallah, M., and Ali, A. (2019). Analytical Study on Urban Expansion using the Spatial and Temporal Dynamics of Land Use Change in Faisalabad City, Pakistan. *International Journal of Economic and Environmental Geology (IJEEG)*. 10 (3) 102-108. <https://doi.org/10.46660/ijeeg.Vol10.Iss3.2019.318>
- Riaz, O., Munawar, H., Nasar-u-Minallah, M., Hameed, K., and Khalid, M., (2017). Geospatial Analysis of Urbanization and its Impact on Land Use Changes in Sargodha, Pakistan. *Journal of Basic & Applied Sciences*, 13, 226-233. <https://doi.org/10.6000/1927-5129.2017.13.39>
- Smith, D. (2000). *Third World Cities*, Routledge, London, New York. <https://www.amazon.com/Third-Cities-Routledge-Perspectives-Development/dp/0415198828>.
- Sokona, O. (1985). Urban primacy in developing countries: the case of Mali. *Popul. Today*, 12266918. Retrieved from <https://pubmed.ncbi.nlm.nih.gov/12266918>
- Sokona, O. (1985). Urban primacy in developing countries: the case of Mali, *Popul Today*. 13(4), 6-7, <https://pubmed.ncbi.nlm.nih.gov/12266918/>.
- Statistical Center of Iran. (2021). Statistical yearbook of the country (2020) - population section. <https://amar.org.ir/Portals/0/PropertyAgent/6200/Files/31073/400-99-03.pdf>
- Songchitruksa, P., & Zeng, X. (2010). Getis-Ord Spatial Statistics to Identify Hot Spots by Using Incident Management Data. *SAGE*. 2165(2165), 42-51. <http://dx.doi.org/10.3141/2165-05>
- Seifoldini, F., Mansourian, H., Pourahmad, A., & Darvishzadeh, R. (2013). Spatial-Temporal Dynamics of Iran's Urban System (1956-2011). *Geographical Urban Planning Research (GUPR)*, 1(1), 21-42. <https://doi.org/10.22059/jurbangeo.2013.50550>
- UNCTAD (2020). Handbook of Statistics – Population, https://unctad.org/system/files/official-document/tdstat45_FS11_en.pdf.
- Wagner, M., Grove, A., (2021). Research on Small and Medium-Sized Towns: Framing a New Field of Inquiry, *World*, 2(1), 105-126. <https://doi.org/10.3390/world2010008>.
- Wilsonyudho, S., Rijanta, R., Keban, Y.T., and Setiawan, B. (2017). Urbanization and Regional Imbalances in Indonesia, *Indonesian Journal of Geography*, 49(2), PP 125-132. <http://dx.doi.org/10.22146/ijg.13039>, website: <https://jurnal.ugm.ac.id/ijg>.
- Wang, B., Shi, W., & Miao, Z. (2015). Confidence Analysis of Standard Deviation Ellipse and Its Extension into Higher Dimensional Euclidean Space. *PLoS One*, 10(3), e0118537. <https://doi.org/10.1371/journal.pone.0118537>
- Zebardast, E. (2007). Study of the Urban Primacy developments in Iran, *Journal of Honar-HA-YE-Ziba*. 29(29), 29-38. <https://www.sid.ir/Fa/Journal/ViewPaper.aspx?ID=61367>, <https://jhz.ut.ac.ir/?lang=en>
- Zebardast, E. (2007). Investigating the primate city index's developments in Iran. *Honar-ha-ye Ziba*, 29(29), 29-38. https://jhz.ut.ac.ir/article_17466.html?lang=fa
- Zia, S., Mohsin, M., Nasar-u-Minallah, M. and Hanif, A. (2022). Site Suitability Analysis for Urban Settlements along River Jhelum, Pakistan using GIS and Remote Sensing Techniques. *Indonesian Journal of Geography*, 54(2), 223 – 239. <https://doi.org/10.22146/ijg.72354>

GEOSPATIAL DYNAMICS OF DENGUE FEVER DENSITY IN KUANTAN, MALAYSIA: GIS-BASED APPROACH

Abdul Hadi Z.¹, Che Dom N.^{1,2,*}, Ishak A.R.¹, Salleh S. A.³, Abdullah S.⁴, Precha N.⁵

¹ Faculty of Health Sciences, Universiti Teknologi MARA (UiTM), UiTM Cawangan Selangor, 42300, Puncak Alam, Selangor, Malaysia

² Integrated Mosquito Research Group (I-MeRGe), Universiti Teknologi MARA (UiTM), UiTM Cawangan Selangor, 42300, Puncak Alam, Selangor, Malaysia

³ Institute for Biodiversity and Sustainable Development (IBSD), Universiti Teknologi MARA, 40450, Shah Alam, Selangor, Malaysia

⁴ Faculty of Ocean Engineering Technology and Informatics, Universiti Malaysia Terengganu, 21030, Kuala Nerus, Terengganu, Malaysia

⁵ Department of Environmental Health and Technology, School of Public Health, Walailak University, Nakhon Si Thammarat, Thailand

*Corresponding author: nazricd@uitm.edu.my

Received: March 25th 2024 / Accepted: January 1st 2024 / Published: March 31st 2025

<https://doi.org/10.24057/2071-9388-2025-3298>

ABSTRACT. Dengue fever (DF) presents a significant public health challenge, particularly in tropical regions like Kuantan, Malaysia. This study utilizes Geographic Information System (GIS) technology to analyze spatial and temporal patterns of DF cases from 2011 to 2020. The aim is to understand geographical distribution, identify high-density areas, and discern temporal trends to guide targeted interventions. Kuantan, a rapidly urbanizing city with a notable DF incidence, serves as the study area. Leveraging a decade of Ministry of Health data encompassing 11,330 confirmed cases, ArcGIS 10.6 software maps disease distribution and identifies high-density clusters. Statistical analyses, including Kernel Density Estimation (KDE) and Standard Deviational Ellipses (SDE), reveal directional spread with Kuala Kuantan as the epicenter. Collaboration with vector control units validates high-density areas, linking environmental conditions and infrastructure to DF incidence. Demographic and socioeconomic variables, urbanization, and transportation connections are identified as influential factors. The study underscores the importance of collaborative data sharing and validates GIS-based approaches for targeted interventions. Integration into an early warning system is proposed, enhancing public health strategies in Kuantan and similar regions. Overall, this research contributes to understanding DF transmission dynamics and offers proactive frameworks for mitigating its impact through advanced technologies and collaborative efforts.

KEYWORDS: dengue, risk, kernel density estimation, risk mapping

CITATION: Abdul Hadi Z., Che Dom N., Ishak A.R., Salleh S.A., Abdullah S., Precha N. (2025). Geospatial Dynamics Of Dengue Fever Density In Kuantan, Malaysia: GIS-Based Approach. *Geography, Environment, Sustainability*, 54-64
<https://doi.org/10.24057/2071-9388-2025-3298>

Conflict of interests: The authors reported no potential conflict of interest.

INTRODUCTION

Dengue fever (DF), a viral illness transmitted by *Aedes spp* mosquitoes¹, poses a substantial global health threat. Its prevalence in tropical and subtropical regions, particularly in urban and semi-urban areas², has been exacerbated by rapid urbanization and climate change. Dengue is often underreported due to asymptomatic or mild cases that are self-treated³, dengue affects a staggering number of people globally, with an estimated 390 million infections annually. The disease's impact is evident in the growing number of cases reported to the World Health Organization (WHO). Between 2000 and 2018, reported cases surged from 505,430 to 5.2 million, accompanied by a notable increase in reported deaths, predominantly among younger age groups. Although a decline in cases and deaths was observed between 2020 and 2021, the reliability of the data remains uncertain, potentially influenced by the ongoing COVID-19 pandemic.

Southeast Asia bears a disproportionate burden of DF, largely due to its tropical climate. High humidity and temperatures create an ideal breeding environment for *Aedes* mosquitoes, the primary vectors of the disease⁴. The region's rapid urbanization, high population density, and insufficient infrastructure have exacerbated the problem, leading to recurring epidemics that strains healthcare systems and impacts economic productivity^{5,6}. The severity of the situation is evident in the dramatic increase in dengue cases, rising from 4.88 million in 1990 to 7.7 million in 2019 a staggering 72.95% increase⁷. Within the region, the Philippines, Malaysia, Lao People's Democratic Republic, and Cambodia face the highest age-standardized incidence rates⁸. The World Health Organization's South-East Asia Region (SEAR) encompasses ten dengue-endemic countries, where an estimated 1.3 billion people—approximately 52% of the global population at risk—reside. With the exception of North Korea, these countries experience frequent and cyclical epidemics, demonstrating an overall expansion of dengue's reach in recent

decades⁹ (Tsheten 2021). This trend underscores the urgent need for improved prevention and control strategies across Southeast Asia.

Malaysia exemplifies the increasing trend of dengue cases over recent decades, with rapid urban expansion and population growth creating more mosquito breeding sites and intensifying disease control challenges. Alongside neighbors like Thailand and Indonesia, Malaysia struggles with this persistent public health threat. The drivers of dengue in Malaysia are multifaceted, including viral virulence, human biological factors, climate conditions like high temperatures, relative humidity, increased rainfall, human movement and behavior, and economic and infrastructure development¹⁰ (Ahmad et al., 2018). These factors can influence human susceptibility to infection, promote mosquito breeding, and increase interactions between viruses, vectors, and hosts. DF has become endemic in Malaysia, with the Malaysian Ministry of Health reporting over 123,133 cases and 100 deaths in 2023, a significant rise from 66,102 cases and 56 deaths in 2022, an 86.3% increase¹¹ (Abu Hassan, 2024). This surge imposes a heavy economic burden due to substantial healthcare costs and productivity losses.

Within Malaysia, the state of Pahang has emerged as a significant hotspot for dengue outbreaks. Pahang's diverse topography, encompassing both urban and rural areas, provides varied environments for mosquito breeding. The state's healthcare system has been increasingly strained by the rising number of dengue cases, necessitating enhanced vector control and public health interventions. In recent years, specific districts in Pahang have reported alarming increases in dengue incidence, highlighting the urgent need for targeted strategies to combat the disease¹² (Sapuan et al., 2023). Kuantan, the capital city of Pahang, is a focal point for DF in the state^{12,13} (Hanapi et al., 2021; Sapuan et al., 2023). The city's rapid urbanization, combined with its tropical climate, creates optimal conditions for *Aedes aegypti* and *Aedes albopictus* mosquitoes. The urban landscape, characterized by dense housing and inadequate waste management, provides abundant breeding sites for mosquitoes¹⁴ (Tan et al., 2022). As a result, Kuantan has experienced recurrent dengue outbreaks, with significant morbidity and mortality rates.

The transmission dynamics in Kuantan are complex, with cases occurring throughout the year and peaking during the rainy seasons¹⁴ (Tan et al., 2022). The burden of dengue in Kuantan not only affects public health but also places a considerable economic strain on the community. Efforts to control the spread of dengue have included community engagement, improved

vector control measures, and public awareness campaigns^{15,16} (Subramaniam et al., 2021; Rahman et al., 2022). However, the persistent challenge underscores the need for more effective and sustainable approaches. Dengue primarily spreads through *Aedes aegypti* mosquitoes¹⁷, with *Aedes albopictus* acting as a secondary vector. Transmission occurs before and after symptomatic phases, highlighting the intricate dynamics of the disease. Given the influence of environmental and ecological factors on geographical and temporal patterns, Geographic Information System (GIS) becomes indispensable for depicting and modelling the spatial relationships between causes and disease.

Kernel Density Estimation (KDE), a technique for incident location estimation, has proven crucial in identifying areas with a high density of dengue cases^{18,19}. Urbanization, a significant driver behind increased mosquito density, is creating favorable conditions for disease transmission, especially in unplanned urban settings and peri-urban areas^{20,21}. Understanding the epidemiologic patterns of dengue in these contexts is essential for effective prevention and control. While dengue is a significant public health concern in Malaysia, there is a notable lack of comprehensive spatial data on dengue cases specifically in Kuantan, a rapidly urbanizing city in Pahang. This gap in knowledge limits our understanding of the local transmission patterns and hinders the development of targeted prevention and control strategies. Our study aims to address this deficiency by providing detailed spatial-temporal analysis of dengue cases in Kuantan. Through this analysis, the research not only calculates incidence rates but also elucidates clustering patterns of dengue transmission. The findings contribute to the understanding of dengue in urban and peri-urban settings and advocate for the increased use of GIS technology in public health applications, thereby enhancing the efficiency of dengue surveillance programs and providing crucial information for more effective dengue management in this rapidly urbanizing area.

METHODS

Study area

Kuantan, positioned 250 kilometers east of Kuala Lumpur (3.816667N, 103.333333E), stands as an expanding city on the east coast of Peninsular Malaysia. This city, divided into six sub-districts (refer to Fig. 1), has undergone rapid industrialization and urbanization over the past decade, resulting in significant economic growth and a surge in both population and vehicular

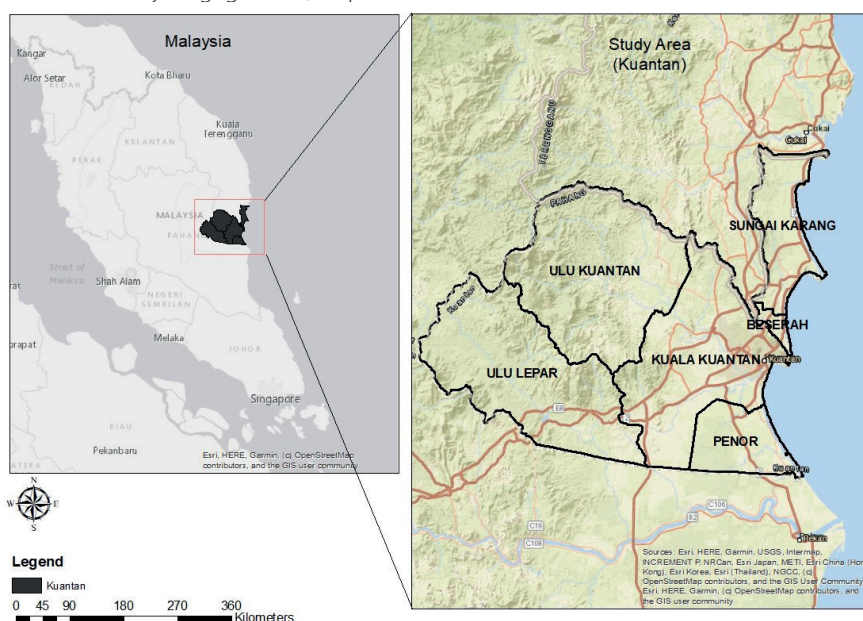


Fig. 1. Location of the study area of Kuantan, Pahang is a rising city on the east coast of Peninsular Malaysia

density. Boasting a populace of approximately 608,000 individuals, Kuantan holds the distinction of being Malaysia's ninth-largest city. The diverse land uses within Kuantan, spanning traffic, industry, enterprise, residential areas, gardens, and tourism, mirror various activity patterns, population movements, and potential mosquito breeding grounds.

Kuantan was chosen as the focal point for this study due to a dearth of recent research in the area, offering an opportunity to provide valuable insights. Additionally, Kuantan has registered the highest number of DF incidences in the state of Pahang. These unique characteristics position the study to effectively identify and analyse the spatial and temporal distribution of high-density areas for DF within the city.

Dengue fever cases data

A comprehensive compilation of DF cases was precisely conducted using the official DF website of the Malaysian government (<http://edenguev2.moh.gov.my/>). The dataset was carefully curated from the registered entries at the Kuantan District Health Office, spanning 2011 to 2020. This meticulous process resulted in a total of 11,330 confirmed dengue cases within Kuantan during this timeframe, forming the foundational basis for subsequent analysis.

Geographic Information System (GIS)

To visually and spatially analyze the distribution of DF cases, x and y coordinates corresponding to each patient's location were extracted from the dataset. The spatial mapping process was carried out using ArcGIS version 10.6 (ESRI, Redlands, CA, USA). This geospatial analysis facilitated the generation of a detailed map that highlights the geographical spread of DF incidences across Kuantan.

Statistical Analysis

To comprehensively assess the spatial distribution of DF cases and identify contributing factors, various statistical analysis tools within ArcGIS v10.6 were employed.

Geographic Distribution Pattern Assessment: The spatial pattern of dengue density was evaluated using essential metrics, including spatial mean center, directional distribution, and standard distance. These measurements provided valuable insights into the dispersion of dengue cases across the geography of Kuantan.

Kernel Density Estimation (KDE) and Standard Deviational Ellipses (SDE): KDE and SDE played crucial roles in delineating distributions within uncertain areas. KDE, in particular, facilitated the identification of problematic dengue areas characterized by high-density incidence. SDE added a valuable dimension by establishing ellipses that highlighted the standard deviations of the distribution, aiding in the interpretation of spatial patterns.

Spatiotemporal Distribution Analysis

Transformation of DF Cases: DF cases underwent transformation into weighted data points on a map using ArcGIS v10.6. Each data point, characterized by X and Y centroid coordinates, represented a distinct number of cases. This transformation enabled a nuanced depiction of the spatiotemporal distribution of DF cases.

Analysis of Emerging Spatial and Temporal Density: A strategy was developed to analyze emerging spatial and temporal density based on the geographical locations of dengue cases in the Kuantan district. The KDE method played a pivotal role in simulating density analysis and mapping the spreading pattern of the epidemic. The study incorporated specific bandwidths in accordance with a defined formula, with the aim of identifying

the distribution pattern of DF density through a comprehensive density map, as formulated below.

$$\lambda(s) = \sum_{i=1}^n \frac{1}{2} k \left(\frac{(s - s_i)}{\tau} \right) \quad (1)$$

Where $\lambda(s)$ is the estimated infected value by dengue per area; τ is the smoothing factor; $k()$ is the kernel weighting function; s is the center of the area and s_i is the location of the point.

Standard Deviational Ellipses (SDE): function as a robust tool for characterizing the properties of geographical spaces, encompassing central tendency, dispersion, and trend direction²². Traditionally, trends within a geographic area are measured by applying standards to compute distances independently along the x and y axes. The resulting elliptical distribution characteristics are defined in both measurements, yielding ellipses with specific orientations and elongated features. The term "standard deviation ellipses" is derived from the method of calculating the standard deviation of the x and y coordinates of the center axis. Central tendency and dispersion are pivotal aspects in epidemiological studies, prompting the use of ellipses to model the geographical distribution of diseases. In this study, geographical statistical analyses were conducted using ArcGIS 10.5 to employ SDE, providing insights into the spatial characteristics of DF distribution in Kuantan, as depicted below.

$$SDE_x = \sqrt{\frac{\sum_{i=1}^n (x - \bar{X})^2}{n}} \quad (2a)$$

$$SDE_y = \sqrt{\frac{\sum_{i=1}^n (y - \bar{Y})^2}{n}} \quad (2b)$$

where x_i and y_i are the coordinates for feature i , $\{\bar{X}, \bar{Y}\}$ shows mean center, and n is the total number of features. The SDE generated a new feature class that comprised centered ellipse polygons on mean center for all attributes (or for cases when values were defined). The attributes of the ellipse polygon comprised standard distance (long and short axis) and ellipse orientation. The orientation represented the rotation of the long axis clockwise from noon. In this study, SDE was used to quantitatively examine the direction of DF cases to determine the extent to which these dengue outbreaks may have spread.

Apart from that, it also indicated the number of standard deviations. When characteristics have a normal spatial distribution; i.e., highest density in the center that decreases towards the edges; one standard deviation can account for up to 68% of all centroid input data while two standard deviations can account for up to 95% of all features and three can account for up to 99% of all centroid features.

Validation and Expert Input

To enhance the credibility of our findings and gain expert insights into the causes of high-density DF occurrences, we proactively collaborated with the head of vector control units. This proactive engagement involved soliciting responses to three pivotal questions as shown in Table 1

RESULTS

Spatiotemporal distribution of dengue fever cases in Kuantan.

In 2011, the study revealed a scattering of DF cases concentrated primarily in the Kuala Kuantan sub-district. However, a significant shift unfolded over the subsequent nine

Table 1. Overview of key questions and the rationale for DF high-density analysis

Indicator	Question	Rationale
Correlation with Dengue Problems	Does the observed high-density correspond to areas where dengue problems are prevalent?	To evaluate the alignment between our identified high-density areas and those recognized by on-the-ground experts, we sought confirmation on the spatial congruence of our findings with the practical experiences of the vector control units
Factors Facilitating High Density:	What factors might facilitate the occurrence of high-density dengue fever cases?	Understanding the local factors contributing to high-density areas is crucial for contextualizing our spatial analysis. Insights from the vector control units help elucidate environmental, ecological, or demographic determinants influencing dengue fever prevalence
Surveillance and Control Measures	What surveillance and control measures can be implemented in high-density areas?	Expert recommendations on effective surveillance and control strategies provide practical implications for public health interventions. By incorporating these suggestions, our study aims to contribute not only to the understanding of high-density occurrences but also to the development of targeted and efficient control measures

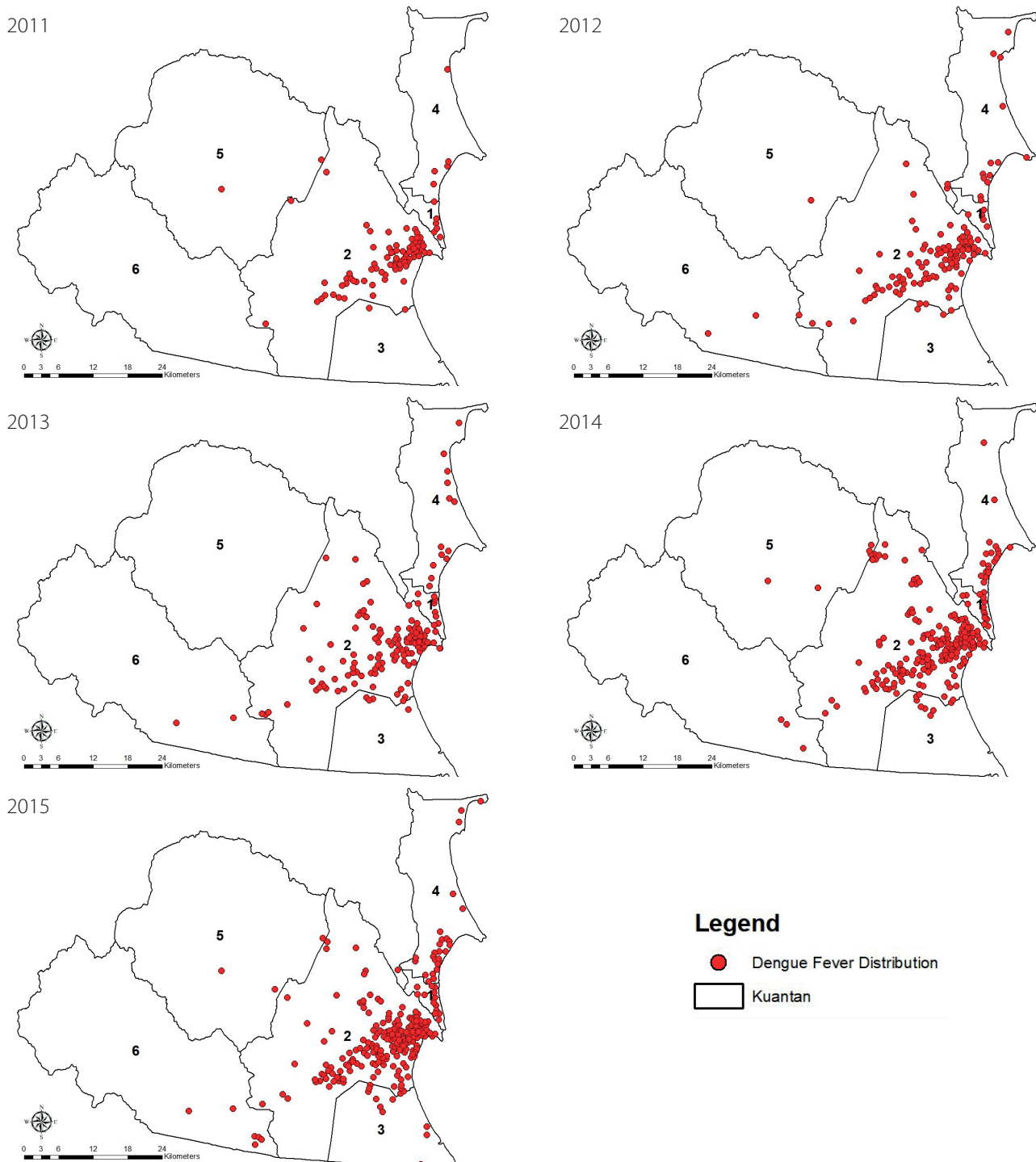


Fig. 2. Density mapping of DF cases in Kuantan, Malaysia from January 2011 to December 2020. (1) Beserah, (2) Kuala Kuantan, (3) Penor, (4) Sungai Karang, (5) Ulu Kuantan and (6) Ulu Lepar

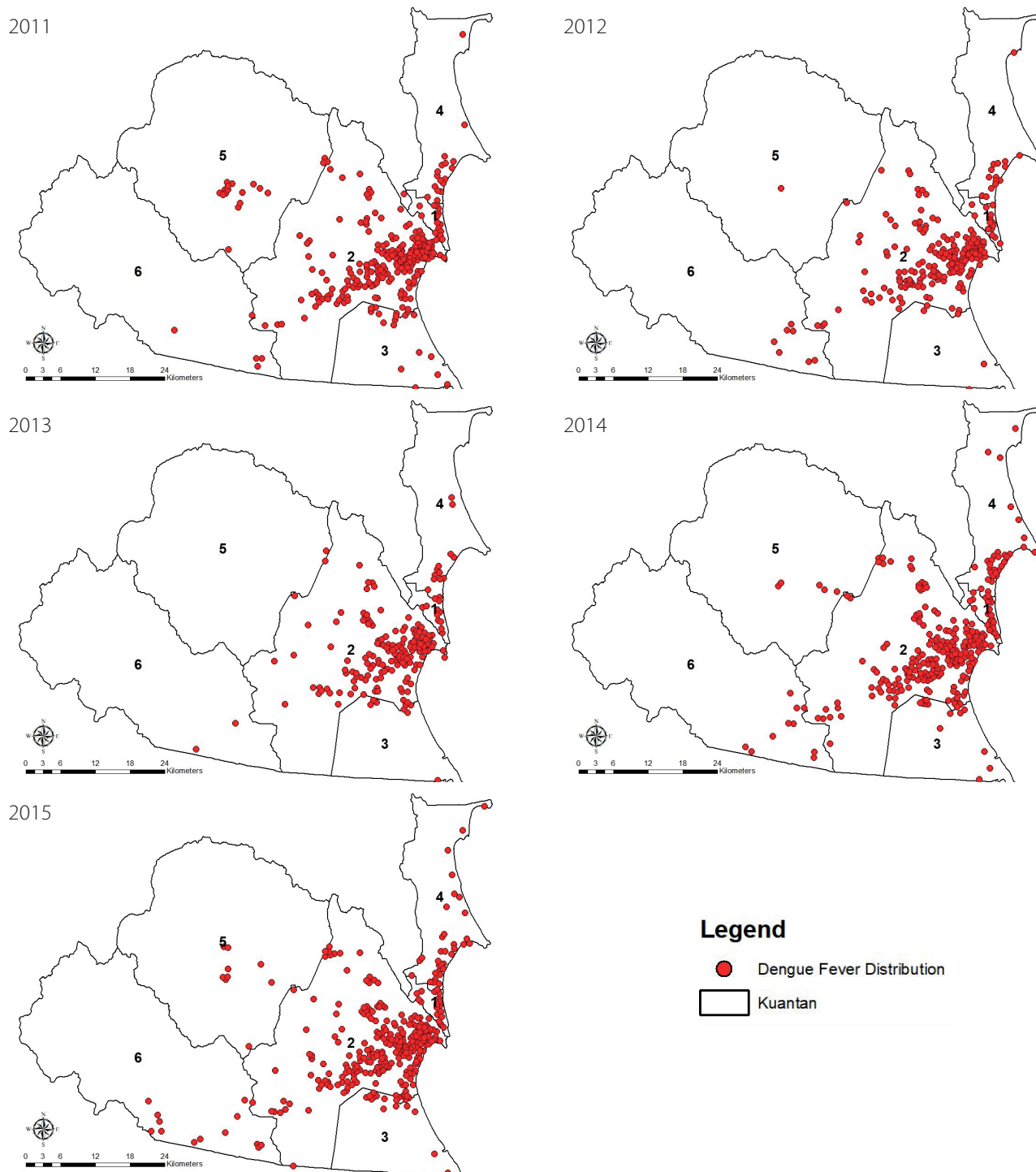


Fig. 2. Continued

years, spanning from 2012 to 2020. During this period, there was a marked escalation in the frequency of DF cases, indicating a consistent upward trend in disease incidence. Simultaneously, the spatial distribution underwent a notable transformation, extending beyond the initial hotspot in Kuala Kuantan to encompass neighboring sub-districts, notably Beserah and Sungai Karang. The persistent increase in the density of DF incidents from 2012 to 2020 underscores an enduring and expanding public health challenge in Kuantan.

Spatial density of dengue fever in Kuantan

The study covering DF cases from 2011 to 2020 focused on identifying high-density areas, a task accomplished through the utilization of KDE maps (refer to Fig. 3). These maps vividly illustrate the spatial distribution of DF occurrences, distinguishing high-density zones represented by red points, denoting an

elevated frequency of cases, and low-density areas indicated by green-tinted points, signifying a lower incidence of DF. Notably, a discernible spatial pattern of DF emerged, with the Kuantan sub-district serving as the epicenter of this public health concern. The Kuala Kuantan sub-district exhibited the highest density of DF occurrences, closely followed by Sungai Karang and Penor sub-districts. Over the nine-year period, the high-density area consistently expanded, underscoring a growing density pattern in Kuantan. In the year 2020 alone, this expansion manifested in 22 additional high-density localities. Further granularity in the analysis revealed that 82% of these localities were concentrated in Kuala Kuantan, while Penor accounted for 9%, and both Ulu Kuantan and Sungai Karang sub-districts contributed 9% collectively. These findings not only provide insights into the temporal evolution and distribution of high-density areas but also inform the development of targeted public health strategies for effective DF control in Kuantan.

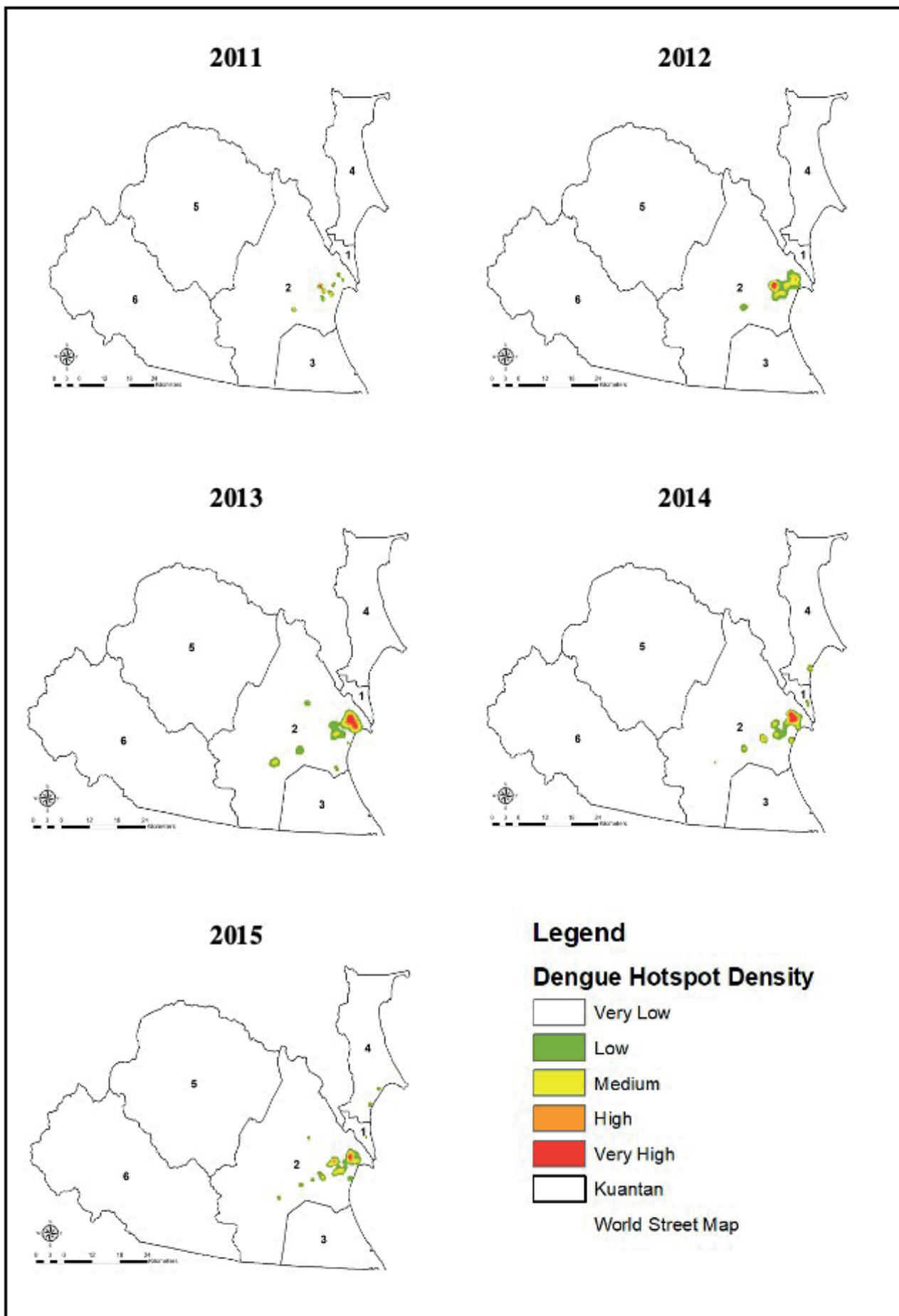


Fig. 3. High density detection of DF incidence in Kuantan based on Kernel Density Estimation statistic from 2011 – 2020. (1) Beserah, (2) Kuala Kuantan, (3) Penor, (4) Sungai Karang, (5) Ulu Kuantan and (6) Ulu Lepar

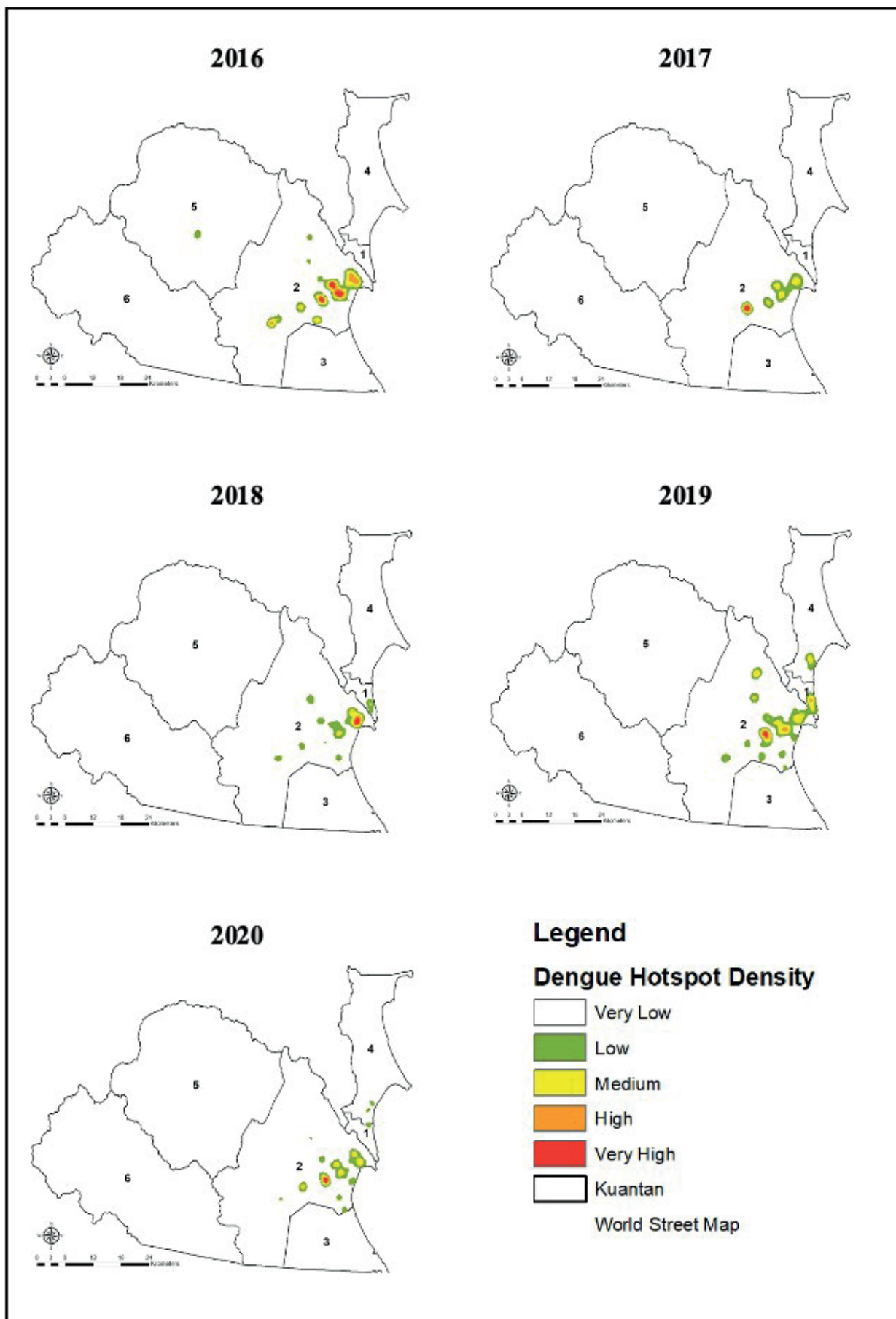


Fig. 3. Continued

The collaboration with the head of the vector control units yielded valuable insights, indicating a high agreement between the identified high-density areas and those historically contributing the most DF cases in sub-districts within Kuantan. This alignment reinforces the reliability of our spatial analyses and holds significant implications for subsequent research, surveillance, and control measures concerning DF outbreaks in the region.

The findings from this collaborative assessment underscore critical environmental and social factors as root problems in high-density areas, as elucidated by the head of vector control. Table 2 outlines these identified factors, emphasizing the need for a holistic approach to address the root causes of dengue incidence. Environmental conditions, including poorly built and improperly managed drainage systems, as well as inadequacies in solid waste management, emerged as pivotal contributors to the heightened density of DF cases. Additionally, social

factors play a role, emphasizing the interconnectedness of urban planning, infrastructure, and public health outcomes. This comprehensive assessment not only strengthens the understanding of the spatial distribution of dengue cases but also guides the formulation of targeted interventions. The identified root problems serve as a foundation for further research endeavors and the development of strategic surveillance and control measures aimed at mitigating the impact of DF outbreaks in Kuantan.

Directional distribution of dengue fever cases

Fig. 4 illuminates the directional distribution of DF cases over a decade, providing a comprehensive overview of the spatial dynamics within the entire sub-district of Kuala Kuantan. Remarkably, the directional patterns exhibited notable consistency over the ten-year period, following

Table 2. High density analysis agreement with locations indicated as vulnerable for DF transmission²³

Sub-district	Does the high-density area match with areas you identify as problematic (yes, partially, no)?	What local conditions determine the occurrence of high density (ecological, environmental, infrastructure, social, or other determinants)?	What surveillance or control activities could you implement in your city considering the presence of high-density area?
Kuala Kuantan	Yes: most problematic area coincides with density analysis	Sociodemographic: regions with a high population density and varying levels of education. Ecological: high frequency of infested dwellings with a variety of breeding place during the rainy season, mostly by plastic containers that people amass and are difficult to remove.	Surveillance: improved surveillance using ovitraps and active case detection. Control: preventative vector control (health education, source and reduction), as well as response employing truck-mounted ultra-low volume and interior space spraying. Other enhancements include housing and public infrastructure upgrades.
Beserah	Partially: The regions are not issue zones, although places on the outside of the sub-district contribute to many cases.	Sociodemographic: regions with a medium population density and varying levels of education. Environmental: premises with big and planted (shady) patios, new vs. old low-middle-class dwellings. Other: include a lack of community participation in the removal and control of larval habitats.	Control: integrated vector management (IVM), which includes larval control, residual pesticide applications, monthly spatial spraying, and impact evaluation on a regular basis.
Penor	No	Not associate	Monitoring: increased surveillance using ovitraps, as well as an aggressive active case detection (ACD). Control: immediate larval control, followed by high coverage indoor residual spraying and ultra-low volume spraying once cases are detected.
Sungai Karang	Partially: The regions are not issue zones, although places on the outside of the sub-district contribute to many cases.	Environmental: premises with big and planted (shady) patios, new vs. old low-middle-class dwellings. Sociodemographic: regions with a medium population density and varying levels of education.	Surveillance: improved surveillance using ovitraps and active case detection. Control: include preventative vector control before to transmission season (information campaigns, source reduction, and indoor residual spraying).
Ulu Kuantan	Partially: The regions are not issue zones, although places on the outside of the sub-district contributed to many cases.	Ecological: Small plastic containers are the most common in terms of environmental impact, followed by large tanks.	Control: immediate larval control, followed by high coverage indoor residual spraying and ultra-low volume spraying once cases are detected.
Ulu Lebar	No	Not associate	Monitoring: increased surveillance using ovitraps, as well as an aggressive active case detection (ACD). Control: immediate larval control, followed by high coverage indoor residual spraying and ultra-low volume spraying once cases are detected.

a trajectory from the northeast to the southwest. The representation of these patterns through ellipse polygons offers a nuanced understanding of temporal changes. In 2011, the directional distribution was characterized by an ellipse polygon with a rotation of 51.046° on the long axis. Subsequent years witnessed variations, including expansions, contractions, and shifts in rotation angles. Noteworthy changes include the enlargement and southwestward extension in 2012, a reduction in size in 2015, and a wider, longer configuration in 2016. The year 2020 marked the occurrence of the outermost, largest, and longest ellipse polygon. These variations, while subtle, hint at evolving spatial dynamics in DF cases over time. The persistent directionality from northeast to southwest underscores the enduring spatial pattern, providing crucial information for the strategic planning of public health interventions tailored to the evolving spatial trends in Kuala Kuantan.

DISCUSSIONS

The integration of epidemiology with computational information management proves crucial for effective health-based surveillance and control²⁴, a principle exemplified by our statistical analysis of geographical data in this study. The concentration of DF cases within specific areas from the south to the west of Kuantan, covering nearly half of the study area, suggests these regions as high-density areas and preferred breeding sites for dengue vectors. This spatial pattern becomes more pronounced with the saturation of Kuantan’s urban development. The rise in DF cases from 2011 to 2016, followed by a subsequent decrease in 2017 and a resurgence in 2018, underscores the dynamic nature of dengue transmission. This study’s identification of high-density areas within Kuantan from 2011 to 2020 reveals distinct temporal and spatial patterns, influenced by demographic and socioeconomic factors.

Demographic variables, including urban population density, residence income, and single-story homes, play significant roles in shaping the frequency and spread of DF²⁵. Dengue’s adaptability to urban environments, facilitated by the *Aedes aegypti* mosquito vector, contributes to its prevalence in urban and suburban settings²⁶. Notably, high a few studies revealed that population density, proximity to transportation arteries, and urban development correlate with increased DF incidence^{27,28,29}. The impact of urbanization, characterized by high-rise buildings and modifications for development, is evident in its influence on land surface temperature and DF incidences³⁰.

Collaboration with the Kuantan district health officer corroborates the susceptibility for DF transmission in high-density areas identified through KDE and SDE analyses. The expansion of suburban regions in Kuala Kuantan’s sub-districts contributes to the rise in mosquito population and DF transmission. Poor environmental hygiene further promotes conducive breeding sites in urban areas³¹, aligning with research showing higher potential breeding sites in urban compared to suburban and rural areas³². The study emphasizes the need for additional data on the primary mosquito vector and breeding site control methods to enhance our understanding of DF transmission dynamics.

The study also revealed the role of urban livestock as a potential source of disease transmission. While valuable for food and revenue, urban livestock may increase the risk of vector-borne diseases, including DF^{33,34}. Addressing this requires a balance between the benefits of urban livestock and the potential health risks. Additionally, raising public awareness of DF and its prevention techniques, especially in peri-urban areas, plays a pivotal role in disease control. Considering the broader context, climate variability, environmental issues, and land use warrant further investigation at the sub-scale to micro-scale level. Such a comprehensive understanding is essential for the

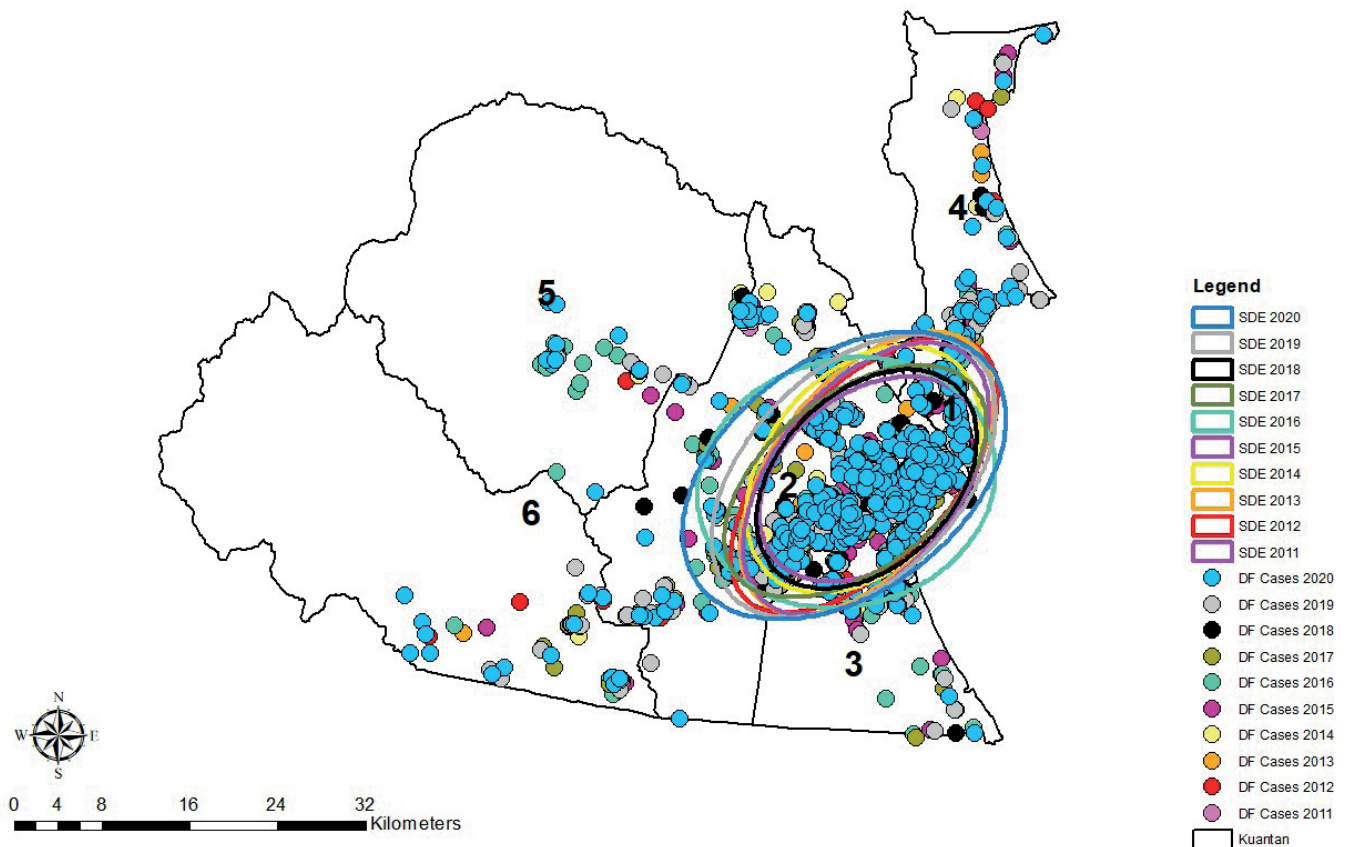


Fig. 4. Standard deviational ellipses of dengue cases in Kuantan from 2011 to 2020. (1) Beserah, (2) Kuala Kuantan, (3) Penor, (4) Sungai Karang, (5) Ulu Kuantan and (6) Ulu Lepar

development of effective dengue control strategies, taking into account the intricate interplay of climatic factors, human-mosquito interactions, and the urban landscape.

CONCLUSIONS

This study provides valuable insights into the spatiotemporal dynamics of DF in Kuantan, Malaysia from 2011 to 2020, revealing distinct patterns in the distribution and density of DF cases with significant implications for public health strategies. Our analysis identified specific high-density areas for DF, primarily concentrated in the Kuala Kuantan sub-district and expanding to neighboring areas over time. The temporal trends and consistent northeast to southwest directional pattern of DF cases provides critical information for predicting the future spread and planning preventive measures.

Our findings, corroborated by local health officials, highlight the role of urbanization, population density, and

environmental conditions in facilitating DF transmission. The successful application of spatial analysis techniques demonstrates the potential for developing an early warning system for dengue outbreaks. The integration of diverse datasets, including meteorological, environmental, and entomological information, could further refine our understanding of DF transmission dynamics.

This study underscores the value of a multidimensional, data-driven approach to dengue control, leveraging advanced spatial analysis techniques and collaborative data sharing across agencies. We recommend the implementation of targeted interventions in identified hotspots, the development of an interactive dengue surveillance system, and increased collaboration between urban planners and public health officials. Such an approach has the potential to significantly improve prevention and management strategies, not only in Kuantan but also in other regions facing similar challenges with dengue and other vector-borne diseases. ■

REFERENCES

- Suman, D. S., Chandel, K., Faraji, A., Gaugler, R., & Chandra, K. (2018). Mosquito-Borne Diseases: Prevention Is the Cure for Dengue, Chikungunya and Zika Viruses. *Mosquito-borne Diseases: Implications for Public Health*, 235-279.
- Dávalos-Becerril, E., Correa-Morales, F., González-Acosta, C., Santos-Luna, R., Peralta-Rodríguez, J., Pérez-Rentería, C., & Moreno-García, M. (2019). Urban and semi-urban mosquitoes of Mexico City: A risk for endemic mosquito-borne disease transmission. *PLoS One*, 14(3), e0212987.
- Martins, I. C., Ricardo, R. C., & Santos, N. C. (2022). Dengue, west nile, and Zika viruses: potential novel antiviral biologics drugs currently at discovery and preclinical development stages. *Pharmaceutics*, 14(11), 2535.
- Edillo, F., Ymbong, R. R., Bolneo, A. A., Hernandez, R. J., Fuentes, B. L., Cortes, G., & Sakuntabhai, A. (2022). Temperature, season, and latitude influence development-related phenotypes of Philippine *Aedes aegypti* (Linnaeus): Implications for dengue control amidst global warming. *Parasites & Vectors*, 15(1), 74.
- Caballero-Anthony, M., Cook, A. D., Amul, G. G. H., & Sharma, A. (2022). Health governance and dengue in Southeast Asia. *S. Rajaratnam School of International Studies*.
- Gibb, R., Colón-González, F. J., Lan, P. T., Huong, P. T., Nam, V. S., Duoc, V. T., & Lowe, R. (2023). Interactions between climate change, urban infrastructure and mobility are driving dengue emergence in Vietnam. *Nature communications*, 14(1), 8179.
- Du, M., Jing, W., Liu, M., & Liu, J. (2021). The global trends and regional differences in incidence of dengue infection from 1990 to 2019: an analysis from the global burden of disease study 2019. *Infectious diseases and therapy*, 10(3), 1625-1643.
- Tian, N., Zheng, J. X., Guo, Z. Y., Li, L. H., Xia, S., Lv, S., & Zhou, X. N. (2022). Dengue incidence trends and its burden in major endemic regions from 1990 to 2019. *Tropical medicine and infectious disease*, 7(8), 180.
- Tsheten, T., Gray, D. J., Clements, A. C., & Wangdi, K. (2021). Epidemiology and challenges of dengue surveillance in the WHO South-East Asia Region. *Transactions of The Royal Society of Tropical Medicine and Hygiene*, 115(6), 583-599.
- Ahmad, R., Suzilah, I., Wan Najdah, W. M. A., Topek, O., Mustafakamal, I., & Lee, H. L. (2018). Factors determining dengue outbreak in Malaysia. *PLoS one*, 13(2), e0193326.
- Abu Hassan, R., (2024). *Kenyataan Media Ketua Pengarah Kesihatan*. Kementerian Kesihatan Malaysia, 52.
- Sapuan, I., Hassan, N. A., Rus, R. M., & Aidid, E. M. (2023). Effect of climate variability on Dengue cases in pahang. *Transforming medical healthcare through research (IIUM)*, 2.
- Hanapi, M. H. M., & Shafie, F. A. (2021). Spatio-Temporal analysis of Dengue distribution pattern in Kuantan from 2015-2019. *Healthscope: The Official Research Book of Faculty of Health Sciences, UiTM*, 4(1), 31-37.
- Tan, C. H., Lee, S. N., & Ho, S. B. (2022). Assessing the environmental effects on dengue fever and Malaysian economic growth. *International Journal of Environmental Science and Development*, 13(2), 49-56.
- Subramaniam, N., Anua, S. M., & Mat, N. F. C. (2021). Knowledge, Attitude and Practices (KAP) On *Aedes* Mosquito-Borne Diseases Amongst Community Members in Malaysia: A Review. *Malaysian Journal of Medicine & Health Sciences*, 17(2).
- Rahman, A. B., Jasman, N., Ahmad, N., Salleh, K. Z., Harun, S. N. F., & Krishnan, M. (2022). Scoping Review: Barrier to The Knowledge, Attitude and Practice on Dengue Prevention. *Malaysian Journal of Social Sciences and Humanities (MJSSH)*, 7(4), e001421-e001421.
- Pereira, T. N., Carvalho, F. D., De Mendonça, S. F., Rocha, M. N., & Moreira, L. A. (2020). Vector competence of *Aedes aegypti*, *Aedes albopictus*, and *Culex quinquefasciatus* mosquitoes for Mayaro virus. *PLOS Neglected Tropical Diseases*, 14(4), e0007518.
- Cantrell, D. L., Rees, E. E., Vanderstichel, R., Grant, J., Filgueira, R., & Revie, C. W. (2018). The use of kernel density estimation with a bio-physical model provides a method to quantify connectivity among salmon farms: spatial planning and management with epidemiological relevance. *Frontiers in Veterinary Science*, 5, 269.
- Yajid, M. Z. M., Che Dom, N., Camalxaman, S. N., & Nasir, R. A. (2020). Spatial-temporal analysis for identification of dengue risk area in Melaka Tengah district. *Geocarto International*, 35(14), 1570-1579.
- Cruz-Bello, G. M., Galeana-Pizaña, J. M., & González-Arellano, S. (2023). Urban growth in peri-urban, rural and urban areas: Mexico City. *Buildings and Cities*, 4(1).
- Kolimenakis, A., Heinz, S., Wilson, M. L., Winkler, V., Yakob, L., Michaelakis, A., ... & Horstick, O. (2021). The role of urbanisation in the spread of *Aedes* mosquitoes and the diseases they transmit—A systematic review. *PLoS neglected tropical diseases*, 15(9), e0009631.
- Zhang, X., Zhang, B., Yao, Y., Wang, J., Yu, F., Liu, J., & Li, J. (2022). Dynamics and climatic drivers of evergreen vegetation in the Qinling-Daba Mountains of China. *Ecological Indicators*, 136, 108625.
- Dzul-Manzanilla, F., Correa-Morales, F., Che-Mendoza, A., Palacio-Vargas, J., Sánchez-Tejeda, G., González-Roldan, J. F., ... & Vazquez-Prokopec, G. M. (2021). Identifying urban hotspots of dengue, chikungunya, and Zika transmission in Mexico to support risk stratification efforts: a spatial analysis. *The Lancet Planetary Health*, 5(5), e277-e285.

- Khashoggi, B. F., & Murad, A. (2020). Issues of healthcare planning and GIS: a review. *ISPRS International Journal of Geo-Information*, 9(6), 352.
- Kikuti, M., Cunha, G. M., Paploski, I. A., Kasper, A. M., Silva, M. M., Tavares, A. S., ... & Ribeiro, G. S. (2015). Spatial distribution of dengue in a Brazilian urban slum setting: role of socioeconomic gradient in disease risk. *PLoS neglected tropical diseases*, 9(7), e0003937.
- Siriyasatien, P., Chadsuthi, S., Jampachaisri, K., & Kesorn, K. (2018). Dengue epidemics prediction: A survey of the state-of-the-art based on data science processes. *IEEE Access*, 6, 53757-53795.
- Freitas, L. P., Cruz, O. G., Lowe, R., & Sá Carvalho, M. (2019). Space-time dynamics of a triple epidemic: dengue, chikungunya and Zika clusters in the city of Rio de Janeiro. *Proceedings of the Royal Society B*, 286(1912), 20191867.
- Aalto, E. A., Lafferty, K. D., Sokolow, S. H., Grewelle, R. E., Ben-Horin, T., Boch, C. A., & De Leo, G. A. (2020). Models with environmental drivers offer a plausible mechanism for the rapid spread of infectious disease outbreaks in marine organisms. *Scientific reports*, 10(1), 5975.
- Alkhalidy, I., & Barnett, R. (2021). Explaining neighbourhood variations in the incidence of dengue fever in Jeddah City, Saudi Arabia. *International Journal of Environmental Research and Public Health*, 18(24), 13220.
- Marti, R., Li, Z., Catry, T., Roux, E., Mangeas, M., Handschumacher, P., & Gong, P. (2020). A mapping review on urban landscape factors of dengue retrieved from earth observation data, GIS techniques, and survey
- Almeida, L. S., Cota, A. L. S., & Rodrigues, D. F. (2020). Sanitation, Arboviruses, and Environmental Determinants of Disease: impacts on urban health. *Ciencia & saude coletiva*, 25, 3857-3868. questionnaires. *Remote Sensing*, 12(6), 932.
- Abílio, A. P., Abudasse, G., Kampango, A., Candrinho, B., Sitori, S., Luciano, J., & Gudo, E. S. (2018). Distribution and breeding sites of *Aedes aegypti* and *Aedes albopictus* in 32 urban/peri-urban districts of Mozambique: implication for assessing the risk of arbovirus outbreaks. *PLoS neglected tropical diseases*, 12(9), e0006692.
- Gwee, S. X. W., St John, A. L., Gray, G. C., & Pang, J. (2021). Animals as potential reservoirs for dengue transmission: A systematic review. *One Health*, 12, 100216.
- Ren, H., Wu, W., Li, T., & Yang, Z. (2019). Urban villages as transfer stations for dengue fever epidemic: A case study in the Guangzhou, China. *PLoS neglected tropical diseases*, 13(4), e0007350.

FEATURES OF UNIQUE LAKES DEVELOPMENT ON THE KURGALSKY PENINSULA IN THE SOUTHEAST BALTIC SEA BASED ON THE RESULTS OF INTERDISCIPLINARY RESEARCH

Sapelko T.V.*, Lapenkov A.E., Guzivaty V.V., Karetnikov S.G., Gazizova T.V., Ignatyeva N.V., Kuznetsov D.D., Rusanov A.G.

Institute of Limnology of the Russian Academy of Sciences, SPC RAS, St. Petersburg

*Corresponding author: tsapelko@mail.ru

Received: October 11th 2024 / Accepted: November 29st 2024 / Published: March 31st 2025

<https://doi.org/10.24057/2071-9388-2025-3512>

ABSTRACT. The increased number of extreme marine events is one of the most serious hazards to coastal areas around the world. The study of the impacts of marine events on coastal lakes has enabled us to gain important insights into the coastal ecosystem's response to these events. On the Baltic Sea southeast coast as a result of studying Lake Lipovskoye and Lake Belye on the Kurgalsky Peninsula obtained data on hydrology and hydrochemistry of the lakes, structure of lakes' sediments, the distribution of macrophytes and features of the vegetation reflection in the lakes' surface sediments based on pollen data. Bathymetric maps of lakes and their watersheds were constructed. Our complex studies confirmed the lakes' uniqueness. According to hydrochemical data, Lake Lipovskoye has mesotrophic status and is classified as brackish water, whereas Lake Belye is oligotrophic and freshwater. It was found that the lakes are characterized by small values of specific catchments – 10.3 for Lake Lipovskoye and 2.7 for Lake Belye. Subrecent pollen spectra of lake surface samples quite adequately reflect modern aquatic vegetation, especially the communities of submerged hydrophytes in Lake Lipovskoye and floating hydrophytes in both lakes. *Potamogeton (P. pectinatus L., P. perfoliatus L.)* and *Myriophyllum sp.* are dominants in the pollen spectra and modern aquatic plant communities in the lakes. Over a short-term period, there are substantive differences in the species composition and dynamics of macrophyte pollen for both lakes. The study of lake sediments found a link between the Holocene sedimentation in Lipovskoye and Belye lakes and the Baltic's transgressive and regressive stages (Ancylus, Littorina, and Baltic Ice Lake stages).

KEYWORDS: lakes, Baltic Sea coast, modern status, bathymetry, hydrochemistry, macrophytes, pollen, lake sediments, sea level

CITATION: Sapelko T.V., Lapenkov A.E., Guzivaty V.V., Karetnikov S.G., Gazizova T.V., Ignatyeva N.V., Kuznetsov D.D., Rusanov A.G. (2025). Features Of Unique Lakes Development On The Kurgalsky Peninsula In The Southeast Baltic Sea Based On The Results Of Interdisciplinary Research. *Geography, Environment, Sustainability*, 65-74
<https://doi.org/10.24057/2071-9388-2025-3512>

ACKNOWLEDGEMENTS: The study was supported by the Russian Science Foundation under grant No. 23-27-00128
<https://rscf.ru/project/23-27-00128/>

Conflict of interests: The authors reported no potential conflict of interest.

INTRODUCTION

Extreme events such as marine level changes or extreme wind events affect coastal areas of seas around the world. Disastrous consequences for people also usually have impacts on lakes and other coastal ecosystems. When saltwater gets into coastal lakes, it mostly affects the plants and organisms that live there. This is especially true if the communities are mostly made up of species with limited osmoregulatory abilities (Cunillera-Montcusí et al. 2022). Impacts of extreme winds mainly come from their influence on water turbidity. These events are critical for the function and state of coastal lake ecosystems, often accompanying widespread coastal erosion and landscape transformation as well (Mallin and Corbett 2006). Predicting ecosystem responses to marine extreme events is challenging due to a limited understanding of the attributes that drive the

resilience of lakes (Pleskot et al., 2024). All these extreme events were characteristic of the lakes of the Kurgalsky Peninsula during the Holocene period and for Lake Lipovskoye - even at present.

The first studies of the lakes on the Kurgalsky Peninsula were conducted in the mid-19th century by the hydrographic party of the maritime department for the production of the Baltic survey. The measurements of Lake Lipovskoye bottom were taken at 31 points. The measured maximum depth was then about 15 m. In connection with the design of the port in the 1920s, Lake Lipovskoye, after a long break, again became the subject of research, during which depth measurements were made. The lake department of the Russian Hydrological Institute clarified the maximum depth of the lake, which was 16.25 m and the average depth was 9.6 m (Arnold-Alyabyev, 1924). In 1922 the Main Hydrographic Directorate near the rapper near

the bridge over the channel connecting Lake Lipovskoye to the Baltic Sea, a water gauge was installed. Observations of the water levels are made along this gauge. It was then established that the level of water fluctuations in the channel was determined not by the spring flood but by changes in the sea level. The wind from the sea led to an increase in the water level in the channel. Lake Beloye was of interest to researchers of those periods only due to its proximity to Lake Lipovskoye; practically no research was carried out on it. It was assumed that the two lakes were connected by a channel. A.A. Sokolov has a small mention of the lakes of the Kurgalsky Peninsula (Sokolov, 1952). He clarified the areas of Lake Lipovskoye (5.6 km²) and Beloye (3.6 km²).

The next largest study of lakes of the Kurgalsky Peninsula was started by the Institute of Limnology of the Russian Academy of Sciences in 2019. The modern algae developments in lakes have been studied (Stanislavskaya et al., 2021). He studies concluded that the ecological status of both lakes, based on trophic conditions and algae species compositions (II–III classes of water quality), is satisfactory. The modern Flora underwent the most comprehensive research on the Kurgalsky Peninsula. The research revealed the coastal, aquatic, semiaquatic biotopes, rare plant communities, and rare vascular plant species (Glazkova & Bubyreva, 1997; Glazkova et al., 2020). Thanks to these studies, we chose Lipovskoye and Beloye lakes for their history study using macrophytes.

In the 1920s, K.K. Markov (1927, 1931) began geomorphological and paleogeographical studies of the Kurgalsky Peninsula that were continued by S.A. Yakovlev, I.I. Krasnov, O.M. Znamenskaja, D.D. Kvasov, D.B. Malakhovsky, and others (State geological map, 2021). Paleolimnological studies on the Kurgalsky Peninsula have not previously been carried out.

This work aims to investigate the effects of marine extreme events on coastal lakes located in the Kurgalsky Peninsula.

STUDY AREA

The Kurgalsky Peninsula was deglaciated about 12,700 calibrated years before the present and was subsequently flooded by waters of Baltic Ice Lake, the Yoldia Sea, Ancylus Lake, and the Littorina Sea (Rosentau, 2013; 2021). The Kurgalsky Peninsula is on the lower terrace of the southern coast of the Gulf of Finland (Fig. 1). The Paleozoic clays

overlain by marine Pleistocene sediments - boulder loams of moraines reworked by the sea, as well as clays and sands.

The climate is temperate and maritime. The average temperature in July is +15°C, in January it is -5°C. The Atlantic cyclones, which occur 200 days a year, determine the weather. The annual precipitation is approximately 700 mm; most of it falls in the summer. The average snow cover lasts 120 days; its thickness is 40 cm. The active growing season with average daily temperatures above +10°C lasts approximately 120 days. The prevailing winds are from the south, south-west, and west.

The vegetation belongs to the southern taiga subzone. Most of the Kurgalsky Peninsula is occupied by dry green moss pine forests. In the south of the peninsula, pine forests with blueberries and lingonberries predominate (Glazkova & Bubyreva, 1997). There are areas with broad-leaved and spruce-deciduous forests, raised sphagnum bogs, black alder coastal swamps with oak, upland, steppe, and floodplain meadows with a variety of plants, coastal marshes and meadow communities, and reed communities in the coastal zone.

The zonal soils are characterized by varying degrees of podzolic sodality. However, due to the widespread occurrence of swamps on the peninsula, boggy gley soils predominate here.

MATERIALS AND METHODS

Investigations included hydrological, hydrochemical and paleolimnological studies. Bathymetric surveys allowed obtaining depth maps. We also determined the area of the lakes' watersheds.

Field work

Using a Russian corer with a 5 cm chamber diameter and 1 m length, sediment cores were taken from Lipovskoye and Beloye lakes' ice in March 2023 (Sapelko et al., 2023). Additionally, we collected 16 surface samples from lakes using the Voronkov sampler (Fig. 2). We collected surface sediment samples from the lakes on the Kurgalsky Peninsula in 2019 and 2023.

Morphometry

To describe the distribution of depths and identify bottom features, measurements were made according to

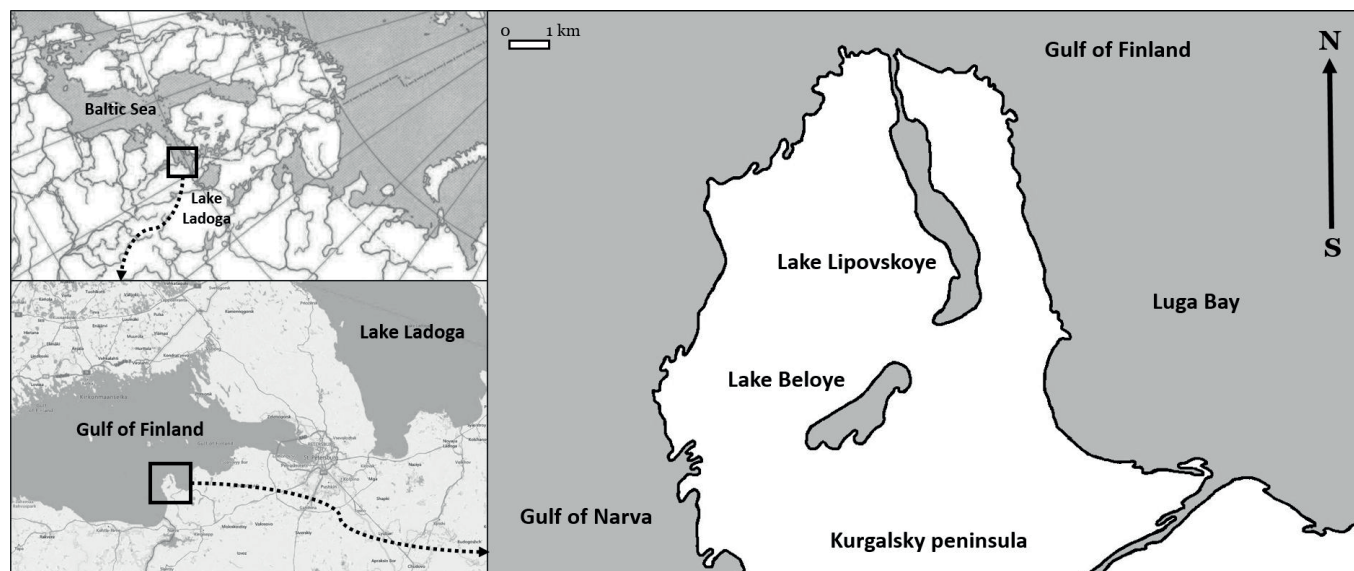


Fig. 1. Location map

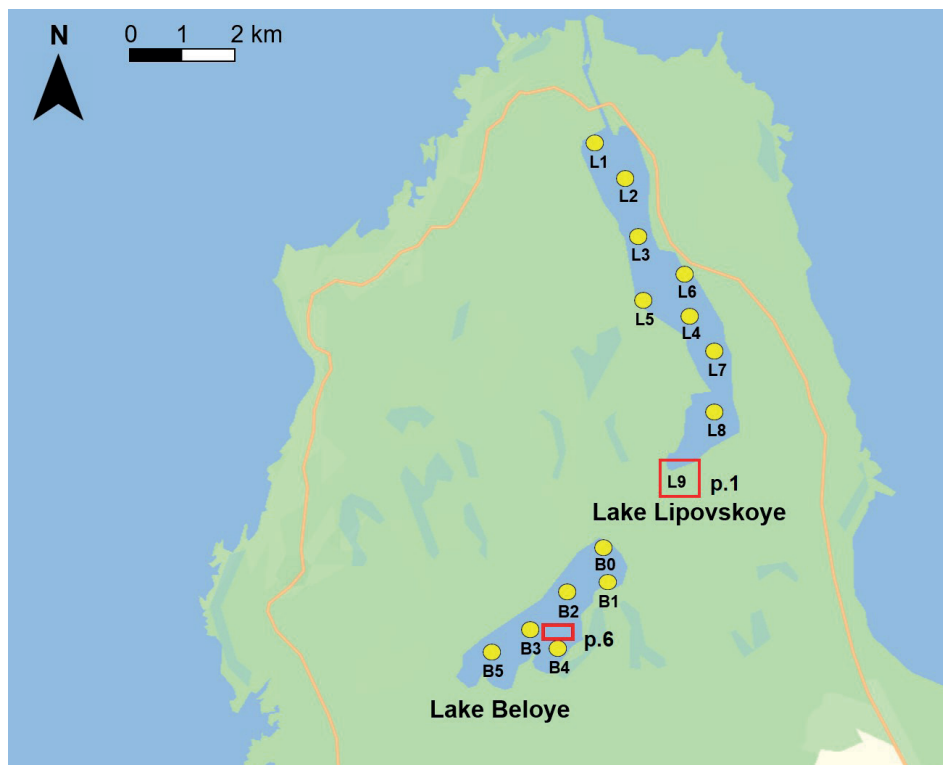


Fig. 2. Map with surface sampling points (yellow circles) and points of cores (p.1 and p.6)

the instructions (Instructions for creation, 1985; Manual for hydrometeorological stations, 1972), with 100 m between each tack. To measure the depth of reservoirs, a LOWRANCE HDS-7 echo sounder was used, featuring a double-beam emitter, a maximum echolocation depth of 300 m (at 800 KHz), an output power of 500 (RMS) / 4000 (peak), and an operating frequency of 200, 455. The power supply range was 9.5 - 32 V. The device allows you to synchronously record depth with resolution up to 1.0 cm and the location of the vessel with an accuracy of ± 2.0 m. Work was carried out from an inflatable boat with a draft of 0.2 m to reduce errors. The echo sounder emitter was installed on a special extension at the side of the boat, which made it possible to control the depth of its immersion and bring it as close as possible to the water's edge when moving to new tacks. Before carrying out the measuring work, a temporary water-measuring station and maps of lakes with planned tacks were prepared. To obtain the absolute level of water in Lake Lipovskoye on the date of measurement work, the average level of the Baltic Sea was taken according to data in Narva and Sosnovy Bor. To obtain the absolute water level in Lake Belye, a leveling course was carried out with a length of 4.5 km with a mark of 23 m from the Baltic Sea level. During the measurement work in the water area of Lake Lipovskoye, 33,767 depth measurements were made, and on Lake Belye, 27,645 depth measurements were taken. In the water area of Lake Lipovskoye, 80 tack intersection points were selected, and in Lake Belye, 87 tack intersection points. Lake Lipovskoye has mean square errors of 10 cm for depths at the points where tacks meet, and Lake Belye has them at 9 cm. These are less than the allowed standard deviations (Manual for hydrometeorological stations, 1972). To better construct diagrams of the depths of lakes, data on the elevations of the territories adjacent to them, taken from topographic maps, was added to the data on bottom marks.

Watershed area calculation

In our research, we used data from TessaDEM for calculations of the watershed area. TessaDEM is a

global digital elevation model with a resolution of 30 m. We employed TessaDEM to obtain accurate terrain elevation data. We utilized vector layers that contained the boundaries of Lake Lipovskoye and Lake Belye. We conducted bathymetry measurements to gather information about the lake depths. During the processing of the Digital Elevation Model (DEM) using the SAGA (System for Automated Geoscientific, 2006 Analyses) software, the "Fill Sinks" module (Wang & Liu) was applied prior to the watershed calculation. The "Fill Sinks" module, available within SAGA, is utilized to fill sinks or depressions in the digital elevation model. Sinks can occur in the DEM due to measurement errors or missing data. By employing the "Fill Sinks" module, we eliminated these sinks and smoothed the terrain to obtain more accurate and continuous data. Following the application of the "Fill Sinks" module to the DEM, we obtained an amended digital elevation model, which was subsequently used for the calculation of the watershed of the lakes. To calculate the watershed for each lake, we employed the "Upslope Area" module from the SAGA software. The "Upslope Area" module provides functionality for determining watersheds based on the digital elevation model.

Hydrochemistry

In order to compile the hydrochemical characteristics of the lakes and study the seasonal dynamics of hydrochemical variables, water samples were taken in March, May, July and September 2019 in different parts of Lake Lipovskoye (at 7 points) and Lake Belye (at 5 points). Additionally, Lake Lipovskoye was sampled at 2 stations in August 2023. Water samples were taken from the surface and bottom layers using a 2L Limnos sampler.

Chemical analyses were performed in two laboratories: the Laboratory of Hydrochemistry of the Institute of Limnology RAS and the Ecological and Analytical Laboratory of the State Hydrometeorological University. The conventional methods were used: dissolved oxygen content was determined by the Winkler titration (iodometric method); specific electrical conductivity (SEC) – conductometrically; pH –

potentiometrically with a glass electrode; color – by visual colorimetry; chemical oxygen demand (COD_{Cr}) – oxidation with $K_2Cr_2O_7$ and H_2SO_4 followed by titration with Mohr salt; HCO_3^- – potentiometrically; SO_4^{2-} – turbidimetrically; Cl^- – mercurimetrically; Ca^{2+} and Mg^{2+} – titration with EDTA; $\Sigma(Na^+ + K^+)$ and CO_2 – by calculation methods; ions content (dry residue) – gravimetrically, inorganic phosphorus (IP) – by molybdate method; total phosphorus (TP) – in the same manner following oxidation with $K_2S_2O_8$ and H_2SO_4 ; ammonium-ions – colorimetric method with hypochlorite and phenol; nitrite-ions – colorimetric method with Griess reagent; nitrate-ions – reduction of NO_3^- to NO_2^- (Cu-Cd) followed by determination of NO_2^- ; total nitrogen (TN) – by alkaline persulfate oxidation followed by determination of $\Sigma(NO_3^- + NO_2^-)$; Fe_{total} – by photometric method with sulfosalicylic acid.

Pollen

Samples for pollen analysis were prepared using the separation technique by V.P. Grichuk (1940) modified at the Institute of Limnology RAS with $K-CdI_2$ heavy liquid. Pollen identification refers to guides (Kupriyanova and Aleshina, 1972; 1978), electronic pollen databases, and the collection of the Institute of Limnology RAS. Pollen percentages were calculated based on the sum of trees, herbs, and spores pollen grains. Pollen diagrams were generated using Tilia, TiliaGraph, and TGView software (Grimm, 2004).

RESULTS AND DISCUSSION

Morphometric data of Lipovskoye and Belye lakes

As a result of the watershed area calculations, the following values were determined for the lakes: the

watershed of Lake Lipovskoye is 58.12 km² and the watershed of Lake Belye is 8.9 km² (Fig. 3).

Lake Belye

Fig. 4(a) presents the distribution of lake depths. A special feature of the lake is the small area of its watershed and the lack of surface runoff from it. Currently, the level of the lake varies little by season, however, in Fig. 4(b), which represents a diagram of the distribution of slopes of the lake bottom, one can see the presence of an underwater terrace at a depth of 1.5 - 2 m, indicating a long-term standing of the lake's water level below the present level in the past. Below the underwater terrace, there is a coastal slope, highlighted in gray, with bottom slopes ranging from 2 to 17°. With an interpolation step of 10 m, the average slope of the bottom of Lake Belye is 1.5°. The central part of the lake, occupying more than 70% of the lake's area, has a flat bottom with slopes of up to 2° and a small depression of up to 13.1 m.

Lake Lipovskoye

Fig. 5(a) presents the distribution of lake depths. The level regime of Lake Lipovskoye depends on the level of the Baltic Sea, which varies little over time; therefore, the coastal slope with bottom slopes from 2 to 24° is formed along the shores, without underwater terraces. In Fig. 5(b), the zone of the lake with maximum bottom slopes, which occupies less than 30% of the lake area, is shaded in gray. With an interpolation step of 10 m, the average slope of the bottom of Lake Lipovskoye is 2°. The rest of the lake has a flat bottom with a gradual decline toward the central part with maximum depth.

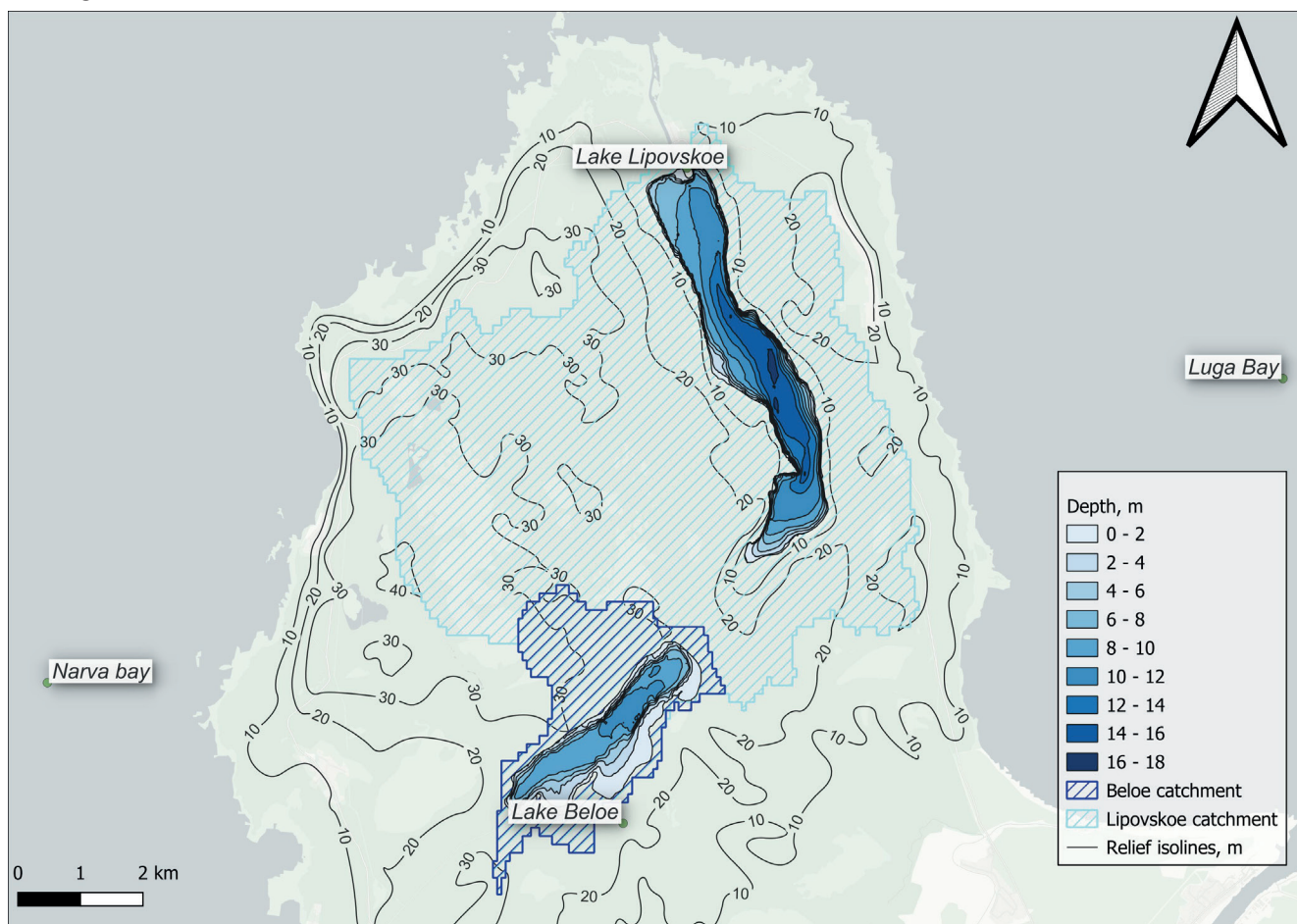


Fig. 3. The watersheds of Lake Lipovskoye and Lake Belye

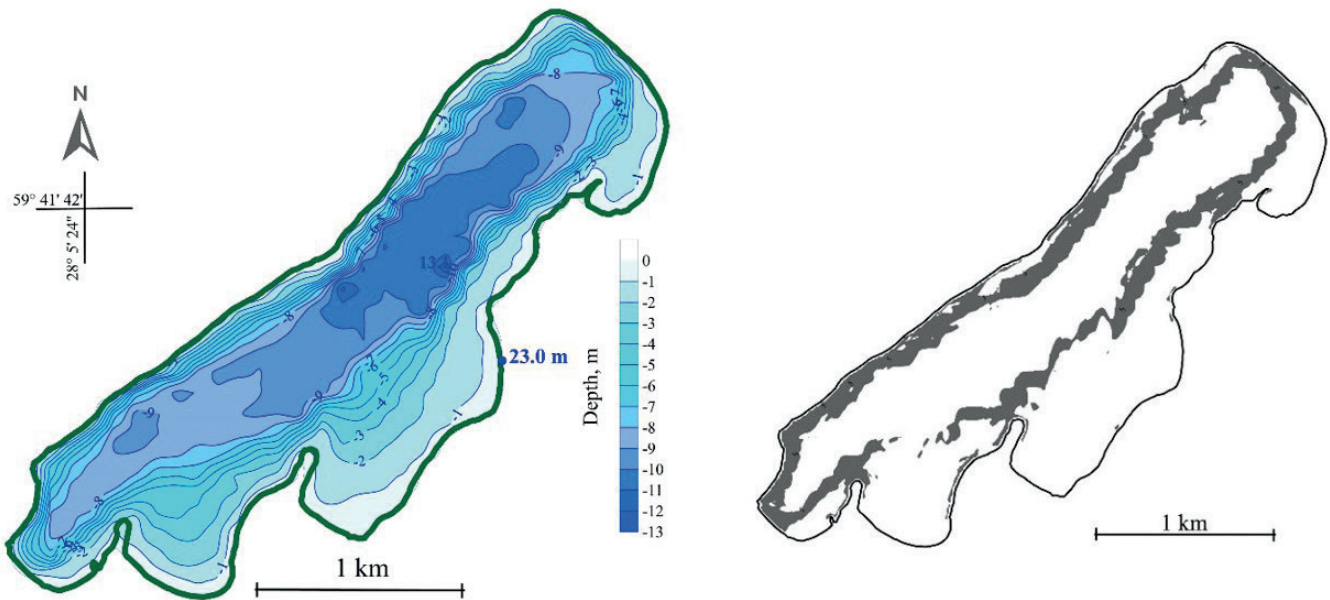


Fig. 4. Morphometry (a) and the zone of Lake Belye with bottom slopes from 2 to 17 degrees (b)

Fig. 6 presents the distribution of lake bottom slopes as a percentage of their area. Both distributions are exponential in nature, but Lake Belye is characterized by a greater differentiation of bottom slopes compared to Lake Lipovskoye. Table 1 provides the comparative statistical characteristics of the bottom slopes of the two lakes.

The shape of the bathymetric curve of Lake Lipovskoye displays three sections of its basin. Up to a depth of 6 m there is a coastal slope with an area of 1.3 km², which starts

directly from the water's edge without shallow waters of significant area, below to a depth of 12 m the bottom flattens out, the area of this area is 2.8 km², deep-sea depressions occupy the bottom with an area of 1.5 km². For Lake Belye, three sections can also be distinguished: up to 3 km² of shallow water with depths of up to 2 m; a steep coastal slope is noted to depths of 8 m; below there is a bottom with a gentle slope to a depression with an area of 1.2 km².

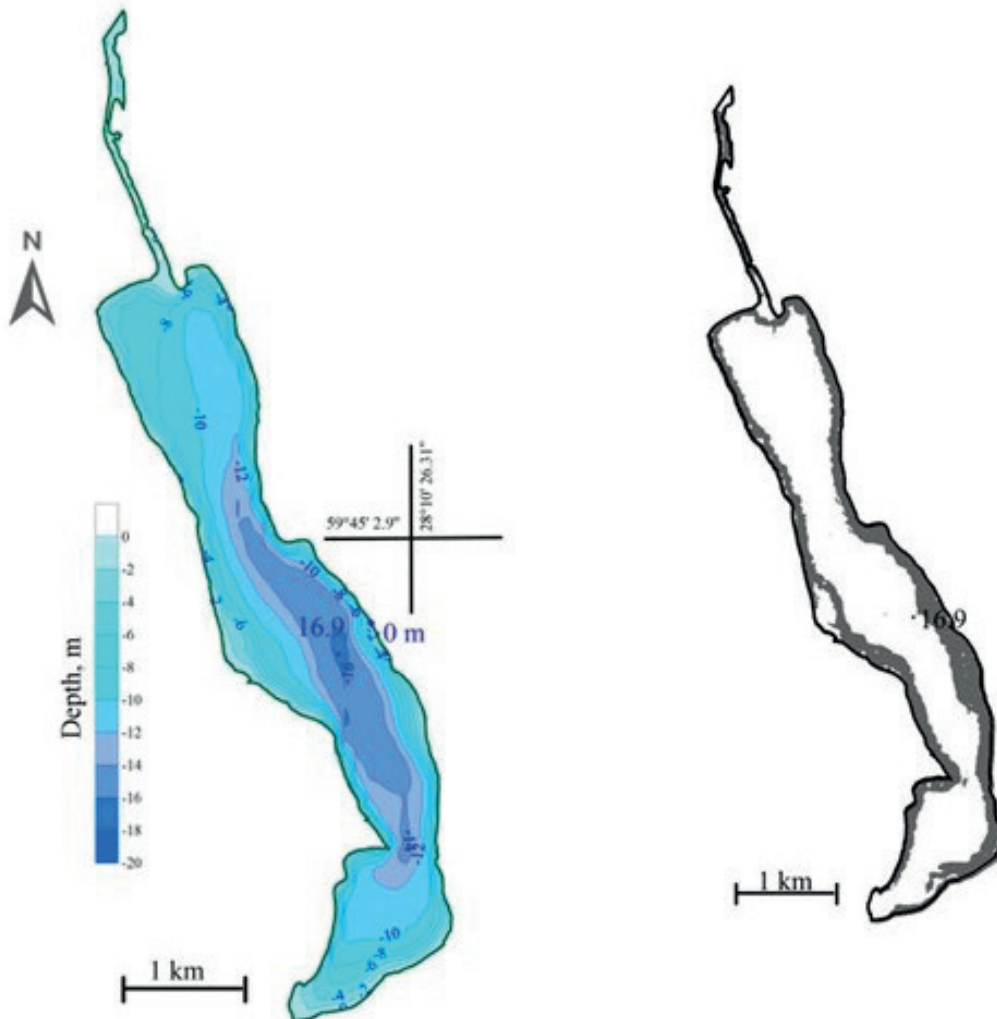


Fig. 5. Morphometry (a) and the zone of Lake Lipovskoye with bottom slopes from 2 to 24 degrees (b)

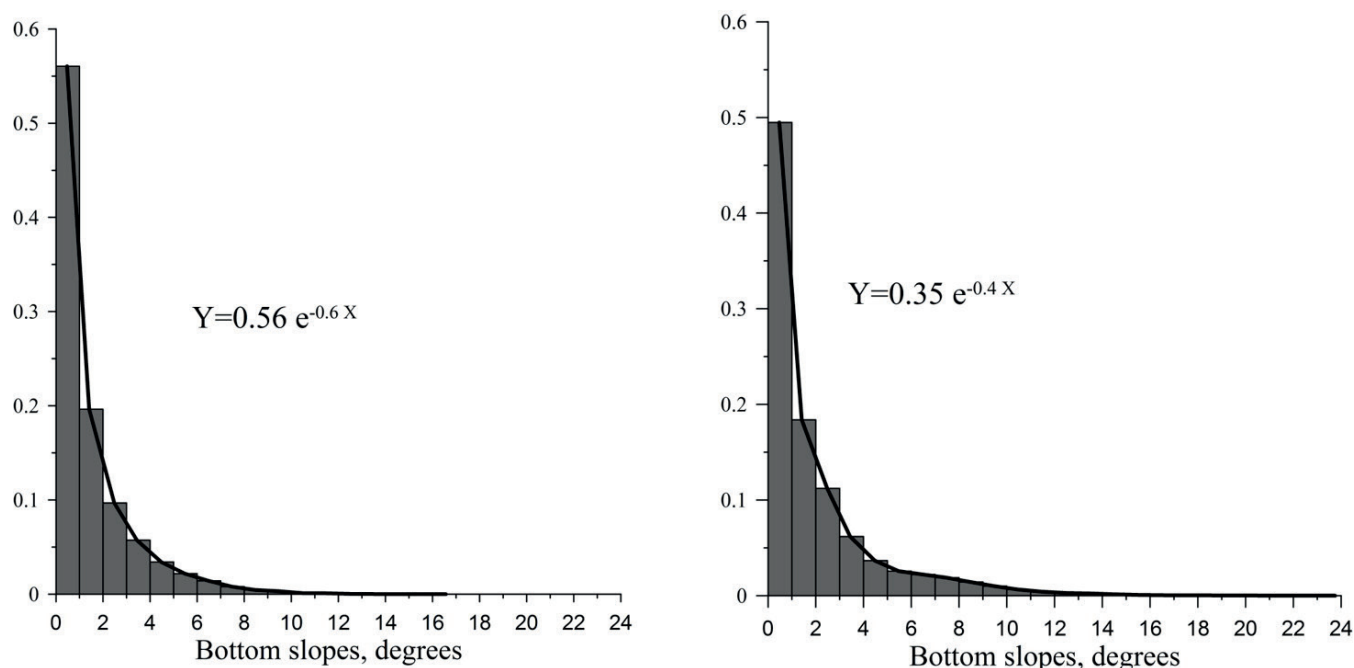


Fig. 6. Histograms of the relative distribution of bottom slopes of lakes Belye (a) and Lipovskoye (b)

Table 1. Comparative characteristics of lake bottom slopes

Lake	Belye	Lipovskoye
Average slope	1.491724	2.032837
Standard error	0.009596	0.010709
Median	0.839381	1.016122
Standard deviation	1.729976	2.527355
Sample variance	2.992816	6.387521
Excess	6.568455	6.857175
Asymmetry	2.283405	2.375512
Maximum, deg.	16.96576	23.74195
Number of cells	32503	55694

Hydrochemistry

According to Table 2, Lake Lipovskoye is salty by the average value of ions content (dry residue). The reason for this is the hydraulic connection of the lake with the Gulf of Finland. Extreme values were recorded at the end of the ice-covered period: the highest – in the near-bottom layer, the lowest – in the surface layer, directly under the ice. In the ice-free period, the water mass of the lake is more homogeneous, and ion content varies in a rather narrow range of values 4.07 – 4.89 g l⁻¹ (average 4.47 g l⁻¹), while the difference of values between the surface and near-bottom layers does not exceed 0.6 g l⁻¹. According to the classification of O.A. Alekin (Alekin, 1970) the lake water belongs to the chloride class, sodium group, third type. This type is typical for strongly mineralized waters. In spite of the fact that the lake is stretched in a meridional direction, with saline waters inflowing to its northern end, and in the ice-covered period the ion content in the surface and bottom layers differs by an order of magnitude, the ratio of main ions is practically not subjected to spatial and temporal changes. The average relative contents of major ions in the anionic composition are the following (eq. %): Cl⁻ – 90, HCO₃⁻ – 2, SO₄²⁻ – 8; in the cationic composition (eq. %): Σ(Na⁺ + K⁺) – 76, Ca²⁺ – 5, Mg²⁺ – 19.

The fact that Lake Belye, located on the Kurgalsky Peninsula at a distance of 1.8 km south of Lake Lipovskoye, has no direct connection with the Gulf of Finland determines significant differences in the chemical composition of the water in the two lakes. As can be seen from Table 2, the ion content in Lake Belye for the same observation period is about 80 times lower than in Lake Lipovskoye, which allows us to classify it as an ultra-freshwater lake. At the same time, the ratio of major ions also differs significantly. In contrast to Lake Lipovskoye, sulfates dominate the anionic composition of Lake Belye, while calcium dominates the cationic composition. The average content of major anions is the following (eq. %): SO₄²⁻ – 47, HCO₃⁻ – 28, Cl⁻ – 25; major cations (eq. %): Ca²⁺ – 48, Mg²⁺ – 27, Σ(Na⁺ + K⁺) – 24. According to the classification of O.A. Alekin, the lake water belongs to the sulfate class, calcium group, second, or third type.

The values of chemical oxygen demand (COD_{Cr}), indirectly characterizing the content of organic matter, in the water of Lake Lipovskoye are twice as high as in Lake Belye, while the average value of the watercolor in the ice-free period in both lakes is the same (Table 2). The highest COD_{Cr} values refer to the surface layer in the deep-water zone of the southern half of the lake at the end of winter. The same waters are also characterized by the highest

Table 2. Average and extreme (in parentheses) values of chemical variables of lakes Lipovskoye and Belye in March – September 2019*

Chemical variable	Lipovskoye	Belye
O ₂ , %	74 (0 ÷ 124)	92 (73 ÷ 100)
SEC, μS cm ⁻¹	6320 (948 ÷ 8230)	40 (34 ÷ 47)
pH, unit pH	7.58 (6.00 ÷ 8.38)	7.34 (5.90 ÷ 8.25)
Color, degree Pt-Co	31 (13 ÷ 172)	15 (10 ÷ 19)
COD _{Cr} , mg O l ⁻¹	34.1 (11.3 ÷ 74.1)	16.8 (5.5 ÷ 35.1)
HCO ₃ ⁻ , mg l ⁻¹	84.1 (9.2 ÷ 273)	5.95 (2.75 ÷ 9.15)
SO ₄ ²⁻ , mg l ⁻¹	202 (64 ÷ 332)	7.70 (3.99 ÷ 9.52)
Cl ⁻ , mg l ⁻¹	1791 (208 ÷ 2260)	3.01 (2.02 ÷ 4.77)
Ca ²⁺ , mg l ⁻¹	53.9 (9.3 ÷ 66.0)	3.34 (3.13 ÷ 3.69)
Mg ²⁺ , mg l ⁻¹	132 (15.0 ÷ 167)	1.14 (0.57 ÷ 1.73)
Σ(Na ⁺ + K ⁺), mg l ⁻¹	1062 (142 ÷ 1405)	2.10 (0.12 ÷ 4.57)
Ions content, g l ⁻¹	4.03 (0.46 ÷ 5.05)	0.052 (0.018 ÷ 0.078)
CO ₂ , mg l ⁻¹	3.3 (0.4 ÷ 16.0)	0.5 (0.1 ÷ 1.3)
IP, mg P l ⁻¹	0.038 (0.003 ÷ 0.299)	0.003 (0.001 ÷ 0.007)
TP, mg P l ⁻¹	0.064 (0.020 ÷ 0.355)	0.010 (0.007 ÷ 0.017)
NH ₄ ⁺ , mg N l ⁻¹	0.183 (0.011 ÷ 0.914)	0.067 (0.033 ÷ 0.130)
NO ₂ ⁻ , mg N l ⁻¹	0.001 (0.000 ÷ 0.003)	0.001 (0.000 ÷ 0.011)
NO ₃ ⁻ , mg N l ⁻¹	0.076 (0.000 ÷ 0.930)	0.026 (0.004 ÷ 0.074)
TN, mg N l ⁻¹	0.53 (0.17 ÷ 1.56)	0.27 (0.14 ÷ 0.46)
Fe _{total} , mg l ⁻¹	0.30 (0.02 ÷ 1.49)	0.12 (0.01 ÷ 0.54)

* The hydrochemical variables' values at two Lake Lipovskoye sampling stations that were sampled on August 10, 2023, were within the ranges of values found in 2019.

color values due to both the presence of colored forms of organic matter (humus) and high iron content, which is a peculiarity of this geochemical province. Probably, it is connected with sub-ice flooding of water coming with slope runoff during the period of snow melting and the appearance of edges on the lake.

Lake Belye is characterized by a favorable oxygen regime, whereas in the hypolimnion of Lake Lipovskoye, a decrease in the concentration of O₂ until its complete disappearance and the formation of H₂S was observed from the end of the ice-covered period until mid-summer. The anaerobic situation in the near-bottom water layer persisted at least until the end of September. The value of pH varied in the range from slightly acidic to slightly alkaline waters and was approximately the same for both lakes.

According to the value of the average annual total phosphorus content (TP) in the water, Lake Lipovskoye is classified as eutrophic, Lake Belye is oligotrophic (upper limit). The seasonal dynamics of the TP content in Lake Belye are practically absent. In Lake Lipovskoye, there was a progressive increase in the phosphorus reserve in the lake water from the end of the ice-covered period to autumn. During this period, bottom sediments serve as the primary source of phosphorus, and the establishment of anaerobic conditions significantly increases their phosphorus release. Similarly to phosphorus, the nitrogen

content in Lake Lipovskoye is higher than in Lake Belye (Table 2). Despite the good aeration of the water mass, the reduced ammonium form dominates among the inorganic forms of nitrogen in both lakes. In Lake Lipovskoye, the N/P ratio (w/w) in the annual cycle averages 13, while during the open water period, it averages 9. This means that during the vegetation period, the ratio of the main nutrient content in the lake water is close to the optimal value for phytoplankton growth. In Lake Belye, the N/P ratio in the annual cycle averages 28, varying in different seasons from 21 to 35. Thus, Lake Belye's water has a significant excess of nitrogen, and the phosphorus content limits primary production.

Hence, it was found that two lakes located in close proximity to each other in the same climatic and landscape conditions differ significantly in hydrochemical characteristics. The main differences are the presence of a hydraulic connection between Lake Lipovskoye and the Gulf of Finland, which is most noticeable in winter (during the ice-covered period), whereas Lake Belye does not, and the differences in the external load on the lakes due to the differing specific catchments.

Lake sediments

Lake sediments are represented by grey clayey-layered silt with black layers of hydrotroilite and gyttya. The lower

part of the sediments is possibly associated with the Baltic Ice Lake (BIL). Layered clay sediments of the BIL were noted in the studied region in cores located at sea level, like Lake Lipovskoye (Markov, 1931), as well as in the lower part of the lake sediment sequence of the Narva-Luga Lowland (Subetto et al., 2002; Sandgren et al., 2004).

On Lake Belye, cores were taken at two points in the lake's central part. However, it was not possible to obtain long cores here. At one point a core of fine-grained sand with a thickness of 10 cm was taken from a depth of 6 m, and at another point a core of 35 cm was taken from a depth of 8.1 m (Fig. 7). At the second point, the sediments are represented by silt, fine-grained sand, and gyttja. The lower part of the sediments may have been formed during the Ancylus Lake period. Sediments of this type, represented by clays and clayey silts, are described in the

region under consideration as sediments of Ancylus Lake (Rosentau et al., 2013; Spiridonov et al., 2010).

Modern vegetation from surface pollen

We have collected pollen data from subrecent lake sediments, specifically from Lipovskoye and Belye lakes (Fig. 8). The pollen analysis was carried out in order to identify the reflection features of macrophyte pollen in lake sediments. Further pollen analysis of lake sediment sequences requires these results (Fig. 7). In Lake Lipovskoye, there is no specific dominant aquatic vegetation, and the presence of macrophyte pollen varies during the entire period. Pollen of the genus *Potamogeton* (*P. pectinatus* L., *P. perfoliatus* L.), which is the dominant according to the studies of modern aquatic vegetation, are predominated in the surface sample from the

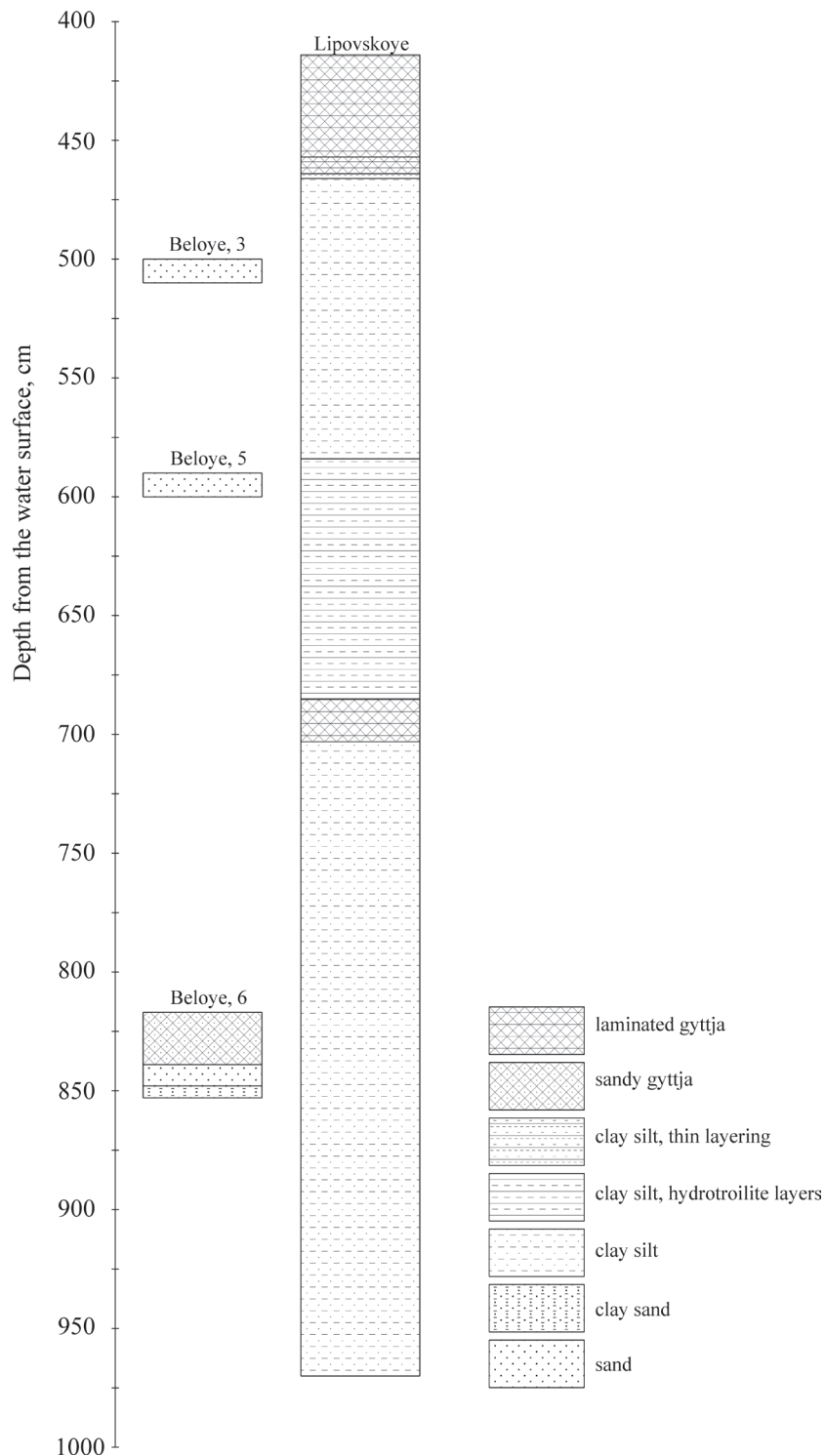


Fig. 7. Lithology of Belye and Lipovskoye lakes sediments

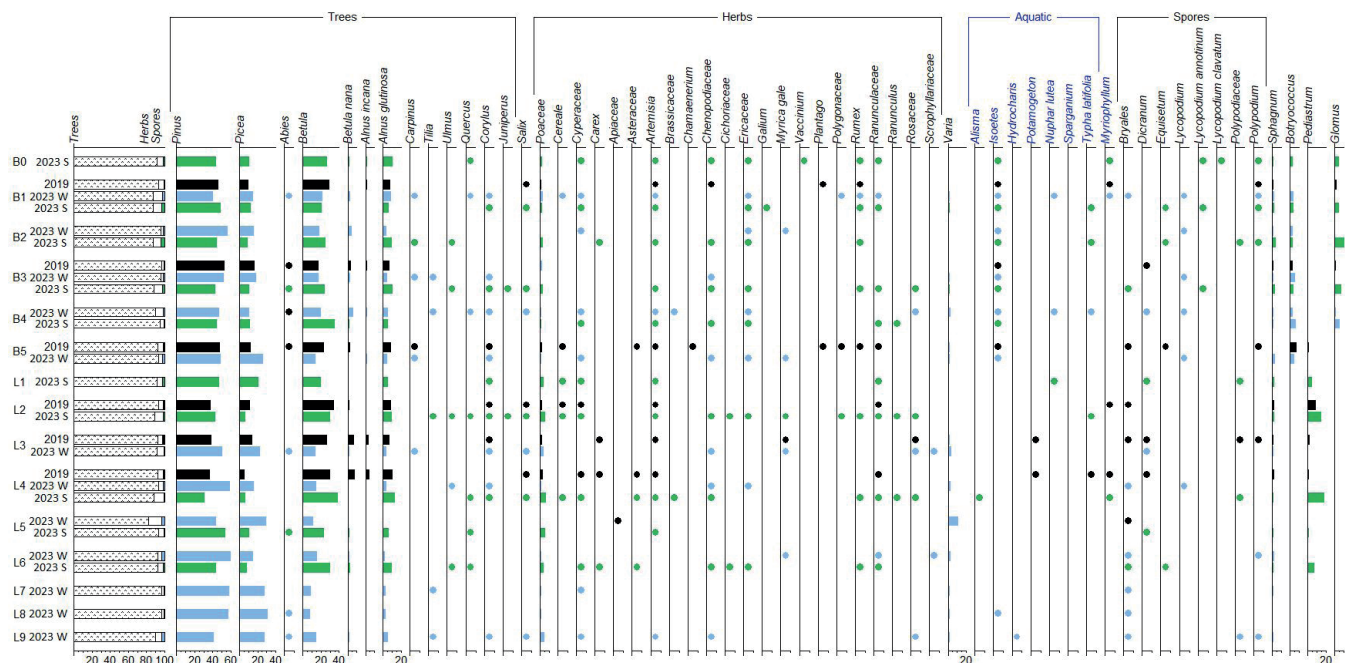


Fig. 8. Pollen diagram of surface samples from Beloye (B 0-5) and Lipovskoye (L 1-9) lakes. S-summer, W- winter

northern part of the lake. Pollen of the genus *Myriophyllum* (*M.alterniflorum* DC., *M.sibiricum* Kom.) can be found in samples from the central and northern parts in 2019. In both winter and summer samples in 2023, the diversity of macrophyte pollen differs significantly; however, the species composition in the summer samples in 2023 is similar to that in 2019 (*Myriophyllum* sp., *Potamogeton* sp., *Typha latifolia* L.).

In Lake Beloye, pollen of the main dominant, the rare species *Lobelia dortmanna* L., are not represented in SPS, although it takes an important place in submerged plant communities. *Isoetes echinospora* Durieu and *I. lacustris* L. spores are also dominant and can be found in all samples over a short period of time. Meanwhile, its quantity is higher in summer samples than in winter samples in 2023. Pollen of *Myriophyllum alterniflorum* is present in samples from the northern part of the lake in 2019 and in the winter in 2023, but not in the summer samples in 2023, although the plant has been described during the studies of modern aquatic vegetation (Rusanov et al., 2024). In addition to the vegetation typical of freshwater lakes, in Lake Lipovskoye, we described *Najas marina* L., which is found in sea waters (Rusanov et al., 2024).

CONCLUSION

By looking at how the extreme coastal events affected the ecosystems of brackish Lake Lipovskoye and freshwater Lake Beloye, we reconstructed how lake ecosystems responded to these events. The morphometric characteristics of the lakes were obtained, the areas of their watersheds were calculated, and maps of lakes and bottom slopes were constructed. As a result, we received a conclusion that lakes have big areas but small watersheds (Lake Lipovskoye - 5,65/58.12 km²; Lake Beloye - 3,28/8.9 km²).

- Most of the hydrochemical variables of Lake Lipovskoye are characterized by pronounced seasonal dynamics. The periodic inflow of saline water from the Gulf of Finland into the northern end of Lake Lipovskoye largely determines its chemical composition and hydrochemical regime, which is evident when comparing it with Lake Beloye, located a little south, but has not hydraulic connections to the Gulf of Finland. Hydrochemical data on the current state of the lakes show the eutrophic status (by phosphorus) of Lake Lipovskoye, and allow it to be classified as brackish water. Lake Beloye is oligotrophic and freshwater.

- Subrecent pollen spectra of lake surfaces sediments on the Kurgalsky Peninsula quite adequately reflect modern aquatic vegetation, especially the communities of submerged hydrophytes in Lake Lipovskoye and floating hydrophyte (*Nuphar lutea* (L.) Smith) in both lakes. *Potamogeton* (*P. pectinatus* L., *P. perfoliatus* L.) and *Myriophyllum* sp. are the dominant in the pollen spectra and modern aquatic plant communities in the lakes. Over a short-term period, there are substantive differences in the species composition and dynamics of macrophyte pollen for both lakes.

- The first results from the lake sediments cores showed a between the Holocene sedimentation in Lipovskoye and Beloye lakes and the transgressive-regressive phases of the Baltic, the Ancylus and Littorina stages, and the stage of the Baltic Ice Lake.

- The sediments of both lakes showed us lithological changes associated with extreme changes (sharp lithological boundaries) during the Holocene. The obtained hydrological, hydrochemical results and the study of the dynamics of modern vegetation have shown that now the influence of extreme marine events on Lake Beloye has ended but is still affecting Lake Lipovskoye. ■

REFERENCES

- Alekin O.A. (1970) Fundamentals of hydrochemistry. L.: Gidrometeoizdat, 444 p. (in Russian).
- Arnold-Alyabyev V.I. (1924) Study of lakes of the Kurgalov Peninsula. *Izvestia. RGI*, 10, pp. 21–30 (in Russian).
- Cunillera-Montcusí, D., Beklioğlu, M., Cañedo-Argüelles, M., Jeppesen, E., Ptacnik, R., Amorim, C.A., Arnott, S.E., Berger, S.A., Brucet, S., Dugan, H.A., Gerhard, M., Horváth, Z., Langenheder, S., Nejtgaard, J.C., Reinikainen, M., Striebel, M., Urrutia-Cordero, P., Vad, C.F., Zadereev, E., Matias, M. (2022) Freshwater salinisation: a research agenda for a saltier world. *Trends Ecol. Evol.* S0169534721003402. <https://doi.org/10.1016/j.tree.2021.12.005>
- Glazkova E.A., Bubyreva V.A. (1997) Flora Kurgal'skogo poluostrova [Flora of the Kurgalsky Peninsula]. St. Petersburg: SPbGU, 164 p. (in Russian).
- Glazkova E.A., Liksakova N.S., Doronina A.Yu., Himelbrant D.E., Stepanchikova I. S., Ginzburg E.G., Potemkin A.D. (2020) Valuable botanical objects of the Kurgalsky nature reserve (Leningrad region). 3. Coastal, aquatic and semiaquatic biotopes of high conservation value. The Kurgalsky reserve as an important plant area. *Transactions of Karelian Research Centre of Russian Academy of Science*, 1, pp. 5–16 (in Russian). <https://doi.org/10.17076/bg833>
- Grichuk V.P. (1940) Method of treatment of the sediments poor in organic remains for the pollen analysis. *Probl. Phys. Geogr.* 8. p. 53–58 (in Russian).
- Grimm EC (2004) *TGView 2.0.2 (Software)*. Springfield: Illinois State Museum, Research and Collections Center
- Instructions for creating topographic maps of the shelf and inland waters (1985) *GKINP-11-152-83*, Moscow, 80 p. (in Russian).
- Kupriyanova L.A., Alyoshina L.A. (1972) Pollen and spores of plants of the flora of the European part of the USSR. Nauka, Leningrad (in Russian).
- Kupriyanova L.A., Alyoshina L.A. (1978) Pollen of dicotyledonous plants of the flora of the European part of the USSR. Nauka, Leningrad (in Russian).
- Mallin, M.A., Corbett, C.A. (2006) How hurricane attributes determine the extent of environmental effects: multiple hurricanes and different coastal systems. *Estuar. Coasts* 29, pp. 1046–1061.
- Manual for hydrometeorological stations and posts (1972), Issue 7: Part of Observations on Lakes and Reservoirs, Moscow (in Russian).
- Markov K.K. (1927) A short geological and geomorphological abstract of the northern part of Kingisepp district. L., pp. 91–118 (in Russian).
- Markov, K. (1931) Development of the relief in the northwestern part of the Leningrad District. Geological Survey of USSR, Moscow-Leningrad, 117 p. (in Russian).
- Pleskot K., Cwynar L. C., Kołaczek P., Mroczkowska A., Suchora M., Kowalczyk C., Kokociński M. (2024) Impact of extreme coastal events on a brackish lake on the Burin Peninsula, Newfoundland, Canada. *Science of the Total Environment*, 935, 173330. <https://doi.org/10.1016/j.scitotenv.2024.173330>
- Rosentau, A., Muru, M., Kriiska, A., Subetto, D.A., Vassiljev, J., Hang, T., Gerasimov, D., Nordqvist, K., Ludikova, A., Lougas, L., Raig, H., Kihno, K., Aunap, R., Letyka, N. (2013) Stone age settlement and Holocene shore displacement in the Narva-Luga Klint Bay area, eastern Gulf of Finland, *Boreas*, 42 (4), pp. 912–931.
- Rosentau, A., Klemann V., Bennike O., Steffen H., Wehr J., Latinović M., Bagge M., Ojala A. (2021) A Holocene relative sea-level database for the Baltic Sea. *Quaternary Science Reviews*, 266: 107071. <https://doi.org/10.1016/j.quascirev.2021.107071>
- Rusanov A.G., Gazizova T.Yu., Lapenkov A.E., Sapelko T.V. (2024) Current state of vegetation cover of lakes Beloe and Lipovskoe (Kurgalsky Peninsula). *Transactions of Karelian Research Centre of Russian Academy of Science. Limnology and oceanology*, 2, pp. 51–64. <https://doi.org/10.17076/lim1864>
- Sandgren P., Subetto D.A., Berglund B.E., Davydova N.N., Savelieva L.A. (2004) Mid-Holocene Littorina Sea transgressions based on stratigraphic studies in coastal lakes of NW Russia. *GFF*. Vol. 126 (4), pp. 363–380. <https://doi.org/10.1080/11035890401264363>
- Sapelko T.V., Lapenkov A.E., Gazizova T.Yu., Rusanov A.G., Kuznetsov D.D., Guzivaty V.V. (2023) First results of expeditional work on the lakes of the Kurgalsky Peninsula (southern coast of the Gulf of Finland). Relief and Quaternary deposits of the Arctic, Subarctic and North-West Russia. *Proceedings of the annual conference on the results of expedition research*. St. Petersburg, 10, pp. 395–400. <https://doi.org/10.24412/2687-1092-2023-10-395-400>
- Sokolov A.A. (1952) *Hydrography of the USSR*. Leningrad: Gidrometeoizdat (in Russian).
- Spiridonov M.A., Ryabchuk D.V., Orviku K.K., Sukhacheva L.L., Nesterova E.N., Zhamoida V.A. (2010) Changes in the coastal zone of the eastern part of the Gulf of Finland under the influence of natural and anthropogenic factors. *Regional Geology and Metallogeny*, 41, pp. 107–118 (in Russian).
- Stanislavskaya E.V., Afanas'eva A.L., Pavlova O.A. (2021) Algoflora of lakes in the Kurgal'sky Nature reserve (Leningrad region). *Povolzhskiy Journal of Ecology*, 3, pp. 335–347. <https://doi.org/10.35885/1684-7318-2021-3-335-347>
- State geological map of the Russian Federation, scale 1: 200,000. Second edition. Ilmen series. Sheet O-35-V (Kingisepp). Explanatory note (2021) Moscow branch of the Federal State Budgetary Institution "VSEGEI", 108 p. (in Russian).
- Subetto D.A., Sevastyanov D.V., Savelyeva L.A., Arslanov Kh.A. (2002) Bottom sediments of Leningrad lakes region as a chronicle of Baltic transgressions and regressions. *Bulletin of St. Petersburg State University*, 7.Issue. 4 (31), pp. 75–85 (in Russian).
- Wang L., Liu H. (2006) An efficient method for identifying and filling surface depressions in digital elevation models for hydrologic analysis and modelling. *International Journal of Geographical Information Science*, Vol. 20, (2), pp. 193–213.

ASSOCIATION OF SPATIAL AND TEMPORAL WINDTHROW DISTRIBUTION WITH CONVECTIVE PARAMETERS AND LIGHTNING DENSITY IN RUSSIA

Andrey N. Shikhov^{1,2*}, Yulia I. Yarinich^{2,3,4}, Alexander V. Chernokulsky^{2,5}

¹ Perm State University, 15 Bukireva street, Perm, 614068, Russia

² A.M. Obukhov Institute of Atmospheric Physics, 3 Pyzhevsky per., Moscow, 119017 Russia

³ Faculty of Geography, Lomonosov Moscow State University, 1 Lenniskie Gory, Moscow, 119991 Russia

⁴ Research Computing Center, Lomonosov Moscow State University, 1 Lenniskie Gory, Moscow, 119991, Russia

⁵ Institute of Geography RAS, 29 Staromonetny per., Moscow, 119017, Russia

*Corresponding author: shikhovan@gmail.com

Received: September 4th 2024 / Accepted: February 20th 2024 / Published: March 31st 2025

<https://doi.org/10.24057/2071-9388-2025-3590>

ABSTRACT. Windthrow is one of the major causes of forest loss in most forest types, depending on the frequency and intensity of severe winds and forest vulnerability. This study focuses on analyzing of the association of the spatio-temporal distribution of windthrow with the atmospheric convective parameters and lightning activity in the Russian forest zone for the period 2001-2020. The windthrow data include 1816 events that are associated with tornadoes and non-tornadic convective windstorms and are obtained from the previously developed satellite-derived database. Convective parameters are calculated based on the ERA5 reanalysis, while the Worldwide Lightning Location Network (WWLLN) is used for lightning data. It is found that both the spatial distribution and the interannual variability of windthrow events are significantly correlated with the corresponding variability of convective parameters, especially with the significant tornado parameter (STP), both in the European Russia (ER) and in Siberia. The spatial correlation between windthrow events and lightning density is also significant, with a stronger relationship in the ER than in Siberia. For inter-annual variability, it is also found a strong relationship between the number of days with supercritical STP values and the total windthrow area per season. Our results highlight STP and lightning density as informative predictors that can be used as characteristics of windthrow in the Russian forests and for further estimation of associated risks, which is important for sustainable forest management.

KEYWORDS: windthrow, non-tornadic convective windstorms, tornadoes, ERA-5 reanalysis, convective indices, lightning density

CITATION: Shikhov A. N., Yarinich Y. I., Chernokulsky A. V. (2025). Association Of Spatial And Temporal Windthrow Distribution With Convective Parameters And Lightning Density In Russia. *Geography, Environment, Sustainability*, 75-88 <https://doi.org/10.24057/2071-9388-2025-3590>

ACKNOWLEDGEMENTS: This study has been funded by the Russian Scientific Foundation and Perm Krai, Project Number 24-27-20111

Conflict of interests: The authors reported no potential conflict of interest.

INTRODUCTION

Strong winds, squalls, and tornadoes cause substantial loss and damage to forests every year. Predicting and mapping wind-related risks to forests remains both a scientific challenge and an important issue for sustainable forest management, especially in the context of climate change (Panferov et al. 2009). Previously developed methods for windthrow risk prediction include an assessment of hazard (i.e., frequency and intensity of severe wind events causing damage to forests), and vulnerability (i.e., forest stand characteristics, landscape parameters such as slope, aspect, soil type, forest management, etc.) [Seidl et al. 2011; Venäläinen et al. 2020]. The previously compiled datasets of windthrow events [e.g. Shikhov et al. 2020; Forzieri et al. 2020; Senf and Seidl 2021b] are used for training and validation of the prediction models.

Numerous studies present an assessment of forest vulnerability to windthrow events at a regional scale,

based on statistical or mechanistic (tree-based) models [see e.g., Peltola et al. 1999; Dobbertin et al. 2002; Gardiner et al. 2008; Panferov and Sogachev 2008; Seidl et al. 2011, Suvanto et al. 2019]. Estimates of the frequency of severe wind events for windthrow risk prediction are based on 10-year maximum wind speeds interpolated from long-term observational data [Laapas et al. 2019, 2023] or the same calculation from reanalysis data and downscaled with digital elevation models [Venäläinen et al. 2017]. However, the characteristics of severe wind events observed by weather stations or extracted from reanalysis data are not suitable for local convective windstorms and tornadoes, which induced more than 50% of the windthrow area in the forest zone of European Russia and Siberia [Shikhov et al. 2023]. The observational network (Chernokulsky et al. 2021) misses most of these events due to their local nature and the low density of weather stations. Other data sources, such as the European Severe Weather Database [Groenemeijer et al. 2017] also do not provide a reliable

estimate of the spatial distribution of convective wind events due to a strong "population bias" [Taszarek et al. 2020a].

In recent decades, several proxy parameters have been widely used to estimate the climatic characteristics of the atmospheric environment that favor the occurrence of convective hazardous events, rather than the events themselves [Rasmussen and Blanchard, 1998; Brooks et al. 2018]. In total, more than 50 atmospheric parameters are now used to estimate the main so-called 'ingredients' necessary for the formation of severe convective storms that produce non-tornadic convective windstorms (squalls) and tornadoes, such as convective instability, precipitable water content, wind shear, helicity, and others [Doswell and Shultz, 2006; Taszarek et al. 2023;]. In recent studies, these parameters are mainly calculated from reanalysis data, which allows for the obtaining of a homogeneous data series and for its comparison with the spatial and temporal distribution of observed convective events [Taszarek et al. 2017, 2020b; Chernokulsky et al. 2023].

Previously published studies for Russia [Shikhov et al. 2021; Chernokulsky et al. 2023] analyzed convective parameters only for specific days when hazardous convective events occurred. It was shown that the so-called composite convective parameters are the most informative for diagnosing and predicting the environments favorable for the formation of such events. However, the climatic characteristics of these parameters have not been considered, except for long-term trends [Chernokulsky et al. 2022a], and have not been compared with the data on the spatial distribution and interannual variability of windstorms and tornadoes. This study presents such a relationship. Additionally, this study presents the relationship between the spatial and temporal distribution of lightning density and that of tornadoes and non-tornadic convective windstorms.

MATERIALS AND METHODS

Windthrow data

Data on windthrow events is obtained from the GIS database [Shikhov et al. 2020; Tornadoes..., 2024]. The sample includes 1816 windthrow events caused by non-tornadic convective windstorms and tornadoes in the period from 2001 to 2020, including 1068 cases in the ER and 748 cases in Siberia. Among them, 1052 cases (total area 57,359 ha) are tornado-induced events, and 764 cases (total area 325,942 ha) are squall-induced events. For each year, the number of windthrow events, the number of days with events, and the total windthrow area were calculated separately for the forest zone of the ER and Siberia. Note that the number of days with windthrow events is calculated taking into account only those events whose date of occurrence is known with an accuracy of at least one month.

Convective parameters

The statistical properties of the convective atmospheric parameters were evaluated based on a dataset of these parameters previously developed for Northern Eurasia [Chernokulsky et al. 2022a] using the ERA5 reanalysis [Hersbach et al. 2020]. The calculation of the indices is based on 20 vertical levels from the surface to 300 hPa, with high spatial (0.25°) and temporal (1 h) resolution. The output dataset includes 50 convective parameters

characterizing thermodynamic instability, precipitable water, condensation level, wind shear, and helicity. It also includes several composite parameters. We have selected several key parameters that indicate favorable environments for the formation of convective windstorms and tornadoes.

We used such well-known and widely used parameters as convective available potential energy calculated for air parcel characteristics averaged in a mixed 0-1000 m layer above ground level (hereafter ML CAPE), and deep layer shear (DLS), which represent thermodynamic and dynamic 'ingredients', respectively [Rasmussen and Blanchard, 1998; Brooks et al. 2018]. We also used composite convective parameters, which have been found to be the most informative for diagnosing and predicting the environments favorable for the formation of severe convective windstorms and tornadoes for Europe [Taszarek et al. 2017, 2020b] and Russia [Shikhov et al. 2021; Chernokulsky et al. 2023]. In particular, we selected three composite parameters, such as ML WMAXSHEAR, significant tornado parameter (STP) and supercell composite parameter (SCP), which represent strong predictors for severe convective storms, tornadoes, and supercell storms, respectively [Taszarek et al. 2017, Thompson et al. 2003].

The ML WMAXSHEAR (Eq. 1) parameter characterizes the maximum vertical velocity (associated with CAPE) combined with wind shear in the 0-6 km layer [Taszarek et al. 2017]:

$$MLWMAXSHEAR = (2MLCAPE)^{0.5}DLS \quad (1)$$

where denotes maximum vertical velocity, and is the deep-layer shear (the magnitude of the vector difference between the winds at 10 m (near-surface wind) and 6 km). The Supercell Composite Parameter (SCP) (Eq. 2) takes into account convective instability, helicity, and wind shear and is calculated as follows:

$$SCP = \left(\frac{MUCAPE}{1000Jkg^{-1}} \right) \left(\frac{SRH_{0-3km}}{100m^2s^{-2}} \right) \left(\frac{DLS^2}{40m^2s^2} \right) \quad (2)$$

where is convective available potential energy calculated for a parcel lifted from the most unstable layer, is the storm-relative helicity in the 0-3 km layer¹.

The Significant Tornado Parameter (STP) is calculated as follows (Eq. 3):

$$STP = \left(\frac{DLS}{20} \right) \left(\frac{SRH_{0-1km}}{150} \right) \left(\frac{SBCAPE}{1500} \right) \left(\frac{2000 - SBLCL}{1000} \right) \left(\frac{200 + SBCIN}{150} \right) \quad (3)$$

where is the storm-relative helicity in the 0-1 km layer, is the convective available potential energy calculated for a parcel lifted from the surface, is the lifted condensation level for that parcel, and is the convective inhibition for it [Thompson et al. 2003].

The summer months (June-August) of 2001-2020 were chosen as the study period because data on windthrow for these years are available for the forest zone both in the ER and in Siberia [Shikhov et al. 2023]. On the basis of hourly data, statistical characteristics of the convective variables, such as the mean value for each summer season and the recurrence of critical values (Table 1), were calculated. The critical thresholds (median and 90th percentile) were

¹ Grieser J. Convection parameters [online]. Available at:

<http://www.juergen-grieser.de/CovectionParameters/ConvectionParameters.pdf> [Accessed 20 Aug. 2024].

obtained from a sample of 281 cases of severe windstorms and tornadoes that caused forest damage in the ER and Western Siberia [Chernokulsky et al. 2023]. The median values are further considered as the critical values, which are typical for the formation of windstorms and tornadoes. The 90th percentile threshold characterizes the extremely high values of the convective parameters (the most favorable environments for the formation of severe windstorms and tornadoes). We picked these critical values, which were found specifically for the forest zone of Russia, because windstorms and tornadoes happen in different regions of the world at substantially different values of convective parameters [Taszarek et al. 2020b].

Lightning data

We used global lightning climatology data from the WWLLN for the period 2010-2020 [Kaplan et al. 2021], and calculated the annual lightning density (for summer months only, as for convective parameters) per 1000 km². We also used another global lightning detection system, LIS-OTD (Lightning Imaging Sensor – Optical Transient Detector), available for the period from 1995 to 2014 [Christian et al. 2003], and calculated the mean lightning density for the period 2001-2014.

Relationship assessment

Correlations between windthrow characteristics, WWLLN-based lightning density and convective parameters derived from the ERA5 reanalysis were evaluated both in time and in space. To calculate correlations in space, we aggregated all the above data into a 100×100 km grid. Such a grid size corresponds approximately to three cells of the ERA5 reanalysis and is close to the size (1.25°×1.00°) that was used by [Taszarek et al. 2020b] to avoid duplication of convective environments at the local scale. In addition, 100×100 km cells were used to estimate the spatial distribution of the wind-damaged area and to smooth out local anomalies associated with the rarity of these events [Shikhov et al. 2020].

Cells with < 10% forest cover according to the vegetation map of Russia [Bartalev et al. 2016] were excluded from further calculations. In total, the forest zone of the ER and Siberia is covered by 787 grid cells (266 cells in the ER and 521 cells in Siberia). In each grid cell, the ratio of the total windthrow area for the period 2001-2020 to the forest area was calculated and then considered as the dependent variable (predictand). Convective parameters and lightning density were averaged in each grid cell and considered as the predictors. Correlations between the predictors and predicted were calculated based on the averaged values for each grid cell. As the distribution in the data deviated from the normal law, both Pearson (linear) and Spearman (rank) correlation coefficients were calculated. The significance level was set as 0.05.

Relationships between windthrow characteristics and convective atmospheric variables in time were evaluated on the basis of the data averaged annually and over the study area (separately for the forest zone of the ER and Siberia). Thus, we calculated correlation coefficients between windthrow characteristics and convective parameters averaged for June-August of each year (i.e., the sample size was 20 values).

RESULTS

Spatial distribution of windthrow events, convective atmospheric parameters and lightning density in forests

On average, the area of windthrow as a percentage of the total forested area in the ER is about 4 times larger than in Siberia [Shikhov et al. 2023]. In the ER, squall- and tornado-induced windthrow events are most widespread in the central part of the forest zone, approximately along 60°N (from the Leningrad region in the west to the Komi Republic in the east) (Fig. 1a). The largest area of windthrow (up to 1% of the forest area) is observed in the Yaroslavl, Vologda, and Novgorod regions, where two catastrophic windthrow events occurred in the summer of 2010 [Chernokulsky et al. 2022b; Shikhov et al. 2023]. In the spatial distribution of windthrow events in Siberia, several local peaks are observed east of the Yenisei River (where tornado-induced damage predominates), in the west and northeast of the Irkutsk region (due to squall-induced windthrow), and in the Tomsk region, where both squall- and tornado-induced windthrow events are widespread (Fig. 1).

The spatial distribution of windthrow events in the forest zone has a statistically significant correlation with lightning density according to the WWLLN data (Fig. 1b). In the forest zone of the ER, lightning density is highest northwest of Moscow, where windthrow density is also higher than the average for the ER. In Siberia, lightning density is highest in the central part of the forest zone of Western Siberia and decreases further east, especially over Eastern Siberia (in the Irkutsk region). Such a decrease in lightning density is not consistent with the spatial distribution of windthrow. For example, the area of wind-damaged forest in the Irkutsk region is larger than in the neighboring regions (Fig. 1). It is likely that this inconsistency is related to the uneven coverage of WWLLN stations and hence, lightning data [Holzworth et al. 2021; Tarabukina and Kozlov, 2020].

According to the LIS-OTD data, the lightning density in the ER is generally similar to the WWLLN data and also agrees well with the distribution of windthrow events (not shown). The highest lightning density is observed along the Urals and over the central regions of the ER, while in Siberia several local peaks can be highlighted. According to the LIS-OTD data, the lightning density over the Irkutsk region is slightly lower than over the more western regions of Siberia (i.e., a strong decrease observed according

Table 1. Median and 90th percentile thresholds of convective variables for a sample of cases with linear convective windstorms and tornadoes [Chernokulsky et al. 2023]

Variable	Median	90 th percentile
ML WMAXSHEAR	850	1126
STP	0.5	1.42
SCP	3.71	11.75
ML CAPE	887	1330
DLS	23.8	29.7

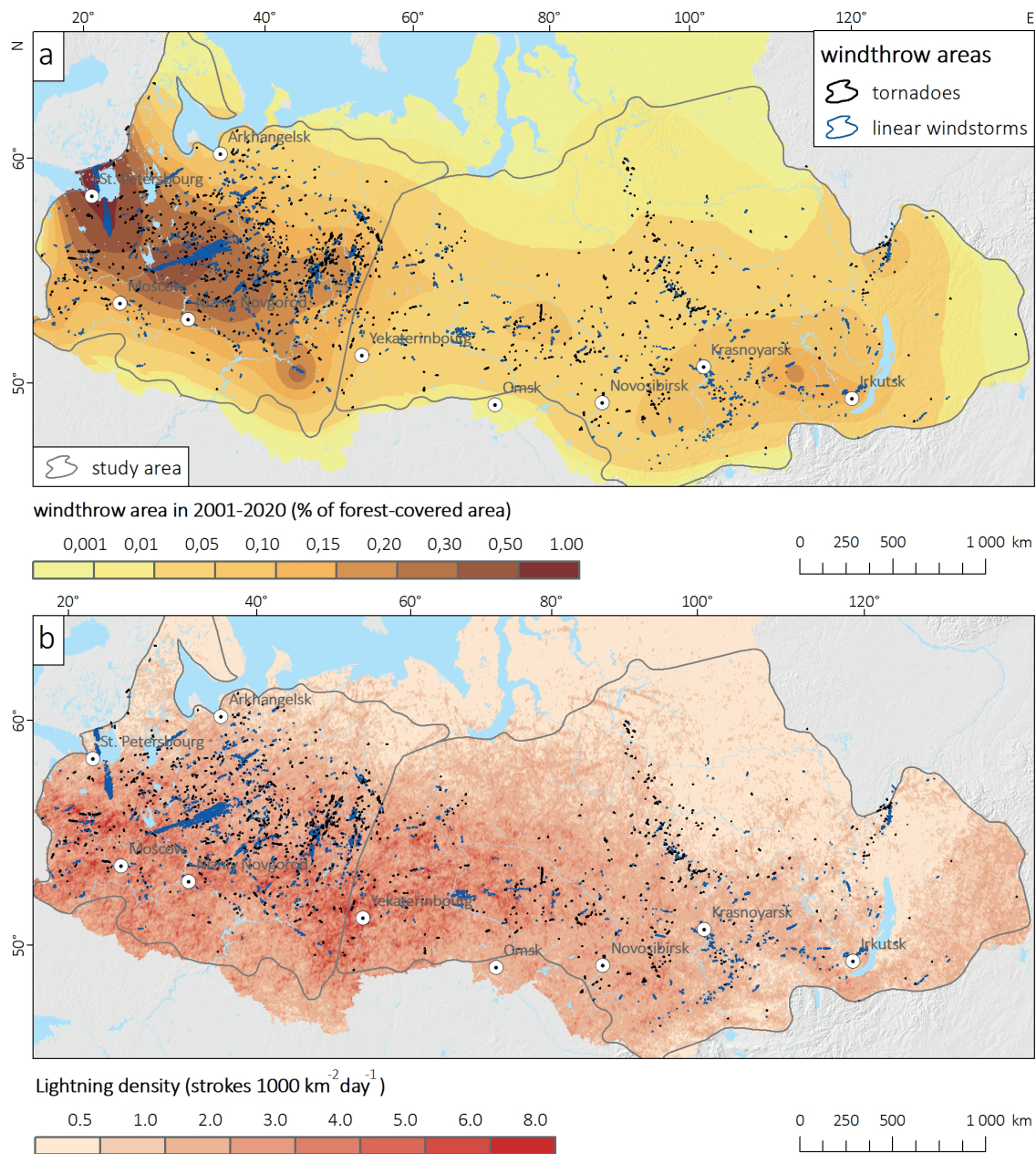


Fig. 1. Ratio of windthrow area to forest-covered area (a) and lightning density averaged over summer seasons 2010-2020 (b) in the ER and Siberia

to the WWLLN data is not confirmed). However, the LIS-OTD dataset has a much lower spatial resolution than the WWLLN. In addition, it has a large number of no data cells over Central Siberia, the northern part of the ER, and Western Siberia, which prevents us from further using this dataset in the present study.

Fig. 2-6 show the values of convective variables averaged for the summer months of 2001-2020 over the forest zone of ER and Siberia, as well as the number of days with excess convective parameters over critical values (Table 1). The frequency of extremely high values of convective parameters, corresponding to the 90th percentile for the cases with non-tornadic convective windstorms and tornadoes [Chernokulsky et al. 2023] is not shown since such high values are rarely observed and their spatial distribution mainly coincides with that of the days with supercritical values.

The spatial distribution of all convective parameters considered, except for DLS, has a significant positive correlation (Spearman rank coefficient) with the spatial distribution of windthrow events (Table 2). However, the Pearson linear correlation coefficient is statistically

significant only when the ER and Siberia are considered together (probably due to a larger sample size). For the ER and Siberia separately, only certain convective parameters are significantly correlated with the wind-damaged forest area (STP in the ER, ML CAPE and ML WMAXSHEAR in Siberia). In contrast to other convective indices, which have their highest values located in the southern part of the forest zone, the highest values of DLS are often associated with the climatic location of the Arctic front, which extends along the Arctic coast in summer (Fig. 2). Thus, DLS is negatively correlated with the spatial distribution of windthrow events. In the ER, the distribution of windthrow events coincides quite well with the distribution of STP values (both mean and number of days with supercritical values). The highest STP values are observed in the western Urals and in the central part of the forest zone of the ER, where squall- and tornado-induced windthrow events are widespread (Fig. 6). Further south, the mean STP values decrease due to an increase in the lifted condensation level (LCL). The obtained estimates of the spatial distribution of STP are consistent with those previously published for Europe [Taszarek et al. 2020b].

The highest values of other composite convective parameters are observed south of the zone of the maximum density of windthrow events. Thus, the highest values of ML WMAXSHEAR (Fig. 4) and SCP (Fig. 5) are observed in the Southern Urals, Tatarstan, and the Nizhny Novgorod region, and for ML WMAXSHEAR also southwest of Moscow. It is important to note that the maximum in the Southern Urals is associated with mountainous terrain and does not coincide with the distribution of windthrow events. At the same time, the ML CAPE distribution (especially the number of days with supercritical values) has a well-defined maximum east and northeast of Moscow, while the maximum in the South Urals is absent. Thus, ML CAPE has a stronger correlation with the distribution of windthrow events than ML WMAXSHEAR and SCP (Table 2). It is also noteworthy that the lowest values of convective parameters within the forest zone of the ER are observed in the northwest (Republic of Karelia). This corresponds to the lowest windthrow area and indicates a low frequency of severe convective windstorms and tornadoes.

In Siberia, the mean values of convective parameters are substantially lower than in the ER, and their correlation with the distribution of windthrow events is weaker than in the ER (according to the Spearman rank coefficient). Note that the highest values of most of the convective parameters, especially the SCP and STP, are observed in the mountains of southern Siberia, which does not correspond to the spatial distribution of windthrow events. Only ML CAPE does not increase in the mountains compared to the plains of Western Siberia, which explains its higher correlation with the distribution of windthrow events (Table 2). It is also important to note that the southern part of the forested zone of Western Siberia, where the values of convective parameters are close to the highest in Siberia, is characterized by a relatively low percentage of forest area (20-40%) and a high proportion of deciduous forests [Bartalev et al. 2016], which leads to a decrease in the frequency and area of windthrow in comparison with the adjacent regions of the Urals and Central Siberia.

As in the ER, the spatial distribution of windthrow in Siberia corresponds better to the distribution of STP than to other convective indices (Fig. 6). The highest values of other convective parameters are observed in the southern part of the forest zone (east of Ekaterinburg, north of Omsk), and in the mountains of southern Siberia. For STP, a secondary maximum is also found east of the Yenisei River, where the density of tornado-induced windthrow has a well-defined maximum (Fig. 6). In the Irkutsk region, the values of convective parameters (except for ML CAPE) are rather low, which does not correspond to a large windthrow area.

Interannual variability of windthrow characteristics and convective atmospheric parameters

For the period 2001-2020, we found a statistically significant correlation between the annual number of windthrow events and the damaged area and the values of the composite convective parameters averaged over the summer months. A particularly strong correlation is found for the SCP and STP (Table 3), while it is absent for ML CAPE. In the forest zone of ER, the interannual variability of the number of windthrow events and convective parameters SCP, STP, and ML WMAXSHEAR are similar (Fig. 7). Consequently, the years 2004, 2006-2007, 2010, and 2020 recorded the highest mean values of these parameters and the highest number of days with supercritical values. In the same years (except for 2006), the number of windthrow events and the damaged area were also higher than average. In 2002-2003 and 2018-2019, the lowest values of convective parameters coincide with a relative decrease in the number of windthrow events. The coefficient of determination (square of the Pearson correlation coefficient) shows that 37% of the interannual variability in the number of windthrow events can be explained by the variability in STP. However, this relationship cannot be applied to the windthrow area, because specific events, such as two derechos in the summer of 2010 [Chernokulsky et al. 2022b], contribute significantly to the interannual variability of the damaged area.

In Siberia, the correlation between the values of the composite convective parameters and the windthrow characteristics is somewhat weaker than in the ER, but it is also statistically significant for ML WMAXSHEAR, STP, and SCP (Table 3 and Fig. 8). The peaks of 2007, 2015, and 2020 are well pronounced in terms of the number of windthrow events. In addition, 2004 and 2020 are characterized by the largest windthrow area. At the same time, 2002, 2007 and 2015 have the highest values of convective parameters. In both the ER and Siberia, there is no increase in the values of convective parameters for the period 2001-2020, and in Siberia there is even a downward trend, which is somewhat in contrast to previously published trend estimates [Chernokulsky et al. 2022a]. However, these results are not directly comparable because [Chernokulsky et al. 2022] considered a longer time interval (1979-2020), excluding the spring and autumn months.

Seasonal mean ML CAPE values have no correlation with the number of windthrow events and their area, but such a correlation is statistically significant for DLS (Table 3). The interannual variability of windthrow events shows a

Table 2. Spearman (numerator) and Pearson (denominator) correlation coefficients between windthrow characteristics and convective parameters. Statistically significant coefficients are shown in bold

Windthrow area (% of forest- covered area)	Lightning density	ML WMAXSHEAR			SCP			STP			ML CAPE			DLS		
		Mean*	N_{crit}^*	N_{90p}^*	Mean	N_{crit}	N_{90p}	Mean	N_{crit}	N_{90p}	Mean	N_{crit}	N_{90p}	Mean	N_{crit}	N_{90p}
ER and Siberia	0.48/ 0.16	0.40/ 0.12	0.39/ 0.07	0.33/ 0.02	0.36/ 0.09	0.31/ 0.10	0.40/ 0.05	0.43/ 0.10	0.44/ 0.09	0.34/ 0.03	0.40/ 0.13	0.52/ 0.18	0.54/ 0.23	-0.06/ -0.02	-0.17/ -0.11	-0.26/ -0.14
ER only	0.41/ 0.10	0.35/ 0.10	0.36/ 0.07	0.32/ 0.10	0.37/ 0.11	0.46/ 0.10	0.42/ 0.09	0.57/ 0.13	0.55/ 0.10	0.31/ 0.00	0.31/ 0.09	0.41/ 0.10	0.46/ 0.13	-0.07/ -0.08	-0.01/ -0.09	0.02/ -0.10
Siberia only	0.37/ 0.10	0.36/ 0.15	0.34/ 0.06	0.26/ 0.01	0.30/ 0.09	0.23/ 0.00	0.20/ -0.02	0.31/ 0.04	0.32/ 0.05	0.26/ 0.01	0.39/ 0.19	0.44/ 0.15	0.43/ 0.17	-0.18/ -0.14	-0.26/ -0.18	-0.29/ -0.17

*Mean – mean value for June-August, N_{crit} – number of days with supercritical values (values above the critical level), N_{90p} – number of days with values above the 90th percentile of the sample from [Chernokulsky et al. 2023]

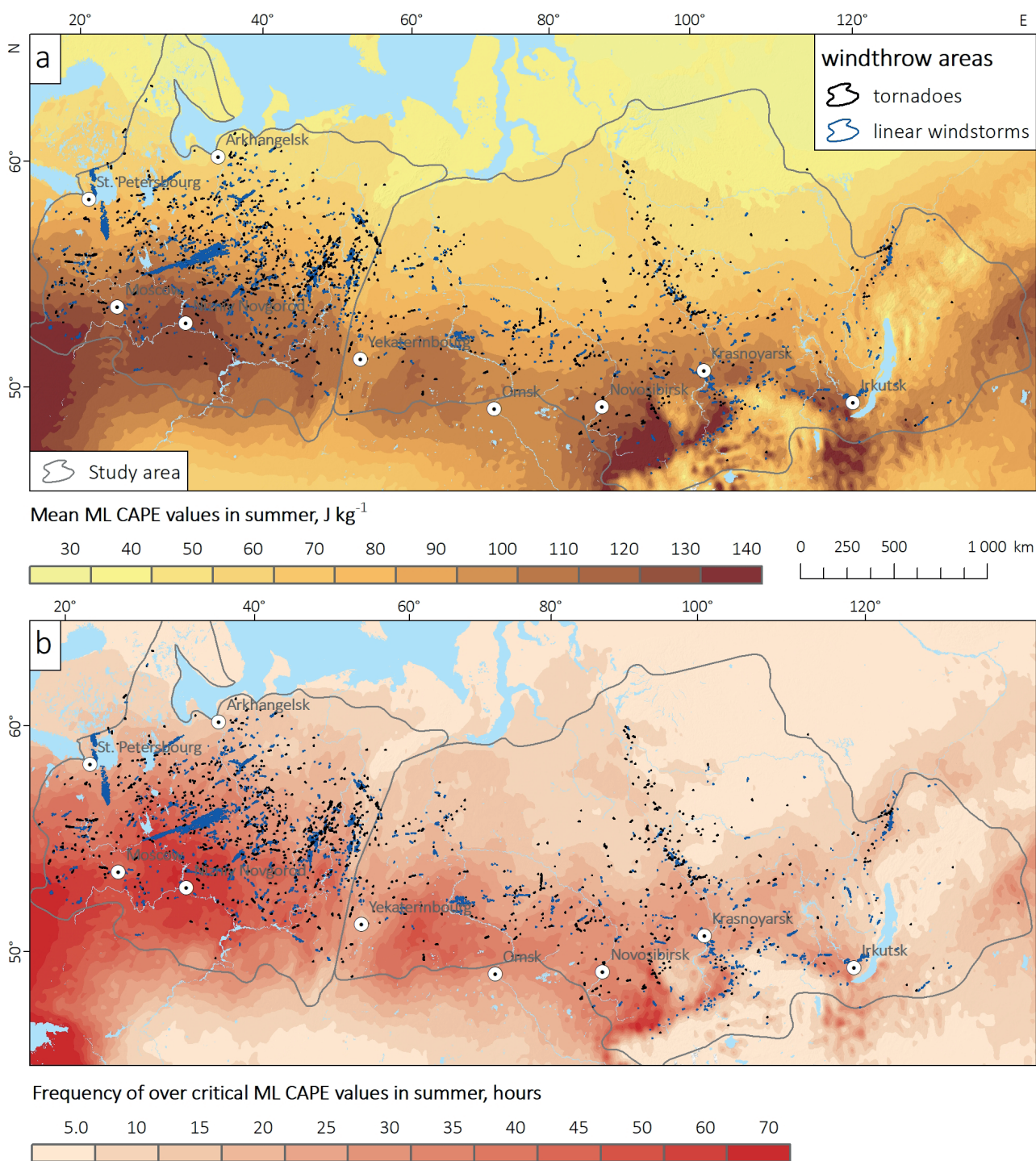


Fig. 2. Spatial distribution of ML CAPE and windthrow events in the forest zone of the ER and Siberia: a) mean values for the summer seasons in 2001-2020; b) number of days with supercritical values

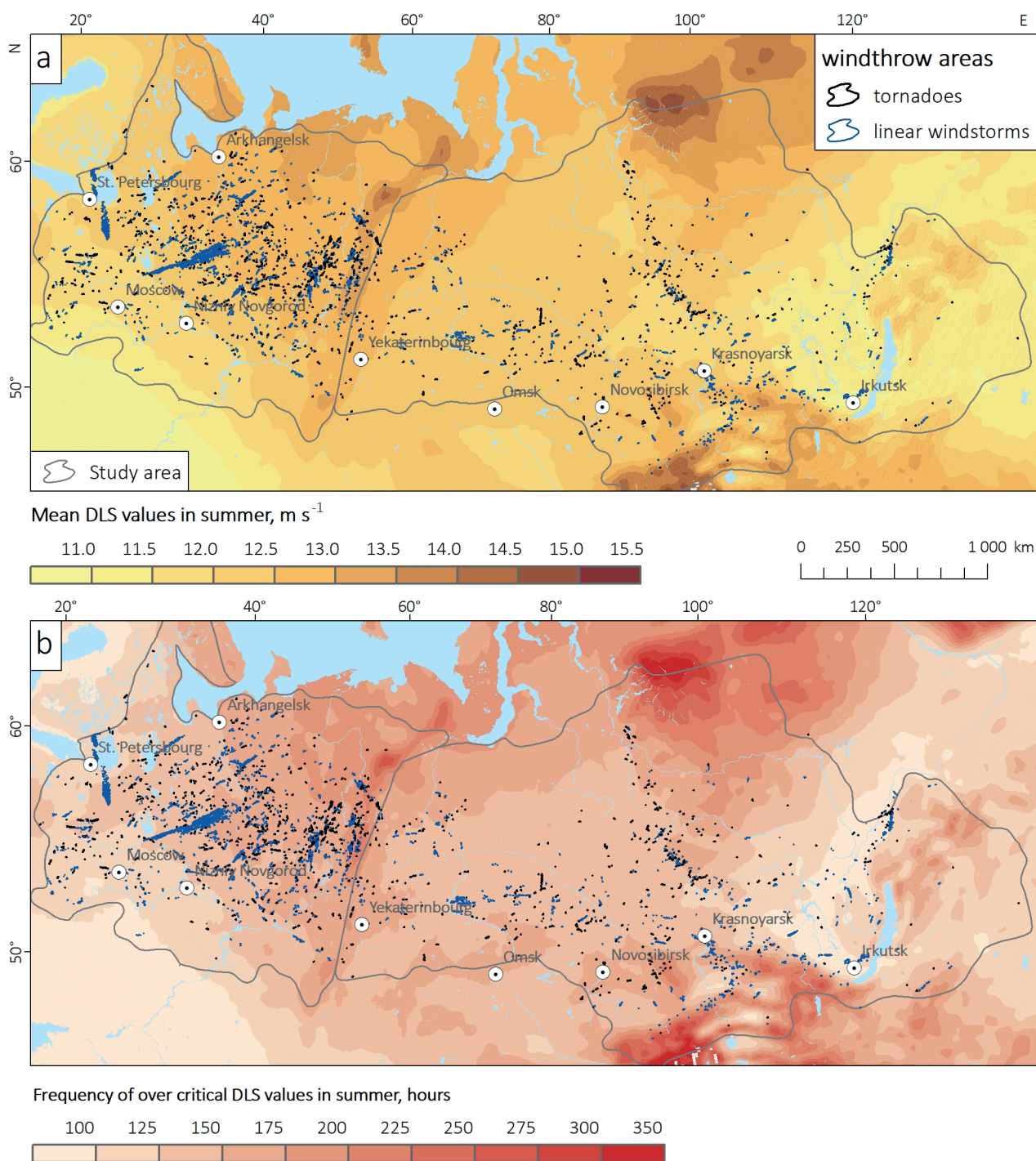
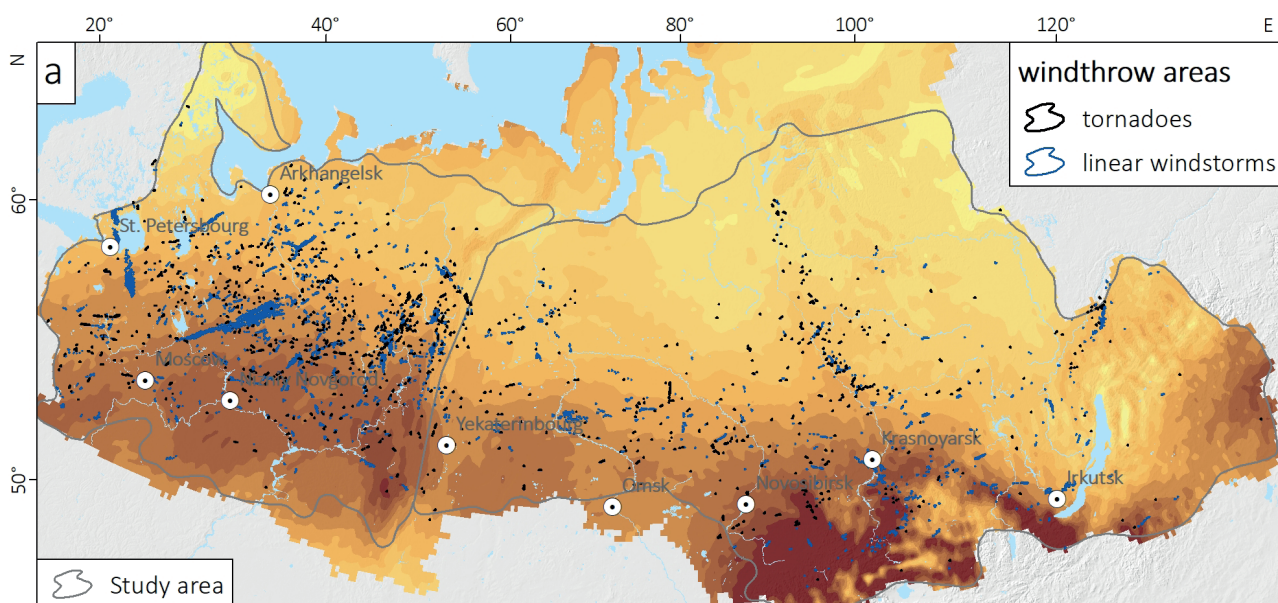
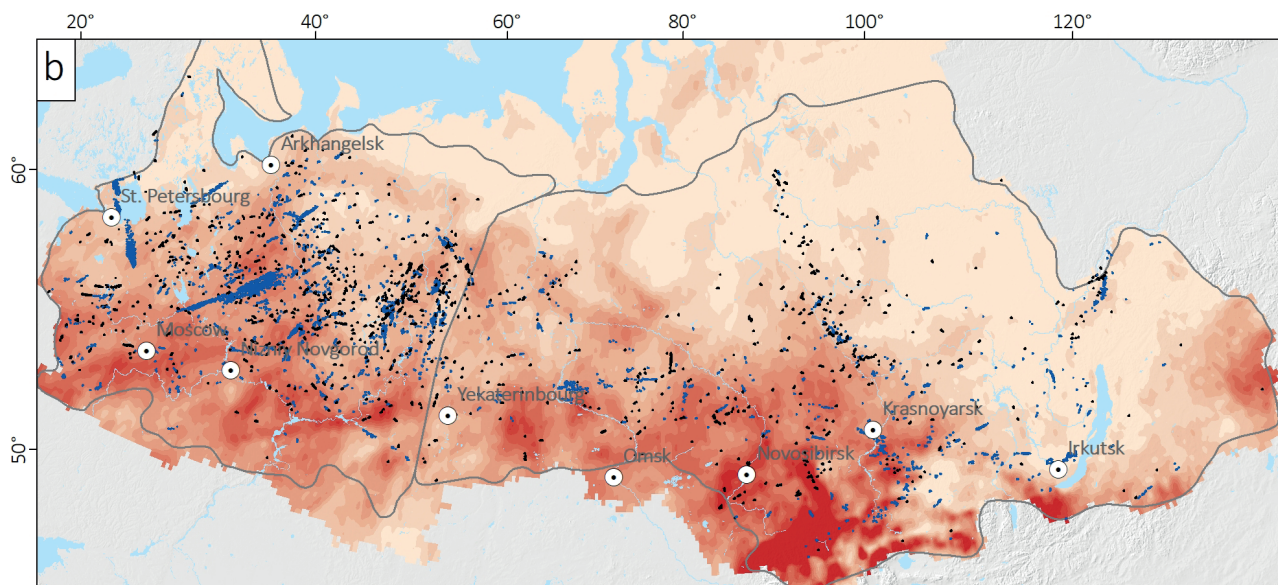
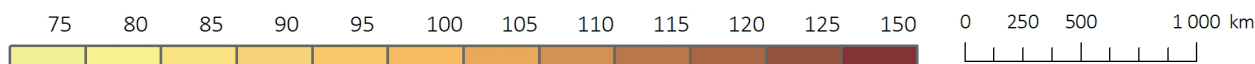


Fig. 3. Spatial distribution of DLS and windthrow events in the forest zone of the ER and Siberia: a) mean values for the summer seasons in 2001-2020; b) number of days with super-critical values



Mean ML WMAXSHEAR values in summer



Frequency of over critical ML WMAXSHEAR values in summer, hours

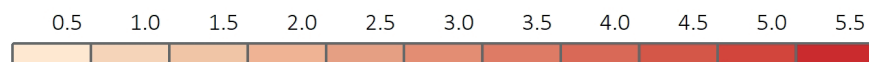


Fig. 4. Spatial distribution of ML WMAXSHEAR and windthrow events in the forest zone of the ER and Siberia: a) mean values for the summer seasons in 2001-2020; b) number of days with supercritical values

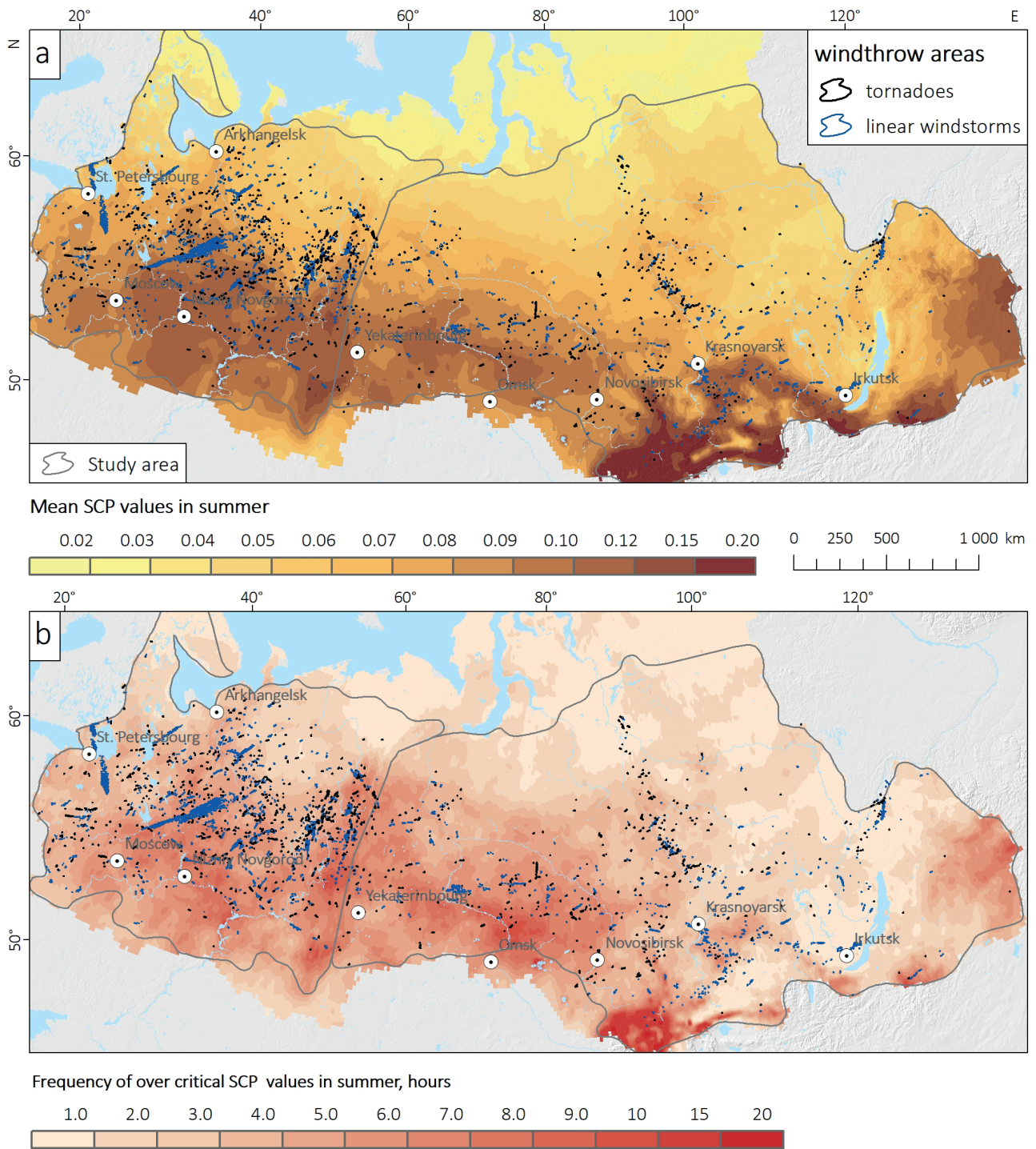


Fig. 5. Spatial distribution of SCP and windthrow events in the forest zone of the ER and Siberia: a) mean values for the summer seasons in 2001-2020; b) number of days with supercritical values

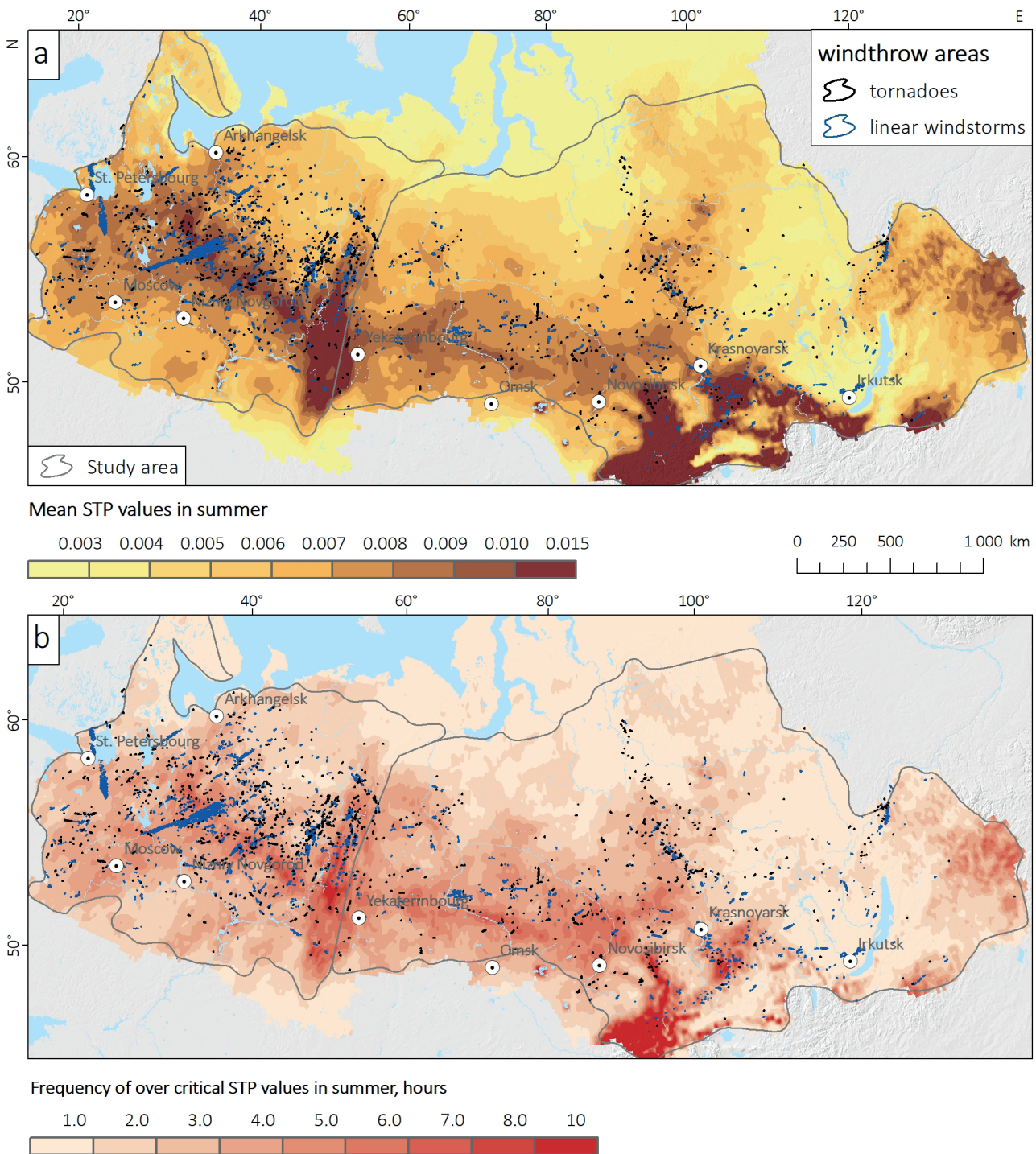


Fig. 6. Spatial distribution of STP and windthrow events in the forest zone of the ER and Siberia: a) mean values for the summer seasons in 2001-2020; b) number of days with supercritical values

weak relationship with the variability of DLS with several coincident maxima and minima, and the corresponding correlation is much weaker than for SCP and STP.

Additionally, convective parameters did not correlate with windthrow days in the ER or Siberia. The strong dependence of the number of days with windthrow events on the accuracy of windthrow date determination explains this. This accuracy increases continuously from 2001 to 2020 due to the opening of additional data sources such as Sentinel-2 satellite images, storm reports in social networks, etc. This issue is discussed in more detail in [Shikhov et al., 2020]. Therefore, the number of days with windthrow events is not very meaningful in the context of the present study.

DISCUSSION AND CONCLUSION

This study presents the results of the coupled analysis of three datasets characterizing windthrow events caused by convective windstorms and tornadoes in the forest zone of the ER and Siberia (1), the values of convective atmospheric parameters as predictors of the occurrence of such hazardous wind events, calculated from the ERA5 reanalysis data (2), and the lightning density from the WWLLN dataset (3). Empirical relationships between these datasets in space and in time (correlation of inter-annual variability) are considered.

It is found that the spatial distribution of windthrow has a statistically significant correlation with the spatial distribution of convective parameters ML CAPE, ML WMAXSHEAR, STP, and SCP both in the ER and in Siberia.

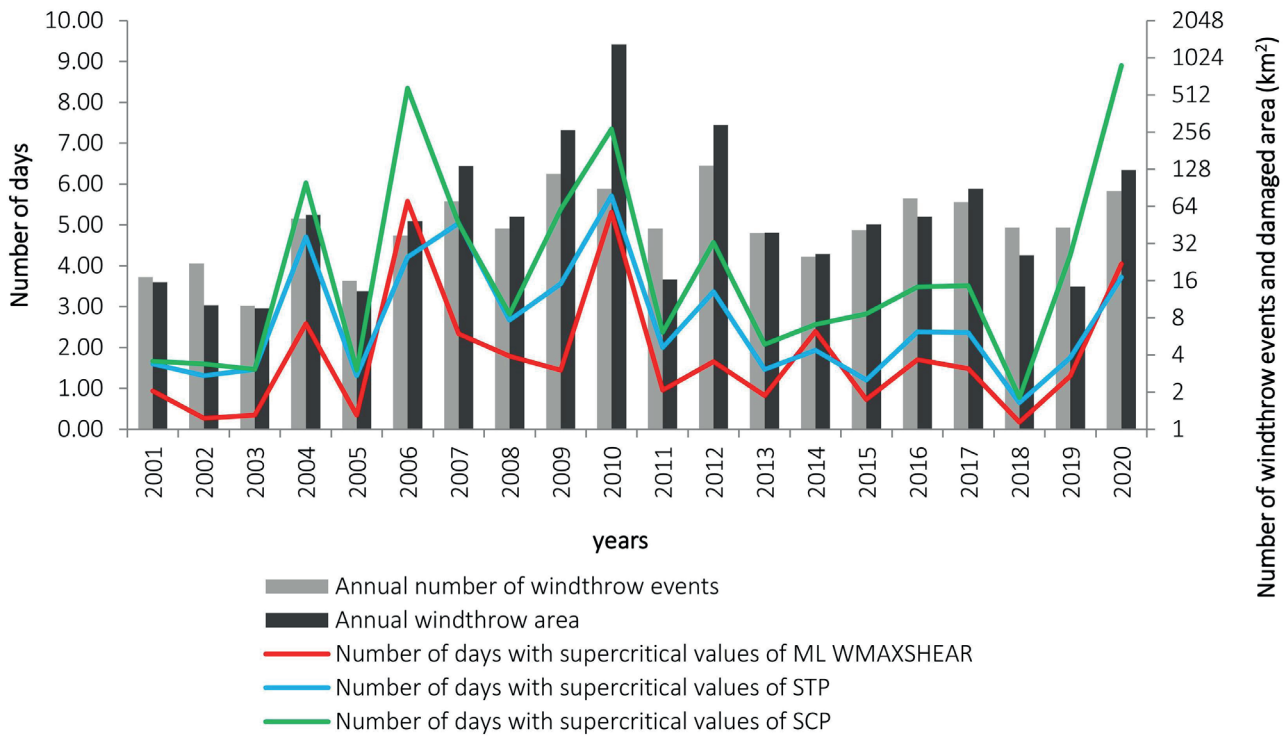


Fig. 7. Interannual variability of windthrow characteristics and the number of days with supercritical values of convective variables in the forest zone of the ER in 2001-2020

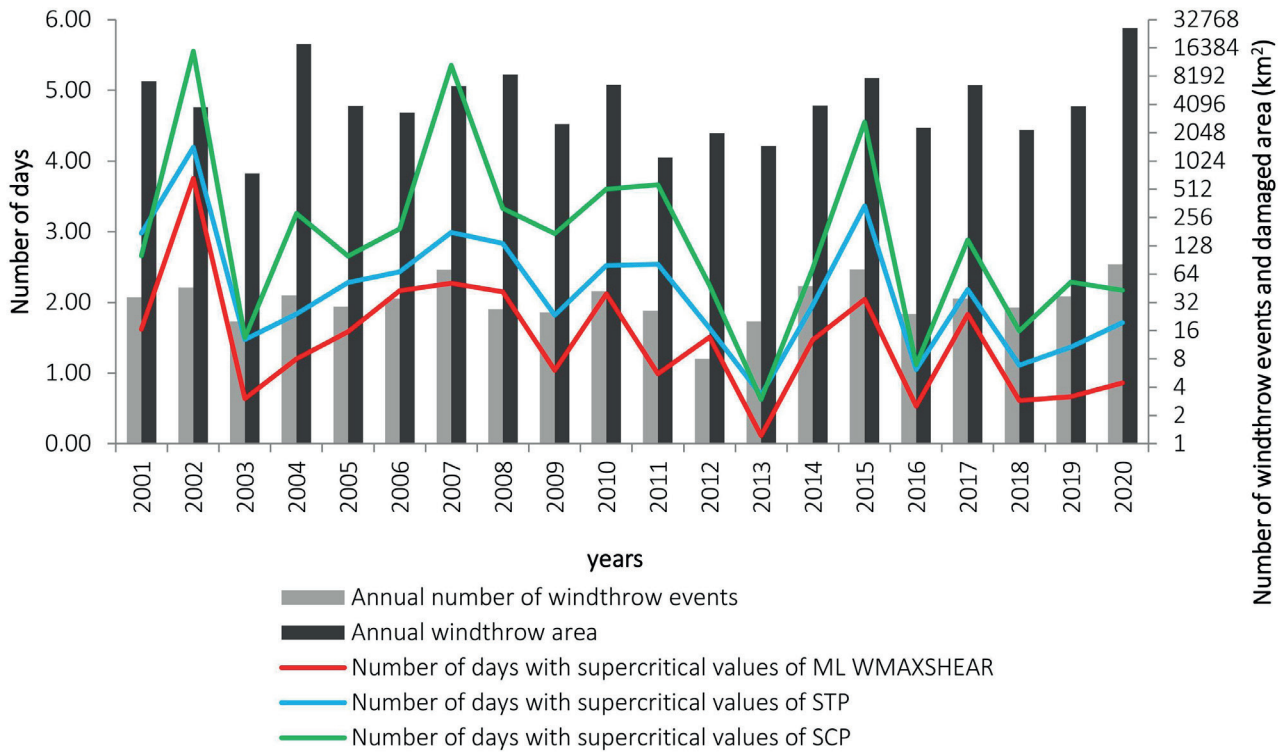


Fig. 8. Interannual variability of windthrow characteristics and the number of days with supercritical values of convective variables in the forest zone of Siberia in 2001-2020

Table 3. Spearman (numerator) and Pearson (denominator) correlation coefficients of the annual number of windthrow events and the damaged area with the convective parameters' values averaged over the summer months of each year. Underlined text indicates statistically significant coefficients

Region	Windthrow characteristics	ML WMAXSHEAR			SCP			STP			ML CAPE			DLS		
		Mean	N_{crit}	N_{90p}	Mean	N_{crit}	N_{90p}	Mean	N_{crit}	N_{90p}	Mean	N_{crit}	N_{90p}	Mean	N_{crit}	N_{90p}
ER	Number of events	0.41/ 0.42	0.49/ 0.34	0.47/ 0.13	0.61/ 0.59	0.69/ 0.55	0.49/ 0.41	0.65/ 0.61	0.64/ 0.58	0.47/ 0.13	-0.13/ -0.06	0.02/ 0.03	-0.18/ 0.13	0.57/ 0.49	0.48/ 0.31	0.45/ 0.23
	Number of days	0.09/ 0.72	0.27/ 0.56	0.33/ 0.27	0.33/ 0.70	0.49/ 0.46	0.39/ 0.25	0.30/ 0.56	0.33/ 0.62	0.33/ 0.27	-0.30/ 0.50	-0.15/ 0.69	-0.33/ 0.84	0.57/ 0.44	0.63/ 0.33	0.65/ 0.40
	Area	0.57/ 0.32	0.69/ 0.43	0.63/ 0.28	0.79/ 0.47	0.79/ 0.52	0.59/ 0.42	0.80/ 0.38	0.78/ 0.46	0.63/ 0.28	0.13/ -0.10	0.30/ 0.04	0.11/ 0.24	0.47/ 0.55	0.35/ 0.54	0.32/ 0.58
Siberia	Number of events	0.40/ 0.24	0.48/ 0.34	0.38/ 0.25	0.62/ 0.51	0.51/ 0.52	0.60/ 0.43	0.33/ 0.42	0.32/ 0.44	0.76/ 0.25	-0.15/ -0.03	0.20/ -0.10	0.07/ 0.27	0.43/ 0.32	0.56/ 0.45	0.46/ 0.43
	Number of days	-0.16/ 0.06	-0.01/ 0.04	-0.11/ -0.05	0.11/ 0.23	0.07/ 0.12	0.24/ -0.03	-0.22/ 0.18	-0.26/ 0.09	0.30/ -0.05	-0.28/ -0.15	-0.26/ -0.10	0.13/ -0.09	0.13/ 0.18	0.20/ 0.21	0.20/ 0.19
	Area	0.44/ -0.21	0.47/ -0.19	0.31/ -0.27	0.60/ 0.09	0.40/ 0.05	0.34/ -0.08	0.56/ -0.04	0.46/ -0.1	0.31/ -0.27	-0.08/ -0.36	0.16/ -0.35	0.04/ -0.27	0.38/ 0.01	0.42/ 0.07	0.35/ 0.10

*Mean – mean value for June–August, N_{crit} – number of days with values above the critical level, N_{90p} – number of days with values above the 90th percentile from the sample [Chernokulsky et al. 2023]

This correlation is strongest for STP, whose highest values are observed in the central part of the forest zone both in the ER and in Siberia, close to the areas with the highest windthrow density. However, in Siberia these correlations are generally weaker than in the ER, since the values of the convective parameters, in contrast to the windthrow area, increase significantly in the mountains of southern Siberia. A similar effect, but to a lesser extent, occurs over the Ural Mountains.

There is also a strong correlation between the spatial distribution of windthrow and that of lightning density. The highest lightning density in the ER is observed in the central part of the forest zone, where windthrow events also occur regularly. Thus, STP and lightning density are the most informative variables for identifying the areas with the highest probability of convective storms and tornadoes capable of causing damage to forests. The highest values of other composite parameters, ML WMAXSHEAR and SCP, are observed in the southern part of the forest zone, which is less consistent with the distribution of windthrow events.

The interannual variability of the values of the convective parameters and the windthrow characteristics is found to co-occur, especially in the ER. The strongest correlation is found between the number of days with supercritical values of the STP and the number of windthrow events per season, which shows that the climatic characteristics of the STP can be considered as strong predictors of linear convective windstorms and tornadoes. About 37% of the interannual variability in the number of windthrow events can be explained by the variability in the SCP. It is also interesting to note that the interannual variability of ML CAPE has no correlation with windthrow characteristics, while such correlation is statistically significant for DLS. Thus, the number of windthrow events and the damaged area increased in those years when DLS values were higher than the average.

The identified empirical relationships have a number of limitations or substantial limitations. Firstly, only climatic factors of windthrow occurrence were considered in this study (and only those associated with convective storms), while the level of vulnerability is assumed to be

the same for different forest species. Further analysis of the association between windthrow and forest stand characteristics such as species composition, age, and tree height may be useful since these characteristics are also important for windthrow risk [Suvanto et al. 2019]. Second, the relatively short time series of windthrow data results in an insufficient sample size of large windthrow events. The distribution of windthrow area is known to be left-skewed, similar to other forest disturbances [Baumann et al. 2014; Senf and Seidl 2021a]. Thus, among 1816 windthrow events considered, the largest 1% of them is responsible for about 50% of the total damaged area. These large events have a key influence on the spatial distribution of windthrow damage in the entire forest zone of Russia. Thus, the patterns of their spatial distribution and their relationship with convective parameters may change significantly with the increasing length of the observation series. Thirdly, the spatial distribution of the climatic characteristics of convective parameters is strongly influenced by the terrain. If mountainous areas were excluded from the analysis, the results would change significantly, especially in Siberia, but the sample of windthrow events would also be greatly reduced. Finally, the windthrow dataset used has several limitations, which are discussed in [Shikhov et al. 2020]. In particular, the windthrow area may be underestimated in deciduous forests, which are widespread in the southern part of the ER forest zone and in Western Siberia.

Despite these limitations, the results may be of interest both for the climatology of severe convective storms and for forestry and sustainable forest management. For example, the first coupled analysis of the windthrow dataset with climatic characteristics of convective variables for a 20-year period showed different degrees of agreement for different variables. STP and lightning density were found to be the most informative predictors of the spatial distribution of severe convective wind events causing forest damage. Together with other predictors of forest vulnerability to wind, they can be used to estimate windthrow risk in the Russian forest zone. However, such estimates are best interpreted in the long term (several decades) in order to reduce the impact of individual major storm events.

A similar approach can be used to predict windthrow risk in future climates, as convective variables can be calculated from CMIP6 model outputs [Lepore et al. 2021]. As climate warming leads to an increase in severe thunderstorm environments [Diffenbaugh et al. 2013;

Chernokulsky et al. 2022], the wind-related forest damage may also increase. An increased risk of windthrow should be taken into account for sustainable forest management and long-term forest development planning. ■

REFERENCES

- Bartalev S.A., Egorov V.A., Zharko V.O., Lupyán E.A., Plotnikov D.E., Khvostikov S.A., Shabanov N.V. (2016). Satellite-based mapping of the vegetation cover of Russia Moscow, Space Research Institute of RAS, 208 p. (in Russian).
- Baumann M., Ozdogan M., Wolter P.T., Krylov A.M., Vladimirova N.A., and Radeloff V.C. (2014). Landsat remote sensing of forest windfall disturbance. *Remote Sensing of Environment*, 143, 171-179, DOI: 10.1016/j.rse.2013.12.020.
- Brooks H.E., Doswell III C.A., Zhang X., Chernokulsky A., Tochimoto E., Hanstrum B., Nascimento E., Sills D., Antonescu B., and Barrett B. (2019). A century of progress in severe convective storm research and forecasting. in: *A Century of Progress in Atmospheric and Related Sciences: Celebrating the American Meteorological Society Centennial*. AMS, Meteorol. Monographs, Chapter 18. P.18.1–18.41.
- Chernokulsky A.V., Eliseev A.V., Kozlov F.A., Korshunova N.N., Kurgansky M.V., Mokhov I.I., Semenov V.A., Shvets' N.V., Shikhov A.N., and Yarinich Y.I. (2022). Atmospheric severe convective events in Russia: Changes observed from different data. *Russian Meteorology and Hydrology*, 47(5), 343-354, DOI: 10.3103/S106837392205003X.
- Chernokulsky A.V., Kurgansky M.V., Mokhov I.I., Shikhov A.N., Azhigov I.O., Selezneva E.V., Zakharchenko D.I., Antonescu B., and Kuhne T. (2021). Tornadoes in the Russian Regions. *Russian Meteorology and Hydrology*, 46(2), 69-82. DOI: 10.3103/S1068373921020023.
- Chernokulsky A., Shikhov A., Bykov A., Kalinin N., Kurgansky M., Sherstyukov B., and Yarinich Y. (2022). Diagnosis and modelling of two destructive derecho events in European Russia in the summer of 2010. *Atmospheric Research*, 267, 105928, DOI: 10.1016/j.atmosres.2021.105928.
- Chernokulsky A., Shikhov A., Yarinich Yu., and Sprygin A. (2023). An Empirical Relationship among Characteristics of Severe Convective Storms, Their Cloud-Top Properties and Environmental Parameters in Northern Eurasia. *Atmosphere*, 14(1), 174, DOI: 10.3390/atmos14010174.
- Christian H.J. (2003). Global frequency and distribution of lightning as observed from space by the Optical Transient Detector. *Journal of Geophysical Research*, 108, 4005, DOI: 10.1029/2002jd002347.
- Diffenbaugh N.S., Scherer M., and Trapp R.J. (2013). Robust increases in severe thunderstorm environments in response to greenhouse forcing. *Proceedings of the National Academy of Sciences of the USA*, 110, 16361–16366, DOI: 10.1073/pnas.1307758110.
- Dobbertin M. (2002). Influence of stand structure, site factors on wind damage comparing the storms Vivian and Lothar. *Forest, Snow and Landscape Research*, 77(1-2), 187–205.
- Forzieri G. et al. (2020). A spatially explicit database of wind disturbances in European forests over the period 2000–2018. *Earth System Science Data*, 12, 257-276, DOI: 10.5194/essd-12-257-2020.
- Gardiner B., Byrne K., Hale S., Kamimura K., Mitchell S. J., Peltola H., and Ruel J-C. (2008). A review of mechanistic modelling of wind damage risk to forests. *Forestry*, 81(3), 447-463, DOI: 10.1093/forestry/cpn022.
- Groenemeijer P., Púčik T., Holzer A.M., Antonescu B., Riemann-Campe K., Schultz D.M., Kühne T., Feuerstein B., Brooks H.E., and Doswell C.A. (2017). Severe convective storms in Europe: Ten years of research and education at the European Severe Storms Laboratory. *Bulletin of the American Meteorological Society*, 98, 2641-2651. DOI:10.1175/BAMS-D-16-0067.1.
- Hersbach H. et al. (2020). The ERA5 global reanalysis. *Quarterly Journal of the Royal Meteorological Society*, 146, 1999-2049, DOI: 10.1002/qj.3803.
- Holzworth R.H., Brundell J.B., McCarthy M.P., Jacobson A.R., Rodger C.J., and Anderson T.S. (2021). Lightning in the Arctic. *Geophysical Research Letters*, 48, e2020GL091366, DOI: 10.1029/2020GL091366.
- Kaplan J.O. and Lau K.H.-K. (2021). The WGLC global gridded lightning climatology and time series. *Earth System Science Data*, 13, 3219-3237, DOI: 10.5194/essd-13-3219-2021.
- Laapas M., Lehtonen I., Venäläinen A., and Peltola H. (2019). 10-year return levels of maximum wind speeds under frozen and unfrozen soil forest conditions in Finland. *Climate*, 7, 62, DOI: 10.3390/cli7050062.
- Laapas M., Suvanto S., Peltoniemi M., and Venäläinen A. (2023). Combining interpolated maximum wind gust speed and forest vulnerability for rapid post-storm mapping of potential forest damage areas in Finland, *Forestry*. *International Journal of Forest Research*, 96(5), 690-704, DOI: 10.1093/forestry/cpad005.
- Lepore C., Abernathey R., Henderson N., Allen J.T., and Tippet M.K. (2021). Future global convective environments in CMIP6 models. *Earth's Future*, 9, e2021EF002277, DOI: 10.1029/2021EF002277.
- Panferov O., Doering C., Rauch E., Sogachev A., and Ahrends B. (2009). Feedbacks of windthrow for Norway spruce and Scots pine stands under changing climate. *Environmental Research Letters*, 4, 045002, DOI 10.1088/1748-9326/4/4/045002.
- Panferov O. and Sogachev A. (2008). Influence of gap size on wind damage variables in a forest. *Agricultural and Forest Meteorology*, 148(11), 1869-1881, DOI: 10.1016/j.agrformet.2008.06.012.
- Peltola H., Kellomäki S., Väisänen H., and Ikonen V.P. (1999). A mechanistic model for assessing the risk of wind, snow damage to single trees and stands of Scots pine, Norway spruce and birch. *Canadian Journal of Forest Research*, 29(6), 647-661, DOI: 10.1139/x99-029.
- Rasmussen E.N. and Blanchard D.O. (1998). A Baseline Climatology of Sounding-Derived Supercell and Tornado Forecast Parameters. *Weather and Forecasting*, 13, 1148-1164, DOI: 10.1175/1520-0434(1998)013<1148:ABCOSD>2.0.CO;2.
- Seidl R. et al. (2011). Modelling natural disturbances in forest ecosystems: A review. *Ecological Modelling*, 222(4), 903–924. DOI: 10.1016/j.ecolmodel.2010.09.040.
- Senf C. and Seidl R. (2021a). Mapping the forest disturbance regimes of Europe. *Nature Sustainability*, 4, 63-70, DOI: 10.1038/s41893-020-00609-y.
- Senf C. and Seidl R. (2021b). Storm and fire disturbances in Europe: Distribution and trends. *Global Change Biology*, 27, 3605-3619, DOI: 10.1111/gcb.15679.
- Shikhov A.N., Chernokulsky A.V., Azhigov I.O., and Semakina A.V. (2020). A satellite-derived database for stand-replacing windthrow events in boreal forests of European Russia in 1986–2017. *Earth System Science Data*, 12, 3489-3513, DOI: 10.5194/essd-12-3489-2020.
- Shikhov A.N., Chernokulsky A.V., Kalinin N.A., and Pyankov S.V. (2023). Windthrow events in the forest zone of Russia and the environments of their occurrence. Perm, Perm State University, 2023, 284 p. (in Russian).
- Shikhov A., Chernokulsky A., Kalinin N., Bykov A., and Pischalnikova E. (2021). Climatology and Formation Environments of Severe Convective Windstorms and Tornadoes in the Perm Region (Russia) in 1984–2020. *Atmosphere*, 12(11), 1407, DOI: 10.3390/atmos12111407.

Suvanto S., Peltoniemi M., Tuominen S., Strandström M., and Lehtonen A. (2019) High-resolution mapping of forest vulnerability to wind for disturbance-aware forestry. *Forest Ecology and Management*, 453, 117619, DOI: 10.1016/j.foreco.2019.117619.

Taszarek M., Brooks H.E., and Czernecki B. (2017). Sounding-derived parameters associated with convective hazards in Europe. *Monthly Weather Review*, 145, 1511-1528, DOI: 10.1175/MWR-D-16-0384.1.

Taszarek M., Groenemeijer P., Allen, J.T., Edwards R., Brooks H.E., Chmielewski V., and Enno S.E. (2020a). Severe convective storms across Europe and the United States. Part I: Climatology of lightning, large hail, severe wind, and tornadoes. *Journal of Climate*, 33, 10239-10261, DOI: 10.1175/JCLI-D-20-0345.1.

Taszarek M., Allen J.T., Púčik T., Hoogewind K.A., and Brooks H.E. (2020b). Severe convective storms across Europe and the United States. Part II: ERA5 environments associated with lightning, large hail, severe wind, and tornadoes. *Journal of Climate*, 33(24), 10263-10286, DOI: 10.1175/JCLI-D-20-0346.1.

Taszarek M., Czernecki B., and Szuster P. (2023). ThundeR – a rawinsonde package for processing convective parameters and visualizing atmospheric profiles, 11th European Conference on Severe Storms, Bucharest, Romania, 8–12 May 2023, ECSS2023-28, <https://doi.org/10.5194/ecss2023-28>.

Tarabukina L. and Kozlov V. (2020). Seasonal Variability of Lightning Activity in Yakutia in 2009–2019. *Atmosphere*, 11, 918. DOI: 10.3390/atmos11090918.

Thompson R.L., Edwards R., Hart J.A., Elmore K.L., and Markowski P. (2003). Close proximity soundings within supercell environments obtained from the Rapid Update Cycle. *Weather and Forecasting*, 18, 1243-1261, DOI: 10.1175/1520-0434(2003)018<1243:CPSWSE>2.0.CO;2.

Venäläinen A., Laapas M., Pirinen P., Horttanainen M., Hyvönen R., Lehtonen I., Junila P., Hou M., and Peltola H.M. (2017). Estimation of the high-resolution variability of extreme wind speeds for a better management of wind damage risks to forest-based bioeconomy. *Earth System Dynamics*, 8, 529-545, DOI: 10.5194/esd-8-529-2017.

Venäläinen A., Lehtonen I., Laapas M., Ruosteenoja K., Tikkanen O-P., Viiri H., Ikonen V.P., and Peltola H. (2020). Climate change induces multiple risks to boreal forests and forestry in Finland: A literature review. *Global Change Biology*, 26(8), 4178-4196, DOI: 10.1111/gcb.15183.

A REVIEW OF UPSCALING ALGORITHMS FOR FLOW DIRECTION RASTERS

Mikhail V. Uzhegov¹, Andrey L. Entin^{1*}

¹ Department of Cartography and Geoinformatics, Faculty of Geography, Lomonosov Moscow State University, Leninskie Gory 1, Moscow, 119991, Russia

*Corresponding author: aentin@geogr.msu.ru

Received: November 17th 2024 / Accepted: December 11th 2024 / Published: March 31st 2025

<https://doi.org/10.24057/2071-9388-2025-3737>

ABSTRACT. Modern Earth system models and global hydrological models require input data in the form of flow direction grids (rasters) with a relatively low resolution. Typical resolution for these models is about 0.5–1°. At high resolution, up to 1 km cell size, flow direction grids are usually generated from digital elevation models (DEMs), but for coarse-resolution grids, more specialized approaches need to be used. In this paper we review upscaling methods for flow direction grids, including grid-based flow tracing, catchment area aggregation and vector network processing. We also indicate methods that have been used to create publicly available datasets in global coverage (DRT and IHU), and provide links to these datasets. The paper also considers methods for estimating the result of flow direction generation on coarse-resolution grids, as well as the results of applying these estimates to existing methods. It is shown that the task of estimating the result requires further development, including the development of new estimation methods and comparative comparison of the most modern upscaling approaches.

KEYWORDS: flow direction, upscaling, generalization, Earth system models

CITATION: Uzhegov M. V., Entin A. L. (2025). A Review Of Upscaling Algorithms For Flow Direction Rasters. *Geography, Environment, Sustainability*, 89-96

<https://doi.org/10.24057/2071-9388-2025-3737>

ACKNOWLEDGEMENTS: The work is supported by the grant of the Russian Science Foundation, project no. 23-27-00232.

Conflict of interests: The authors reported no potential conflict of interest.

INTRODUCTION

The shape of the Earth's surface can be shown by a regular grid, which can be rectangular, triangular, hexagonal, or any other shape. Flow direction is a morphometric parameter that describes this shape. For a grid cell, flow direction is a value representing the direction (or multiple directions) water will flow out of the cell. There are different schemes (algorithm) of flow direction assignment; they can route flow from the cell to the one (D8 (O'Callaghan and Mark 1984)), or many (Dinf (Tarboton 1997), MFD (Freeman 1991; Quinn et al. 1991), or one of its derivatives (Qin et al. 2017)). Depending on the applied algorithm, flow direction could be presented as actual azimuth (e.g. for Dinf) or a coded value substituting one or many of the allowed directions. For example, the output of the D8 flow direction computation is presented as integer values in the domain $\{0; 2^n, n \in [0, 7]\}$, where each code stands for a direction multiple of 45°.

Global Earth system models, macroscale hydrologic models, and many other applications require river networks at coarse resolutions. These models typically use gridded data as an input, so river networks are usually formalized as flow directions. Typical resolution for macroscale land surface models ranges from 0.5° to 1° (Decharme et al. 2010; Oki and Sud 1998; Pappenberger et al. 2010). The same resolution is applied in global hydrological models (Sood and Smakhtin 2015), although there are more recent examples of direct implementation of a finer resolution river network data (Lin et al. 2019).

The concept of flow directions was initially introduced in morphometric analysis of digital elevation models (DEMs) (Jenson and Domingue 1988; O'Callaghan and Mark 1984). According to the D8 algorithm, the flow direction of the cell is the direction of the steepest slope line between the central cell and the one of its 8 neighbors. This modeling principle only considers the movement of water down the slope due to gravity. If this principle is applied to a global scale and coarse grid resolutions, it can lead to a substantial error because the typical gradient between cells is relatively lower than in fine resolutions, so the 'formally' calculated slope between neighboring cells will not always reflect real flow behavior (Döll and Lehner 2002; Fekete et al. 2001; O'Donnell et al. 1999; Vörösmarty et al., 2000). However, relatively simple methods of aggregating more detailed (fine-resolution) data, such as calculating mean or modal value, are not suitable for flow directions because they are strictly related to the grid geometry (Decharme et al. 2010). Therefore, several upscaling methods were developed to produce flow direction coverage on coarse-resolution grids.

It should be noted that different research fields have opposite interpretations of the terms 'upscaling' and 'downscaling'. In Earth sciences, downscaling is usually understood as increasing spatial resolution, i.e. decreasing cell size, while upscaling means decreasing spatial resolution and increasing cell size (Eilander et al. 2021; Peng et al. 2017; Wu et al. 2011). At the same time, in the practice of digital image processing, upscaling is a synonym for increasing image resolution (Panda and Meher 2024). In this paper, we follow the tradition established in the

Earth sciences and understand upscaling as the production of coarse-resolution grids based on more detailed data.

The literature presents many approaches to creating low spatial resolution flow direction grids. These approaches could be divided into the following groups:

1) manual flow direction assignment based on map image analysis (e.g. Miller et al. 1994);

2) resampling high-resolution flow direction grids and/or their derivatives to a coarser resolution, often with additional coverages (e.g. Fekete et al. 2001; O'Donnell et al. 1999; Reed 2003);

3) tracing vector stream network to derive raster flow direction coverage (Mayorga et al. 2005; Olivera and Raina 2003).

Manual data processing is very labor-intensive, and the use of methods based on the vector representation of the hydrographic network is limited by the availability of initial global coverage data. Therefore, in this paper, we will focus on methods for the second and third groups.

FLOW DIRECTION UPSCALING ALGORITHMS

Grid-based tracing

All algorithms for generalizing flow directions by tracing flow on fine-resolution grids are based on similar principles. Firstly, it is implicitly assumed that the geometry of the target grid is aligned to the geometry of the source grid. The target grid's cell size is an integer multiple of the source grid's cell size, and source and target grids' reference points, which are usually in the lower and left corners, are either the same or are moved by an integer number of the source grid cell size. In most cases, both grids are constructed in a geographic coordinate system (latitude-longitude), although there are exceptions to this rule. Then, based on the flow direction raster, we obtain a catchment area (contributing area, upstream area) raster before performing the actual upscaling procedure. Finally, the procedure is usually based on overlaying a source (fine-resolution) grid and a target (coarse-resolution) grid; for each target grid cell, an 'outlet' source grid cell is determined. This 'outlet' cell has the highest catchment area value among other fine cells within the coarse cell; it is also often (but not always) adjacent to the edge of the coarse cell. The outlet is later used as a starting point to trace flow downstream along the initial (fine-resolution) drainage graph. Tracing is performed until a certain condition is met. The resulting flow direction for the current target cell is determined from the position of the cell where tracing was stopped.

It should also be noted that a certain terminology has developed in the works devoted to this problem. In particular, the term "cell" usually refers to a coarse-resolution grid cell, while fine-resolution grid cells are denoted as "pixels". Hereinafter we, while possible, do not follow this terminology and always use 'coarse cell' and 'fine cell', respectively.

One of the first implementations of the principle described above was presented in (Döll and Lehner 2002). First, it finds outlet cells for each target cell. Then, it simply assigns flow direction for the target cell according to the direction of the outlet cell. This procedure itself leads to an uneven distribution of resulting flow directions: cardinal directions (north, east, south, and west) prevail over diagonal directions (northeast, southeast, southwest, and northwest). In the work of Döll and Lehner (2002), this procedure was used as a first step in an iterative procedure, which included manual review and correction. It is also stated that the 'automatic' part of this method is used in the mRM routing model (Thober et al. 2019).

A more complicated technique was presented earlier by O'Donnell et al. (1999). They expand the concept of corner cells, including not only a fine-resolution grid cell located exactly at the corner of a coarse-resolution target cell but also its fine-resolution neighbors. The exact number of neighbors is a parameter of the algorithm. For non-corner cells, the procedure is the same; for corner cells, the flow is traced within a 3x3 vicinity of the central target cell, and the water is routed to the coarse cell when the tracing is stopped.

The COTAT method (Cell Outlet Tracing with an Area Threshold) applies tracing of the source flow directions from all outlet cells (Reed 2003). It also utilizes different stopping conditions. For each coarse grid cell, the procedure starts with its fine-resolution outlet; the catchment area value of the outlet is stored for further processing. Next, flow is traced from each outlet cell along the fine-resolution grid. During tracing, the following conditions are checked: 1) catchment area difference between the current source grid cell and the outlet cell should be lower than the user-defined threshold; 2) the current source grid cell should be within the 3x3 vicinity of the central target cell. If one of the conditions is violated, tracing stops, and the coarse cell where the tracing ended is identified. The identified coarse cell receives the central coarse grid cell direction. If the outlet cell has the highest catchment area value among all its fine-resolution neighbors, it practically means that this cell represents a local sink, and flow direction for the target cell is set to zero, which stands for no outward flow. The basic principle of the COTAT procedure is shown in Fig. 1.

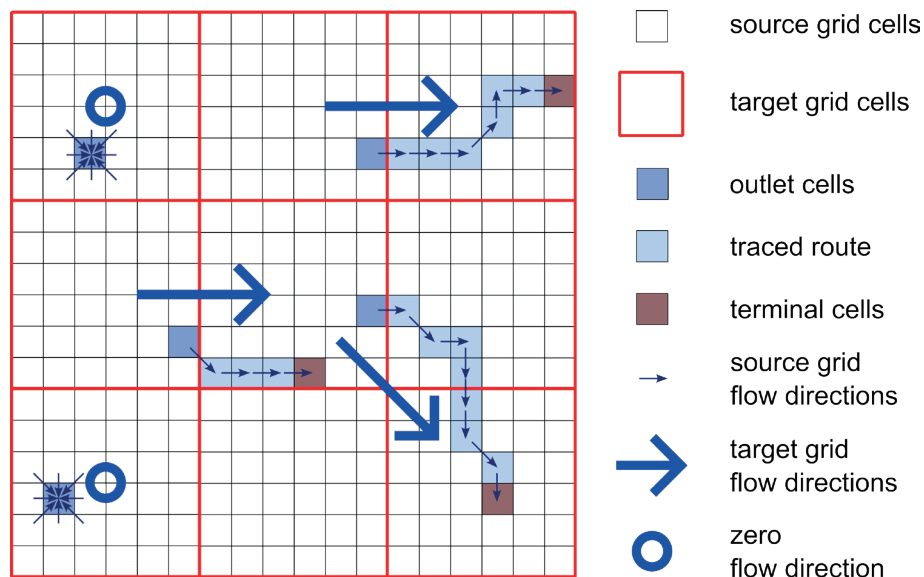


Fig. 1. COTAT flow tracing and upscaling principle

Upon completion of the routing, COTAT implements a post-processing procedure to prevent instances of crossing paths. When the flow directions of adjacent coarse cells intersect, a special reclassification table reassigns one of them to the non-crossing pattern.

An upgraded version of COTAT was presented in (Paz et al. 2006); this method is referred to as COTAT+ (Davies and Bell 2009) or the effective area method (EAM) (Eilander et al. 2021). This modification has three differences from the original COTAT procedure. First, it introduces one more limiting parameter: minimum distance along the flow path. If the threshold catchment area difference is exceeded, but the distance of the constructed path is less than the assigned minimum, the tracing continues until the minimum is reached. The second modification affects cases when no valid outlet fine-resolution cell could be defined; in this case, the last visited cell is assigned as the draining cell. The third modification is introduced for crossing flow directions: instead of a reclassification table, a more sophisticated decision rule is used. According to the authors (Paz et al. 2006), these modifications improve flow direction assignment over flat areas with large parallel flows, e.g., in the Amazon River basin.

The next method is FLOW, proposed by Yamazaki et al. (2009). In this method, flow is traced down from the outlet cell until the next outlet cell (of the neighbor target cell) is reached, and the length of the flow path is measured. If the length is lower than the user-defined threshold, the second outlet cell is rejected as an outlet cell. If so, the outlet cell for the neighbor target cell is reassigned: a new outlet is selected among the cells allocated on the border of a (neighbor) target cell, excluding the one previously rejected. The procedure repeats until the flow path length becomes longer than the threshold value for each target grid cell. After that, flow directions of a coarse-resolution grid are assigned following the constructed paths. A distinctive feature of the method is that the resulting flow directions do not follow the D8 pattern. Instead, flow from the "central" target cell may be directed to a cell that does not belong to its immediate neighborhood. According to Yamazaki et al. (2009), this allows for more realistic flow patterns and better catchment area matching between source and target datasets.

The method developed by Lucas-Picher et al. (2003) for the Canadian Regional Climate Model (CRCM) is significantly different from the above methods because it does not require grid alignment and is specifically designed for the situation where the coordinate systems of the source and

target datasets are not coincident. The method consists of the following steps: 1) derive spatial extent of the target grid cell in the domain of the source grid; 2) select all the source grid cells which intersect the computed extent; 3) from the cells selected in step 2, select cells whose flow direction is oriented outside the extent; 4) from the cells selected in step 3, find a cell with the highest catchment area value; 5) identify the coarse grid cell that covers the fine cell selected in step 4; 6) assign flow direction from the central coarse cell to the coarse cell identified in step 5. The process is shown in Fig. 2.

The Dominant River Tracing (DRT) method was proposed by Wu et al. (2011). It also relies on tracing the flow over a regular grid, but this is done in a specially defined hierarchical order. DRT applies the concept of the longest effective dominant river (LEDR) segment—a river segment that dominates the local drainage of the cell. For a coarse cell, the LEDR is identified as the river segment that has a relatively large (but not necessarily the largest) catchment area value compared to other river segments in this cell and is longer than a minimum length threshold set by the user within the cell. The method calculates flow directions consequently, analyzing one basin at a time. The basins are sorted and ordered according to their respective catchment areas.

DRT starts by finding the dominant basin and river of the study area and assigns flow directions for cells along dominant rivers beginning from headwater cells to basin, also called sink cells. Subdominant rivers and tributary flow paths are then identified and ordered according to their respective catchment areas. The priority for assigning flow directions is assigned to successively higher-order rivers until all cells in the most dominant basin have assigned flow directions. The DRT then selects progressively smaller, less dominant basins and rivers and assigns flow directions in a similar manner until all cells in the given study area have been assigned flow directions.

The assignment of the flow direction itself for a cell in the DRT is performed as follows. First, the cell is divided into eight $\pi/4$ sectors radiating from the cell center. Then, an LEDR from the cell is traced downstream for a specified length (0.6 of cell size for cardinal sectors and 0.8 of cell size for diagonal sectors). The cell where the tracing stopped receives the flow direction from the target cell. DRT also applies two supplementary procedures to preserve subdominant rivers and sinuous flow paths.

DRT was applied to create a set of global coverages of flow directions and related parameters at 2°, 1°, 30' (1/2°),

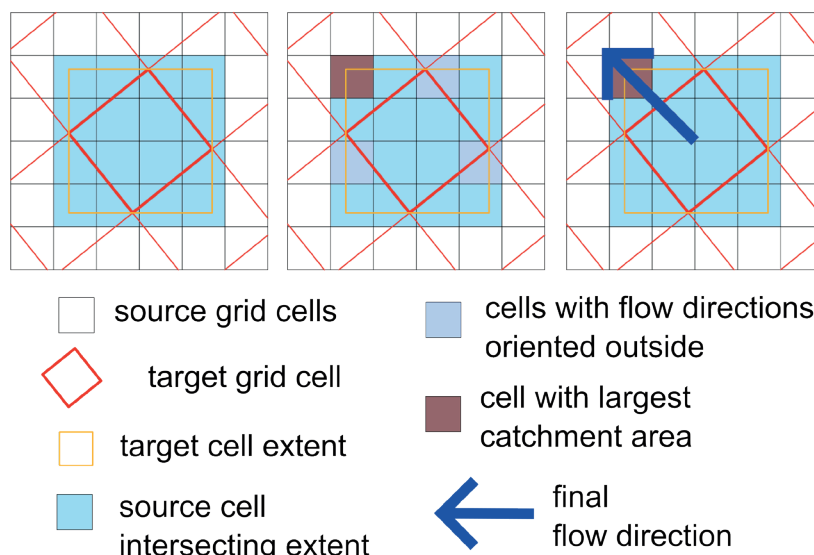


Fig. 2. Upscaling procedure proposed by (Lucas-Picher et al. 2003)

15'(1/4°), 7.5' (1/8°), 3.75' (1/16°) resolutions (Wu et al. 2012)¹. HYDRO1K² and HydroSHEDS (Lehner et al. 2008) were used as input data for these coverages..

Another upscaling procedure based on flow tracing was presented in (Eilander et al. 2021). The method, called Iterative Hydrography Upscaling (IHU), consists of four consecutive stages (iterations). The first stage involves computing initial flow directions for coarse grid cells. The following stages are needed to correct initial directions to fix errors (stage 2), optimize in-between outlet distances (stage 3), and minimize the error caused by erroneous flow directions (stage 4). At the first stage, like all methods listed above, IHU is based on identifying outlet fine-resolution cells for each coarse-resolution cell and tracing flow downstream; but unlike the above approaches, here the output cell is not located at the edge of the target cell, but rather in the inner region. The inner region is defined as a rounded rectangle excluding edge cells and some corner cells adjacent to them. The flow is traced from the outlet cell down to the next outlet cell. The second step is repairing erroneous flow directions. The authors recognize direction as erroneous if the first outlet cell downstream (from fine-resolution grid) is not coincident with the coarse-resolution downstream cell. An iterative procedure identifies and assigns potential alternatives at this step. Not all erroneous situations could be repaired; if there are any, they are further addressed in stage 4. The third stage aims to optimize the distance between outlet pixels, measured along the fine-resolution flow directions. If this distance is short, one of the outlet pixels can potentially be removed in favor of another river segment within the same cell. The fourth stage addresses erroneous directions that were not corrected at stage 2; for these cells, tracing is performed again but now flow path length is considered. The IHU procedure was implemented in the open-source PyFlowDir package³. The authors also prepared a generalized datasets based on MERIT Hydro data (Yamazaki et al. 2019) with the resolution of 30", 5' and 15'; these datasets are called MERIT Hydro IHU⁴.

Deriving flow directions from catchment area grids

Two methods allow producing coarse-resolution flow direction grids directly from fine-resolution catchment area grids without flow tracing. These methods are NSA (Network Scaling Algorithm) and DMM (Double Maximum

Method). Both methods have the same requirements for source and target grids as flow tracing methods: the geometry of grids should be aligned, and the cell size of the target grid should be an integer multiple of the cell size of the source grid.

The NSA proposed by Fekete et al. (2001) works as follows. First, it aggregates (summarizes) catchment area values from a source grid to the target grid. Then, the flow direction for each target grid cell is assigned to the neighbor cell with the largest aggregated catchment area value. The procedure is shown in Fig. 3.

The DMM procedure proposed by Olivera et al. (2002) is more complicated. To implement it, two grids with coarse spatial resolution are constructed (primary and auxiliary). The auxiliary grid's origin is shifted relative to the origin of the primary grid by a half of the coarse grid cell size. First, an outlet (fine) cell is identified for a cell of the primary grid. Second, an auxiliary coarse cell is identified for the outlet cell found in step 1. Third, an outlet cell is found for the auxiliary grid cell identified in step 2. Fourth, a primary grid cell is identified for the outlet found in step 3. This primary grid cell is a target cell for the 'starting' primary grid cell, which was processed in step 1. The final flow direction is assigned from the 'starting' cell to the 'target' cell. An overview of the process is shown in Fig. 4.

Tracing flow along vector hydrographic network

Another two methods were proposed to derive flow directions from a vector representation of the hydrographic network. Network Tracing Method (NTM) performs an overlay between vector streamlines and the target grid and traces the flow along vector lines (Olivera and Raina 2003). The procedure begins with a preprocessing step: a geometric intersection of the input river network lines graph with the boundaries of the target grid cells is performed. As a result, the vector network is divided into separate segments; each segment lies entirely within one cell. Then, endpoints of the lines lying on the cell boundaries are identified. After that, for each cell, its output point is determined as one of the previously identified endpoints of the lines through which rivers leave the cell, which has the greatest flow path length. The flow path length of a point is determined as the longest possible path upwards along the graph of the hydrographic network. The algorithm then traces network down along the graph,

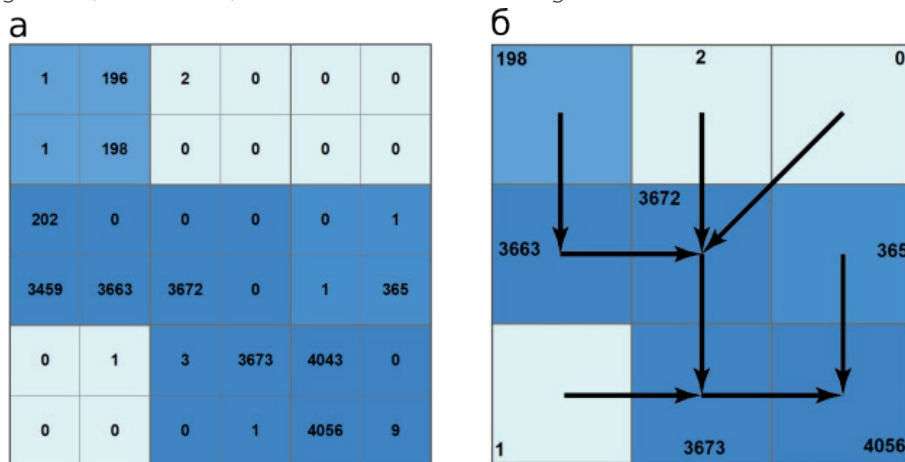


Fig. 3. The principle of the Network Scaling Algorithm (NSA). Numbers are catchment area values

¹ Materials are available at <http://files.ntsug.umt.edu/data/DRT/>

² HYDRO1K | The Long Term Archive [online]. Available at: <https://www.usgs.gov/centers/eros/science/usgs-eros-archive-digital-elevation-hydro1k>

³ The package is available at <https://github.com/Deltares/pyflwdir>

⁴ Datasets are available at <https://zenodo.org/records/5166932>

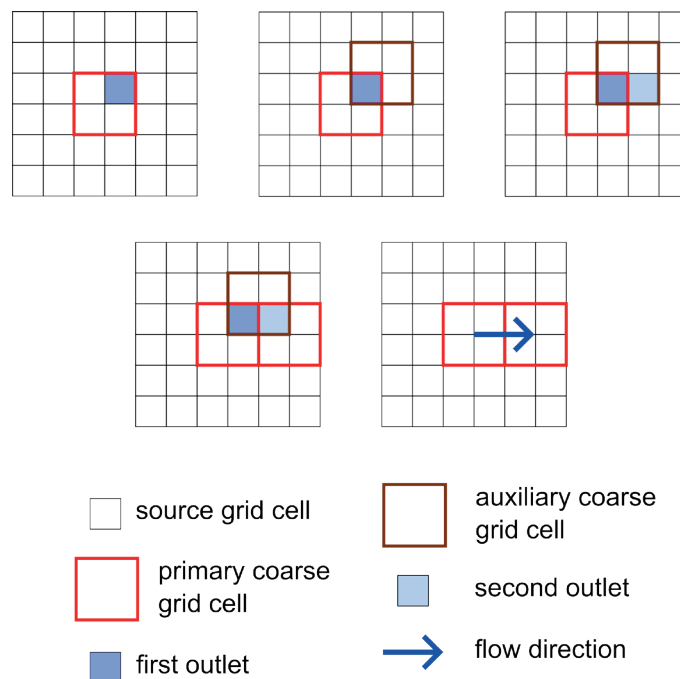


Fig. 4. The principle of Double Maximum Method (DMM)

starting from the output point. The conditions for stopping tracing are reaching a threshold of length increase, crossing more than two coarse cells, and falling beyond the 3×3 neighborhood of the cell. Comparing the increment of the upstream flow length with the threshold value when choosing the flow direction allows skipping cells during tracing, through which the flow passes too short a path. This parameter is also used to balance orthogonal and diagonal flow directions. The higher this threshold, the more often the algorithm will choose diagonal directions over orthogonal ones.

An important drawback of NTM is high requirements to the input data. To obtain a correct result, the initial hydrographic network graph must be planar, have a tree structure, and have all its edges oriented strictly downstream (Olivera and Raina 2003). To satisfy the planarity condition, all rivers must be divided into separate segments at confluence points. The tree structure implies that bifurcation is forbidden. The orientation of the vector lines downstream is important since it determines the scanning direction along the graph. In addition, the density of the initial network is also important for the NTM algorithm: it must be dense enough for modeling at a desired resolution. To satisfy this condition, at least one network segment should intersect each cell boundary.

Another method was proposed in (Mayorga et al. 2005). This method is limited to single basins and requires an outlet point for the processing area. It first converts the vector stream network into a flow direction grid and then applies an iterative procedure to correct the resulting flow directions. The method imposes very strict requirements on the input vector data: the entire network must be interconnected; network segments should form a tree-like structure (channels that form loops or are split into parallel braided channels must be simplified to single channels following single, well-defined directions); no polygons are allowed; and all segments should be presented as polylines.

INPUT DATA FOR UPSCALING

The methods discussed above use different types of data as input datasets. Grid-oriented upscaling procedures require catchment area coverage, or a catchment area

with a flow direction grid. There are three global datasets that provide these coverages: a relatively old HYDRO1K, and more recent HydroSHEDS (Lehner et al. 2008; Lehner and Grill 2013) and MERIT Hydro (Yamazaki et al. 2019). HydroSHEDS grids were utilized in the work of (Wu et al. 2011, Wu et al. 2012). MERIT Hydro coverage is implied in (Eilander et al. 2021).

The issue of input data for vector-based approaches appears to be more complex. The work of Mayorga et al. (2005) relied on Digital Chart of the World (DCW) data (Danko 1991), but the authors emphasize that this data requires careful and time-consuming preprocessing. Another vector-based approach (Olivera and Raina 2003) used a stream network derived from the HYDRO1K dataset. HydroSHEDS and MERIT Hydro also include vector river networks derived from flow direction rasters. However, if raster coverages are the main sources for these datasets, it begs the question of whether vector-based methods are necessary or whether grid-based methods are better.

EVALUATION OF UPSCALING RESULTS

All the above methods produce reliable flow direction distributions at low spatial resolution and global coverage, but the computational results still differ in detail. Fig. 5 shows upscaling results according to three different approaches (COTAT, DRT, NTM) for a limited area in the lower Mississippi River basin. The overall distribution of flow directions is similar between all three results, but the details are noticeably different: for example, the main course of the Mississippi in the result obtained by the DRE algorithm is oriented strictly from north to south, while other algorithms show some sinuosity for the same river.

Since the upscaling results vary, quantitative criteria for their evaluation are needed. Several criteria were proposed to evaluate flow direction distribution, including:

- visual comparison of the generated network with reference data (Döll and Lehner 2002; O'Donnell et al. 1999);
- estimation of basin and sub-basin areas for the selected points (Döll and Lehner 2002; Fekete et al. 2001; O'Donnell et al. 1999; Olivera et al. 2002; Vörösmarty et al. 2000; Wu et al. 2011);

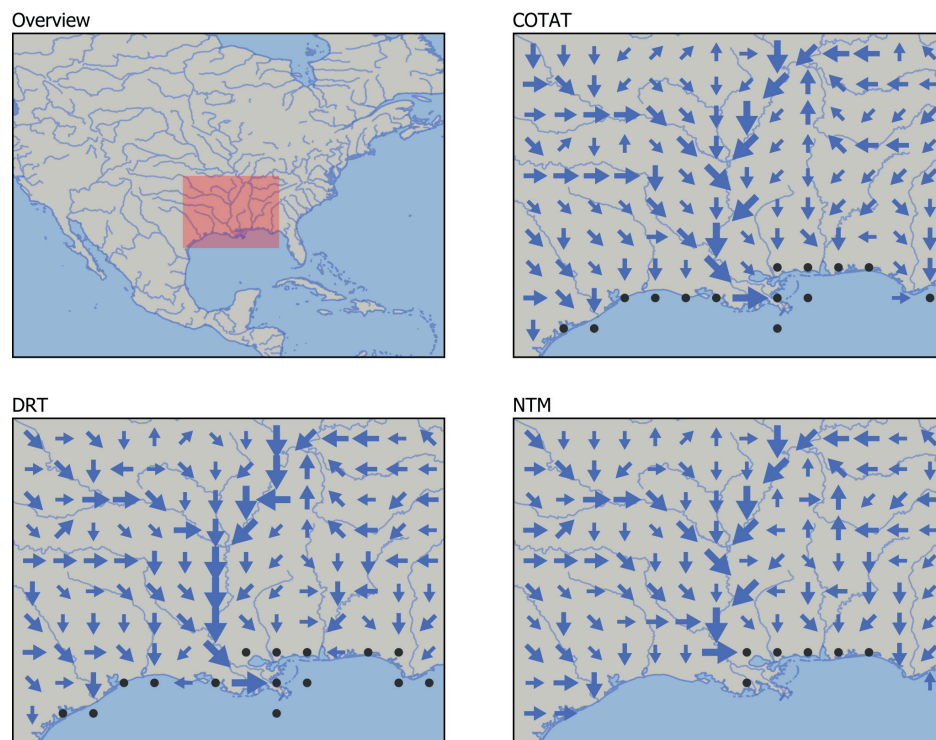


Fig. 5. Demonstration of the upscaling results with different methods (COTAT, DRT, NTM) in the lower Mississippi River area. Flow directions are shown with arrows; arrow size is proportional to the catchment area; black dots stand for an undefined flow direction

- comparison of the overall river segment distribution and statistics, including length and number of segments (Vörösmarty et al. 2000) ;

- calculation and evaluation of flow direction distribution statistics itself (Olivera et al. 2002; Reed 2003)

The comparison is usually made relative to some reference distribution, which is based on higher resolution flow directions. Basin and sub-basin areas are estimated directly through overlay with reference polygons or indirectly via comparison of catchment areas. In the latter case, a linear regression between the upscaled and reference results is calculated, and typical statistics (R^2 , RMSE, etc.) are computed. The process of comparing river segments follows a similar way. For flow direction distribution, Olivera et al. (2002) proposed a following criterion, called 'side-to corner ratio': 59% of the cells should have orthogonal flow direction (north, east, south, west), and 41% of the cells should have diagonal flow direction. This criterion is based on a theoretical assumption and has not been tested for fine-resolution datasets.

A small number of papers compare different upscaling methods with each other. Davies and Bell (2009) compared COTAT, COTAT+ (EAM) and NTM methods, suggesting that COTAT+ shows the best results among tested approaches. Wu et al. (2011) evaluated their DRT algorithm against the approach of Döll and Lehner (2002). The results of the IHU application were compared with COTAT+ (EAM) and DMM (Eilander et al. 2021). Cohesive testing of all modern upscaling methods in global coverage has not been conducted to date.

DISCUSSION

There are many algorithms that have been developed for upscaling flow directions and/or creating coarse-resolution flow direction coverage. Most of them use procedures based on flow tracing over a grid of lower spatial resolution. The two most novel algorithms of this kind (Dominant River Tracing, DRT, and Iterative

Hydrography Upscaling, IHU) also belong to this group. Alternative approaches include the derivation of flow directions from fine-resolution catchment area coverages (e.g. Double Maximum Method, DMM) and the calculation of flow directions from vector hydrography network data (e.g. Network Tracing Method, NTM). The authors of DRT and IHU also made sets of global coarse-resolution flow direction coverages; typical cell size within these datasets varies from 30 arc seconds to 1 degree. These datasets have been shown to have acceptable accuracy for application in modeling hydrological and climatic processes in global coverage.

Higher-resolution flow direction and catchment area coverage, such as HydroSHEDS and MERIT Hydro, are most often used as input data for generating low-resolution flow directions. In some cases, vector representations of the hydrographic network based on raster coverage are also used. Alternative sources of vector representations of the hydrographic network, such as Digital Chart of the World, are used less frequently because existing algorithms have high input data requirements that these sources do not possess. In particular, river segments should form a continuous network with a tree-like structure; branching of the channel is not allowed. Data sets created by digitizing geographic maps do not have these properties.

There are several ways to evaluate the results of upscaling. They include visual assessment of the result, calculation of catchment area statistics, estimation of length distributions and number of river network segments, and calculation of direct flow direction statistics. While all the above methods allow characterization of the distribution as a whole (and are used accordingly), their ability to detect local differences on coarse-resolution grids still needs to be assessed. This is especially the case for the criterion proposed in (Olivera et al. 2002) to evaluate the distribution of flow directions (59/41 ratio). It is necessary to find out whether such a ratio is observed in the raw data used for upscaling. It also seems important to automate the estimation of river network shape generated from coarse-

resolution flow directions; to date, no effective solution to this problem has been proposed.

CONCLUSIONS

The paper considers contemporary methods for generating flow direction grids (rasters) at coarse spatial resolution (about 1°). Most of these methods can be seen as specific algorithms of generalization, or in this case, the upscaling of flow direction grids with relatively fine resolution. These methods are based on flow tracing in fine resolution and further derivation of directions at coarse resolutions. The most advanced methods of this type are Dominant River Tracing (DRT) and Iterative Hydrography Upscaling (IHU). DRT output data (resolutions 2°, 1°, 1/2°, 1/4°, 1/8°, 1/16°). These coverages are generated from fine-resolution datasets: HYDRO1K, HydroSHEDS, and MERIT

Hydro, respectively. Alternative approaches include the generation of the desired datasets directly from catchment area grids (without flow tracing) and the aggregation of vector stream networks. There are no publicly available ready-made datasets based on these methods, making them less frequently used.

Assessing the validity of the resulting distributions is still an underdeveloped issue. Although several estimation methods have been proposed, all of them mostly reveal global characteristics of the obtained distributions, while local features of flow direction distribution remain unclear. It is necessary to develop estimation methods that would allow efficient (and automatic) analysis of river network configurations derived from coarse-resolution flow directions and to apply these approaches to generation results based on all modern upscaling methods. ■

REFERENCES

- Danko D.M. (1991). The digital chart of the world project. In: Proceedings of the Eleventh Annual ESRI User Conference, 1, 169–180.
- Davies H.N. and Bell V.A. (2009). Assessment of Methods for Extracting Low-Resolution River Networks from High-Resolution Digital Data. *Hydrological Sciences Journal*, 54(1), 17–28. DOI: 10.1623/hysj.54.1.17
- Decharme B., Alkama R., Douville H., Becker M. and Cazenave A. (2010). Global Evaluation of the ISBA-TRIP Continental Hydrological System. Part II: Uncertainties in River Routing Simulation Related to Flow Velocity and Groundwater Storage. *Journal of Hydrometeorology*, 11(3), 601–617. DOI: 10.1175/2010JHM1212.1
- Döll P. and Lehner B. (2002). Validation of a New Global 30-min Drainage Direction Map. *Journal of Hydrology*, 258(1–4), 214–231. DOI: 10.1016/S0022-1694(01)00565-0
- Eilander D., Van Verseveld W., Yamazaki D., Weerts A., Winsemius H.C. and Ward P.J. (2021). A Hydrography Upscaling Method for Scale-Invariant Parametrization of Distributed Hydrological Models. *Hydrology and Earth System Sciences*, 25(9), 5287–5313. DOI: 10.5194/hess-25-5287-2021
- Fekete B.M., Vörösmarty C.J. and Lammers R.B. (2001). Scaling Gridded River Networks for Macroscale Hydrology: Development, Analysis, and Control of Error. *Water Resources Research*, 37(7), 1955–1967. DOI: 10.1029/2001WR900024
- Freeman T. (1991). Calculating Catchment Area with Divergent Flow Based on a Regular Grid. *Computers and Geosciences*, 17, 413–422.
- Jenson S.K. and Domingue J.O. (1988). Extracting Topographic Structure from Digital Elevation Data for Geographic Information System Analysis. *Photogrammetric Engineering and Remote Sensing*, 54(11), 1593–1600.
- Lehner B. and Grill G. (2013). Global River Hydrography and Network Routing: Baseline Data and New Approaches to Study the World's Large River Systems. *Hydrological Processes*, 27(15), 2171–2186. DOI: 10.1002/hyp.9740
- Lehner B., Verdin K. and Jarvis A. (2008). New Global Hydrography Derived from Spaceborne Elevation Data. *EOS, Transactions American Geophysical Union*, 89(10), 93–94.
- Lin P., Pan M., Beck H.E., Yang Y., Yamazaki D., Frasson R., David C.H., Durand M., Pavelsky T.M., Allen G.H., Gleason C.J. and Wood E.F. (2019). Global Reconstruction of Naturalized River Flows at 2.94 Million Reaches. *Water Resources Research*, 55(8), 6499–6516. DOI: 10.1029/2019WR025287
- Lucas-Picher P., Arora V.K., Caya D. and Laprise R. (2003). Implementation of a Large-Scale Variable Velocity River Flow Routing Algorithm in the Canadian Regional Climate Model (CRCM). *Atmosphere - Ocean*, 41(2), 139–153. DOI: 10.3137/ao.410203
- Mayorga E., Logsdon M.G., Ballester M.V.R. and Richey J.E. (2005). Estimating Cell-to-Cell Land Surface Drainage Paths from Digital Channel Networks, with an Application to the Amazon Basin. *Journal of Hydrology*, 315(1–4), 167–182. DOI: 10.1016/j.jhydrol.2005.03.023
- Miller J.R., Russell G.L. and Caliri G. (1994). Continental-Scale River Flow in Climate Models. *Journal of Climate*, 7(6), 914–928. DOI: 10.1175/1520-0442(1994)007<0914:CSRFIC>2.0.CO;2
- O'Callaghan J.F. and Mark D.M. (1984). The Extraction of Drainage Networks from Digital Elevation Data. *Computer Vision, Graphics, and Image Processing*, 28(3), 323–344.
- O'Donnell G., Nijssen B. and Lettenmaier D.P. (1999). A Simple Algorithm for Generating Streamflow Networks for Grid-Based, Macroscale Hydrological Models. *Hydrological Processes*, 13(8), 1269–1275. DOI: 10.1002/(SICI)1099-1085(19990615)13:8<1269::AID-HYP806>3.0.CO;2-R
- Oki T. and Sud Y.C. (1998). Design of Total Runoff Integrating Pathways (TRIP)—A Global River Channel Network. *Earth Interactions*, 2(1), 1–37. DOI: 10.1175/1087-3562(1998)002<0001:dotrip>2.3.co;2
- Olivera F., Lear M.S., Famiglietti J.S. and Asante K. (2002). Extracting Low-Resolution River Networks from High-Resolution Digital Elevation Models. *Water Resources Research*, 38(11), 13-1-13–18. DOI: 10.1029/2001wr000726
- Olivera F. and Raina R. (2003). Development of Large Scale Gridded River Networks from Vector Stream Data. *Journal of the American Water Resources Association*, 39(5), 1235–1248. DOI: 10.1111/j.1752-1688.2003.tb03705.x
- Panda J. and Meher S. (2024). Recent Advances in 2D Image Upscaling: A Comprehensive Review. *SN Computer Science*, 5(6). DOI: 10.1007/s42979-024-03070-2
- Pappenberger F., Cloke H.L., Balsamo G., Ngo-Duc T. and Oki T. (2010). Global Runoff Routing with the Hydrological Component of the ECMWF NWP System. *International Journal of Climatology*, 30(14), 2155–2174. DOI: 10.1002/joc.2028
- Paz A.R., Collischonn W. and Lopes da Silveira A.L. (2006). Improvements in Large-Scale Drainage Networks Derived from Digital Elevation Models. *Water Resources Research*, 42(8), 1–7. DOI: 10.1029/2005WR004544
- Peng J., Loew A., Merlin O. and Verhoest N.E.C. (2017). A Review of Spatial Downscaling of Satellite Remotely Sensed Soil Moisture. *Reviews of Geophysics*, 55(2), 341–366. DOI: 10.1002/2016RG000543
- Qin C.-Z., Ai B.-B., Zhu A.-X. and Liu J.-Z. (2017). An Efficient Method for Applying a Differential Equation to Deriving the Spatial Distribution of Specific Catchment Area from Gridded Digital Elevation Models. *Computers and Geosciences*, 100(2), 94–102. DOI: 10.1016/j.cageo.2016.12.009

- Quinn P., Beven K., Chevallier P. and Planchon O. (1991). The Prediction of Hillslope Flow Paths for Distributed Hydrological Modelling Using Digital Terrain Models. *Hydrological Processes*, 5(1), 59–79. DOI: 10.1002/hyp.3360050106
- Reed S.M. (2003). Deriving Flow Directions for Coarse-Resolution (1–4 km) Gridded Hydrologic Modeling. *Water Resources Research*, 39(9), 1–11. DOI: 10.1029/2003WR001989
- Sood A. and Smakhtin V. (2015). Global Hydrological Models: a Review. *Hydrological Sciences Journal*, 60(4), 549–565. DOI: 10.1080/02626667.2014.950580
- Tarboton D.G. (1997). A New Method for the Determination of Flow Directions and Upslope Areas in Grid Digital Elevation Models. *Water Resources Research*, 33(2), 309–319.
- Thober S., Cuntz M., Kelbling M., Kumar R., Mai J. and Samaniego L. (2019). The Multiscale Routing Model mRM v1.0: Simple River Routing at Resolutions from 1 to 50 km. *Geoscientific Model Development*, 12(6), 2501–2521. DOI: 10.5194/gmd-12-2501-2019
- Vörösmarty C.J., Fekete B.M., Meybeck M. and Lammers R.B. (2000). Geomorphometric Attributes of the Global System of Rivers at 30-minute Spatial Resolution. *Journal of Hydrology*, 237(1–2), 17–39. DOI: 10.1016/S0022-1694(00)00282-1
- Wu H., Kimball J.S., Li H., Huang M., Leung L.R. and Adler R.F. (2012). A New Global River Network Database for Macroscale Hydrologic Modeling. *Water Resources Research*, 48(9), 1–5. DOI: 10.1029/2012WR012313
- Wu H., Kimball J.S., Mantua N. and Stanford J. (2011). Automated Upscaling of River Networks for Macroscale Hydrological Modeling. *Water Resources Research*, 47(3), 1–18. DOI: 10.1029/2009WR008871
- Yamazaki D., Ikeshima D., Sosa J., Bates P.D., Allen G.H. and Pavelsky T.M. (2019). MERIT Hydro: A High-Resolution Global Hydrography Map Based on Latest Topography Dataset. *Water Resources Research*, 55(6), 5053–5073. DOI: 10.1029/2019WR024873
- Yamazaki D., Oki T. and Kanae S. (2009). Deriving a Global River Network Map and Its Sub-Grid Topographic Characteristics from a Fine-Resolution Flow Direction Map. *Hydrology and Earth System Sciences*, 13(11), 2241–2251. DOI: 10.5194/hess-13-2241-2009.

SEAGRASS CARBON STOCKS AND SEQUESTRATION IN HABITAT IMPACTED BY TIN MINING ACTIVITIES IN BANGKA BELITUNG, INDONESIA

Wahyu Adi^{1,2*}, Agus Hartoko¹, Pujiono W. Purnomo¹, Okto Supratman², Udhi E. Hernawan³

¹ Aquatic Resources Management Faculty of Fisheries and Marine Sciences Diponegoro University, Jl. Prof. Soedarto No.13 Tembalang, Semarang, 50275, Indonesia

² Aquatic Resources Management Faculty of Agriculture Fisheries and Marine University of Bangka Belitung, Gang IV No. 1 Balun Ijuk Merawang, Bangka, 33172, Indonesia

³ Research Center for Oceanography National Research and Innovation Agency Indonesia, Jl. Pasir Putih I Ancol Timur, Jakarta, 14430, Indonesia

*Corresponding author: wahyuadi@ubb.ac.id

Received: October 28th 2024 / Accepted: January 16th 2025 / Published: March 31st 2025

<https://doi.org/10.24057/2071-9388-2025-3459>

ABSTRACT. Seagrass meadows are important blue carbon ecosystems. They are threatened by various anthropogenic activities, including mining, which affect the ecological health. This study investigates the impact of sea-based tin mining activities on the carbon storage capabilities of seagrass meadows in Bangka Belitung, Indonesia. The objective of the study is to quantify carbon stocks and sequestrations in these ecosystems and understand how mining influences these critical natural resources. The research was conducted at various seagrass sites with different levels of mining impacts. Carbon stocks and sequestration were measured using the Loss on Ignition method, and net primary productivity was calculated. Remote sensing data from Landsat 7 and Sentinel-2A satellites were used to monitor changes in seagrass cover over time. Sedimentation rates and total suspended solids were measured to assess environmental impacts. Statistical analysis, including correlation and cluster analysis, examined the relationship between mining activity and seagrass health. The findings indicate a significant decrease in seagrass coverage and carbon storage in areas with high levels of tin mining. Specifically, areas with intensive mining showed higher rates of sedimentation and total suspended solids, which correlated with reduced seagrass biomass and carbon sequestration. This decrease compromises the ecological role of seagrass meadows as effective carbon sinks, highlighting the destructive impact of mining activities on these ecosystems.

KEYWORDS: carbon stock, carbon sequestration, seagrass, tin mining

CITATION: Adi W., Hartoko A., Purnomo P. W., Supratman O., Hernawan U. E. (2025). Seagrass Carbon Stocks And Sequestration In Habitat Impacted By Tin Mining Activities In Bangka Belitung, Indonesia. *Geography, Environment, Sustainability*, 97-104

<https://doi.org/10.24057/2071-9388-2025-3459>

ACKNOWLEDGEMENTS: We express our appreciation to the Indonesia Education Scholarship (Beasiswa Pendidikan Indonesia, BPI) for generously funding our dissertation. Our sincere gratitude also goes to the collaborative research team at the University of Bangka Belitung for their valuable contributions to the seagrass research project.

Conflict of interests: The authors reported no potential conflict of interest.

INTRODUCTION

Seagrass ecosystems play a crucial role in carbon sequestration, representing essential components of the marine environment. Although they cover a small fraction of the ocean floor, seagrasses contribute significantly to oceanic carbon storage, accounting for up to 20% of the ocean's carbon (Khairunnisa et al. 2023; McHenry et al. 2023). This capacity for carbon storage indicates their critical role in global carbon cycles and climate change mitigation efforts (Wahyudi et al. 2020; Mashoreng et al. 2021). Seagrasses can store carbon in their bodies and in the soil by creating biomass and trapping carbon particles that settle from the water. (Harahap et al. 2021; Hartoko et al. 2021). Although seagrass meadows can release small amounts of methane

(CH₄) into the atmosphere, recent studies indicate that CH₄ emissions from these ecosystems are minimal and offset less than 2% of the carbon sequestered in their sediments (Yau et al. 2023). Incorporating seagrass ecosystems into the blue carbon framework further emphasizes their importance in mitigating anthropogenic CO₂ emissions (Marbà et al. 2015).

Despite their crucial roles, seagrass habitats and ecological conditions have declined due to human activities, including mining. This poses a serious threat to their carbon sequestration potential (Fourqurean et al. 2012; Unsworth et al. 2019; McKenzie and Yoshida 2020). In Bangka Belitung, Indonesia, tin mining significantly impacts coastal waters. Water turbidity from mining activities impedes seagrass growth by reducing essential

sunlight penetration for photosynthesis (van Katwijk et al. 2011; Adams et al. 2016; Yamamoto et al. 2019). Offshore tin mining, initiated in 2001, has expanded annually, escalating environmental pressure on coastal ecosystems (Ibrahim et al. 2018; Irzon 2021).

Previous studies has highlighted the importance of conserving seagrass ecosystems as global carbon sinks, with Indonesia's seagrass meadows offering valuable insights into their carbon storage potential (Alongi et al. 2016; Wahyudi et al. 2020; Hernawan et al. 2021). Seagrasses are known for their ability to sequester carbon and store it as organic carbon in underwater sediments, making them one of the vital blue carbon ecosystems for climate change mitigation (Wahyudi et al. 2020; Stankovic et al. 2021). Human activities can cause the release of carbon that has been in sediments for hundreds of years, which may lead to higher greenhouse gas emissions (Fourqurean et al. 2012; Luo et al. 2022). Effective conservation and management strategies are needed, given the ability of seagrasses to store carbon and act as significant marine carbon sinks (Dewi et al. 2021; Hernawan et al. 2021). This study hypothesizes that tin mining significantly affects seagrass carbon storage. To test the hypothesis, it assessed the carbon stock and sequestration in three mining-affected areas in Bangka Belitung.

Data on seagrass carbon storage in Bangka Belitung remains limited, despite their acknowledged important role. Previous studies have primarily focused on seagrass distribution and the environmental consequences of mining (Syafutra et al. 2018; Haryati and Dariah 2019; Nopiansyah et al. 2021; Akhrianti et al. 2023). This study seeks to fill the gap by examining the effects of tin mining on seagrass carbon dynamics to inform conservation efforts and sustainable management practices. This study aims to assess seagrass meadows' carbon storage and ecological condition in tin-mining-impacted coastal waters in Bangka Belitung, Indonesia. It specifically focuses on how tin mining affects seagrass carbon dynamics, an area previously underexplored. By quantifying seagrass meadows' carbon storage capacity in mining-impacted regions, this study contributes to understanding their role in climate change mitigation and the effects of anthropogenic activities on their function. The study was conducted on two islands, Bangka and Belitung, Indonesia, over two years, 2022 and 2023 (Fig. 1). Sampling focused on marine seagrass beds affected by tin mining activities near Bangka and in non-impacted areas around Belitung.

MATERIALS AND METHODS

Grouping and Mapping of Tin Mining Impacts

Sampling areas were initially categorized based on the intensity of mining impacts. This involved creating a map highlighting the potential impacts of tin mining based on the Bangka Belitung Islands Provincial Regulation No. 3 of 2020 on Coastal and Small Island Spatial Zoning. The spread of Total Suspended Solids (TSS) can reach 16 miles from mining sites

(Pamungkas and Husrin 2020), and TSS levels over 20 mg/L can harm seagrass ecosystems, according to Government Regulation of the Republic of Indonesia No. 22 of 2021 on Environmental Protection, Organization, and Management. These factors were important in making this classification..

Seagrass Area Mapping

For temporal comparison, Landsat 7 ETM+ imagery was used to assess water conditions in 2000, a year before offshore tin mining began, while Sentinel L2A imagery from 2022 was employed for depicting the latest conditions. Landsat 7 ETM+ has a spatial resolution of 30 m, while Sentinel-2 offers a higher spatial resolution of 10–20 m with 13 spectral bands, making it particularly effective for seagrass mapping in shallow coastal waters (Traganos et al. 2018; Bannari et al. 2022). Sentinel was selected as its operation began in 2016, rendering it unsuitable for earlier assessments. Previous studies showed that Sentinel-2 can effectively map seagrass using its multispectral images to identify different seagrass species and the algae that grow with them (Nur et al. 2021; Bannari et al. 2022). Landsat, while operating at a lower spatial resolution, has been invaluable for its long-term data continuity, enabling researchers to assess seagrass dynamics and temporal changes over decades (Carpenter et al. 2022; Rosalina et al. 2023). Image processing, including unsupervised classification, was performed using QGIS software to determine changes in seagrass coverage over time. The satellite image acquisition dates are presented in Table 1.

Seagrass, Sedimentation, and Carbon Measurement

At the seagrass meadow research site, quantified species diversity, density (shoots/m²), and coverage (%) at the seagrass meadow research site using three 100 m line transects and 50×50 cm quadrat transects (Hernawan et al. 2021). The amount of seagrass (measured in g/m²) and the organic carbon stock (measured in tC/Ha) were calculated using the Loss on Ignition (LOI) method (Fourqurean et al. 2012). Carbon Sequestration (CS) is defined as net primary productivity measured using the Eq. (1): $CS = 1.743 + 0.087$ (seagrass coverage), with units of tC/ha/year (Wahyudi et al. 2020). This Eq. (1) was chosen because it was developed using seagrass data from Indonesia, making it highly applicable to this study. The sedimentation rate was measured to assess the rate of sediment accumulation over time at the site, expressed in g/m²/day (Roswaty et al. 2014). The Total Suspended Solids (TSS) were measured gravimetrically, with results reported in mg/l (Wisha and Ondara 2017).

Statistical analysis

The statistical analyses provided a robust framework for understanding the impacts of tin mining on seagrass ecosystems by quantifying the relationships between mining activities and seagrass health metrics. These

Table 1. Satellite data related to the impact of tin mining

Location	Sentinel L2A, Acquisition Date	Landsat L7 ETM+, Acquisition Date	Tin Mining Impact
Bakit	27/05/2022	23/05/2000	High
Tukak	08/06/2022	14/04/2000	Moderate
Tanjung Kerasak	18/07/2022	14/04/2000	Moderate
Pegantungan	08/06/2022	06/03/2000	Low
Tanjung Kelayang	08/06/2022	03/12/2000	Low

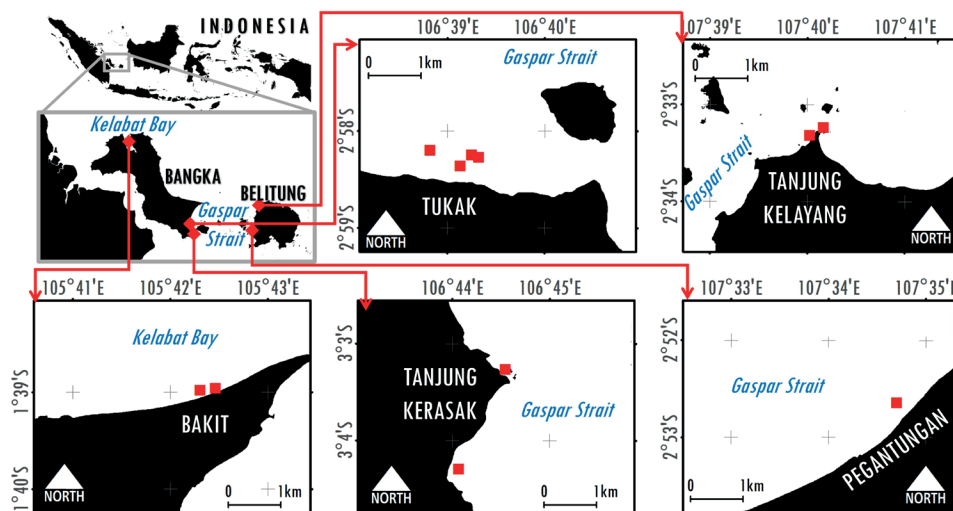


Fig. 1. Study sites in Bangka Belitung, Indonesia. Red boxes indicate sampling sites

relationships were analyzed using PAST 4.03 (Hammer et al. 2001), a program made for statistical and graphical analysis, particularly in paleontological studies. The analysis used correlation and clustering methods to understand how different factors relate to each other and to group research locations based on their environmental traits.

RESULTS AND DISCUSSION

Seagrass Coverage Decline

The study of seagrass meadows at five locations showed a big decrease in seagrass coverage, linked to the level of tin mining nearby (Fig. 2). Over the 22-year study period, the most significant decline was observed in Bakit. In this high-mining impact area, seagrass coverage decreased by 41.46 Ha/year (Fig. 2, Fig. 3, and Table 2). In contrast, Tukak, with a moderate mining impact, showed the least decline (0.27 Ha/year). These results highlight the harmful impact of mining on seagrass habitats, which matches the loss of seagrass reported in other studies (Brodie et al. 2020; Supriyadi et al. 2021; Sjafrie et al. 2022; Nugraha et al. 2023). The seagrass meadows at the study included nine types of seagrass: *Thalassia hemprichii*, *Enhalus acoroides*, *Cymodocea rotundata*, *Cymodocea serrulata*, *Halodule uninervis*, *Halodule pinifolia*, *Halophila ovalis*, *Halophila minor*, and *Syringodium isoetifolium*. The decline in seagrass coverage diminishes the ecosystem's ability to perform essential functions such as carbon sequestration and threatens marine biodiversity.

Sedimentation Rates and Water Turbidity

The results indicate significantly higher sedimentation rates in areas with high mining activities (Table 2 and Fig. 3). Bakit, the area with the highest mining impact, recorded a sedimentation rate of 146.93 g/m²/day, which is nearly double that observed in areas with lower mining impacts. These elevated Higher sedimentation rates are linked to more Total Suspended Solids (TSS), which makes the water muddier (Samper-Villarreal et al. 2016). The negative correlation between sedimentation rates and seagrass canopy coverage suggests that increased sediment deposition obscures light penetration, which is essential for seagrass health and productivity (Ahmad-Kamil et al. 2013).

Seagrass Biomass and Carbon Dynamics

Analysis of seagrass biomass revealed that areas with lower mining impacts exhibited significantly higher biomass (e.g., Pegantungan and Tanjung Kelayang averaging 104.66 g/m²) compared to highly impacted areas like Bakit (3.4 g/m²) (Fig. 4 and Table 2). The reduction of biomass in areas with high mining activities directly impacts the ecosystem's carbon storage capacity. These findings align with Greiner et al. (2013), highlighting the role of healthy seagrass meadows in enhancing carbon sequestration.

Furthermore, an inverse relationship was observed between mining impact intensity, carbon stock, and

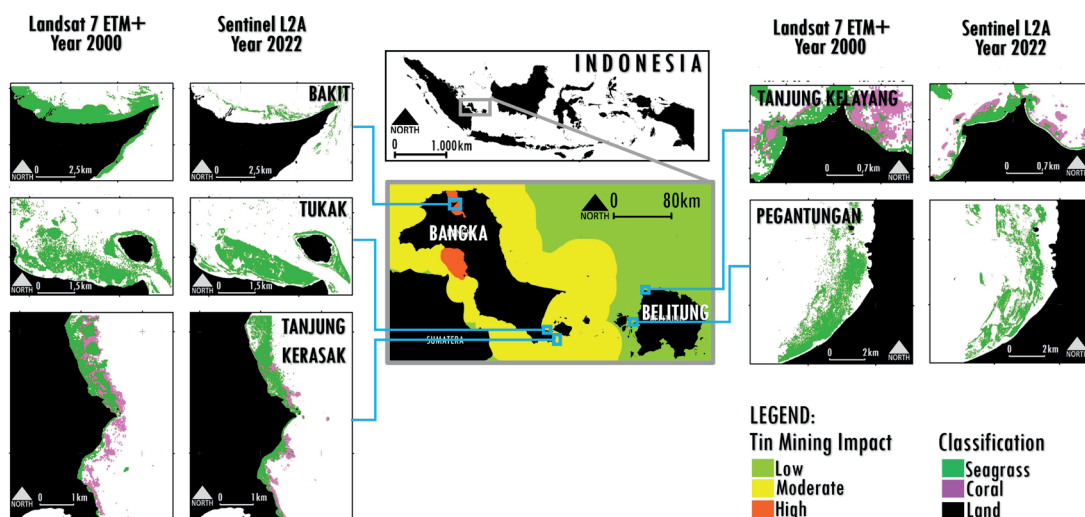
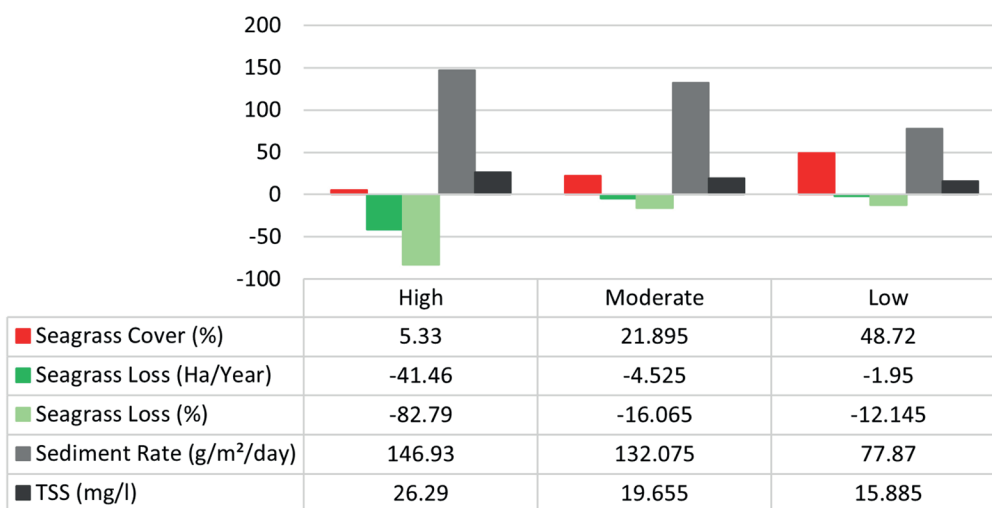


Fig. 2. Potential Impacted Areas of Tin Mining and Changes in Seagrass Area (2000-2022)



Tin Mining Impact
Fig. 3. Seagrass and Sedimentation in Tin Mining Impacted Areas

Table 2. Seagrass Condition

	Location				
	Bakit	Tanjung Kerasak	Tukak	Pegantungan	Tanjung Kelayang
Tin Mining Impact	High	Moderate	Moderate	Low	Low
Sedimentation and Total Suspended Solid (TSS)					
Sedimentation Rate (g/m ² /day)	146.93	135.11	129.04	61.59	94.15
TSS (mg/l)	26.29	17.3	22.01	16.53	15.24
Seagrass Mapping					
Total Station	2	2	4	1	2
Seagrass Species	3	10	8	3	8
Seagrass Cover (%)	5.33	17.66	26.13	73.28	24.16
Seagrass Area in 2000 (Ha)	1,101.72	183.43	669.32	865.72	65.23
Seagrass Area in 2022 (Ha)	189.66	177.46	476.05	790.03	55.08
Seagrass Loss (Ha/Year)	-41.46	-8.78	-0.27	-3.44	-0.46
Seagrass Loss in 22 years (%)	-82.79	-28.88	-3.25	-8.74	-15.55
Seagrass Biomass and Carbon					
Total Sampel	16	32	109	14	36
Biomass, Above Ground (g/m ²)	1.03	18.51	15.37	33.82	16.75
Biomass, Below Ground (g/m ²)	2.37	46.54	74.51	102.99	55.76
Total Biomass (g/m ²)	3.4	65.06	89.88	136.81	72.51
Organic Carbon, Below Ground (tC/Ha)	0.006	0.138	0.216	0.262	0.122
Organic Carbon, Above Ground (tC/Ha)	0.003	0.055	0.045	0.101	0.047
Standing Stock Carbon (tC/Ha)	0.009	0.193	0.261	0.363	0.169
Carbon Sequestration (tC/Ha/Year)	5.33	17.66	26.13	73.28	24.16
Sediment Carbon					
Total Sampel	35	9	34	44	79
Organic Carbon Stock (tC/Ha)	57.36	80.12	110.53	173.05	151.56

sequestration in seagrass meadows. In high-impact areas, the carbon sequestration was as low as 5.33 tC/Ha/year, whereas, in low-impact areas, it averaged 162.31 tC/Ha/year. This inverse correlation supports the hypothesis that physical disturbances such as sedimentation impair the seagrass meadows' ability to sequester carbon effectively (Mazarrasa et al. 2018).

The detrimental effects of mining on seagrass ecosystems have been demonstrated by several studies indicating a decline in seagrass area and health due to various mining activities. Rosalina et al. (2019) and Adi et al. (2024) described how mining waste affects seagrass ecosystems. This includes metal accumulation and altered seagrass dynamics, leading to less biomass and disrupted ecological functions seen in this study. Studies on Bintan Island and Taka Bonerate National Marine Park also report significant seagrass area reductions and health declines due to increased turbidity from mining activities (Supriyadi et al. 2021; Nugraha et al. 2023). Moreover, the broader decline of seagrass meadows in Indonesia, as noted by Sjafrie et al. (2022), reflects a trend where development and mining operations, including dredging and land cover changes, exacerbate the vulnerability of these ecosystems.

Statistical Analysis

Employing the Unweighted Pair Group Method with Arithmetic Mean (UPGMA) and Euclidean distance, the cluster analysis revealed significant spatial differences among the sampling locations (Fig. 5). Bakit, experiencing the highest impact of mining, displayed the greatest differences. In contrast, Tanjung Kerasak and Tukak, areas with moderate

mining impacts, showed close similarities. This analysis supports the spatial differentiation of the study sites into three distinct groups based on the degree of mining impact.

Pearson's *r* correlation statistics were used to examine the connections between sedimentation rates, seagrass canopy cover, and carbon stocks (see Fig. 5). The results indicate a significant negative correlation ($p < 0.05$) between sedimentation rates and both seagrass canopy cover and sediment carbon. This means that higher sedimentation from mining harms seagrass and reduces carbon stored in sediments. On the other hand, there were positive correlations found between seagrass cover, biomass, and above-ground organic carbon stock, indicating that areas with healthier seagrass canopies tend to have higher biomass and carbon storage capabilities. These findings are crucial for understanding the dynamic interactions within seagrass ecosystems under stress from anthropogenic activities.

These statistical findings not only reinforce the visual and descriptive observations made during the study but also provide a quantitative basis for the conclusions drawn concerning the impacts of tin mining on seagrass ecosystems. The significant correlations and spatial distinctions highlighted by the analyses underscore the complex nature of the interactions between environmental disturbances and ecological responses in these critical marine habitats.

Ecological and Conservation Implications

The degradation of seagrass meadows due to tin mining activities poses significant risks to marine biodiversity and the livelihoods dependent upon these

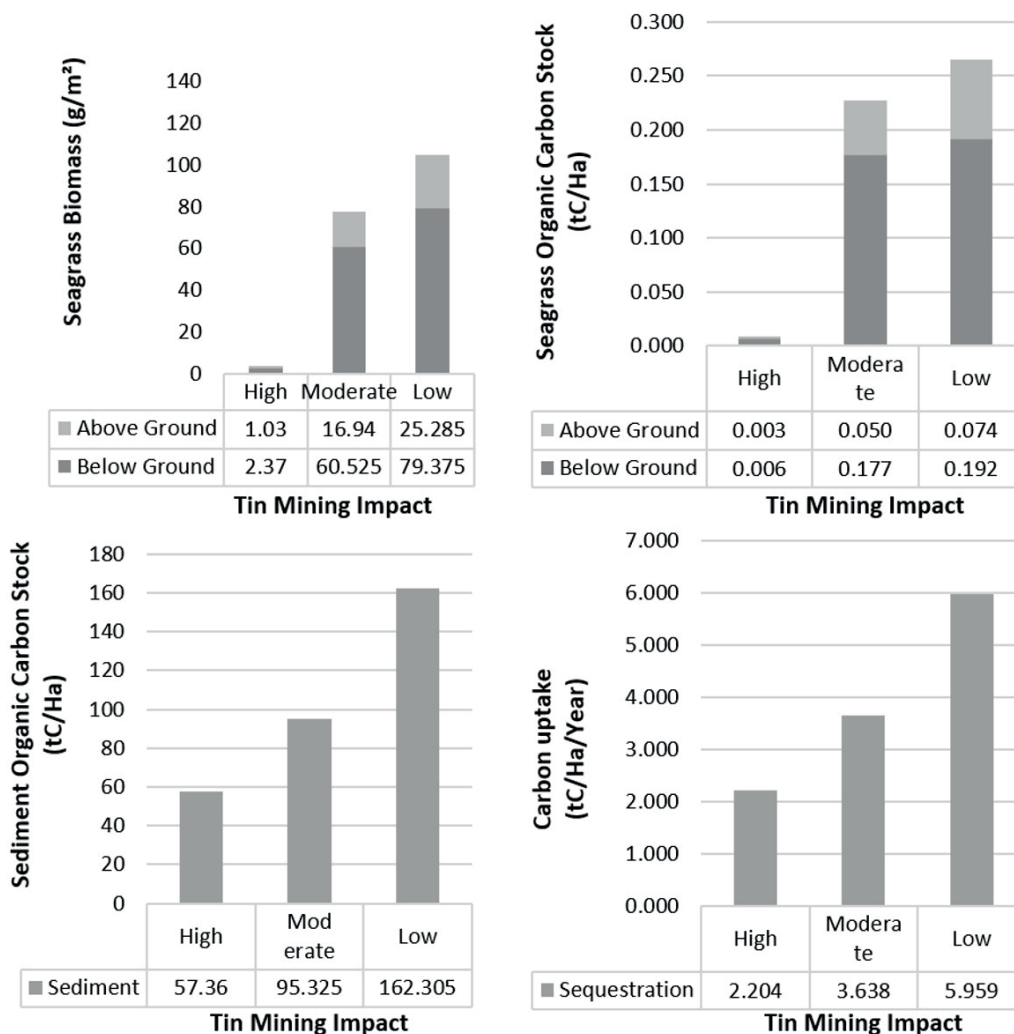


Fig. 4. Biomass, Carbon Stock, and Sequestration in Tin Mining Impacted Areas

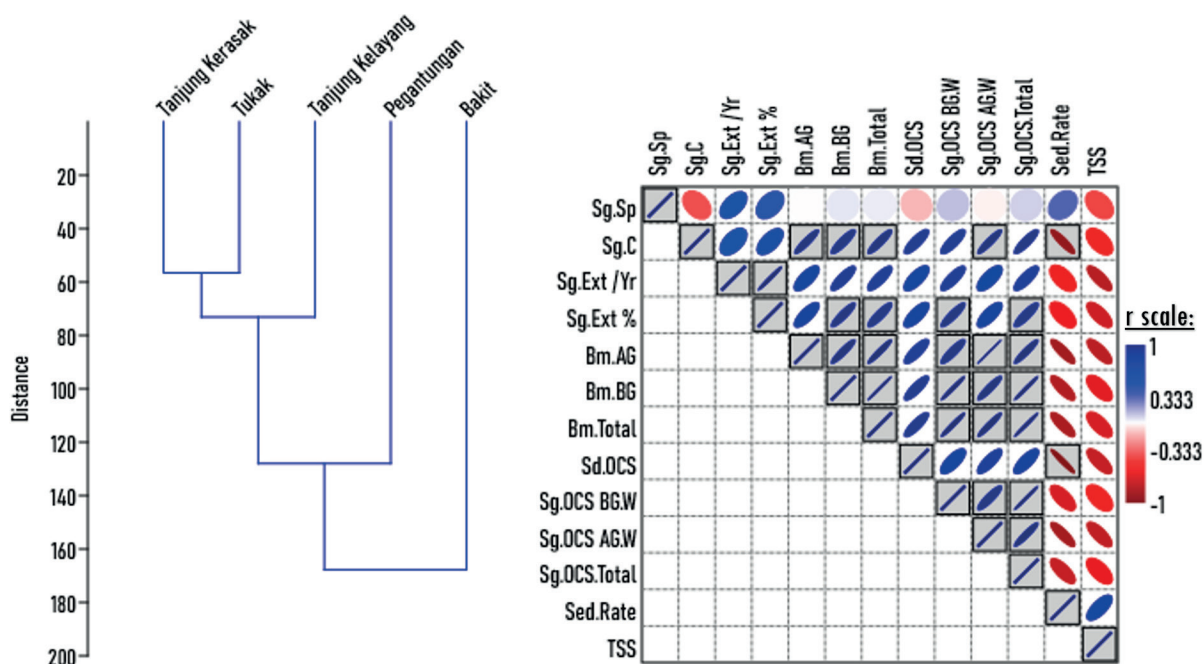


Fig. 5. Cluster Analysis of research location (left) and correlation between research variables (right), significance ($P < 0.05$) shown in a square box. Sg.Sp= Seagrass Species; Sg.C= Seagrass Cover; Sg.Ext/Yr= Seagrass Changes (Ha/Year); Sg.Ext = Seagrass Change in 22 year (%); Bm.AG= Biomass Above ground; Bm.BG= Biomass Below ground; Bm.Total = Biomass above ground + below ground; Sd.OCS= Carbon Organic Sediment; Sg.OCS.BG.W= Seagrass Carbon Organic Stock Below Ground; Sg.OCS.AG.W= Seagrass Carbon Organic Stock Above Ground; Sg.OCS.Total Seagrass Standing Stock Carbon; Sed.Rate Sedimentation Rate; TSS Total Suspended Solid

ecosystems. Our findings emphasize the urgent need for conservation strategies that mitigate the impacts of such anthropogenic activities. Establishing protected marine areas and regulating mining practices near critical habitats are potential measures that could be taken to preserve these valuable ecosystems (Sugianti and Mujiyanto 2020; Tebaiy et al. 2021; Rifai et al. 2022).

Seagrass conservation and restoration in turbid waters present unique challenges and require tailored strategies to ensure ecosystem health and sustainability. Turbidity, influenced by factors such as water depth, canopy complexity, and sediment resuspension, plays a crucial role in shaping seagrass habitats and their associated ecosystem services (Samper-Villarreal et al. 2016). The stability of seagrass ecosystems, particularly in shallow coastal lagoons, relies heavily on feedback processes linked to the stirring up of sediments and the reduction of light (Adams et al. 2016; Park et al. 2016; Lanuru et al. 2018). Understanding these interactions is essential for effective conservation and restoration efforts.

Restoration initiatives have shown their potential to recover the health of coastal ecosystems rapidly. Programs such as the establishment of marine protected areas have been effective in maintaining ecosystem health and enhancing organic carbon storage in seagrass meadows (Adams et al. 2016; Stankovic et al. 2021; Tanner et al. 2021). In Asia, where seagrass beds are a critical component of marine biodiversity, conservation efforts are crucial for protecting these valuable habitats and the services they provide. The work by Sudo et al. (2021) highlights the importance of understanding the distribution, temporal changes, and conservation status of tropical seagrass beds to inform and tailor conservation strategies effectively.

Using advanced techniques like remote sensing to map how much seagrass there is can give important information

that helps improve conservation and management efforts in turbid waters (Koedsin et al. 2016). These techniques are useful not only for monitoring the current state of seagrass meadows but also for predicting their responses to environmental changes and human impacts.

CONCLUSIONS

The study shows that in areas affected by mining, there are major decreases in seagrass growth and the ability to store carbon. This was determined by looking at data on biomass, sediment rates, total suspended solids (TSS), and organic carbon levels.

The strong association between mining intensity and the degradation of seagrass meadows, which are vital for carbon sequestration and marine biodiversity, suggests the need for immediate conservation efforts and a re-evaluation of mining practices to protect the seagrass ecosystem from continuously degrading. Management actions should prioritize protection, particularly in areas heavily affected by mining activities. The findings of this research have significant implications for policy-making and environmental management, particularly in promoting sustainable mining practices that consider the ecological value of seagrass meadows. This study calls for protective measures to safeguard the role of seagrass ecosystems as critical carbon sinks and biodiversity reservoirs. These actions are essential not only for the preservation of marine ecosystems but also for contributing to global climate change mitigation efforts. In addition, this study also fills a knowledge gap regarding the impact of tin mining on seagrass carbon dynamics while providing a foundation for future research and conservation strategies to ensure the sustainability of seagrass habitats in Bangka Belitung amidst increasing anthropogenic pressures. ■

REFERENCES

- Adams M.P., Hovey R.K., Hipsey M.R., Bruce L.C., Ghisalberti M., Lowe R.J., Gruber R.K., Ruiz-Montoya L., Maxwell P.S., Callaghan D.P., Kendrick G.A. and O'Brien K.R. (2016). Feedback between sediment and light for seagrass: Where is it important? *Limnology and Oceanography*, 61(6), 1937–1955. DOI: 10.1002/lno.10319
- Adi W., Hartoko A., Purnomo P.W., Supratman O., Pringgenies D. and Hernawan U.E. (2024). Ecological condition of seagrass meadows around sea-based tin mining activities in the waters of Bangka Belitung Islands, Indonesia. *Marine Pollution Bulletin*, 209(PA), 117151. DOI: 10.1016/j.marpolbul.2024.117151
- Ahmad-Kamil E.I., Ramli R., Jaaman S.A., Bali J. and Al-Obaidi J.R. (2013). The Effects of Water Parameters on Monthly Seagrass Percentage Cover in Lawas, East Malaysia. *The Scientific World Journal*, 2013, 1–8. DOI: 10.1155/2013/892746
- Akhrianti I., Nugraha M.A., Pamungkas A. and Gustomi A. (2023). Total suspended solid distribution as impact tin mining at surrounded Pangkalpinang seawater Bangka Island. *IOP Conference Series: Earth and Environmental Science*, 1207(1). DOI: 10.1088/1755-1315/1207/1/012029
- Alongi D.M., Murdiyoso D., Fourqurean J.W., Kauffman J.B., Hutahaean A., Crooks S., Lovelock C.E., Howard J., Herr D., Fortes M., Pidgeon E. and Wagey T. (2016). Indonesia's blue carbon: a globally significant and vulnerable sink for seagrass and mangrove carbon. *Wetlands Ecology and Management*, 24(1), 3–13. DOI: 10.1007/s11273-015-9446-y
- Bannari A., Ali T.S. and Abahussain A. (2022). The capabilities of Sentinel-MSI (2A/2B) and Landsat-OLI (8/9) in seagrass and algae species differentiation using spectral reflectance. *Ocean Science*, 18(2), 361–388. DOI: 10.5194/os-18-361-2022
- Brodie G., Brodie J., Maata M., Peter M., Otiawa T. and Devlin M.J. (2020). Seagrass habitat in Tarawa Lagoon, Kiribati: Service benefits and links to national priority issues. *Marine Pollution Bulletin*, 155(May), 111099. DOI: 10.1016/j.marpolbul.2020.111099
- Carpenter S., Byfield V., Felgate S.L., Price D.M., Andrade V., Cobb E., Strong J., Lichtschlag A., Brittain H., Barry C., Fitch A., Young A., Sanders R. and Evans C. (2022). Using Unoccupied Aerial Vehicles (UAVs) to Map Seagrass Cover from Sentinel-2 Imagery. *Remote Sensing*, 14(3), 477. DOI: 10.3390/rs14030477
- Dewi S.K., Setyati W.A. and Riniatsih I. (2021). Stok Karbon pada Ekosistem Lamun di Pulau Kemujan dan Pulau Bengkoang Taman Nasional Karimunjawa. *Journal of Marine Research*, 10(1), 39–47. DOI: 10.14710/jmr.v10i1.28273
- Fourqurean J.W., Duarte C.M., Kennedy H., Marbà N., Holmer M., Mateo M.A., Apostolaki E.T., Kendrick G.A., Krause-Jensen D., McGlathery K.J. and Serrano O. (2012). Seagrass ecosystems as a globally significant carbon stock. *Nature Geoscience*, 5(7), 505–509. DOI: 10.1038/ngeo1477
- Greiner J.T., McGlathery K.J., Gunnell J. and McKee B.A. (2013). Seagrass Restoration Enhances “Blue Carbon” Sequestration in Coastal Waters. *PLoS ONE*, 8(8), 1–8. DOI: 10.1371/journal.pone.0072469
- Hammer Ø., Harper D.A.T. and Ryan P.D. (2001). PAST: Paleontological Statistics software package for education and data analysis. *Palaeontologia Electronica*, 4(1), 9. https://palaeo-electronica.org/2001_1/past/past.pdf
- Harahap Z.A., Khairunnisa, Susetya I.E. and Rahayu Y.P. (2021). Estimation of carbon stock in seagrass communities in Central Tapanuli. *IOP Conference Series: Earth and Environmental Science*, 944(1), 012064. DOI: 10.1088/1755-1315/944/1/012064
- Hartoko A., Sembiring Y.T. and Latifah N. (2021). Seagrass Chlorophyll-a, Biomass and Carbon Algorithms Based on the Field and Sentinel-2A Satellite Data at Karimunjawa Island, Indonesia. *Science and Technology Indonesia*, 6(3), 121–130. DOI: 10.26554/sti.2021.6.3.121-130
- Haryati U. and Dariah A. (2019). Carbon emission and sequestration on tin mined land: A case study in Bangka Belitung Province. *IOP Conference Series: Earth and Environmental Science*, 393(1), 012097. DOI: 10.1088/1755-1315/393/1/012097
- Hernawan U.E., Rahmawati S., Ambo-Rappe R., Sjafrie N.D.M., Hadiyanto H., Yusup D.S., Nugraha A.H., La Nafie Y.A., Adi W., Prayudha B., Irawan A., Rahayu Y.P., Ningsih E., Riniatsih I., Supriyadi I.H. and McMahan K. (2021). The first nation-wide assessment identifies valuable blue-carbon seagrass habitat in Indonesia is in moderate condition. *Science of The Total Environment*, 782, 146818. DOI: 10.1016/j.scitotenv.2021.146818
- Ibrahim I., Haryadi D. and Wahyudin N. (2018). From Charm To Sorrow: The Dark Portrait Of Tin Mining In Bangka Belitung, Indonesia. *PEOPLE: International Journal of Social Sciences*, 4(1), 360–382. DOI: 10.20319/pijss.2018.4.1.360382
- Irzon R. (2021). Penambangan timah di Indonesia: Sejarah, masa kini, dan prospekti. *Jurnal Teknologi Mineral Dan Batubara*, 17(3), 179–189. DOI: 10.30556/jtmb.Vol17.No3.2021.1183
- Khairunnisa K., Harahap Z.A. and Farahisah H. (2023). The Variability of Sedimentary Carbon Stock in Seagrass Ecosystem in Central Tapanuli, Indonesia. *IOP Conference Series: Earth and Environmental Science*, 1221(1), 012081. DOI: 10.1088/1755-1315/1221/1/012081
- Koedsin W., Intararuang W., Ritchie R. and Huete A. (2016). An Integrated Field and Remote Sensing Method for Mapping Seagrass Species, Cover, and Biomass in Southern Thailand. *Remote Sensing*, 8(4), 292. DOI: 10.3390/rs8040292
- Lanuru M., Ambo-Rappe R., Amri K. and Williams S.L. (2018). Hydrodynamics in Indo-Pacific seagrasses with a focus on short canopies. *Botanica Marina*, 61(1), 1–8. DOI: 10.1515/bot-2017-0037
- Luo H., Liu S., Ren Y., Jiang Z., Wu Y., Zhang X., Li J. and Huang X. (2022). Eutrophication decreases *Halophila beccarii* plant organic carbon contribution to sequestration potential. *Frontiers in Marine Science*, 9(August), 1–11. DOI: 10.3389/fmars.2022.986415
- Marbà N., Arias-Ortiz A., Masqué P., Kendrick G.A., Mazarrasa I., Bastyan G.R., Garcia-Orellana J. and Duarte C.M. (2015). Impact of seagrass loss and subsequent revegetation on carbon sequestration and stocks. *Journal of Ecology*, 103(2), 296–302. DOI: 10.1111/1365-2745.12370
- Mashoreng S., Nafie Y.A. La, Selamat B., Isyirini R. and Amri K. (2021). Changes in seagrass carbon stock: implications of decreasing area and percentage cover of seagrass beds in Barranglompo Island, Spermonde archipelago, South Sulawesi, Indonesia. *IOP Conference Series: Earth and Environmental Science*, 763(1), 012014. DOI: 10.1088/1755-1315/763/1/012014
- Mazarrasa I., Samper-Villarreal J., Serrano O., Lavery P.S., Lovelock C.E., Marbà N., Duarte C.M. and Cortés J. (2018). Habitat characteristics provide insights of carbon storage in seagrass meadows. *Marine Pollution Bulletin*, 134, 106–117. DOI: 10.1016/j.marpolbul.2018.01.059
- McHenry J., Rassweiler A., Hernan G., Dubel A.K., Curtin C., Barzak J., Varias N. and Lester S.E. (2023). Geographic variation in organic carbon storage by seagrass beds. *Limnology and Oceanography*, 68(6), 1256–1268. DOI: 10.1002/lno.12343
- McKenzie L.J. and Yoshida R.L. (2020). Over a decade monitoring Fiji's seagrass condition demonstrates resilience to anthropogenic pressures and extreme climate events. *Marine Pollution Bulletin*, 160(August), 111636. DOI: 10.1016/j.marpolbul.2020.111636
- Nopiansyah D., Adi W. and Febrianto A. (2021). Struktur Komunitas Gastropoda Di Ekosistem Lamun Di Pantai Puding Kabupaten Bangka Selatan. *Journal of Tropical Marine Science*, 4(2), 59–64. DOI: 10.33019/jour.trop.mar.sci.v4i2.2123
- Nugraha A.H., Syahputra I.P., Dharmawan I.W.E., Arbi U.Y., Hermanto B., Kurniawan F., Roni S., Wibisono G. and Rivani A. (2023). Sebaran Jenis dan Kondisi Tutupan Lamun di Perairan Kepulauan Riau. *Journal of Marine Research*, 12(3), 431–438. DOI: 10.14710/jmr.v12i3.36274
- Nur S., Nurdjaman S., Dika Praba P Cahya B. and Haidar Dzar Al-Ghifari K. (2021). Integrating sentinel-2 spectral-imagery and field data of seagrass coverage with species identification in the coastal of Riau Islands, Indonesia. *Borneo Journal of Marine Science and Aquaculture (Bjomsa)*, 5(2), 78–82. DOI: 10.51200/bjomsa.v5i2.2710

- Pamungkas A. and Husrin S. (2020). Pemodelan Sebaran Sedimen Tersuspensi Dampak Penambangan Timah Di Perairan Bangka. *Jurnal Ilmu Dan Teknologi Kelautan Tropis*, 12(2), 353–368. DOI: 10.29244/jitkt.v12i2.27875
- Park S.R., Kim S., Kim Y.K., Kang C.-K. and Lee K.-S. (2016). Photoacclimatory Responses of *Zostera marina* in the Intertidal and Subtidal Zones. *PLOS ONE*, 11(5), e0156214. DOI: 10.1371/journal.pone.0156214
- Rifai H., Hernawan U.E., Zulpikar F., Sondakh C.F.A., Ambo-Rappe R., Sjafrie N.D.M., Irawan A., Dewanto H.Y., Rahayu Y.P., Reenyan J., Safaat M., Alifatri L. ode, Rahmawati S., Hakim A., Rusandi A. and Wawo M. (2022). Strategies to Improve Management of Indonesia's Blue Carbon Seagrass Habitats in Marine Protected Areas. *Coastal Management*, 50(2), 93–105. DOI: 10.1080/08920753.2022.2022948
- Rosalina D., Herawati E.Y., Musa M., Sofarini D., Amin M. and Risjani Y. (2019). Lead Accumulation and Its Histological Impact on *Cymodocea serrulata* Seagrass in the Laboratory. *Sains Malaysiana*, 48(4), 813–822. DOI: 10.17576/jsm-2019-4804-13
- Rosalina D., Jamil K., Arafat Y., Amalia R. and Leilani A. (2023). Mapping of seagrass ecosystem on Bontosua Island, Pangkep District, South Sulawesi, Indonesia. *Biodiversitas Journal of Biological Diversity*, 24(4). DOI: 10.13057/biodiv/d240411
- Roswaty S., Muskananfolia M.R. and Purnomo P.W. (2014). Tingkat Sedimentasi di Muara Sungai Wedung Kecamatan Wedung, Demak. *Management of Aquatic Resources*, 3(2), 129–137. DOI: <https://doi.org/10.14710/marj.v3i2.5016>
- Samper-Villarreal J., Lovelock C.E., Saunders M.L., Roelfsema C. and Mumby P.J. (2016). Organic carbon in seagrass sediments is influenced by seagrass canopy complexity, turbidity, wave height, and water depth. *Limnology and Oceanography*, 61(3), 938–952. DOI: 10.1002/lno.10262
- Sjafrie N.D.M., Triyono, Zulpikar F., Rahmawati S. and Hernawan U.E. (2022). Preliminary study on community's perception of seagrass restoration on Pari Island, Seribu Islands Regency. *IOP Conference Series: Earth and Environmental Science*, 967(1), 012028. DOI: 10.1088/1755-1315/967/1/012028
- Stankovic M., Ambo-Rappe R., Carly F., Dangan-Galon F., Fortes M.D., Hossain M.S., Kiswara W., Van Luong C., Minh-Thu P., Mishra A.K., Noiraksar T., Nurdin N., Panyawai J., Rattanachot E., Rozaimi M., Soe Htun U. and Prathep A. (2021). Quantification of blue carbon in seagrass ecosystems of Southeast Asia and their potential for climate change mitigation. *Science of The Total Environment*, 783, 146858. DOI: 10.1016/j.scitotenv.2021.146858
- Sudo K., Quiros T.E.A.A.L., Prathep A., Luong C. Van, Lin H.-J.J., Bujang J.S., Ooi J.L.S., Fortes M.D., Zakaria M.H., Yaakub S.M., Tan Y.M., Huang X. and Nakaoka M. (2021). Distribution, Temporal Change, and Conservation Status of Tropical Seagrass Beds in Southeast Asia: 2000–2020. *Frontiers in Marine Science*, 8. DOI: 10.3389/fmars.2021.637722
- Sugianti Y. and Mujiyanto M. (2020). Current Status and Species Diversity of Seagrass in Panjang Island, Banten. *ILMU KELAUTAN: Indonesian Journal of Marine Sciences*, 25(1), 15–22. DOI: 10.14710/ik.ijms.25.1.15-22
- Supriyadi I.H., Cappenberg H.A.W., Wouthuyzen S., Hafizt M., Rahmawati S., Alifatri L.O. and Suyarso S. (2021). Seagrass Condition at Some Small Islands in The Taka Bonerate National Marine Park, South Sulawesi Indonesia. *Jurnal Segara*, 17(2), 83. DOI: 10.15578/segara.v17i2.9575
- Syafutra R., Adi W., Iqbal M. and Yustian I. (2018). Short communication: Dugong dugon Müller, 1776 (*Sirenia*, *Dugongidae*) in Bangka Island, Indonesia. *Biodiversitas*, 19(3), 773–780. DOI: 10.13057/biodiv/d190310
- Tanner J.E., McSkimming C., Russell B.D. and Connell S.D. (2021). Rapid restoration of belowground structure and fauna of a seagrass habitat. *Restoration Ecology*, 29(1). DOI: 10.1111/rec.13289
- Tebaij S., Mampiooper D.C., Batto M., Manuputty A., Tuharea S. and Clement K. (2021). The Status of Seagrass Health: Supporting Sustainable Small-Scale Fisheries in Misool Marine Protected Area, Raja Ampat, Indonesia. *ILMU KELAUTAN: Indonesian Journal of Marine Sciences*, 26(3), 136–146. DOI: 10.14710/ik.ijms.26.3.136-146
- Traganos D., Aggarwal B., Poursanidis D., Topouzelis K., Chrysoulakis N. and Reinartz P. (2018). Towards Global-Scale Seagrass Mapping and Monitoring Using Sentinel-2 on Google Earth Engine: The Case Study of the Aegean and Ionian Seas. *Remote Sensing*, 10(8), 1227. DOI: 10.3390/rs10081227
- Unsworth R.K.F.F., McKenzie L.J., Collier C.J., Cullen-Unsworth L.C., Duarte C.M., Eklöf J.S., Jarvis J.C., Jones B.L. and Nordlund L.M. (2019). Global challenges for seagrass conservation. *Ambio*, 48(8), 801–815. DOI: 10.1007/s13280-018-1115-y
- van Katwijk M.M., van der Welle M.E.W., Lucassen E.C.H.E.T., Vonk J.A., Christianen M.J.A., Kiswara W., Inayat al Hakim I., Arifin A., Bouma T.J., Roelofs J.G.M. and Lamers L.P.M. (2011). Early warning indicators for river nutrient and sediment loads in tropical seagrass beds: A benchmark from a near-pristine archipelago in Indonesia. *Marine Pollution Bulletin*, 62(7), 1512–1520. DOI: 10.1016/j.marpolbul.2011.04.007
- Wahyudi A.J., Rahmawati S., Irawan A., Hadiyanto H., Prayudha B., Hafizt M., Afdal A., Adi N.S., Rustam A., Hernawan U.E., Rahayu Y.P., Iswari M.Y., Supriyadi I.H., Solihudin T., Ati R.N.A., Kepel T.L., Kusumaningtyas M.A., Daulat A., Salim H.L., ... Kiswara W. (2020). Assessing Carbon Stock and Sequestration of the Tropical Seagrass Meadows in Indonesia. *Ocean Science Journal*, 55(1), 85–97. DOI: 10.1007/s12601-020-0003-0
- Wisha U.J. and Ondara K. (2017). Total Suspended Solid (TSS) Distributed by Tidal Currents during Low to High Tide Phase in the Waters of Sayung, Demak: Its Relations to Water Quality Parameters. *Journal of Marine and Aquatic Sciences*, 3(2), 154. DOI: 10.24843/jmas.2017.v3.i02.154-162
- Yamamoto T., Malingin M.A.C.L., Pepino M.M., Yoshikai M., Campos W., Miyajima T., Watanabe A., Tanaka Y., Morimoto N., Ramos R., Pagkalinawan H. and Nadaoka K. (2019). Assessment of coastal turbidity improvement potential by terrigenous sediment load reduction and its implications on seagrass inhabitable area in Banate Bay, central Philippines. *Science of The Total Environment*, 656, 1386–1400. DOI: 10.1016/j.scitotenv.2018.11.243
- Yau Y.Y.Y., Reithmaier G., Majtényi-Hill C., Serrano O., Piñeiro-Juncal N., Dahl M., Mateo M.A., Bonaglia S. and Santos I.R. (2023). Methane Emissions in Seagrass Meadows as a Small Offset to Carbon Sequestration. *Journal of Geophysical Research: Biogeosciences*, 128(6), 1–18. DOI: 10.1029/2022jg007295

METHODS OF STUDYING THE ALPINE TREELINE: A SYSTEMATIC REVIEW

Andrey G. Purekhovskiy^{1*}, Alexey N. Gunya¹, Evgeniy Yu. Kolbowski^{1,2}, Alexei A. Aleinikov¹

¹ Institute of Geography, Russian Academy of Science, Staromonetnyi lane, 29, Moscow, 119017, Russia

² Lomonosov Moscow State University, Leninskie Gory, 1, Moscow, 119991, Russia

*Corresponding author: purekhovskii@mail.igras.ru

Received: November 17th 2024 / Accepted: February 16th 2025 / Published: March 31st 2025

<https://doi.org/10.24057/2071-9388-2025-3735>

ABSTRACT. This paper provides a review and comparison of the methods for assessing trends in the dynamics of alpine treeline (ATL) in high mountains are presented in. The methods analyzed are contemporary, traditionally used (dendrochronological and paleocarpological methods, retrospective analysis of historical photographs and geodetic surveying, and multi-temporal aerial photography), and innovative ones developed in recent decades (semi-automatic and automatic methods of interpretation of high- and medium-resolution space imagery and methods of space imagery interpretation using different techniques, such as classification, segmentation, vegetation index analysis, and machine learning algorithms). Different interpretations of the concept of 'alpine treeline', which is currently established in geobotany and landscape sciences, are discussed. The attention to ATL dynamics is caused by global climate change's widespread forest increase and the decline in high mountain pastures. The ATL phenomenon's geographic map is condensed and displayed. There is an overview of the experience with different methods in varying mountain regions around the world. Each method is described in terms of its spatial scale, coverage, advantages, labor intensity, complexity, and limitations. It is shown that The effectiveness of the methods mainly depends on two key factors: the size of the area being studied and the time period over which changes are observed. The problem that still limits the use of remote sensing data is the contradiction between the accuracy of measurements and the coverage of the territories involved. To solve this problem, we suggest using a mix of methods that involve automatically classifying medium-resolution space images. This will be done by training on data collected from both fieldwork and lab experiments using different techniques.

KEYWORDS: altitudinal treeline, mountain treelines, high-mountain landscapes, GIS-modeling of landscape transformation

CITATION: Purekhovskiy A. G., Gunya A. N., Kolbowski E. Yu., Aleinikov A. A. (2025). Methods Of Studying The Alpine Treeline: A Systematic Review. *Geography, Environment, Sustainability*, 105-116

<https://doi.org/10.24057/2071-9388-2025-3735>

ACKNOWLEDGEMENTS: The reported research was funded by the State Assignment of the Institute of Geography, Russian Academy of Sciences, project no. AAAA-A19-119021990093-8 (FMGE-2019-0007).

Conflict of interests: The authors reported no potential conflict of interest.

INTRODUCTION

In mountainous areas, where the growing conditions for tree and shrub species become critically unfavorable, a treeline (alpine treeline [ATL]) is an important integral feature accessible for recording and measurement by both visual and instrumental methods. A relatively narrow ecotone (sometimes several meters but more often the first dozens of meters) between the 'subalpine' forest with a more or less closed forest canopy and open herbaceous vegetation is clearly visible in the upper mountain belt through remote sensing of the Earth. At the same time, a treeline is very sensitive to average, long-term trends in climate change; both of these circumstances make the conventional ATL a popular object of research to monitor the transformation of high-mountain landscapes worldwide (Steinbauer et al. 2016).

There is no doubt that the climate plays an important role in the dynamics of the ATL (Pearson and Dawson 2003). Microclimatic research at the forest edge revealed that the nature of forest growth was decisively influenced

by temperature conditions: the sum of active temperatures in a vegetation period limits tree growth, and winter temperatures play a key role in the survival of young trees and the likelihood of damage to adult specimens (Chen et al. 2011). Changes in air and soil temperature (especially in spring), as well as increases or decreases in precipitation, lead to weaker or stronger impacts of climatic factors on all phases of the life cycle and vegetation of plants. In turn, this affects the germination and survival of undergrowth and predetermines the tree growth rate and mortality of adult trees at the boundaries of their distribution areas. However, the recorded shift and transformation of forest boundaries cannot be explained solely by temperature and moisture exchange factors; this would be an oversimplification. When observing both the upper (altitude) forest boundary in the mountains and the northern (latitudinal) forest boundary, it becomes clear that the changes in these two global ecotones are caused by complex cause-and-effect relationships among various landscape components, primarily climate and vegetation, as well as mesorelief, soil type, soil moisture dynamics, plant succession, and previous

(historical) and current economic use (i.e. anthropogenic load; Lenoir et al. 2009).

In the mountains, the geomorphometric parameters of relief (slope gradient, aspect, plane curvature and profile curvature) play a particularly important role in the formation of heat and moisture exchange conditions and, consequently, in the differentiation of landscape sites. The macrorelief of the mountains (inter- and intra-mountain depressions, long and deeply rugged ravines and ridges) modifies regional climatic regimes and generally causes significant differences in ATL localization. At the local level, the microrelief (slope, peak and saddle, ridge and spur surfaces) predetermines the existence of harsh (windward, dry, extremely arid or 'cold') and favorable (humid, warm and wind-shadowed) habitats. The latter can form a kind of refugium, where both the actual position of the ATL and its response to climatic fluctuations will differ from the general regional one. These factors make a contribution to the different scales of localization and transformation of ATL, the latter being a phenomenon of the landscape structure of mountains (Morley et al. 2018).

High-mountain forests are important carbon accumulation and sequestration zones. They conserve soils and groundwater basins that feed a significant share of the world's population. Studying their changes is necessary for understanding the consequences of the loss of ecosystem services, especially at a time of sharp climate fluctuations associated with global warming (Devos et al. 2022). Current climate change scenarios predict a 0.3°C–4.8°C increase in the average global temperature by 2100 compared to the 1985–2005 average (IPCC 2013). Therefore, there is every reason to expect significant shifts in the geographic distribution of a large number of tree species, for which the change in heat and water availability may affect range expansion, shrinkage, or fragmentation. Mountain areas will experience larger increases in seasonal temperatures compared to other parts of the world, making them important indicators of global climate change effects (Calvin et al. 2023). However, the cause-and-effect relationships between the climate and the ATL are still poorly understood. ATL dynamics manifest themselves differently in various mountain regions; explaining these differences by historical and/or current patterns of nature management is significantly complicated.

The long-term isolation of mountain forests and fragmentation of habitats have resulted in exceptionally large numbers of endemic and rare plant and animal species inhabiting mountain areas. Any changes in the distribution of mountain forests caused by either climate change or anthropogenic load affect the biodiversity of the entire region significantly. Studies of forest distribution in the mountains are relevant for assessing the contribution of global climate change to the dynamics of ecosystems and landscapes. Our research focuses on organizing the ways to study the ATL and identifying the problems with these methods by looking at recent scientific articles and our own research data.

State-of-the-art

The studies of the state and dynamics of the ATL date back to the late 19th–early 20th centuries, when they were based primarily on visual comparison methods and analyzing various kinds of historical evidence (e.g. oral reports, old maps or travelers' texts). This, indeed, provided very rough estimates. Although such estimates were not systematic, they allowed for drawing some conclusions about the key position factors and ATL dynamics. More

specialized studies of the treeline began in the 1930s, alongside the study of the physiological response of trees and undergrowth under critical environmental conditions in the mountains (Holtmeier and Broll 2019). Researchers also conducted both in situ and in vivo experimental studies (Däniker 1923; Steiner 1935).

The catastrophic avalanches in the European Alps in the middle of the 20th century, caused by the super snowy winters of 1951–1954 gave new impetus to fundamental and applied treeline research. In Austria and Switzerland, a detailed analysis of the physiological response of trees located in the marginal zone of their habitat to climatic parameters and human economic impact was performed. These results made it possible to lay the scientific foundations for mountain forest management, including, most importantly, the practices of forest restoration (Holtmeier 2010).

After it was concluded that the modern treeline tends to shift upwards in mountain systems and to northern latitudes on the plain due to climate change, this phenomenon attracted much attention from researchers in the late 20th century. Since the 1990s, the number of publications on this topic has increased rapidly (by about 90%) due to the availability of remote sensing data and the possibility of developing geospatial models (Holtmeier and Broll 2019).

Forest boundary studies by geographers, landscape ecologists, foresters, and forest geobotanists have become focused on the analysis of the configuration of forest area boundaries under the influence of both natural (abiotic and biotic) and anthropogenic factors. The diversity of natural conditions and the multiplicity of invariants of economic impact (including historical and inherited variants) have generated significant inconsistencies in the generalizations and interpretations of results, especially when attempting to use models and extrapolate local data to macro-regional and global levels.

The development of remote sensing methods in recent decades (aerial imagery, orthophotoplanes, medium- and high-resolution satellite images and LiDAR photography), along with geostatistical analysis, initiated building local spatiotemporal models of forest ecosystems. These studies have contributed to a more comprehensive understanding of the driving factors of ATL changes, including the influence of the entire complex of landscape conditions (lithological, geomorphological, soil, hydrological, etc.) on spatio-temporal patterns of ATL dynamics and associated ecological processes at regional, zonal, and global scales (Morley et al. 2018).

A particular problem in studying the dynamics of mountain landscapes has always been their poor accessibility. Therefore, the model territories of these studies are small in area and unevenly distributed across different mountain systems. As a rule, long-term studies (monitoring) are conducted at the same place (e.g. at university sites); this allows for considering already accumulated field material (geobotanical descriptions, large-scale landscape maps and photographs). Meanwhile, specialists may ignore areas near or far from such sites. Therefore, a significant number of the already completed field studies, when generalized at the global (and even macroregional) scales, represent a set of randomly distributed 'points' (Fig. 1). Even if these studies are supported by geospatial models obtained using modern remote sensing processing methods, the available and even pooled information does not yet allow one to build a reliable overall picture of the localization and transformation of the upper boundary of mountain forests on different continents of the planet.

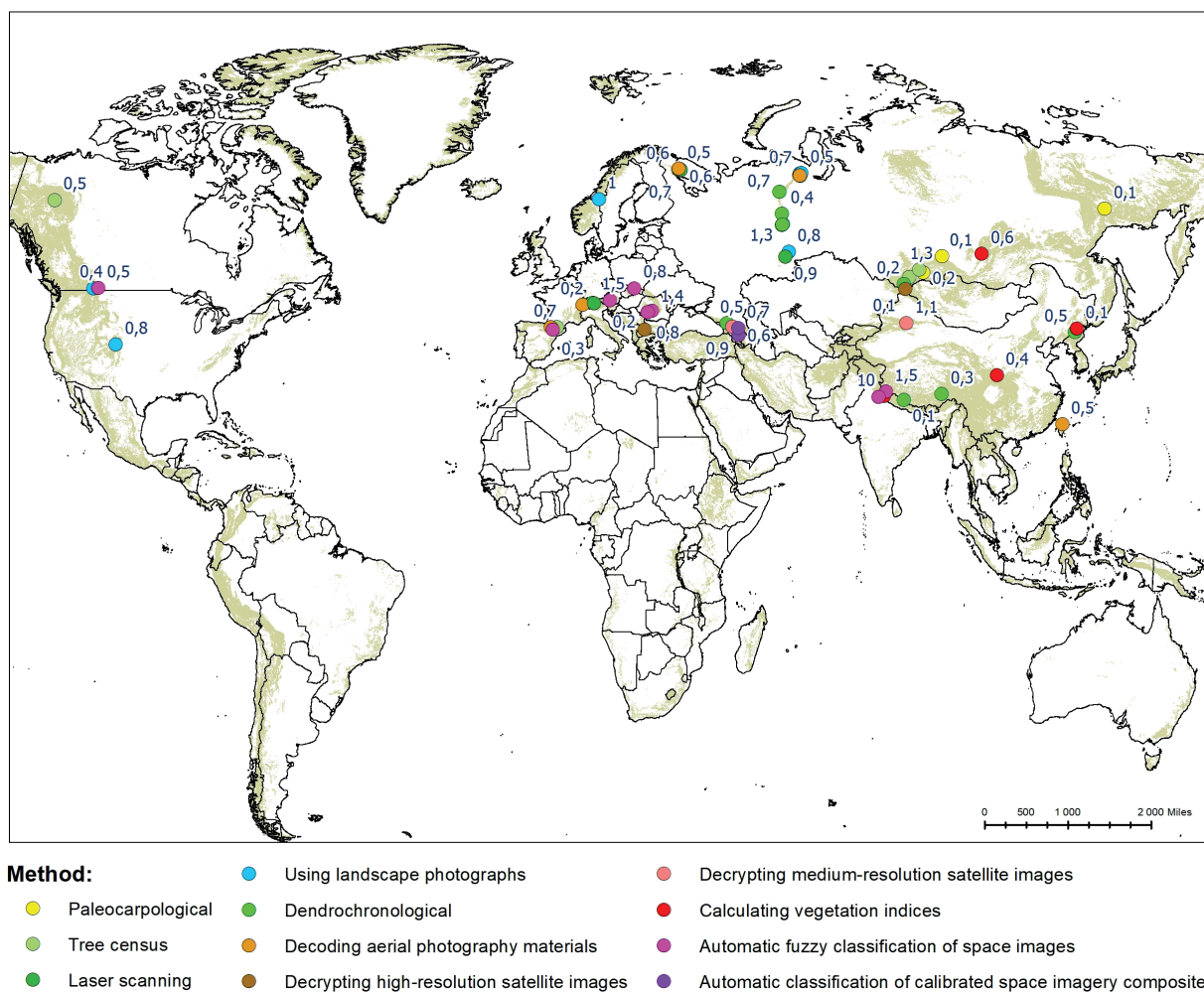


Fig. 1. Places of study of the alpine treeline; values near a point indicate the average speed of the dynamics (meters per year), the color of the point corresponds to the type of research method

It would seem that the processing of remote sensing data with modern methods of geostatistical analysis allows obtaining data on the localization and transformation of the ATL at any spatial level, including the regional one. All current ways of classifying space images rely on local samples for training. These samples might not fully capture the true complexity of the landscape and the specific patterns found in the ATL ecotone. It has been assumed that an accurate assessment of the forest boundary dynamics requires synthetic methods using complex models that consider differentiation at the landscape site scale (facies, elemental landscapes) and that are based on a preliminary understanding of the features of the landscape pattern, so this makes its further interpolation possible at the landscape scales or larger natural units, i.e., physical-geographical regions and countries (Grabherr et al. 2000).

The concept of the upperforest boundary has undergone significant over time. The idea of the boundary as a 'line' is recognized as an unacceptable simplification by researchers of various fields (geobotanists, ecologists, and last but not least, landscape science specialists). It may be considered that the ATL is a kind of strip, a transition between 'forest' and 'non-forest' zones, which varies in width and configuration; its complexity is largely determined by a set of landscape-forming conditions. In this work, the ATL is understood as an ecotone that records the transition from the closed forest canopy to the treeless space in a gradient of deteriorating heat and moisture exchange conditions. The variety of ecotones depends on the types of forests. These can include groups of coniferous or deciduous trees, elfin woodland, or mixed morphological forms of woody vegetation from

different species. On the other hand, these can be the types of open spaces, as the latter can be represented by shrub thickets (e.g. rhododendrons), alpine meadows, and mountain tundra with moss and shrub ground covers.

At the present time, the conceptual framework for studying the ATL is preconditioned by the parameters that characterize the state and dynamics of the ATL, the development of models that explain the driving factors of ATL dynamics, the assessment of the stability of dynamics (short-term dynamics or trends), the representativeness of the identified patterns, and the possibility of their application in other regions.

MATERIALS AND METHODS

We searched ISI Web of Science, Scopus Preview, Springer Nature, ResearchGate, Refseek, BioOne Digital Library, Bioline International and eLIBRARY databases for scientific articles published since 1995 using the following set of keywords in Russian ("верхняя граница леса" OR "граница леса" OR "верхние границы леса" OR "верхняя граница древесной растительности" OR "динамика границ поясов" OR "эктон верхней границы древесной растительности") and English ("Alpine tree line" OR "Alpine treeline ecotone" OR "Treeline, Tree line, Timberline, Treeline ecotone" OR "Tree line advance" OR "Tree line dynamics" OR "Treeline ecotone dynamics" OR "Tree line change rate" OR "Dynamics of borders of belts" OR "Tree stand dynamics and Upper tree-line").

Simultaneously, we selected combinations of terms found in the headings of articles, annotations and keywords

that appealed to techniques using remote sensing data and their processing algorithms: “космические снимки” OR “повторные ландшафтные фотографии” OR “снимки сверхвысокого разрешения” OR “лазерное сканирование” OR “дендрохронологический анализ” OR “remote sensing” (Image classification, Change detection, Repeat photography, Dendroecology, Convolutional neural network, Landsat and LiDAR).

Also, we looked at full-scale literature reviews, including those by F.K. Holtmeier and G. Broll (2019) and P.J. Morley and others (2018), as well as the reference lists from the articles we studied. We excluded articles that looked at the physiological and developmental processes of the ATL but did not examine the changes in the ecotone from the dataset. Due to the disproportionate quantitative predominance of articles on dendrochronological topics, general publications devoted to the main mountain regions of the world were selected from the total pool. If one author had a number of studies published, the article that most reflected the applied methodology and results of the study was taken for the analysis.

The search yielded 591 articles, 55 of which were finally considered after omitting the publications that did not meet the selection criteria and duplicates. The sorting was performed according to the ROSES flow chart for systematic reviews (Haddaway et al. 2017). The articles examined for this analysis discussed various methods used to study the changes in the ATL in the major mountain ranges of Eurasia and North America.

As a result, the final list included only those articles that contained descriptions of methods for studying the ATL and included the following parameters: area of the territory under study, height and localization of the ATL,

1. time range of the study, the speed and nature of the dynamics of the ATL,
2. the set of measurements used, and a general assessment of the effectiveness of the methodology.

The interpretation and comparison of the obtained data also considered the geographical features of the study regions, primarily the role of the anthropogenic factor (see Supplementary material). The data collected in this review have been analyzed using R¹. The map of the spatial distribution of cases was created using QGIS², where the mountain systems (yellow) are presented according to the model of the Global Mountain Biodiversity Assessment (GMBA) (Snethlage et al. 2022).

RESULTS

Tree census

Counting tree volume and determining the age of trees using drilling represent one of the oldest methods for studying the ATL in the mountains; this is an integral part of forest taxation. The technique consists of laying out test zones at model areas, where taxation parameters are measured for each tree, and the core is extracted with a Pressler drill borer at a height of up to 30 cm from the ground surface. Specialized semi-automatic measuring systems, such as LINTAB and TSAP, are used to measure the width of the growth rings with high accuracy (up to 0.01 mm) and cross-date samples. The COFECHA (DPL) program then performs additional dating control. Individual cross-matched chronologies are standardized using a negative exponential or linear regression. The ARSTAN program is used to standardize and calculate general chronologies by averaging individual data series.

This technique has been widely applied in vast territories. Some example ATL studies were conducted in the Khibiny Mountains of the Kola Peninsula (Konstantinov and Volkov 2022), the Caucasus (Dyakonov and Bochkarev 2012), the Altai Mountains (Bocharov 2011), the Western Sayan Mountains (Istomov 2005), the Tuva Republic (Russia; Kolunchukova and Reznikov 2020), the Nepalese Himalayas (Shrestha et al. 2015), the Tibetan Plateau (Liang et al. 2011), the eastern and western mountain systems of China (Du et al. 2018; Wang et al. 2022), the western part of the Mackenzie Mountains (Mamet and Kershaw 2012), the Central Alps (Frei et al. 2023) and the Pyrenees (Batllori et al. 2010).

Laser scanning method

Recent tree census studies have begun to use high-tech tools, such as laser scanning methods. A review of the application of this method can be found in a number of papers, particularly studies performed at the Southern Urals (Vorobyeva et al. 2022), the Swiss Alps (Coops et al. 2013) and the Khibiny Mountains (Nisametdinow et al. 2021). Processed LiDAR data obtained from airborne or ground platforms makes it possible to remotely map tree trunks and shrubs in the transition zone with high accuracy and determine their characteristics, which allows one to expand the research area significantly.

Paleocarpological method

Paleocarpological studies of peat deposits provide the deepest chronological section (up to 4,000 years) of forest boundary dynamics. The technique involves taking kerns in Pleistocene deposits and obtaining organic fractions from them. Carpological remains (seeds, fruits, and megaspores) are identified by referring to collections of fossil carpoids. The results are analyzed by the method of carpological diagrams (the number of taxa remains in a sample of 100 cm³) using specialized programs, such as TILIA. As a result of the reconstruction of coastal and marsh vegetation, based on the analysis of coenotic groups of species, a model of changes in the altitudinal ranges is obtained.

Due to the limited distribution of peat deposits in the ATL and approximate estimates of the dynamics, this method is rarely used in the mountains. Currently, the known studied research areas are only the mountainous territories in Russia: the Sayan Mountains, mountains in the Tuva Republic, and Eastern Siberia (Koshkarov et al. 2019; Lytkin 2019; Murzakmatov et al. 2014).

Method of using landscape photographs

The method of comparing the historical and modern landscape photographs taken from the same points has proven itself in various mountainous regions (Webb, Boyer 2010). In addition to the visual processing of landscape photographs, the algorithm includes the bookmarking of height profiles, collecting dendrochronological samples, and considering growth tables of forest stands to obtain quantitative characteristics of the latter based on landscape photographs. Usually, a transformed grid is built for the analysis of photographs, and each grid cell is assigned an attribute of vegetation condition. Covariance analysis methods are used to process the obtained matrices.

The technique has long been used in Russia for the

¹ R Core Team (2023). R: A Language and Environment for Statistical Computing. R Foundation for Statistical Computing. Vienna, Austria. URL: <https://www.R-project.org>.

² QGIS Development Team (2019). QGIS Geographic Information System. Open-Source Geospatial Foundation. URL: <https://qgis.org>

Polar, Subpolar, and Southern Urals, where the images first taken in the 1960s were used for comparison (Grigor'ev et al. 2013; Nikolin et al. 2015; Shiyatov 2009; Shiyatov, Mazepa, Moiseev 2001; Shiyatov and Terentyev 2005). In Canada, the photographs taken in 1914 were compared with LiDAR data and repeated photographs from the Mountain Legacy Project in the West Castle Watershed (Alberta) (McCaffrey and Hopkinson 2020). In the USA, a large set of photographs taken over a period of 148 years was analyzed (Peterson et al. 2022). A similar method for the visual determination of the ATL was used in Scandinavia (Kullman and Öberg 2009). Changes in tree height in southern Sweden were quantified for the period 1915–2007 and for two time periods of 1915–1975 and 1975–2007, separately. The algorithm used repeated trips to monitoring sites (altitude belt transects) and measurements of treeline position (in meters above sea level) during the three specific periods.

The method is quite simple, but the authors note its shortcomings, which are the inaccuracies arising during interpretations in the laboratory and the locality of the data obtained, which does not allow the wide extrapolation of the research results.

Dendrochronological method

Dendrochronological analysis is still the most widely used method for studying the ATL. It involves measuring the width of the wood rings from the scanned images of tree trunk cores taken from the study area and their subsequent analysis using statistical processing programs designed especially for dendrochronological series, such as the International Dendrochronological Library, or general statistical software, such as R Core Team. The results of the analysis make it possible to confirm the correlation of tree growth changes with astrophysical (sun position, solar activity), climatic (average monthly positive air temperatures) and geomorphometric (slope gradient and aspect) parameters; the presence of permafrost; the peat layer thickness in soils; the frequency of avalanches; land use; and other factors. Dendrological data allow one to estimate the trends of temporal changes in growth for the region under study and allocate the main parameters of the system's response to climatic fluctuations. Dendrochronological analysis methods are often used together with ground mapping techniques. The limitations of this method are the choice and use of only adult trees for coring without studying other components of the ATL and the locality, the limitation and the complexity of the interpolation of results.

The most systematic and long-term studies using dendrochronological methods were conducted in the Northern and Subpolar Urals (Devi et al. 2018; Dyakonov and Bochkarev 2012; Galaco 2002; Kapralov 2007; Mazepa and Shiyatov 2015; Moiseev and Nagimov 2010; Moiseev et al. 2008). Other important research in mountain regions was done in the Elbrus area of the Caucasus (Dyakonov and Bochkarev 2012), the Tibetan Plateau (Liang et al. 2011), the Changbai Mountains (Du et al. 2018) and the Nepalese Himalayas (Shrestha et al. 2015).

The trends in ATL dynamics were studied comprehensively over the past century (1901–2004) using tree-ring width data from 13 regions representing most of the key mountain landscapes of Eurasia and America (Camarero et al. 2021). A general increase in the treeline altitude was noted during the 20th century, with the trend becoming most pronounced since the 1980s. A positive relationship between tree growth rates and growing season temperatures was confirmed. The highest growth

rates, against the background of pronounced warming, were recorded in the Pyrenees; declines in growth rates were found in some areas in the Rocky Mountains and Scandinavian Mountains. For mountain rainforests of the Southern Hemisphere, significant positive growth trends turned out to be relatively independent of the relatively weakly changed temperature background (in both winter and summer seasons). It was suggested that in the 21st century, tree growth and the rise of the ATL will cease to depend directly on the temperature factor in all mountainous regions of the world.

Method of decoding aerial photography materials

The method of decoding multi-temporal aerial photography of the Earth's surface makes it possible to obtain spatial data on the changes in the upper forest boundary. The algorithm includes procedures for bringing historical aerial images into a single projection, combined with modern satellite images and vector maps of a similar scale. This results in fixing the contrastingly visible forest boundary and comparing the localization using geostatistical tools. The method was used in a study of Taiwan's mountain forests, where a clearly visible forest boundary was drawn using aerial photographs from 1963, 1975, and 2001, and then the contours were compared (Greenwood et al. 2014). At the Polar Urals, aerial photography materials from 1962 and 1964 were used (Mikhailovich 2016). The upward shift of the sparse forest boundary here was assessed on the basis of aerial photography using a digital elevation model in the ArcGIS program (Nizametdinov et al. 2022).

A study on the Catalan Pyrenees used more than 200 pairs of aerial photographs taken 50 years apart, in 1956 and 2006 (Ameztegui et al. 2016). Neural networks were used to analyze aerial photographs in the Swiss Alps, which helped estimate changes in the ATL over 30 years, using black and white aerial photographs taken in 1980 and 2010 (Wang et al. 2022). In this case, a convolutional neural network model was first created based on three classes of objects calculated from airborne laser scanning data, considering black and white aerial photographs from 2010; then, the model was trained on the samples of historical black and white aerial photographs from 1980.

To compare the ATL of different periods, forest boundaries taken from the military topographic maps are sometimes used. In Russia, the latter were developed on the basis of decoding aerial photographs. For example, topographic maps (scale 1:50,000) linked to IRS LISS/PAN space images were used in the study of the Khibiny Mountains (Mikheeva 2010).

Method of decrypting high-resolution satellite images

The method of ATL mapping based on an expert interpretation of space images is similar to the aerial photography method. This method usually uses high-resolution photography (1–5 m per pixel) comparable to the scale of the considered aerial photographs (typically 1:10,000).

For example, in a study of forest boundary changes in the Sangun River watershed in the Tianshan Mountains (Xinjiang, China), a 2006 QuickBird image was compared with aerial photographs from 1962 and 1981. Segmentation methods using an object-oriented image classification algorithm were applied (Luo and Dai 2013).

In the Khibiny Mountains, the results of interpreting high-resolution space images from 2001 and archival

aerial photographs from 1958 were compared based on the classification of landscapes in ERDAS Imagine using the maximum similarity algorithm (Mathisen et al. 2014). Hexagon images obtained in 1976 were used for similar purposes in the study of the Belasitsa Mountains along the border between the Republic of Bulgaria and the Republic of Macedonia (Groen et al. 2012).

All studies using aerial photographs and high-resolution satellite images are local in nature (from 1 to 10 km²), which is due to the labor-intensive nature of manual decryption, limited access to relevant archives, and significantly different quality of historical sources. In addition, the use of modern aerial photography for regional analysis is always difficult due to objective circumstances. Collecting a full set of data is not only associated with large expenditures of time and money but also requires an 'ideal weather' (a certain number of clear days). Overall, the inconsistent data from images taken at different times and the varied geographic coverage make it difficult to apply the research findings to larger regions or countries.

Method of decrypting medium-resolution satellite images

The method of interpreting multi-temporal images of the Landsat and Sentinel satellite series (resolution of 10–30 m/pixel) is used to obtain spatial estimates of the dynamics of mountain forests, when the latter are supported by the available standards of the survey sites (collected during field studies). The delimitation of mountain forests is manually carried out visually, via semi-automatic algorithms, such as maximum similarity in ERDAS Imagine (Kravtsova and Loshkareva 2010); or by means of the GRASS GIS (Zhuravleva, Karanin 2017). Object-oriented classification algorithms using the Definiens eCognition 25 software were also used (Luo and Dai 2013). For example, when studying the dynamics of mountain forests in the Caucasus, the supervised classification method in the ArcGIS program was used to process multi-temporal images of Landsat-5 taken in 1988 and Landsat-7 in 2017 (Alekseeva 2021). In the Tien Shan Mountains, an analysis was carried out via the maximum likelihood method using GRASS GIS tools (Zhang et al. 2021).

Method of calculating vegetation indices

Calculating vegetation indices is the most common method of the automatic analysis of multi-temporal medium-resolution images. It allows the normalization of the images taken by different equipment and thus eliminates interpretation errors. In these studies, the normalized difference vegetation index (NDVI) is calculated by comparing the infrared (near infrared) and visible (red) reflected signal, which can characterize vegetation types and their condition.

For example, Landsat images of the Baikal Ridge in 1975 and 2010 were compared. Changes in the vegetation cover here were determined using the NDVI index calculated from satellite images (Vladimirov 2014). Images from Landsat 5 (1987) and Landsat 8 (2020) of the Taibai Mountain in China converted into vegetation indices were processed using ENVI software module to create vegetation indices with regression analysis (Wang et al. 2022). In a similar study of ATL dynamics at the Changbai Mountains in northeastern China, Landsat images from 1977–1999 were used to obtain the ratio of the calculated normalized vegetation index of birch and coniferous forests at the upper boundary of their distribution (Zhang et al. 2009). In the Indian Himalaya region, IRS-P6, LISS-III, and Landsat MSS images were used from 1972 to 2006, so threshold values of forest edge NDVI

were determined; finally, the rate and magnitude of change were calculated using geostatistical analysis methods (Singh et al. 2012).

Discrete classifications are useful for ATL studies, especially for studying the relationships between the mosaicity of the edge of high-mountain forests and the processes predetermining such mosaicity, as it becomes possible to correlate the characteristics of vegetation types with the field data and published descriptions. However, these methods work only where there is a correlation between the spectral characteristics and observed ground features of objects. No quantitative assessment of the degree of variation in the structures of the ATLs – reflected in the spectral characteristics of the objects that comprise them – has been made so far.

Method of automatic fuzzy classification of space images

The most recent methods process medium-resolution images using a variety of automatic space image classifications. These methods are mainly applied to the images obtained by Landsat series space satellites. The Landsat archive is the most complete archive of medium-resolution space images, with 80-m/pixel images available since 1973 and 30-m/pixel images available since 1982. The duration and precise spatial referencing of Landsat archive data allow for a qualitative assessment of the changes in landscape objects at the macroregion level without additional spatial and brightness corrections. This makes it the best candidate for automatic image classification methods.

In a study on the ATL in the Himalayas, Landsat 5/8 satellite data from 1989–2015 were used to create NDVI and normalized difference snow index (NDSI) raster for a further application of the classification process by a neural network-based algorithm, such as a decision tree (Sushma et al. 2010; Zhang et al. 2021).

Landsat ETM images from 2002 and OLI images from 2015 were analyzed for the Jizera Mountains, the Southern Carpathians, Romania (Mihai et al. 2017). Thematic classification was done using the maximum likelihood algorithm, which is based on calculating the Gaussian probability around each training set of pixels. The training set was based on the forest stand data from INCDS Bucharest (National Institute for Forestry Research and Development).

Landsat satellite images for the periods of 1971–1980, 1981–1990, 1991–2000 and 2001–2014 were analyzed for a large-scale study of the national parks evenly distributed across the dominant European mountain ranges, such as the Pyrenees, the Alps, and the Carpathians (Dinca et al. 2017). Changes in forest boundaries were measured using the post-classification comparison algorithm.

Multi-temporal Landsat TM data (1988–1990) were used to map alpine forests in Montana (Allen and Walsh 1996). Cluster analysis based on the relationship with forest reflectance was applied to create models for each temporal boundary in the compared images. A similar study was conducted in the western Himalayas, where Landsat MSS and TM images over a 30-year period from 1980 to 2010 were used (Bharti et al. 2012). For supervised classification, training signatures of six different classes were specified based on in situ data collected during field surveys. Signatures were assessed for a possible separation of individual classes using the ERDAS transformed divergence method.

Fuzzy classification is an attractive alternative to expert ('manual') ecotone mapping, where there are no clear

boundaries among vegetation classes. Fuzzy classification pre-assigns a score for individual pixels based on the so-called fuzzy membership of the pixel to a finite class. The fuzzy membership itself may be set in different ways in modern GIS tools, which gives the researcher much flexibility to test the algorithm and find an optimal solution. However, in most studies, the use of such fuzzy logic algorithms is limited to the territory of a single Landsat image because normalizing a mosaic of images with different times and angle characteristics is quite a complex process. In addition, the lack of accompanying field data for each image in a series results in the accumulation of interpretation errors when analyzing images of different periods. When using only two images taken within a significant period, the classification error in each image may lead to an incorrect interpretation of changes that do not reflect the real pattern. The use of a continuous multi-temporal series of space images may become a solution to this issue.

Method of automatic classification of calibrated space imagery composites

There are scarce publications aimed at solving the issues of normalizing the mosaics of satellite images and of developing continuous time series. These methods are used to create continuously calibrated composites from the stacks of Landsat space scenes to fill in the gaps associated with cloudiness or haze and develop the sets of phenological and statistical metrics, which can be analyzed by the neural network-based models (Potapov et al. 2020).

A large-scale study of landscape dynamics in the Caucasus (Buchner et al. 2020) used composites of 12651 Landsat images from 1985 to 2016 (all available images with less than 70% cloud cover). The FORCE mask algorithm was used to fill in the gaps. Based on the composites, phenological metrics were calculated using the spline analysis of the time series algorithm associated with climate variability, such as the beginning of the vegetation growth season, its peak, and its end. Correlations of phenological metrics with the algorithm-selected (based on neural

networks) landscape/land cover classes (LandCover/LandUse) were established; these classes comprised, but were not limited to, coniferous forests, mixed forests, deciduous forests, barren lands, pastures, croplands, built-up lands, wetlands, water, snow, and ice. To obtain training samples, the corresponding objects (polygons) verified in the field were digitized on high-resolution images.

When studying the dynamics of landscapes in the North Caucasus in our previous studies, processed Landsat analysis ready data (ARD) were analyzed as 16-day composite data normalized by reflectivity (for the visible, near and shortwave-infrared bands of the channels) and by data quality (Purekhovsky, Gunya, Kolbowski 2022). Areas covered by clouds and haze were corrected based on cloud-free images using a specialized gap-filling method. Annual 16-day GLAD ARD time series were transformed into a set of ranked statistical data (phenological indicators), which made it possible to apply multi-temporal classification and regression models. For each ranking, a set of indicators was calculated, including selected ranks, inter-rank averages, and amplitudes. In addition, a set of indicators reflecting seasonal changes associated with the main stages of vegetation was calculated based on the NDVI index. Phenological metrics were supplemented with geomorphometric indicators (absolute height and slope gradient). The analysis used an algorithm based on neural networks (such as a decision tree); training took place on an array of test objects obtained by analyzing high-resolution space photography and in-kind data.

DISCUSSION

The methods for studying the ATL may be divided into several groups based on methodology (e.g. in situ, remote and their combinations), spatial and temporal scales, parameters measured, and efficiency and limitations of application (Table 1).

The present review allows for tracking the changes and evolution of methods for studying the ATL. The primary methods were the modified forest inventory practices; therefore, they were based exclusively on the data

Table 1. Comparative characteristics of ATL study methods

Methods	Main measured parameters	Spatial size	Time period	Limitations and drawbacks
Paleocarpological methods	Tree composition	Key areas $N \times 10 \text{ km}^2$	Thousands of years	Rare occurrence of peat deposits in highlands
Tree census	Change in the number of trees and timber volume	Key areas $N \times 100 \text{ km}^2$, less often $N \times 1000 \text{ km}^2$	For several hundred years	Locality, difficulty in ensuring representativeness and extrapolation to large areas
Laser scanning methods	Spatial structure of tree cover of ATL on a large scale and its transformation	$N \times 1000 \text{ km}^2$	For decades	Labor-intensive and costly, difficult to ensure representativeness and extrapolation
Method of using landscape photographs	Qualitative (expert) assessment of the trend of change in the boundaries of the ATL on a large size	$N \times 100 \text{ m}^2$ - $N \times 1000 \text{ m}^2$	Decades, rarely hundreds of years	Limited number of places provided by historic landscape photographs, difficulty in applying accurate algorithms to analyze photographs
Dendrochronological method	Estimation of wood growth trend based on tree ring width measurements	$N \times 100 \text{ m}^2$ - $N \times 1000 \text{ m}^2$	For several hundred years	Focus on mature trees, without surveying other components of ATL; Localized, difficult to ensure extrapolation to other areas
Method of decoding aerial photography materials	Spatial structure and boundary of the ATL ecotone on a large scale	$N \times 10 \text{ km}^2$, less often $N \times 100 \text{ km}^2$	For decades	Limited number of places with availability of historical maps, the difficulty of selecting multitemporal imagery of equal resolution, necessity for ground verification

Method for decrypting high-resolution satellite images	Spatial boundary of the ATL ecotone and its changes on a large scale	$N \times 100 \text{ km}^2$	For decades	Limited number of locations with availability of multi-temporal images of equal resolution
Method for decrypting medium-resolution satellite images	Medium-scale localization and configuration of ATLs based on the identification of vegetation cover types	$N \times 100 \text{ km}^2$	For decades	The problem of labor-intensive manual processing of large coverage, inaccuracy of the result by automatic classification method without training
Method of calculating vegetation indices	Medium-scale localization and configuration of ATLs based on the identification of vegetation cover types	$N \times 1000 \text{ km}^2$	For decades	The problem of identifying the mature forest boundary, without investigating other components of the ATL, the need for ground verification
Method of automatic fuzzy classification of space images	Localization of ATL and its configurations on a medium scale	$N \times 10,000 \text{ km}^2$	For decades	Error of automatic processing of images of different quality and partially cloud-covered images, necessity of ground verification
Method for automatic classification of calibrated space imagery composites	Localization and configuration of ATLs: dimensionality parameters (area, width) of the encompassing ecotone	$N \times 100,000 \text{ km}^2$	For decades	Large volumes of data analyzed, complexity of simultaneous processing of data from different natural zones, the need for training

collected in the field. Emphasis was put on the tree age data, which served as a basis for obtaining a final model of standing growth and development within the ATL ecotone. The development of this approach was limited by the possibilities provided by the field taxation description of stand characteristics; subsequently, these possibilities were significantly expanded by the use of dendrochronological analysis. The use of LiDAR imaging technology made it possible to record the stand structure with much greater accuracy. However, when using this method, there was an acute lack of spatial information for approximating and extrapolating data to large areas. These limitations were overcome in part through the use of aerial photography and historical photographs of the mountains.

Nevertheless, a breakthrough in ATL study methods is associated with the introduction of remote sensing data into scientific practice, primarily remote sensing materials from repeated surveys. First, they were tested for small key areas and then in ever-expanding territories. At the same time, the transition from the local to the regional and global levels was accompanied by an exponentially increasing labor intensity of interpretation, which required procedure automation and an almost complete rejection of expert (manual) methods of analysis. The development of methods for semi-automatic (controlled by an expert) and automatic (uncontrolled) processing of space images resulted in promoting various classification ('segmentation')

algorithms for vegetation cover and land-use types, with subsequent comparisons among the boundaries of the identified vegetation types. The introduction of appropriate tools into modern GIS software provided researchers with the ability to process data for large areas and even entire mountain systems. At first, these methods were relatively simple (e.g. calculating vegetation indices), but with training and the use of machine learning algorithms based on neural networks, classification methods began to be applied as GIS analysis technologies were being developed (Fig. 2).

The effectiveness of methods for studying the dynamics and transformation of the ATL is predetermined mainly by the ratio of two main parameters: (1) the size (area) of the studied territory and (2) the time range of the recorded changes. The study area predetermines the data volume to analyze, which, in turn, affects the accuracy largely, bringing some limitations at local and regional scales and thus influencing model correctness. The time depth makes it possible to separate the average long-term trends from random fluctuations of the ATL.

Field methods, such as tree census and dendrochronological analysis, allow for the building of models with a uniquely significant time interval (from 30 to 800 years). However, they still cover extremely small areas of model plots (less than 0.5 km^2). Aerial photography and high-resolution space imagery make it possible to record

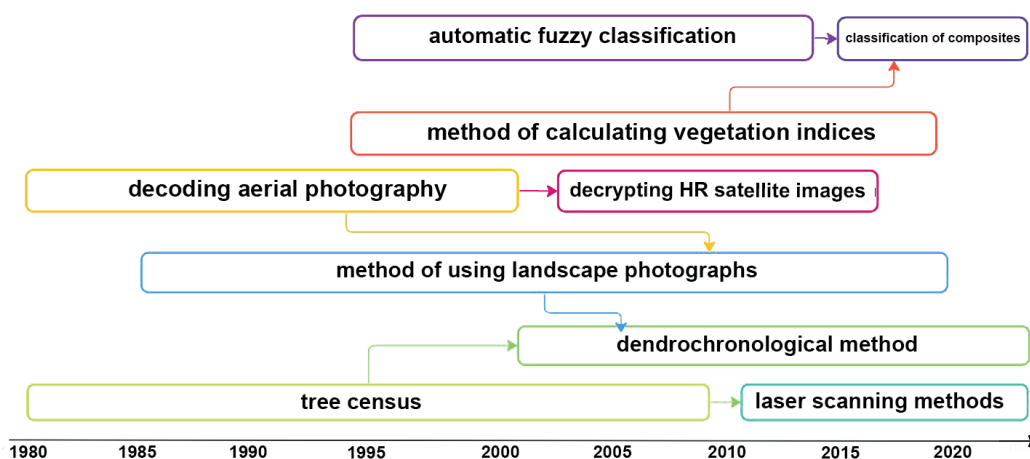


Fig. 2. Development of methods for ATL studying

the ATL changes over the past 20–60 years. However, the analyzed area may cover dozens of thousands of square kilometers, which is commensurate with the size of a physical–geographical region. The methods for the automatic processing of medium-resolution space photography with a relatively low time depth (the last 20–40 years) make it possible to study the areas of hundreds of thousands of square kilometers, which is equal to the size of an entire mountainous country.

The obtained correlation of the area of the study territory with the time coverage was 0.45 (Fig. 3), demonstrating a clearly traceable trend towards an increase in the area of the study territory, which meets the request for an analysis of the dynamics of the ATL on the scale of large regions, physical–geographical territories, and administrative states.

CONCLUSIONS

Analysis of accumulated experience in the application of various approaches and methods for studying the localization and average annual dynamics of the ATL allows for coming up with a list of urgent issues and needs. The ATL, being a relatively narrow ecotone, is, nevertheless, widely distributed in various mountain systems at the global level. As a result, it is characterized by a significant variety of location conditions. Therefore, searching for or applying an ‘ideal’ method for ATL studying is unreal.

The most common field methods (tree census, dendrological analysis and paleocarpological studies) require a large volume of fieldwork, which is especially difficult in rugged mountainous terrain. This predetermines the extremely limited (practically ‘point-scale’) information obtained, which is intended to be applied to analyze the trends in large regions. Landscape photographs aid in partially solving this issue, but their use is very localized and limited by the lack of vast archives of such photographs.

The methods based on the processing of remote sensing data may serve as a solution to the issue of achieving broadly applied and reliable extrapolation. These methods help to develop spatial models of forest boundary changes at the administrative-state, subcontinental, and global scales. However, these innovative approaches also have many limitations. High-resolution images (similar to aerial photography in scale and accuracy), which allow visual identification of individual tree crowns, are usually

limited to the boundaries of a single scene (an area of up to several hundred square kilometers). This is associated with their high cost and the large amount of manual labor required for processing. Medium-resolution images, in which the pixel resolution is greater than the size of the tree crown, require complex classification during analysis that identifies transitional classes of vegetation and corresponds to a complex mosaic of the distribution of species and the morphotypes of tree and shrub vegetation (i.e. crooked forests and dwarf trees) at the boundary of their altitudinal distribution.

Nowadays, the data obtained by the Landsat satellite system (30 m per pixel) is the most effective in analyzing vast territories due to their standard nature and the accuracy of the reference determined by the stability of satellite orientation. Compared to the Landsat archives, Sentinel 2 images, available since 2016, have an improved resolution (10 m per pixel). However, these satellites can operate for less than 10 years, which does not provide sufficient time depth to draw any conclusions about the average long-term dynamics of the ATL using this method. Combining the data from these two series would allow for operating with a depth of up to 50 years, alongside maintaining the image resolution, but this is possible only when using the integral composites.

The contradiction between the accuracy of measurements and the area of the studied territories is a classic problem that characterizes the applicability of remote sensing data. The correction of the results of ATL modeling in mountainous conditions encounters poor accessibility to highlands for field verification methods. Many studies are based on random, point-distributed modern or historical data and surface images covering local model areas. Such studies consider the observations at key sites only and are thus required to be representative when extrapolated to larger territories. To solve the issue of data extrapolation, it is necessary to develop spatial models of ATL changes based on remote sensing data.

Most researchers find a compromise by processing available medium-resolution images using segmentation methods with an excessive simplification of forest classes when studying the ATL. However, at the altitudinal limit of forest distribution, the ecotone transformation mostly refers to the tree growth and the rooting of the species presented rather than to changes in community biodiversity and composition. Therefore, in the classifications obtained

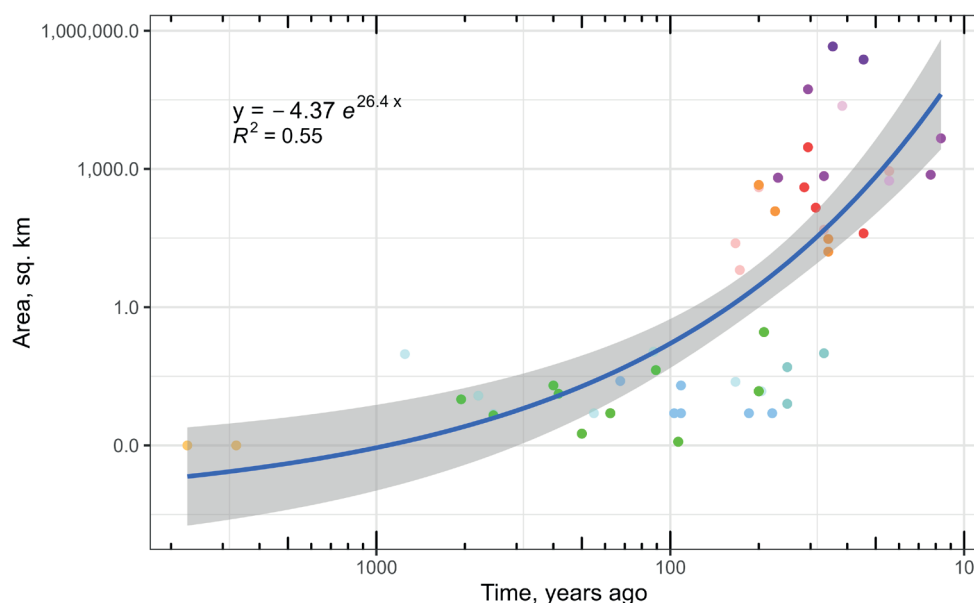


Fig. 3. Correlation of area and time parameters of the ATL dynamics methods. The colors are indicated by different methods. The color designations are shown in Fig. 1

by analyzing the remote sensing data, it is necessary to identify young trees first, as both their number and spatial distribution affect the direction and rate of ATL dynamics. Simple classifications alone cannot accomplish this without training.

Combining methods based on automatic nonlinear classification of medium-resolution space images with training on field and office research data obtained by other techniques may become a solution to the issue stated above. Transformation (or conversion) tables developed in regard to dendrochronological, counting (census) and other field methods of collecting and processing materials could serve as a basis for creating the arrays of objects and models for training algorithms built with neural networks. The use of detailed laser scanning data to train a neural network to interpret Landsat composites is a worthy example of such an approach (Potapov et al. 2021).

Most methods aim to delineate the ecotone boundaries, tracking boundary shifts among landscape–altitude belts (forest, alpine meadow, and nival). However, only some of them allow for the identification of the qualitative changes within the ecotone itself in association with its horizontal and vertical structures and are not necessarily accompanied by a shift in the ATL. Assessing the changes in terms of attributing them to cyclical or unidirectional average long-

term trends is another important issue. Short-term and/or local observations, which have revealed the transformation of the ATL, do not allow one to establish the stability and direction of changes reliably. Finally, both the interpretation of ATL changes and the search for independent variables in the corresponding models often suffer from an overestimation of climatic fluctuations as leading factors, while other important factors, primarily human activity, remain undisclosed or are deliberately ignored. The latter are based on the idea of a pristine environment in mountain forests, which is not true in a number of cases. As a result, the methods currently used to study the altitudinal–zonal (landscape) forest boundary are mostly effective only at the local or, at best, regional scales; when attempting to extrapolate, they often lead to incorrect conclusions.

A critical analysis of the experience accumulated to date in studying the localization and average long-term dynamics of the ATL indicates the need to create synthetic solutions. They must be based on both (1) using the metrics of holistic composites of medium-resolution space imagery and (2) considering large arrays of field-obtained data on the position (for training machine learning algorithms), internal spatial organization and characteristics of forest communities in mountainous countries around the world. ■

REFERENCES

- Alekseeva N. N., Gunya A.N., Cherkasova A.A. (2021). Land cover dynamics during recent 30 years (case study of the "Alanya" National park, the Northern Caucasus). *Lomonosov Geography Journal*, (2), 92–102, (in Russian with English summary).
- Allen T.R. and Walsh S.J. (1996). Spatial and compositional pattern of alpine treeline, Glacier National Park, Montana. *Photogrammetric Engineering and Remote Sensing*, 62(11), 1261–1268.
- Ameztegui A., Coll L., Brotons L. and Ninot J.M. (2016). Land-use legacies rather than climate change are driving the recent upward shift of the mountain tree line in the Pyrenees. *Global Ecology and Biogeography*, 25(3), 263–273, DOI: 10.1111/geb.12407
- Batllo E., Camarero J.J. and Gutiérrez E. (2010). Current regeneration patterns at the tree line in the Pyrenees indicate similar recruitment processes irrespective of the past disturbance regime. *Journal of Biogeography*, 37(10), 1938–1950, DOI: 10.1111/j.1365-2699.2010.02348.x
- Bharti R.R., Adhikari B.S. and Rawat G.S. (2012). Assessing vegetation changes in timberline ecotone of Nanda Devi National Park, Uttarakhand. *International Journal of Applied Earth Observation and Geoinformation*, 18(1), 472–479, DOI: 10.1016/j.jag.2011.09.018
- Bocharov A.Yu. (2011). Structure and dynamics of high-mountain forests of the North Chuysky Ridge (Altai Mountains) under climate change conditions. *Bulletin of Tomsk State University*, (352), 203–206, (in Russian with English summary).
- Buchner J., Yin H., Frantz D., Kuemmerle T., Askerov E., Bakuradze T., Bleyhl B., Elizbarashvili N., Komarova A., Lewińska K.E., Rizayeva A., Sayadyan H., Tan B., Tepanosyan G., Zazanashvili N. and Radeloff V.C. (2020). Land-cover change in the Caucasus Mountains since 1987 based on the topographic correction of multi-temporal Landsat composites. *Remote Sensing of Environment*, 248(September 2019), 111967, DOI: 10.1016/j.rse.2020.111967
- Calvin K., Dasgupta D., Krinner G., Mukherji A., Thorne P.W., Trisos C., Romero J., Aldunce P., Barrett K., Blanco G., Cheung W.W.L., Connors S., Denton F., Diongue-Niang A., Dodman D., Garschagen M., Geden O., Hayward B., Jones C., ... Ha M. (2023). IPCC, 2023: Climate Change 2023: Synthesis Report. Contribution of Working Groups I, II and III to the Sixth Assessment Report of the Intergovernmental Panel on Climate Change [Core Writing Team, H. Lee and J. Romero (eds.)]. IPCC, Geneva, Switzerland. , P. Arias, M. Bustamante, I. Elgizouli, G. Flato, M. Howden, C. Méndez-Vallejo, J. J. Pereira, R. Pichs-Madruga, S. K. Rose, Y. Saheb, R. Sánchez Rodríguez, D. Ürge-Vorsatz, C. Xiao, N. Yassaa, J. Romero, J. Kim, E. F. Haites, Y. Jung, R. Stavins, ... C. Péan eds. DOI: 10.59327/IPCC/AR6-9789291691647
- Camarero J.J., Gazol A., Sánchez-Salguero R., Fajardo A., McIntire E.J.B., Gutiérrez E., Batllori E., Boudreau S., Carrer M., Diez J., Dufour-Tremblay G., Gaire N.P., Hofgaard A., Jomelli V., Kirilyanov A. V., Lévesque E., Liang E., Linares J.C., Mathisen I.E., ... Wilmking M. (2021). Global fading of the temperature–growth coupling at alpine and polar treelines. *Global Change Biology*, 27(9), 1879–1889, DOI: 10.1111/gcb.15530
- Chen I.C., Hill J.K., Ohlemüller R., Roy D.B. and Thomas C.D. (2011). Rapid range shifts of species associated with high levels of climate warming. *Science*, 333(6045), 1024–1026, DOI: 10.1126/SCIENCE.1206432/SUPPL_FILE/CHEN.SOM.PDF
- Coops N.C., Morsdorf F., Schaepman M.E. and Zimmermann N.E. (2013). Characterization of an alpine tree line using airborne LiDAR data and physiological modeling. *Global Change Biology*, 19(12), 3808–3821, DOI: 10.1111/gcb.12319
- Däniker A. (1923). *Biologische Studien über Wald- und Baumgrenze, insbesondere über die klimatischen Ursachen und deren Zusammenhänge*. Vierteljahresschr. Naturfr. Ges. Zürich, 63, 1–102.
- Devi N.M., Kukarskih V.V., Galimova A.A., Bubnov M.O. and Zykov S.V. (2018). Modern Dynamics of High-Mountain Forests in the Northern Urals: Major Trends. *Journal of Siberian Federal University. Biology*, 11(3), 248–259, DOI: 10.17516/1997-1389-0069
- Devos C.C., Ohlson M., Næsset E. and Bollandsås O.M. (2022). Soil carbon stocks in forest-tundra ecotones along a 500 km latitudinal gradient in northern Norway. *Scientific Reports*, 12(1), 13358, DOI: 10.1038/s41598-022-17409-3
- Dinca L., Nita M., Hofgaard A., Alados C., Broll G., Borz S., Wertz B. and Monteiro A. (2017). Forests dynamics in the montane–alpine boundary: a comparative study using satellite imagery and climate data. *Climate Research*, 73(1–2), 97–110. DOI: 10.3354/cr01452
- Du H., Liu J., Li M., Büntgen U., Yang Y., Wang L., Wu Z. and He H.S. (2018). Warming-induced upward migration of the alpine treeline in the Changbai Mountains, northeast China. *Global Change Biology*, 24(3), 1256–1266, DOI: 10.1111/gcb.13963
- Dyakonov K.N., Bochkarev Y.N. and Reteyum A. Yu. (2012). Geophysical and Astrophysical factors governing biological productivity of landscapes at the northern and the upper forest lines. *Bulletin of Moscow University. Series 5. Geography*, (4), 195–222, (in Russian with English summary).

- Frei E.R., Barbeito I., Erdle L.M., Leibold E. and Bebi P. (2023). Evidence for 40 Years of Treeline Shift in a Central Alpine Valley. *Forests*, 14(2), 412, DOI: 10.3390/f14020412
- Galako V.A. (2002). Impact of climate change on the spatial and temporal structure of spruce stands of the upper forest boundary in the Ural Mountains. *Izvestiya Orenburgskogo gosudarstvennogo agrarnogo universiteta*, 9(1), 4–6.
- Goskov E.A., Vorobyeva T.S. and Vorobyev I.B. (2022). Laser scanning in the study of the structure of forest stands of the upper forest boundary in the southern Urals. *Russian Forests and Economy in them*, 2(81), 4–10, (in Russian), DOI: 10.51318/FRET.2022.63.84.001
- Grabherr, Georg, Gottfried M., Pauli and Harald. (2000). GLORIA: A Global Observation Research Initiative in Alpine Environments. *Mountain Research and Development*, 20(2), 190–191, DOI: 10.1659/0276-4741(2000)020
- Greenwood S., Chen J., Chen C. and Jump A.S. (2014). Strong topographic sheltering effects lead to spatially complex treeline advance and increased forest density in a subtropical mountain region. *Global Change Biology*, 20(12), 3756–3766, DOI: 10.1111/gcb.12710
- Grigorev A.A., Moiseev P.A. and Nagimov Z.Y. (2013). Dynamics of the timberline in high mountain areas of the nether-polar Urals under the influence of current climate change. *Russian Journal of Ecology*, 44(4), 312–323, DOI: 10.1134/S1067413613040061
- Grigoryev A.A., Moiseyev P.A., Nagimov Z.Ya. (2010). The effect of climate change on the dynamics of the top timberline in the Subpolar Ural mountains. *Bulletin of Altai State Agricultural University*, 74(12), 34–40.
- Groen T.A., Fanta H.G., Hinkov G., Velichkov I., Van Duren I. and Zlatanov T. (2012). Tree Line Change Detection Using Historical Hexagon Mapping Camera Imagery and Google Earth Data. *GIScience & Remote Sensing*, 49(6), 933–943, DOI: 10.2747/1548-1603.49.6.933
- Haddaway N.R., Land M. and Macura B. (2017). "A little learning is a dangerous thing": A call for better understanding of the term 'systematic review.' *Environment International*, 99, 356–360, DOI: 10.1016/j.envint.2016.12.020
- Holtmeier F.K. and Broll G. (2019). Treeline Research—From the Roots of the Past to Present Time. A Review. *Forests*, 11(1), 38, DOI: 10.3390/f11010038
- Holtmeier K. (2010). Altitudinal and polar treelines in the northern hemisphere Causes and response to climate change. *Polarforschung*, 79(September 2009), 139–153.
- IPCC (2013). *Climate Change 2013: The Physical Science Basis. Contribution of Working Group I to the Fifth Assessment Report of the Intergovernmental Panel on Climate Change*. 1535.
- IPCC (2014). *Climate Change 2014: impacts, adaptation, and vulnerability. Part A: global and sectoral aspects. Contribution of Working Group II to the fifth assessment report of the Intergovernmental Panel on Climate Change*. 1132.
- Istomov S.V. (2005). Current dynamics of timberline in West Sayan MTS. *Proceedings of the Tigirek State Natural Reserve*, 1, 211–214, (in Russian with English summary), DOI: 10.53005/20767390_2005_1_211
- Kapralov D.S. (2007). Study of spatial and temporal dynamics of the upper forest boundary in the northern and southern Urals, 21. Ural State Forestry University.
- Kolunchukova M.A. and Reznikov A.I. (2020). Some results of tree-ring analysis at the upper timberline in the mountains of Western Tuva. *Proceedings of the Russian Geographic Society*, 152(3), 45–58, (in Russian with English summary), DOI: 10.31857/S0869607120030039Koshkarov D.A., Koshkarova L.V. and Ovchinnikov Y.I. (2019). Climatogenic dynamics of phytocenotic diversity in the belt of the upper forest boundary of the Western Sayan over the last four thousand years. *Conifers of the Boreal Area*, 37 (5), 301–306, (in Russian with English summary).
- Kravtsova V.I. and Loshkareva A.R. (2010). Investigation of the northern forest boundary using space images of different resolutions. *Bulletin of Moscow University. Series 5. Geography*, 6, 49–57, (in Russian with English summary).
- Kullman L. and Öberg L. (2009). Post-Little Ice Age tree line rise and climate warming in the Swedish Scandes: a landscape ecological perspective. *Journal of Ecology*, 97(3), 415–429, DOI: 10.1111/j.1365-2745.2009.01488.x
- Lenoir J., Gégout J., Pierrat J., Bontemps J. and Dhôte J. (2009). Differences between tree species seedling and adult altitudinal distribution in mountain forests during the recent warm period (1986–2006). *Ecography*, 32(5), 765–777, DOI: 10.1111/j.1600-0587.2009.05791.x
- Liang E., Wang Y., Eckstein D. and Luo T. (2011). Little change in the fir tree-line position on the southeastern Tibetan Plateau after 200 years of warming. *New Phytologist*, 190(3), 760–769, DOI: 10.1111/j.1469-8137.2010.03623.x
- Luo G. and Dai L. (2013). Detection of alpine tree line change with high spatial resolution remotely sensed data. *Journal of Applied Remote Sensing*, 7(1), 073520, DOI: 10.1117/1.JRS.7.073520
- Lytkin V.M. (2019). Position of the upper forest boundary on the Suntar-Khayata Ridge in the Holocene optimum. *Arctic and Antarctic*, 3(3), 54–60, DOI: 10.7256/2453-8922.2019.3.30385
- Mamet S.D. and Kershaw G.P. (2012). Subarctic and alpine tree line dynamics during the last 400 years in north-western and central Canada. *Journal of Biogeography*, 39(5), 855–868, DOI: 10.1111/j.1365-2699.2011.02642.x
- Mathisen I.E., Mikheeva A., Tutubalina O.V., Aune S. and Hofgaard A. (2014). Fifty years of tree line change in the Khibiny Mountains, Russia: Advantages of combined remote sensing and dendroecological approaches. *Applied Vegetation Science*, 17(1), 6–16, DOI: 10.1111/avsc.12038
- Mazepa V.S. and Shiyatov S.G. (2015). Climatic driven dynamics of the upper tree-line ecotone of light larch forests in the polar Ural mountains for the last one and a half thousand years. *Russian Forests and Economy in them*, 4(55), 4–11.
- McCaffrey D. and Hopkinson C. (2020). Repeat Oblique Photography Shows Terrain and Fire-Exposure Controls on Century-Scale Canopy Cover Change in the Alpine Treeline Ecotone. *Remote Sensing*, 12(10), 1569, DOI: 10.3390/rs12101569
- Mihai B., Săvulescu I., Rujoiu-Mare M. and Nistor C. (2017). Recent forest cover changes (2002–2015) in the Southern Carpathians: A case study of the Iezer Mountains, Romania. *Science of The Total Environment*, 599–600, 2166–2174, DOI: 10.1016/j.scitotenv.2017.04.226
- Mikhailovich A.P. (2016). Spatial and temporal dynamics of the upper forest boundary in the lower reaches of the Yengayu and Kerdomanshor rivers (Polar Urals) in the second half of the 20th - early 21st centuries. *Ecological Equilibrium: Structure of Geographical Space* : Proceedings of the VII International Scientific and Practical Conference November 11, St. Petersburg, 120–124.
- Mikheeva A.I. (2010). Spatial variability of the position of the upper forest boundary in the Khibiny (based on remote sensing materials). *Bulletin of Moscow University. Series 5: Geography*, (4), 18–22, (in Russian with English summary).
- Moiseev P. A., Bartysh A. A., Goryaeva A.V., Koshkina N.B., Nagimov Z.Ya. (2008). Dynamics of subgoltz forest stands on the slopes of Serebryansky Kamen (Northern Urals) in recent centuries. *Conifers of the Boreal Area*, 25(1–2), 21–27.
- Morley P.J., Donoghue D.N.M., Chen J.-C. and Jump A.S. (2018). Integrating remote sensing and demography for more efficient and effective assessment of changing mountain forest distribution. *Ecological Informatics*, 43, 106–115, DOI: 10.1016/j.ecoinf.2017.12.002
- Murzakmatov R.T., Burenina T.A., Koshkarova V.L. and Farber S.K. (2014). Dynamics of the tundra-forest boundary in the highlands of West Tyva. *Conifers of the Boreal Area*, 32(3–4), 38–406 (in Russian with English summary).
- Nikolin A.A., Murzaeva M.K., Pomaznyuk V.A., Velikzhanin P.I., Pisarenko A.I., Mehrentsev A. V and Shiyatov S.G. (2015). Using Repeat Landscape Photos for Estimation of Dynamics of Forest-Tundra Communities in the Polar Urals. *Journal "Russian Forests and Economy in them"*, 3(54), 20–28.
- Nisametdinov N., Moiseev P and Vorobiev I. (2021). Laser Scanning and Aerial Photography with UAV in Studying the Structure of Forest-Tundra Stands in the Khibiny Mountains. *Lesnoy Zhurnal (Forestry Journal)*, 4, 9–22. DOI: 10.37482/0536-1036-2021-4-9-22

- Nizametdinov N.F., Shalaumova Y.V., Mazepa V.S. and Moiseev P.A. (2022). Assessment of Past Decadal Dynamics of Tree Stands in Forest–Tundra Transition Zone on the Polar Ural Mountains Calibrated Using Historical and Modern Field Measurements. *Forests*, 13(12), 2107, DOI: 10.3390/f13122107
- Pearson R.G. and Dawson T.P. (2003). Predicting the impacts of climate change on the distribution of species: are bioclimate envelope models useful? *Global Ecology and Biogeography*, 12(5), 361–371, DOI: 10.1046/j.1466-822X.2003.00042.x
- Peterson A.T., Berthiaume K., Klett M. and Munroe J.S. (2022). Linking repeat photography and remote sensing to assess treeline rise with climate warming: Mount of the Holy Cross, Colorado. *Arctic, Antarctic, and Alpine Research*, 54(1), 478–487, DOI: 10.1080/15230430.2022.2121245
- Potapov P., Hansen M.C., Kommareddy I., Kommareddy A., Turubanova S., Pickens A., Adusei B., Tyukavina A. and Ying Q. (2020). Landsat Analysis Ready Data for Global Land Cover and Land Cover Change Mapping. *Remote Sensing*, 12(3), 426, DOI: 10.3390/rs12030426
- Potapov P., Li X., Hernandez-Serna A., Tyukavina A., Hansen M.C., Kommareddy A., Pickens A., Turubanova S., Tang H., Silva C.E., Armston J., Dubayah R., Blair J.B. and Hofton M. (2021). Mapping global forest canopy height through integration of GEDI and Landsat data. *Remote Sensing of Environment*, 253, 112165, DOI: 10.1016/j.rse.2020.112165
- Purekhovsky A.Zh., Gunya A.N. and Kolbovsky E.Yu. (2022). Dynamics of High-Mountain Landscapes in the North Caucasus According to Remote Sensing Data in 2000–2020. *Izvestiya Dagestanogo gosudagogicheskogo pedagogicheskogo universiteta. Natural and Exact Sciences*, 16(2), 72–84, (in Russian with English summary), DOI: 10.31161/1995-0675-2022-16-2-72-84
- Shiyatov S. G. (2009). Dynamics of tree and shrub vegetation in the Polar Urals mountains under the influence of modern climate change. *Ural Branch of the Russian Academy of Sciences*.
- Shiyatov S.G., Mazepa V.S., Moiseev P.A. and Bratukhina M. Yu. (2001). Climate change and its impact on mountain ecosystems of the national park. Impact of climate change on ecosystems. *Protected Natural Areas of Russia: analysis of long-term observations*, 2, 16–31.
- Shiyatov S.G., Terentyev M.M. and Fomin V.V. (2005). Spatiotemporal dynamics of forest-tundra communities in the Polar Urals. *Russian Journal of Ecology*, 36(2), 69–75.
- Shrestha K.B., Hofgaard A. and Vandvik V. (2015). Recent treeline dynamics are similar between dry and mesic areas of Nepal, central Himalaya. *Journal of Plant Ecology*, 8(4), 347–358. DOI: 10.1093/jpe/rtu035
- Singh C.P., Panigrahy S., Thapliyal A., Kimothi M.M., Soni P. and Parihar J.S. (2012). Monitoring the alpine treeline shift in parts of the Indian Himalayas using remote sensing. *Current Science*, 102(4), 558–562.
- Snethlage M.A., Geschke J., Ranipeta A., Jetz W., Yoccoz N.G., Körner C., Spehn E.M., Fischer M. and Urbach D. (2022). A hierarchical inventory of the world's mountains for global comparative mountain science. *Scientific Data*, 9(1), 149, DOI: 10.1038/s41597-022-01256-y
- Steinbauer M.J., Field R., Grytnes J., Trigas P., Ah-Peng C., Attorre F., Birks H.J.B., Borges P.A.V., Cardoso P., Chou C., De Sanctis M., de Sequeira M.M., Duarte M.C., Elias R.B., Fernández-Palacios J.M., Gabriel R., Gereau R.E., Gillespie R.G., Greimler J., ... Beierkuhnlein C. (2016). Topography-driven isolation, speciation and a global increase of endemism with elevation. *Global Ecology and Biogeography*, 25(9), 1097–1107, DOI: 10.1111/geb.12469
- Steiner M. (1935). Winterliches Bioklima und Wasserhaushalt an der alpinen Waldgrenze. *Bioklim Beiblätter*, 2, 57–65.
- Sushma, P., Singh, C.P., Kimothi, M.M., Soni, P. and Parihar J.S. (2010). The upward migration of alpine vegetation as an indicator of climate change: observations from Indian Himalayan region using remote sensing data. *Bulletin of the National Natural Resources Management System NNRMS*.
- Vladimirov N. (2014). Dynamics of the timberline at the Baikal range. *Izvestiya Irkutskogo Gosudarstvennogo Universitet. Series: Earth Sciences*, 10, 46–56, (in Russian with English summary).
- Wang D., Li S. and Gao S. (2022). Distribution Characteristics of the Alpine Treeline and Vegetation Response to Climate Change of Taibai Mountain, China. *Geofluids*, 2022(May 2009), 1–12, DOI: 10.1155/2022/4517515
- Wang Z., Ginzler C., Eben B., Rehush N. and Waser L.T. (2022). Assessing Changes in Mountain Treeline Ecotones over 30 Years Using CNNs and Historical Aerial Images. *Remote Sensing*, 14(9), 2135, DOI: 10.3390/rs14092135
- Webb Robert H., D.E. Boyer R.M.T. (2010). Repeat Photography: Methods and Applications in the Natural Sciences. <https://lccn.loc.gov/2010009377>
- Zhang Yangjian, Xu M., Adams J. and Wang X. (2009). Can Landsat imagery detect tree line dynamics? *International Journal of Remote Sensing*, 30(5), 1327–1340, DOI: 10.1080/01431160802509009
- Zhang Yong, Liu L. yu, Liu Y., Zhang M. and An C. Bang. (2021). Response of altitudinal vegetation belts of the Tianshan Mountains in northwestern China to climate change during 1989–2015. *Scientific Reports*, 11(1), 1–10, DOI: 10.1038/s41598-021-84399-z
- Zhuravleva O.V., Karanin A.V. (2017). Peculiarities of spatial differentiation of forest ecosystems of the Katun Range. *Izvestiya Tula State University. Earth Sciences*, 1, 19–27, (in Russian with English summary).

CO-LOCATION OF INNOVATORS AND FINAL PRODUCTS: CASE OF WIND ENERGY OF GERMANY

Ekaterina V. Romanova^{1*}, Evgeny I. Vdovkin²

¹ National Research University Higher School of Economics, Malaya Ordynka 17, Moscow, 119017, Russia

² Lomonosov Moscow State University, Leninskie Gory 1, Moscow, 119991, Russia

*Corresponding author: evromanova@hse.ru

Received: September 27th 2024 / Accepted: January 27th 2025 / Published: March 31st 2025

<https://doi.org/10.24057/2071-9388-2025-3628>

ABSTRACT. This study highlights the importance of understanding the geographical context of innovation processes in industries driven by tacit knowledge, with German wind energy as its object of investigation. The subject of the research is the spatial organization of innovation processes in the wind energy sector, focusing on the co-location of inventors, production facilities, and installed capacities, particularly among locally embedded enterprises. The aim of this research is to characterize the geography of innovation in the German wind energy sector by examining the correlation between innovation departments and installed capacities, the degree of company embeddedness, and the industry's stage of development. The novelty lies in the application of a spatial analysis framework combined with network theory to explore how proximity and embeddedness shape the innovation cycle. The study developed a methodology to quantitatively assess the co-location of company branches and installed capacities over time using influence zones. Findings reveal a strong link between the locations of knowledge-generation sites and installed capacities, especially for embedded enterprises, where co-location coefficients within a 50-km radius range from 1.9 to 2.5. This correlation strengthens over time, particularly from 2000–2009 to 2010–2019. Foreign enterprises show high co-location coefficients for manufacturing sites but not for innovation departments. Further research is needed to explore the interplay of tacit and formalized knowledge in increasingly complex innovation processes and to determine causality in co-location patterns between innovators and installed capacities.

KEYWORDS: knowledge spillovers, tacit knowledge, geographical proximity, company embeddedness, wind energy, Germany

CITATION: Romanova E. V., Vdovkin E. I. (2025). Co-location of innovators and final products: case of wind energy of Germany. *Geography, Environment, Sustainability*, 117-129

<https://doi.org/10.24057/2071-9388-2025-3628>

Conflict of interests: The authors reported no potential conflict of interest.

INTRODUCTION

Innovation plays a pivotal role in regional development, as evidenced by a substantial body of literature. Key concepts such as industrial districts (Marshall 1920; Becattini 1979; 1990), clusters (Porter 1990), innovative milieu (Camagni 1991), regional innovation systems (Cooke 2001), and learning regions (Asheim 1996) underscore the importance of geographical factors in fostering innovation. This growing body of research has led to increased attention to the regional dimension of innovation policy.

The successful implementation of innovation policies, however, depends on several factors, including the specific industrial structure of a region. The regional industrial landscape shapes the nature of innovations, the sources of knowledge, and the degree to which players are embedded in the local innovation infrastructure. Among these factors, the significance of geographical proximity is crucial in determining the effectiveness of innovation processes. Geographical areas act as a place for sharing skills and also affect how effectively knowledge, especially specialized knowledge, is shared.

Since geography greatly affects innovation, it is important to understand the knowledge available, especially tacit knowledge, to create good technology

policies. The geography of innovation, including the spatial distribution of knowledge generation and production activities, is crucial for developing targeted support strategies for market participants.

The *object* of this study is wind energy, selected for its reliance on tacit knowledge as a crucial driver of innovation within its production processes. The subject of the research focuses on the spatial organization of various stages of wind energy production, with particular attention to the embeddedness of participants in regional innovation systems. The aim of the study is to characterize the geography of innovation in the German wind energy sector and analyze its evolutionary features in the context of tacit knowledge.

By investigating the relationship between the locations of knowledge-generation hubs and the distribution of installed wind energy capacities, this research seeks to deepen our understanding of how tacit knowledge influences technological innovation. The study further explores the spatial dynamics between production stages and the integration of key actors, providing insights into the role of regional embeddedness in shaping innovation within this sector.

To achieve this aim, the study is structured around three key tasks:

1. To determine whether there is a correlation between the locations of knowledge generation and installed wind energy capacities. This task will identify the geographical patterns of innovation and production in the wind energy sector.

2. To assess the influence of companies' embeddedness in the local regional environment on the spatial organization of innovation activities and installed capacities. This task explores how the degree of integration into the local network affects innovation outcomes.

3. To establish the dependence of the spatial relationship between innovators and final production on the stage of industry development. This task will examine how the evolution of the wind energy sector impacts the spatial distribution of innovation and production activities.

These tasks collectively explore the relationship between spatial factors and innovation in the wind energy sector. The *novelty* of this research lies in its approach, which combines spatial analysis with a network framework to offer a new perspective on how proximity and embeddedness affect the innovation cycle in the wind energy industry.

In contrast to traditional hierarchical models of innovation, which often emphasize top-down control, the network framework focuses on horizontal linkages and decentralized collaboration. While studies such as Jackwerth (2017) have examined the inefficiencies of hierarchical systems in the wind energy industry, this research is the first to investigate the spatial aspects of nonlinear connections between actors in the innovation process. By examining geographical proximity and the spatial distribution of tacit knowledge, this study sheds new light on how localized knowledge spillovers and embedded competencies influence the development of wind energy innovations.

In conclusion, this study's novel contribution lies in its exploration of the spatial dynamics of the wind energy innovation process. The research highlights the critical role of geographical proximity in fostering innovation, with innovation centers often located near existing wind turbines to facilitate access to tacit knowledge. The study also emphasizes how spatially "sticky" competencies within the industry influence the placement of wind turbines, providing a deeper understanding of how tacit knowledge can be formalized and leveraged within the spatial dimension of innovation.

MATERIALS AND METHODS

Literature review

Types of knowledge in the context of sectoral economic activity

There are many approaches that explain the nature of knowledge and its impact on the economy. Charlie Karlsson distinguishes between the concepts of "information" as a form of codified knowledge that is easily transmitted, transferred, and stored at low cost, and "knowledge", which is difficult to codify and interpret due to its inherent complexity and indivisibility, as it is the result of a long period of learning in a specific environment (Karlsson 2012).

Closest to the second one is the concept of "tacit knowledge" which underpins the research paradigm in the works of Michael Polanyi (Polanyi 1958). The transfer of this knowledge between people requires intensive, regular, and trust-based contacts. Such ideas and skills generally arise from experience and are not systematized (Chugh

2015). For example, take the Japanese automobile industry, about which Ikujiro Nonaka wrote: the central element stimulating innovation in a Japanese automobile company is the use of "tacit" and often subjective knowledge, intuition, and guesses of individual employees, which the company tests and utilizes, rather than the "processing" of objective information (Nonaka 2007).

One of the key publications in which innovation processes were explored through the prism of different types of knowledge was the work of a Danish team of authors led by Morten Berg Jensen and Bengt A. Lundvall. They identified two types of knowledge: Science, Technology, Information (STI) knowledge and Doing, Using, Interacting (DUI) knowledge (Jensen et al. 2007). In the first case, the focus is on formal processes within R&D and explicit, codified knowledge, while in the second case, it is about employee learning resulting from informal interactions within and between organizations and the "tacit" nature of knowledge. The first type of knowledge is global, based on "know-what" and "know-why", while the second is local, depending on "know-how" and "know-who". STI knowledge relies on the use of systematized scientific and technical knowledge, whereas DUI knowledge is characterized by informal learning processes and is based on experience.

Bjørn Asheim, Lars Coenen, Meric Gertler, and others offer a more comprehensive view of knowledge, learning, and innovation, shifting away from a binary approach. They identify analytical, synthetic, and symbolic knowledge (Asheim and Gertler 2005; Asheim and Coenen 2005; Asheim 2007).

The analytical knowledge base relies on scientific knowledge grounded in formal methods and codification. Examples of such industries include biotechnology and nanotechnology. The workforce requires research experience or university education. An important form of knowledge application involves the creation of new firms and subsidiaries based on radical innovations.

The synthetic knowledge base relies on the application of knowledge or its combination, typically in response to the need for solving new applied problems (in the form of product or process development). Examples of industries include general and transportation engineering and energy industrial equipment. Cooperation with scientific centers is based on applied research and development, rather than fundamental research. This knowledge is acquired through hands-on learning in professional and polytechnic schools. Innovations are incremental and most often occur within existing companies (Lorenz and Lundvall 2006).

Symbolic knowledge relies on the creation of meanings and desires, as well as aesthetic types of products. These include drawings, images, and symbols (cultural innovations). The dynamically developing creative economy, including fields such as mass media, advertising, design, and branding, has a significant influence on the creation of this type of knowledge (intangible products) (Scott 2007). This type of knowledge requires embedding and understanding the everyday culture of specific social groups. Therefore, acquiring creative skills is associated not with formal university qualifications but with the real practice of the creative process, "know-who" (Asheim et al. 2011). Here, there is also a component of tacit knowledge.

Given the diversity of innovation processes, the strict classification of industries based on knowledge is incorrect. Innovation processes in numerous economic sectors combine elements of all types of knowledge. Each industry can be characterized by the predominance of a particular type of knowledge in its innovation processes (Alhusen

and Bennat 2021). How much one type of knowledge dominates depends on the firms, industries, and activities (like research and production). Using both STI and DUI knowledge together can help companies get better results in developing innovations (Carrillo-Carrillo and Alcalde-Heras 2020; Parrilli and Heras 2016). It should be clarified that the idea of differentiating knowledge is not intended to assess differences in competence and technological complexity but to characterize the nature of innovations and their contribution to innovation activities (Moodysson 2007).

Innovation dynamics in regions by different types of knowledge

The geographical context often determines the role of different types of knowledge in the innovation process (Doloreux and Shearmur 2023). Due to various methods of knowledge creation, the dominance of a particular type of knowledge has different spatial dimensions in the interaction of actors. The generation of analytical knowledge is typically less reliant on intensive local collaboration, which promotes the development of global knowledge networks. Simultaneously, there is a belief that the transfer of synthetic knowledge is more effective when participants in innovation processes directly communicate in a common geographic area. (Moodysson et al. 2008). Geographical clustering of inventive endeavors demonstrates the regional character of tacit knowledge.

Traditionally, it was considered that inventions occurred mostly in large cities. However, there is increasing evidence that innovation can also thrive in peripheral locations outside of major urban areas (Eder 2019). Recent research has shown that in advanced economies (Parrilli et al. 2020) and in the context of product innovations (Carrillo-Carrillo and Alcalde-Heras 2020) the importance of DUI knowledge can be noticeably greater, despite the significance of other types of knowledge in innovation processes. The emphasis on this aspect can be found in Marshall-Becattini's early twentieth-century works based on the concept of industrial districts. The basic idea of grouping several small businesses in certain industries that operate at different stages of a shared production process in a specific location is similar to the current idea of tacit DUI knowledge. Marshall identified specialized labor, diffusion of knowledge, and technology transfer as advantages of industrial districts (Marshall 1920). Becattini integrated these characteristics with the actor's social proximity (Becattini 1979). According to a recent study, such districts are better suited to incremental rather than radical innovations (Hervas-Oliver et al. 2021).

The work of Dutch economist and economic geographer Ron Boschma actively explores the geographical aspect that shapes the context of interactions among players. He explains how many forms of proximity between actors (cognitive, organizational, institutional, social, and geographical) define the process underpinning this impact (Boschma 2005). The latter catalyzes other types of proximity but has no direct impact on how actors in innovation interact. Therefore, geographic proximity has an array of effects, all of which operate together to increase the extent of contact between innovation actors. This is especially crucial when discussing tacit DUI knowledge since face-to-face interaction is the only vehicle for this knowledge to be transferred between individuals and is difficult to codify. Therefore, the localized nature of DUI knowledge is characterized by knowledge spillovers between people over short distances.

Asheim and Coenen found that studying five northern clusters in Denmark, Sweden, and Norway showed that different regional innovation systems (RIS) are shaped by different types of knowledge. Consequently, it influences the type of innovation policy that is implemented into practice, depending on the specifics of the industry. The support and enhancement of localized learning in established industrial specializations distinguishes synthetic (engineering) knowledge. This, in turn, reinforces technological trajectories that rely on tacit knowledge, using an ex-post approach. Territorially integrated RISs emerge as a result. In terms of scientific knowledge, the main goal is to support new business ideas that need partnerships between universities and industries. This can be achieved through places like science parks and incubators (ex-ante approach). The regional knowledge infrastructure is essential in both innovation systems. As a result, national innovation systems, or regionally networked innovation systems, are formed. The first one is science-oriented and may have weak interactions with local industries. The last one, which has more advanced technologies than territorially integrated RIS, combines analytical and synthetic knowledge and is market-oriented, making it the most competitive type of RIS known to arise during an industry's growth stage. The ex-post approach enables locally networked innovation systems to address problems incrementally while at the same time providing initial assistance to the industry in surmounting technological barriers (Asheim & Coenen 2005).

Local knowledge spillovers, or "local buzz", often occur in the context of the tacit nature of knowledge "in itself". Tacit knowledge comprises researchers, engineers, and all persons who play a role in maintaining the efficient operation of the DUI industry at all stages of the value chain. Simultaneously, global knowledge transfer channels, or "global pipelines", facilitate the sharing of scientific, technological, and innovation (STI) knowledge. This exchange requires formal links between players involved in innovation and codified forms of knowledge. As Harald Bathelt notes, both types of knowledge spillovers are necessary for the productive creation of innovations (Bathelt et al. 2004). However, differences in their combination indicate the varying roles of localized and global knowledge spillovers in different industries.

For companies that are part of networked innovation processes, it is necessary to supplement their internal knowledge base with another type of knowledge. The primary methods of acquiring new knowledge include attracting human capital with the required competencies in a different knowledge base, as well as internationalizing scientific collaboration, outsourcing R&D, or engaging in external economic activities. All of this increases the focus on various territorial forms of organizing innovation processes, from clusters and innovation systems to global production networks and value chains, where the type of knowledge used is not internal to the industry but rather external knowledge that has been brought into a range of technologies, actors, and industries from outside (Smith 2000). Thus, there is a global trend toward integration and collaboration in the process of knowledge creation and corporate innovation.

Evolutionary researchers emphasize that the spatial pattern of the innovation process also determines the stages of industry development. According to M. Feldman, tacit knowledge is especially important during the early stages of industry formation (Feldman 2010). In such cases, local knowledge is often in demand, "existing in a tacit and non-formalized shape within informal communication

networks through trusted interactions between closely located economic agents" (Pelyasov 2012). At the same time, formalized knowledge is characteristic of more mature industries, and global knowledge transfer channels serve to disseminate it more effectively over long distances.

Under the influence of scientific and technological progress, the processes of knowledge creation and innovation are becoming increasingly complex, diverse, and interdependent. Different combinations of knowledge types exhibit spatial diversity. They also appear differently in the framework of innovation evolution.

Table 1 provides a brief description of the differences between the two ideal types of knowledge, considering the rationale for knowledge creation, the methods of its development and utilization, and the sensitivity to geographical factors.

Innovative development of wind energy in Germany as a DUI industry

The subject of the research is the wind energy sector in Germany for several reasons. First, wind energy, as a young industry, is well supported by a wide range of scientific and statistical materials that allow for analysis of its innovative development in its early stages. Second, existing publications on the innovative aspects of its development indicate that wind energy is an industry where tacit knowledge is actively sought after (Binz and Truffer 2017; Rohe 2020; Tsouri et al. 2021). Binz and Truffer also note in their work on global innovation systems that new knowledge in wind energy is formed not only through science but, to a greater extent, through on-the-job training (Binz and Truffer 2017). This is also supported by research from Heidenreich and Mattes (2020), which looks at how local innovation in Germany's wind energy sector relies on sharing tacit knowledge.

Therefore, the wind energy innovation system is characterized by its *regional embedding*. Based on research in related fields, the authors conclude that the development of wind energy still primarily relies on DUI knowledge, which contrasts with the general trend toward a shift to STI knowledge in other industries over time. Meanwhile, in the process of creating value chains within global innovation systems, suppliers in offshore wind energy, according to the study by Tsouri, Hanson, and Normann, represent a wide variety of firms that produce products, components, and services and are to some extent involved in the development of innovations in the STI knowledge mode (Tsouri et al. 2021). Some of these firms also have experience in supplying the oil and gas industry, which relies on both DUI and STI modes of innovation (Hanson J. et al. 2021).

In studies on technology life cycles, it is noted that geographical proximity to users only weakens in the

case of mass energy technologies (such as today's solar photovoltaic systems). In contrast, for innovators of complex technologies like wind energy, geographical proximity remains significant (Huenteler et al. 2015; Barua 2012). This must also be considered in the implementation of technological policies: subsidies for market deployment in wind energy are more effective when combined with measures to promote learning and the knowledge spillovers between producers and researchers (Kamp et al. 2004; Tang and Popp 2015). Hence, *the hypothesis arises that there is a high degree of concentration of all links in the value chain within the industry in one place, from invention and product creation to practical use.*

M. Bednarz and T. Broekel scrutinize the industry from the perspective of its reliance on demand and supply factors (Bednarz and Broekel 2020). They compare two types of models: one that shows how supply influences the installation of wind turbines and another that illustrates how demand attracts companies that manufacture wind turbines. The researchers believe that in Germany, the demand factor is more important, especially when looking at regional policy in the context of ex-post approach. This means that the co-location of innovation centers and installed capacities may be driven by consumer demand for innovations in regions with favorable conditions for the development of wind energy.

Thus, wind energy is an industry with a distinctive mode of innovation creation, where certain types of knowledge (tacit, applied, engineering, DUI) play a crucial role. This aligns with findings by Alle et al. (2017), who argue that the localized exchange of tacit knowledge is critical for fostering innovation in complex industries like wind energy, particularly in regions with high embeddedness. Individuals generate this knowledge by acquiring practical skills in the workplace at various stages of the value chain. The dissemination and exchange of this kind of knowledge are most effective within the framework of the spatial concentration of actors. Given *that the degree of embedding can positively influence the role of local tacit DUI knowledge in the innovation processes of companies, this aspect is given special attention in the work. The research question is articulated as follows: How does tacit applied knowledge influence the spatial distribution of wind energy throughout the innovation process, and is the proximity of innovators to final products essential for the effective development of innovations in the industry?*

Against the backdrop of the German government's interest in actively integrating renewable energy sources into the national energy system, embedded companies may receive a particular stimulus for innovative growth alongside the development of institutional structures and framework conditions in the country.

Table 1. Differences between STI knowledge and DUI knowledge

Characteristics	STI knowledge	DUI knowledge
Possibility of formalization	Formalizable	Difficult to formalize, "tacit"
Level of theorization	Theoretical	Applied
Research centers	Fundamental	Experimental
Type of innovator	Scientists	Engineers
Nature of innovations	Radical	Incremental
Scale	Global	Local

METHODS

Studying Germany in the context of innovation's development has methodological advantages. First, the country has strong statistical support, including in the field of spatial data, which enhances the quality of research and expands the possibilities for using various methods. Second, the country's continuous and densely populated space, with a uniformly high level of transport infrastructure development, helps minimize statistical deviations in identifying correlations, a benefit that classics of location theories utilized a century ago.

To test the hypotheses, a methodology was developed to quantitatively characterize the spatial distribution of knowledge generation locations in the field of wind energy and installed capacities. The essence of the methodology is to compare a company's share of installed wind energy capacities within an n -radius from a company branch to the company's share of installed capacities nationwide. Essentially, this indicator functions as a localization coefficient, utilizing radii around company branches instead of regions. These radii can be characterized as *gravitational fields or influence zones* of company branches (Eq. 1):

$$\frac{C_n / G_n}{C_a / G_a} \quad (1)$$

where C_n represents the company's installed capacities within radius n , C_a represents the total installed capacities in the country within radius n , G_n represents the company's installed capacities nationwide, and G_a represents the total installed capacities nationwide. Values of the coefficient significantly greater than 1 suggest a spatial correlation between installed capacities and company branches, indicating a relationship in their placement. The index also shows how much more attractive the placement of generating capacity is within a specific radius of a company branch compared to the national average.

To assess the gravitational fields, various types of company branches were considered. The primary ones are *innovation centers*, where key processes for creating new technological solutions occur. The study also analyzed the spatial distribution of installed capacities in relation to *headquarters*, which are branches with key organizational innovations. Production sites of wind energy companies can also impact innovation processes as repositories of engineering knowledge and serve as indicators of the market supply of wind turbines. The geographical coordinates of the key market players' branches were determined through an analysis of wind energy companies' websites.

Various distances (25, 50, 75, 100, 125, and 150 km) were used as radius values to track at what distance the influence zones of company branches weaken. For each type of company branch, a matrix of coefficients was created to show the level of interdependence between their locations and the company's installed capacities. GE Wind does not have innovation centers or headquarters in Germany, so in two cases, the matrices contain 4 columns instead of 5.

The study covers the period from 2000 to 2019. This range was chosen to avoid statistical deviations that arose during the COVID-19 pandemic and to conduct the research within the framework of the "Renewable Energy Sources Act". Additionally, this interval allows for a comparison of the phenomenon of co-location across two decades: 2000–2009 and 2010–2019. Equal time frames help to determine whether the role of co-location increased

as the industry developed or, conversely, decreased. Some company branches were established in the 2010s, but they were included in the calculations along with earlier wind turbine installations. This is possible because the study examines not just the impact of one factor on the location of the other but their *mutual influence*. It is assumed that the installed wind turbines could have influenced the location of new company branches due to the emergence of a local innovation environment in that area, formed based on tacit and applied knowledge.

To confirm the results obtained and to identify more detailed relationships, a cartographic research method was used. Maps showing the locations of innovation activity centers allowed for the identification of the specifics of their localization at the regional level (e.g., northern and southern Germany) and the urban level (e.g., large or small cities). Additionally, supplementary maps were created to either confirm or refute the results obtained from the index calculations. To visualize the relationship between the locations where companies generate knowledge and where they implement their products, the maps showing the density of wind turbines installed by various companies were overlaid with the locations of the major wind turbine manufacturers' branches. The analysis was conducted using the QGIS tool called Heatmap (Kernel Density Estimation). The weights of the points were based on the wind turbine capacities, and a bi-quadratic kernel shape was used for the calculations and the creation of the maps.

Information about the coordinates of wind turbines, their capacities, and manufacturing companies was obtained using the MaStR¹ database, the register for the German electricity and gas market. This database contains information about wind turbines installed in Germany since 1990, including the company under whose brand the turbine was manufactured, its capacity, and its location (geographical coordinates). On the one hand, this database helps identify the key companies active in the German wind energy market. On the other hand, the inclusion of geographical coordinates for the wind turbines allows for the application of the aforementioned methodology.

This approach may not be appropriate for all industries: wind energy, in particular, has a final product that is anchored in space, allowing for quantitative spatial assessment. The methodology is novel in that it attempts to statistically measure the geographic component of the interconnection between innovators and the final product, allowing for the evaluation of the impact of tacit forms of knowledge on the innovation process.

RESULTS

Specifics of the development of the corporate structure of the wind power market in Germany

In the 1980s, as the potential of wind power became increasingly clear, Germany attempted to develop powerful turbines with the support of government programmers (Ohlhorst 2009). This approach proved less effective than the model of neighboring Denmark. The Danish technology here was developed by local manufacturers. These companies were located in rural areas in regions with steady and strong winds. In the beginning, the firms met the needs of local communities, but they gradually consolidated and expanded, while the state only provided a favorable institutional environment without directly intervening in the innovation processes of the industry.

¹<https://www.marktstammdatenregister.de/MaStR/Einheit/Einheiten/ErweiterteOeffentlicheEinheitenubersicht#stromerzeugung>

This environment then emerged in northern Germany, where the conditions for wind energy development (wind speeds and rural electricity needs) are similar to those in Denmark (Ohlhorst 2009). Here, the first locally embedded German wind turbine manufacturers emerged. The latter is defined through the prism of their evolution: the longer the manufacturer's branches are located in a particular country or region, the more embedded the company is in the local environment. In addition, a company's focus on selling its products primarily domestically reinforces this quality.

The country has the status of a technological leader in the sector. Today, three of the top 10 global wind turbine manufacturers have German roots². German wind power plays a leading role in electricity generation among all energy sources: in 2023, almost 140 TWh of electricity was generated by wind power, accounting for 32% of the country's total electricity, and about 17% of wind generation was provided by offshore installations³. Following the Fukushima accident, the German government has established a consistent policy of abandoning nuclear power and increasing reliance on renewables, the development of which is particularly influenced by the feed-in tariff mechanism. The law enshrines the goal of increasing the share of renewable energy sources in the electricity supply to 80% by 2050⁴.

The most successful German wind turbine manufacturer on the domestic market is Enercon. The headquarters and largest production site of the company are located in Aurich. Other production sites are also located mainly in the north of the country. In 2014, an innovative research and development center and a test center were opened in Aurich. The management notes that the location was chosen based on its proximity to the production units in order to take advantage of the innovative benefits of co-localization and to contribute to the further development of technology and innovation in the company⁵. Enercon's current share of wind turbines in the German market is around 40%.

The second company in terms of production localization is Nordex. Despite the fact that it was founded in Denmark in 1985, after 6 years, the company moved to the town of Rerik in the federal state of Mecklenburg-Western Pomerania, and then in 1999, with the expansion of production, to Rostock. The company's headquarters, main production site, and innovation center are now located

here, while management and the employee training center are localized in Hamburg. However, in the last decade, Nordex management decided to intensify its presence in global markets and merged with another energy company, Spain's Acciona, forming the conglomerate Nordex Group in 2016. It now accounts for about 7% of the German wind turbine market.

The Spanish-German wind energy company Siemens Gamesa Renewable Energy (SGRE) also built its first production site in Denmark. In 1980, Danregn, a Danish company, became involved in the production of wind turbines. In 2004, it was sold to Siemens AG, one of Germany's largest industrial conglomerates. As a result, its headquarters, as a sales and project management center, moved to Hamburg. In doing so, the company chose a different strategy from Enercon, which was focused on the domestic onshore wind energy market and carved out a significant niche for itself in foreign markets. For this purpose, the turbine manufacturer under Siemens has been opening its own production sites around the world, acquiring other companies, and developing offshore wind power. The biggest expansion came in 2016: Siemens and Spanish wind energy company Gamesa announced their plan to create a merged company with a 59 percent stake in Siemens and a 41 percent stake in Gamesa. In 2019, SGRE agreed to acquire for €200 million the European service park of Hamburg-based Senvion, which, before the deal, provided 10% of the German wind energy market, including offshore wind turbines.

The key foreign company in terms of installed capacity in Germany is Denmark's Vestas, the world leader in wind power (with a German market share of more than 20%, the same as SGRE's). Vestas, despite its foreign roots, is present throughout the entire value chain in neighboring Germany, including R&D. Another world leader in the wind power industry, a division of American General Electric (GE Wind Energy), is less active in Germany. The main research departments of the company are not located in Germany, so GE Wind Energy takes almost no part in local innovation processes. It accounts for about 6% of the German wind energy market.

In total, these five companies provide almost the entire German wind energy market (Fig. 1): German Enercon, German-Spanish Siemens Gamesa Renewable Energy (SGRE), and Nordex Group, as well as Danish Vestas and American GE Wind Energy (headquartered in France).

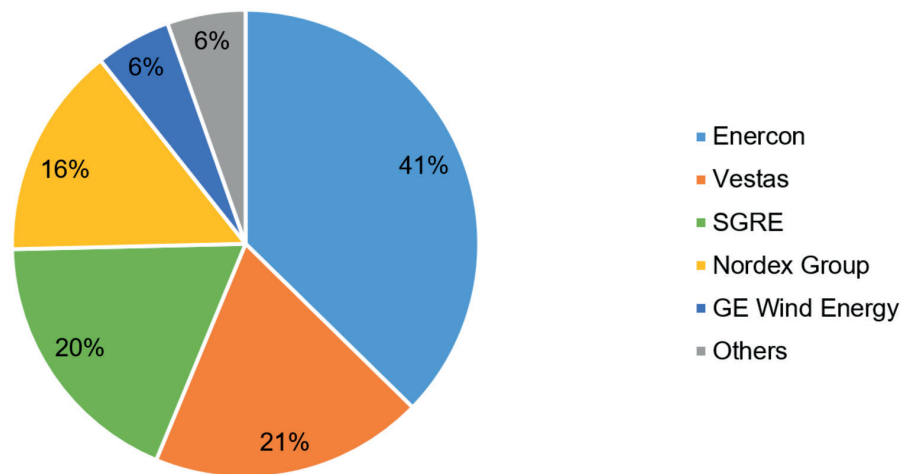


Fig. 1. Shares of wind turbine manufacturers in the German market by installed capacity⁶

² <https://energydigital.com/top10/top-10-wind-turbine-manufacturers>

³ https://www.energy-charts.info/downloads/electricity_generation_germany_2023.pdf

⁴ <https://www.bundesregierung.de/breg-de/schwerpunkte/klimaschutz/wind-an-land-gesetz-2052764>

⁵ <https://www.enercon.de/unternehmen/>

⁶ <https://www.enercon.de/en/company/market-share/>

Location of fundamental and applied research institutes

Although companies are increasingly taking over the R&D functions of research institutes and universities, their role in innovation processes in Germany remains significant. The location of company-independent R&D centers was analyzed in two research-oriented categories: fundamental and applied. Scientific organizations aimed at fundamental research in the field of the wind power industry (DLR, WindForS, and ForWind) are located in cities with decent universities (Fig. 2). In fact, two geographical areas can be allocated: Lower Saxony and Southern Germany (the states of Bavaria and Baden-Württemberg). This shows that fundamental knowledge can arise not only in the locations where wind turbines are directly operated. At the same time, applied research institutes (Fraunhofer IWES, DEWI, and FuE-Zentrum FH Kiel) are located only in the north, where knowledge is put into practice.

The resulting spatial pattern of fundamental and applied research institutes corresponds to the peculiarities of the industry's development at a very early stage. The initial innovation impetus in the country did not originate in the north of Germany, where the main wind power capacities are installed today, but in the south, in Stuttgart, where aerodynamics research was conducted at the local technical university. By 1957, one of the first wind turbines in the world had been commissioned under the direction of aeronautical engineering professor Ulrich Hütter. It was built on the principles of aeronautical engineering: "Anything that rotates should be as light as possible, but also as strong as necessary (Maegaard et al. 2020)". So, the radical innovation within the industry originated in a fundamental university environment rather than in places with favorable

natural conditions for the implementation of wind energy. Soon, the character of innovation transformed from radical to incremental, and innovation activity in the German wind industry shifted from the south of the country to the north, where there are more opportunities for obtaining applied knowledge.

Co-location of R&D departments, production sites, headquarters, and installed capacity

R&D Departments

The calculations show a clear relationship between Enercon's R&D department and its installed capacity (Table 2). The index values correlate with the degree of the company's embeddedness in the local environment. Enercon dominates the domestic market, but its level of presence in global markets is lower than that of other companies⁷. High index values (above 1.25) persist up to a distance of 125 kilometers, with a maximum of 2.50 within a radius of 25 kilometers. Enercon is a key wind energy company in Lower Saxony, the German federal state with the highest wind energy potential.

The example of Enercon's data shows that our hypothesis of *decreasing interdependence in the location of innovation centers and wind generation capacity as the industry reaches maturity* is confirmed only at larger radii of 75, 100, 125, and 150 km (these indices are lower in the 2010s compared to the 2000s). At the same time, at distances of 25 and 50 km from the R&D department, the coefficient in 2010 was higher (2.66 and 2.38) than in the 2000s (2.21 and 2.08). Evidently, the role of tacit knowledge in innovation processes of embedded firms at

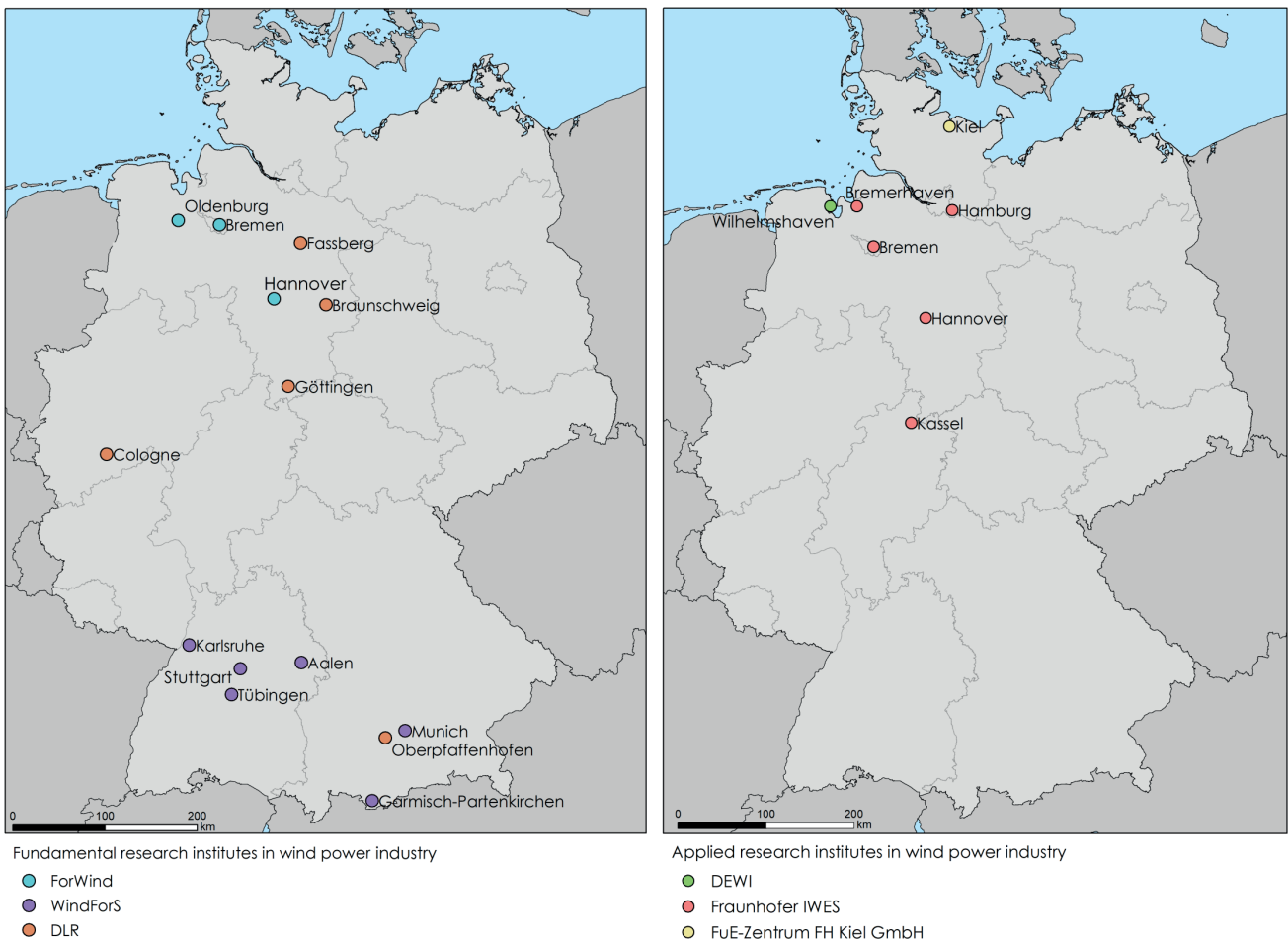


Fig. 2. Location of the main fundamental and applied research centers in the German wind energy industry

⁷ According to the ranking of global wind energy companies: <https://energydigital.com/top10/top-10-wind-turbine-manufacturers>

Table 2. Coefficient matrix of co-location of R&D departments in key companies and installed capacities

R&D departments								
Radius to department, km	Enercon		Nordex Group		SGRE		Vestas	
	2000–2009	2010–2019	2000–2009	2010–2019	2000–2009	2010–2019	2000–2009	2010–2019
25	2.50		2.31		1.53		0.12	
	2.21	2.66	2.18	2.40	0.66	1.44	0.16	0.00
50	2.27		1.92		1.50		0.10	
	2.08	2.38	1.60	2.09	1.73	1.37	0.19	0.00
75	1.64		1.16		1.38		0.45	
	1.89	1.59	1.42	1.09	1.80	1.24	0.52	0.35
100	1.27		1.06		1.34		0.53	
	1.79	1.16	1.43	0.94	1.79	1.20	0.60	0.43
125	1.31		1.14		1.23		0.54	
	1.61	1.24	1.56	1.02	1.58	1.13	0.58	0.51
150	1.17		0.98		1.30		0.55	
	1.42	1.07	1.35	0.87	1.46	1.24	0.62	0.50

close distances does not weaken. The multiplicative effect of the mutual intensification of spatial gravity contributes to the increase in the degree of co-location throughout the development of the industry. This means that there are two trends in the evolution of innovation processes: "localization", which promotes increased concentration in small radii, and "deconcentrating". The latter is characterized by a decrease in the importance of co-location at farther radii (Fig. 3).

It should be noted that Enercon's success is largely due to the inventive skills of the company's founder, local "self-made" entrepreneur and innovator Alloys Wobben. He was born in Rastdorf, graduated from the University of Oldenburg, and his career path is similar to that of Stanford University students W. Hewlett and D. Packard⁸. By 1984, A. Wobben was in Aurich and had established Enercon, a company that later became one of the leaders of the German wind energy industry. Wobben's activities were compactly concentrated in the north-western part of the federal state of Lower Saxony, indicating a high degree of embeddedness for both the company and its founder in the local environment.

A German wind turbine manufacturer close to Enercon in terms of its embeddedness is Nordex. In recent years, the company has embarked on a course to expand its markets worldwide by creating the German-Spanish Nordex Group. The values of the index also reflect its slightly lower focus on the German consumer compared to Enercon. Nevertheless, it shows high results in the 25- and 50-km radius (2.31 and 1.92), indicating the large influence of localization within the northeastern region of Germany. However, already at the 75-km radius, the index decreases significantly. The indices for the different periods reflect similar trends as in the case of Enercon: in the 2010s, the indices were significantly higher at 25- and 50-km radii and lower at 75-, 100-, 125-, and 150-km radii. This suggests the *50-km radius as the 'gold standard' for the processes of sharing tacit DUI knowledge in the German wind industry in the case of locally embedded companies.*

Like Nordex Group, SGRE is a German-Spanish conglomerate, but its roots in Germany are even weaker. This is partly due to the fact that the company was Danish for quite a long time. With the merger in 2016 with Spain's Gamesa, the company became a global company specializing in large wind power projects, including offshore projects. With a significant share of the German wind energy market (more than 20%), the company shows high index values (above 1.25) up to a 150 km radius, but in the closest radius from innovation centers, the company is behind Enercon and Nordex (Fig. 4).

Starting from the 50-km radius for SGRE, a decrease in the localization coefficient was observed in the 2010s compared to the previous decade. This reflects SGRE's less localized approach to the location of innovation centers compared to Enercon and Nordex. At the closest distance (25 km radius), however, the previously identified logic of increasing mutual attraction of innovation centers and installed capacity persists: in the 2010s, the coefficient values in the 25 km radius became higher than in all other radii (1.44). This indicates that even in a weakly embedded firm, the role of tacit knowledge in innovation processes persists.

For the foreign company Vestas, whose main innovation activity takes place outside Germany, the value of the localization coefficient was significantly lower than 1 at all radii. Thus, there is a spatial disintegration of its economic operation. The company's R&D activities are conducted in Denmark, where its headquarters and main innovation centers are located. In Germany, the company has only located one innovation center in Dortmund during the study period. Here, Vestas has advanced S&T competencies, but there is no demand for a local environment with tacitly applied wind energy knowledge, as there are no locations for generator installations in the highly urbanized Ruhr Area. The low coefficient values (<0.2) for radii of 25 and 50 kilometers are related to this.

Vestas installs wind turbines in East Germany to fill a niche that German manufacturers do not occupy. After the

⁸ <https://www.deutschland.de/de/taxonomy/term/40/der-pionier-aus-dem-norden>
<https://successstory.com/people/alloys-wobben>

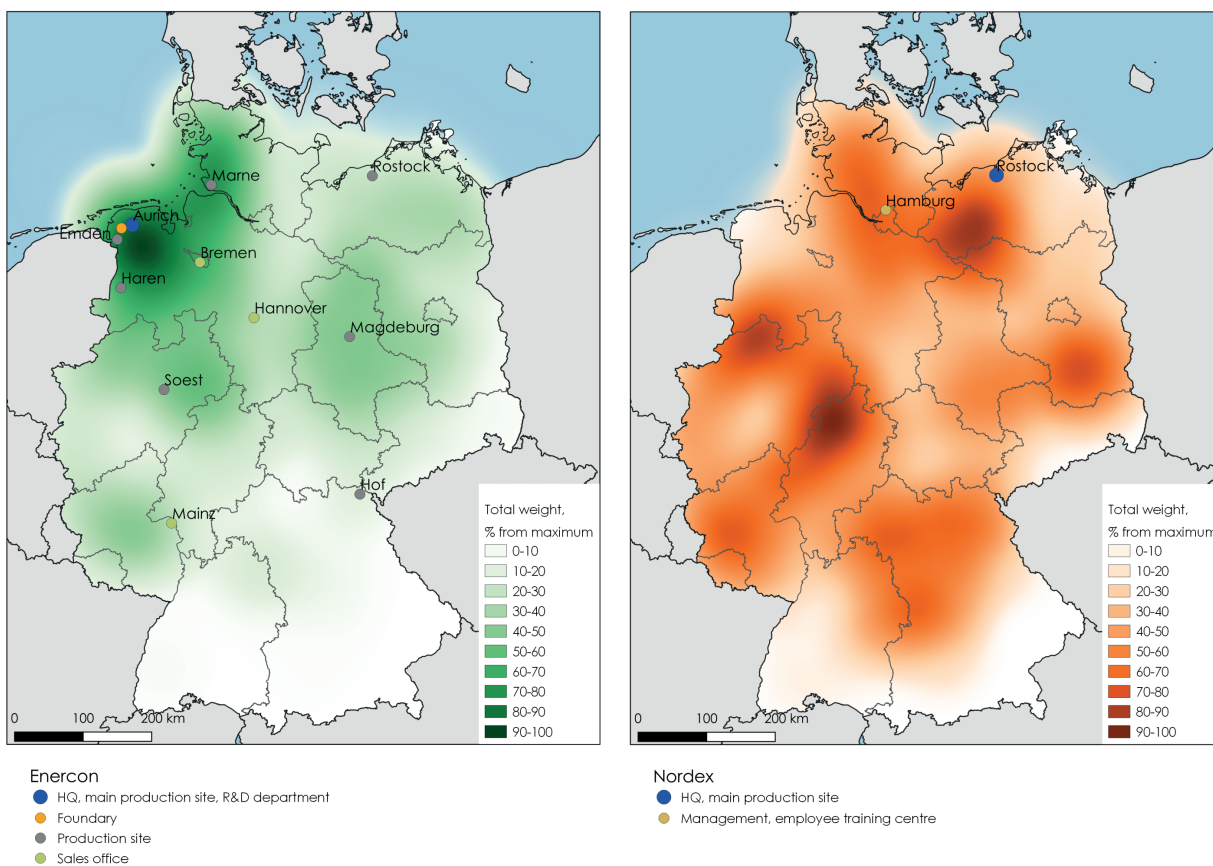


Fig. 3. Density maps of installed wind turbines of embedded companies (Enercon and Nordex) and the location of their main branches

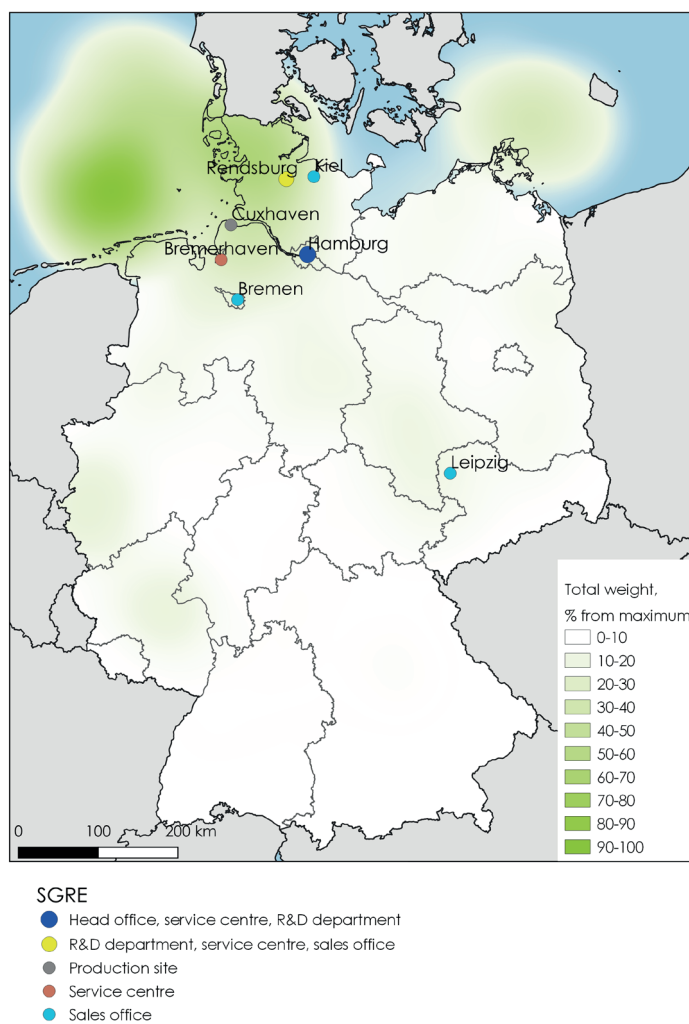


Fig. 4. Density maps of installed SGRE wind turbines and the location of their main branches

country's reunification, due to the lower population density and increased investment attractiveness of new projects (including through institutional support from regional authorities), this part of the country is characterized by a high potential for the industry's development (Fig. 5). Germany seems to downplay tacit knowledge for the company, unlike its home country. There is also a decrease in the localization ratio in the 2010s compared to the 2000s, confirming the weakening of the relationship over time.

Thus, for a foreign company, we should not speak about the lack of connections in the co-location but about the *opposite* nature of such connections. The location of the Vestas wind turbine generators was due to the low density of settlement in the East German lands (on a German scale). The location of the innovation center, on the contrary, was due to its gravitation towards a densely populated environment with a large number of universities and people who are carriers of explicit formalized knowledge.

Headquarters and production sites

The thesis about the different influences of the local environment on national and foreign companies is also confirmed by the coefficients for their headquarters (Table 3). For Enercon and Nordex, they do not differ from the coefficients calculated for innovation centers, which indicates that innovation and management processes are embedded in the same environment. In the case of the transnational SGRE, lower rates persist for HQs as for innovation centers; the centrifugal tendency when comparing the 2000s and 2010s is evident to the same extent as for innovation centers. A low degree of co-location is also observed for the Danish Vestas (indicator values are strongly below 1).

At the same time, American GE Wind has neither headquarters nor innovation centers in Germany, which demonstrates the exclusive role of the demand factor for wind turbines in terms of capacity placement under this brand.

The coefficients calculated for the production sites confirmed it (Table 4). The figures were highest for foreign companies Vestas and GE Wind. Within a radius of 100 kilometers, values consistently exceed 1.4. Moreover, for the geographically more isolated American GE Wind, they are much higher than for the Danish Vestas. Co-location of production centers and installed capacities is also common among embedded companies. The coefficients are comparable to those of innovation centers and headquarters. Such co-location also favors the diffusion of tacit knowledge within the local environment.

The study yielded three main findings. The research revealed a positive correlation between the locations of knowledge generation and the capacities installed by companies.

Furthermore, the higher the level of embeddedness, the greater the impact on innovation co-location and end-product manufacturing within the firm. Close proximity fosters intensive intra-firm exchange of tacit knowledge (doing-using-interaction mode), an effect that is most visible within a radius of 50 km (co-location coefficients range from 1.9 to 2.5). At the same time, foreign enterprises only have high co-location coefficients (2.2–3.9) at manufacturing sites. In this instance, market demand – rather than tacit knowledge embedded in the local environment – determines the location of installed capacities and corporate branches.

Over time, the correlation between knowledge generation locations and their application for embedded

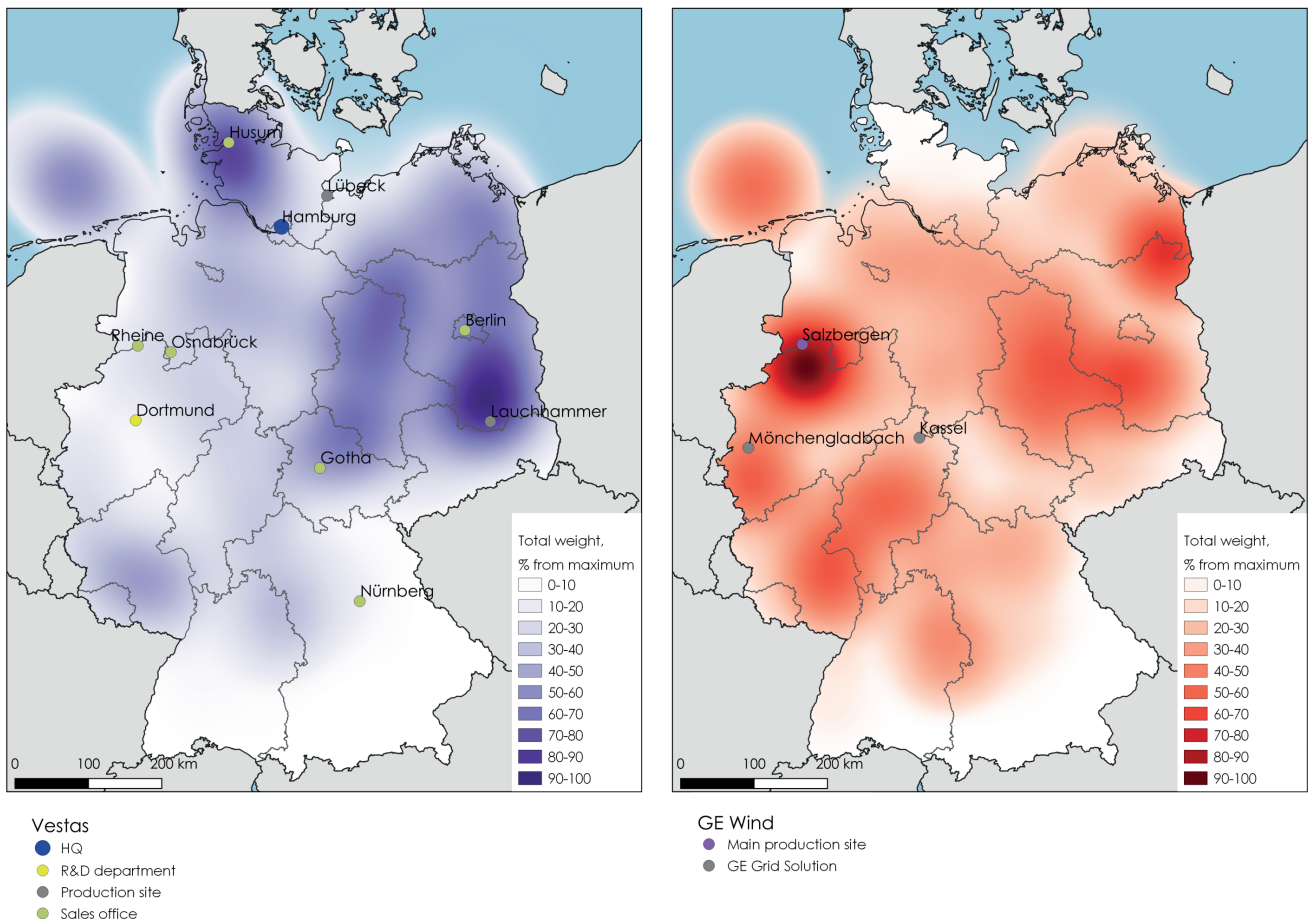


Fig. 5. Density maps of installed wind turbines of foreign companies (Danish Vestas and American GE Wind) and the location of their main branches

Table 3. Coefficient matrix of co-location of headquarters in key companies and installed capacities

Headquarters									
Radius to HQ, km	Enercon		Nordex Group		SGRE		Vestas		
	2000–2009	2010–2019	2000–2009	2010–2019	2000–2009	2010–2019	2000–2009	2010–2019	
25	2.50		2.31		1.31		0.31		
	2.21	2.66	2.18	2.40	1.24	1.28	0.00	0.42	
50	2.27		1.92		1.13		0.86		
	2.08	2.38	1.60	2.09	1.79	0.97	1.24	0.60	
75	1.64		1.16		0.98		0.75		
	1.89	1.59	1.42	1.09	1.69	0.80	1.12	0.49	
100	1.27		1.06		1.06		0.80		
	1.79	1.16	1.43	0.94	1.61	0.93	1.02	0.71	
125	1.31		1.14		0.99		0.83		
	1.61	1.24	1.56	1.02	1.30	0.93	0.97	0.74	
150	1.17		0.98		1.00		0.90		
	1.42	1.07	1.35	0.87	1.24	0.95	0.91	0.89	

Table 4. Coefficient matrix of co-location of production sites in key companies and installed capacities

Production sites										
Radius to PS, km	Enercon		Nordex Group		SGRE		Vestas		GE	
	2000–2009	2010–2019	2000–2009	2010–2019	2000–2009	2010–2019	2000–2009	2010–2019	2000–2009	2010–2019
25	1.95		2.31		1.19		2.55		3.86	
	1.60	2.14	2.18	2.40	2.30	0.96	2.28	2.73	4.35	3.45
50	1.78		1.92		1.18		2.16		2.37	
	1.47	1.96	1.60	2.09	1.79	1.02	2.16	2.06	1.84	2.74
75	1.50		1.16		1.11		1.67		1.82	
	1.39	1.56	1.42	1.09	1.56	0.97	1.58	1.64	2.03	1.54
100	1.31		1.06		1.30		1.41		1.43	
	1.32	1.31	1.43	0.94	1.31	1.21	1.41	1.34	1.61	1.18
125	1.26		1.14		1.55		1.24		1.07	
	1.26	1.27	1.56	1.02	1.54	1.46	1.24	1.20	1.25	0.80
150	1.18		0.98		1.55		1.18		0.87	
	1.22	1.10	1.35	0.87	1.32	1.49	1.18	1.14	1.11	0.60

enterprises declines over greater distances but strengthens within a 50-kilometer radius (at this distance co-location coefficients increase from 1.6–2.5 in 2000–2009 to 2.1–2.7 in 2010–2019). Thus, for local producers, the hypothesis that the relevance of tacit knowledge declines as the industry matures is only partially supported.

DISCUSSION AND CONCLUSIONS

Geographical aspects of innovation processes play a crucial role in sectoral studies, particularly when viewed

through the lens of different types of knowledge. In industries like wind energy, where tacit knowledge (in the doing-using-interacting mode, or DUI) is central to innovation, the importance of geographical proximity becomes particularly pronounced. A wealth of literature supports this view, highlighting the innovation characteristics specific to the wind energy sector (Binz and Truffer 2017; Moodysson et al. 2008; Rohe 2020; Tsouri et al. 2021; Heidenreich and Mattes 2022). Access to tacit knowledge can be significantly enhanced when innovators are co-located with the places where final products are

implemented. This study, for the first time, examined and confirmed the hypothesis that there is a correlation between the locations of knowledge generation and installed capacities in wind energy.

The analysis of co-location between company branches and installed wind power capacities revealed that the degree of spatial mutual influence strongly depends on the level of embeddedness in the local environment. Companies that are locally embedded demonstrate a clear pattern of co-locating their knowledge centers and production sites. This observation underscores the importance of the local environment in the wind energy industry, where much of the production chain – from wind turbine development to installation – takes place. In these settings, innovation processes are heavily shaped by tacit knowledge exchange. The phenomenon of co-location is most pronounced within a 50 km radius, which reflects the importance of local proximity in fostering tacit knowledge sharing. According to Asheim and Coenen's classification, this makes the German wind energy sector closely aligned with territorially embedded regional innovation systems (RIS) (Asheim and Coenen 2005).

This study also provides a novel contribution by examining the evolution of innovation processes in the wind energy industry. It challenges the prevailing idea that the role of DUI knowledge diminishes over time due to the formalization of knowledge (Feldman and Kogler 2010). The hypothesis was not fully supported in the case of German wind energy, where the synergistic effect of knowledge concentration within a small radius (50 km) often outweighed the tendency toward formalizing knowledge. While there was evidence of a "localization" effect (increased co-location at small radii), there was also a "deconcentrating" trend at larger radii, indicating a growing importance of other factors beyond geographic proximity.

This dual process – localization within small radii and deconcentration at larger scales – suggests a nuanced understanding of the spatial dynamics of innovation. For embedded companies, such as Enercon and Nordex, the proximity to tacit knowledge sources in the local environment is crucial. In contrast, foreign firms, which are less embedded in the local context, show a weaker reliance on local tacit knowledge and instead focus on accessing STI knowledge and market niches. This observation verifies the conclusion that the division of industries based on distinct types of knowledge (STI vs. DUI) is overly simplistic (Bathelt et al. 2004; Hanson et al. 2021; Tsouri et al. 2021). The innovation processes of foreign companies in the German wind energy sector align more with STI processes, where the spatial pattern of innovation centers and installed capacities is driven by access to specialized knowledge and market demands, rather than tacit knowledge embedded in the local environment.

Despite these findings, several aspects remain unexplored and warrant further research. The complexity of the wind energy innovation process, coupled with increased skill recombination and outsourcing of certain production stages, results in a mix of knowledge types, blurring the distinction between DUI and STI knowledge. This study did not fully address this phenomenon, but it presents an important avenue for future inquiry.

Additionally, the proposed methodology does not resolve the question of which comes first in co-location: the innovators or the installed capacities. In some cases, the emergence of innovation centers may drive the expansion of installed capacities in close proximity, as innovators seek to observe the practical outcomes of their work. Alternatively, the installation and operation of wind turbines may create the tacit knowledge environment that attracts innovation centers to the region. Furthermore, the study does not account for other potential factors influencing co-location, such as the institutional environment, which could also shape innovation patterns in wind energy.

The practical implications of this study lie in its ability to inform more effective innovation policies for the wind energy sector. The findings suggest that for industries like wind energy, where tacit knowledge plays a central role, a policy approach that reinforces local connections and builds on existing regional innovation systems (RIS) would be most effective. In particular, an ex-post approach, which strengthens existing development trajectories and focuses on the reinforcement of embedded RIS, would likely yield better results. In this context, the emphasis should not be on integrating governmental research centers into the established innovation structures, but rather on reinforcing intra-regional connections between key innovators and local suppliers, who carry critical tacit knowledge.

For regions like northwestern Germany, which lie between the innovation core and the periphery, specialized innovation growth based on embedded tacit knowledge could help establish thriving local innovation systems. This contrasts with broader, one-size-fits-all innovation policies that focus on generic factors such as increased R&D spending or human capital development. These generic approaches often overlook the importance of medium-sized regions, which may lack the critical mass of resources but can still play a key role in localized innovation.

As noted by Zemtsov and Baburin (2019), this is particularly relevant for Russia, characterized by a pronounced spatial polarization in its innovation potential. Our findings indicate that innovative development is also achievable in non-leading regions, creating opportunities for long-term innovation-driven growth in most of Russia, beyond the influence zones of the largest agglomerations. ■

REFERENCES

- Alhusen, H., Berrat, T. (2021). Combinatorial innovation modes in SMEs: Mechanisms integrating STI processes into DUI mode learning and the role of regional innovation policy. *European Planning Studies*, 29 (4), 779-805. DOI: 10.1080/09654313.2020.1786009.
- Asheim, B. (2007). Differentiated knowledge bases and varieties of regional innovation systems. *Innovation*, 20 (3), 223-241. DOI: 10.1080/13511610701722846.
- Asheim B. and Coenen L. (2005). Knowledge bases and regional innovation systems: Comparing Nordic clusters. *Research Policy*, 34(8), 1173-1190. DOI: 10.1016/j.respol.2005.03.013.
- Asheim B. and Gertler M. (2005). The geography of innovation: regional innovation systems. In: Fagerberg J., Mowery D., and Nelson R., (eds) *The Oxford Handbook of Innovation*. Oxford: Oxford University Press, 291-317. DOI: 10.1093/oxfordhb/9780199286805.003.0011.
- Alle, K., Fettke, U., Fuchs, G., Hinderer, N. (2017). Lokale Innovationsimpulse und die Transformation des deutschen Energiesystems. In: Fuchs, G. (eds) *Lokale Impulse für Energieinnovationen*. Energie in Naturwissenschaft, Technik, Wirtschaft und Gesellschaft. Wiesbaden: Springer Vieweg, DOI: 10.1007/978-3-658-14801-0_1.
- Baburin V.L., Zemtsov S.P. (2017). *Innovation potential of russian regions*. Moscow: KDU "University book".
- Barua, P. T. (2012). Delivering on the clean energy economy: The role of policy in developing successful domestic solar and wind industries. World Resources Institute, [online]. Available at: http://pdf.wri.org/delivering_clean_energy_economy.pdf html [Accessed 22 Feb. 2025].

- Bathelt, H., Malmberg, A., & Maskell, P. (2004). Clusters and knowledge: local buzz, global pipelines and the process of knowledge creation. *Progress in human geography*, 28 (1), 31-56. DOI: 10.1191/0309132504ph469oa.
- Beccattini G. (1979). Dal "settore" industriale al "distretto" industriale. Alcune considerazioni sull'unità d'indagine dell'economia industriale. *Rivista di economia e politica industriale*, 1, 7-21.
- Beccattini G. (1990). The Marshallian industrial district as a socio-economic notion. In: Pyke P., Beccattini G. and Sengenberger W. (Eds) *Industrial Districts & Inter-firm Co-operation in Italy*. Geneva: International Institute for Labour Studies (ILO), 13-32. DOI: 10.4000/rei.6507.
- Bednarz, M. Broekel, T. (2020). Pulled or pushed? The spatial diffusion of wind energy between local demand and supply. *Industrial and Corporate Change*, 29 (4), 893-916. DOI: 10.1093/icc/dtaa012.
- Binz, C., Truffer, B. (2017). Global Innovation Systems — A conceptual framework for innovation dynamics in transnational contexts. *Research Policy*, 46 (7), 1284-1298. DOI: 10.1016/j.respol.2017.05.012.
- Boschma, R. (2005). Proximity and innovation: a critical assessment. *Regional Studies*, 39 (1), 61-74. DOI:10.1080/0034340052000320887.
- Camagni, R. (1991). Local 'Milieu', Uncertainty and Innovation Networks: Towards a New Dynamic Theory of Economic Space. In: Camagni, R., Ed., *Innovation Networks: Spatial Perspectives*. London: Belhaven, 121-144.
- Carrillo-Carrillo, F., Alcalde-Heras, H. (2020). Modes of innovation in an emerging economy: a firm-level analysis from Mexico. *Innovation*, 22 (3), 334-352. DOI: 10.1080/14479338.2020.1735395.
- Chugh, R. (2015). Do Australian universities encourage tacit knowledge transfer? *International Conference on Knowledge Management and Information Sharing*, 2, 128-135. DOI: 10.5220/0005585901280135.
- Cooke P. (2001). Regional innovation systems, clusters, and the knowledge economy, *Industrial and Corporate Change*, 10 (4), 945-974. DOI: 10.1093/icc/10.4.945.
- Doloreux, D., Shearmur, R. (2023). Does location matter? STI and DUI innovation modes in different geographic settings. *Tecinnovation*, 119, 102609. DOI: 10.1016/j.technovation.2022.102609.
- Eder, J. (2019). Innovation in the periphery: A critical survey and research agenda. *International Regional Science Review*, 42 (2), 119-146. DOI: 10.1177/0160017618764279.
- Feldman M. P., Kogler D. F. (2010). Stylized facts in the geography of innovation. *Handbook of the Economics of Innovation*, 1, 381-410. DOI: 10.1016/S0169-7218(10)01008-7.
- Hanson J. et al. (2021). The co-evolution of innovation systems and context: Offshore wind in Norway and the Netherlands. *Renewable and Sustainable Energy Reviews*, 138, 110513. DOI: 10.1016/j.rser.2020.110513.
- Heidenreich, M., Mattes, J. (2022). "Wissensgenerierung und -diffusion in der deutschen Windenergiebranche [Bundesländer-Übersicht zu Erneuerbaren Energien]". *Industrial and Corporate Change*, Vol. 31(5), 1285-1306, DOI: 10.1093/icc/dtac022.
- Hervas-Oliver, J. L., et al. (2021). Radical vs incremental innovation in Marshallian Industrial Districts in the Valencian Region: what prevails? In: Luciana Lazeretti, ed., *Rethinking Clusters*. London: Routledge, 46-61. DOI: 10.4324/9781003130222.
- Huenteler, J., Schmidt, T., Ossenbrink, J., and Hoffmann, V. (2015). Technology life-cycles in the energy sector — Technological characteristics and the role. *Technological Forecasting & Social Change*, 104, 102-121. DOI: 10.1016/j.techfore.2015.09.022.
- Jackwerth, T. (2017). Formen der Wissensintegration in Innovationsnetzwerken. Das Beispiel der Windenergie. In *Kollaborative Innovationen. Die innerbetriebliche Nutzung externer Wissensbestände in vernetzten Entwicklungsprozessen*, Göttingen: Universitätsverlag Göttingen, 119-147.
- Jensen, M. B., et al. (2007). Forms of knowledge and modes of innovation. *Research Policy*, 36 (5), 680-693. DOI: 10.1016/j.respol.2007.01.006.
- Kamp, L. M., Smits, R., & Andriess, C. (2004). Notions on learning applied to wind turbine development in the Netherlands and Denmark. *Energy Policy*, 32, 1625-1637. DOI: 10.1016/S0301-4215(03)00134-4.
- Lorenze E. and Lundvall B. (2006). *How Europe's Economies Learn: Coordinating Competing Models*. Oxford: Oxford University Press. DOI: 10.1093/oso/9780199203192.001.0001.
- Maegaard P., Krenz A., Palz W. (2013). Huetter's heritage: The Stuttgart School. In: *Wind power for the world: the rise of modern wind energy*, Boca Raton: CRC Press, 387-407. DOI: 10.1201/b15010.
- Marshall A. (1920). *Principles of Economics*, 8th ed. London: Macmillan and Co.
- Moodysson J. (2007). Sites and modes of knowledge creation: on the spatial organization of biotechnology innovation. Lund: Lund University.
- Moodysson J. (2008). Principles and practices of knowledge creation. On the organization of 'buzz' and 'pipelines' in life science communities, *Economic Geography* 84 (4), 449-469.
- Nonaka, I. (2009). The knowledge-creating company. In: *The economic impact of knowledge*, London: Routledge.
- Ohlhorst, D. (2009). Windenergienutzung in Deutschland – Konstellations- und Policy-Analyse des Innovationsverlaufs. In: *Windenergie in Deutschland: Konstellationen, Dynamiken und Regulierungspotenziale im Innovationsprozess*. Wiesbaden: VS-Research.
- Parrilli, M. D., Balavac, M., Radicic, D. (2020). Business innovation modes and their impact on innovation outputs: Regional variations and the nature of innovation across EU regions. *Research Policy*, 49 (8), 104047. DOI: 10.1016/j.respol.2020.104047.
- Parrilli, M. D., Heras, H. A. (2016). STI and DUI innovation modes: Scientific-technological and context-specific nuances. *Research Policy*, 45 (4), 747-756. DOI: 10.1016/j.respol.2016.01.001.
- Pelyasov A. N. (2012). Innovation and regional development. In: *Synergy in Space: regional innovation systems, clusters, and knowledge spillovers*. Smolensk: Oecumene.
- Polanyi, M. (1958). *Personal knowledge: Towards a post-critical philosophy*. London: Routledge & Kegan Paul.
- Rohe, S. (2020). The regional facet of a global innovation system: Exploring the spatiality of resource formation in the value chain for onshore wind energy. *Environmental Innovation and Societal Transitions*, 36, 331-344. DOI: 10.1016/j.eist.2020.02.002.
- Scott T A. (2007). Capitalism and urbanization in a new key? The cognitive-cultural dimension. *Social Forces* 85 (4), 1465-1482. DOI: 10.1353/sof.2007.0078.
- Smith, K. (2000). What is the 'knowledge economy'? Knowledge-intensive industries and distributed knowledge bases. Sydney: AEGIS, University of Western Sydney.
- Tang, T., & Popp, D. (2015). The Learning Process and Technological Change in Wind Power: Evidence from China's CDM Wind Projects. *Journal of Policy Analysis and Management*, 34, 195-222. DOI: 10.1002/pam.21879.
- Tsouri, M., Hanson, J., & Normann, H. (2021). Does participation in knowledge networks facilitate market access in global innovation systems? The case of offshore wind. *Research Policy*, 50 (5), 104227. DOI: 10.1016/J.RESPOL.2021.104227.

SMART DETECTION OF ILLICIT CANNABIS PLANTATIONS USING REMOTE SENSING TECHNOLOGY AND MACHINE LEARNING

Dedi Irawadi^{1,3*}, Tuga Mauritsius¹, Dony Kushardono², Syarif Budhiman², Karunika Diwyacitta², Bayu S. Adhitama², Fauzan A. Ayubi², Olivia Maftukhaturrizqoh², Ika S. Supriyani²

¹ Information Systems Management Department, Bina Nusantara University, Jakarta, 11480, Indonesia

² Research Center for Geoinformatics, Research Organization for Electronics and Informatics, National Research and Innovation Agency (BRIN), Bandung, 40135, Indonesia

³ Research Center for Satellite Technology, Research Organization for Aeronautics and Space, National Research and Innovation Agency (BRIN), Bogor, 16310, Indonesia

*Corresponding author: dedi004@brin.go.id; dedi.irawadi@binus.ac.id

Received: December 19th 2024 / Accepted: February 6th 2025 / Published: March 31st 2025

<https://doi.org/10.24057/2071-9388-2025-3538>

ABSTRACT. Remote sensing technology and machine learning classifiers can be utilized to develop smart detection systems for illicit crops such as *Cannabis sativa L.* Machine learning algorithms for classifying medium-resolution optical satellite data can be compared to identify the best model for enhancing law enforcement's detection of illicit crops efficiently and accurately. Remote sensing-based smart detection systems have been developed in South America and Central Asia; however, these methods cannot be used effectively for Indonesia due to high cloud coverage, geographical differences, and the smaller area of *Cannabis sativa L.* plantations. This research developed an agile methodology that employs backpropagation neural networks to analyze the statistical growth phenology of cannabis derived from multitemporal medium-resolution remote sensing data. Using datasets derived from Indonesian law enforcement eradication records, the method achieved 94% accuracy and a kappa coefficient of 0.9. Further, plant growth phenology based on vegetation index values from multitemporal data was used to assess the condition of identified cannabis plantations.

KEYWORDS: smart detection, *Cannabis sativa L.*, remote sensing data, machine learning classifiers

CITATION: Irawadi D., Mauritsius T., Kushardono D., Budhiman S., Diwyacitta K., Adhitama B. S., Ayubi F. A., Maftukhaturrizqoh O., Supriyani I. S. (2025). Smart Detection Of Illicit Cannabis Plantations Using Remote Sensing Technology And Machine Learning. *Geography, Environment, Sustainability*, 130-138

<https://doi.org/10.24057/2071-9388-2025-3538>

ACKNOWLEDGEMENTS: This research was supported by Bina Nusantara University, Research Organization for Aeronautics and Space, National Research, and Innovation Agency. The authors thank the Indonesian National Intelligence Agency, the Indonesian National Narcotics Agency, and the Research Organization for Electronics and Informatics, as well as the National Research and Innovation Agency, for their support.

Conflict of interests: The authors reported no potential conflict of interest.

INTRODUCTION

According to the World Drug Report 2022 released by UNODC, *Cannabis sativa L.*, or marijuana, is the most widely used addictive substance globally, with over 209 million users in 2022. The Indonesian National Narcotics Agency (BNN) reported that marijuana accounts for 65.5% of all illicit drug abuse cases, with the prevalence of drug use rising from 1.80% in 2019 to 1.95% in 2021¹. The drug eradication programs, including detecting cannabis plantations, will contribute to decreasing the availability of these prohibited substances. New approaches, such as remote sensing technology and artificial intelligence, are imperative for the rapid and efficient detection of illegal cannabis plantations, particularly in extensive areas.

An herbal plant originating from Central Asia, *Cannabis sativa L.* or marijuana, has been widely used for medicinal

purposes and as a source of textile materials (Andre et al. 2016). Cannabis, which has a wide range of applications, grows well with little maintenance as long as it gets enough sunlight and water. These characteristics have led to cannabis' rapid globalization and increasing attention.

Cannabis is an annual tropical plant; it can be harvested 4-6 months after planting. Its fingered leaves can grow up to 2 m, and it thrives at an elevation of 1000 meters above sea level. There are 3 species of cannabis plants (*Cannabis sativa L.*, *Cannabis indica*, and *Cannabis rudelis*) with different tetrahydrocannabinol (THC) contents. This level of THC in cannabis can harm mental health and the nervous system (Karst 2018). It may make users more tolerant to its negative effects, lead to dependence, and cause withdrawal symptoms. (Lim et al. 2017; Wilkinson et al. 2016).

¹ Research Data and Information Center. (2022). Indonesia Drugs Report 2022. Jakarta: National Narcotics Board of Indonesia.

Due to the negative effects of cannabis, some countries, including Indonesia, have banned its use. Law enforcement has put a lot of effort into eliminating the distribution and the source of cannabis. The operations to eradicate cannabis plantations carried out by law enforcers have not been effective; there is still a high number of cannabis users' prevalence. Using technology, such as remote sensing technology, to detect these illegal plantations will help law enforcement operate more efficiently to eradicate cannabis plantations.

Various classification methods based on optical remote sensing and SAR satellite data are used to monitor forest dynamics (Armenteras et al. 2013; Diwediga et al. 2017; Sirro et al. 2018), extract LULC information (Chen and Tsou 2021), calculate agricultural land area for harvest prediction (Dahal et al. 2018; Duraisamy et al. 2018; Elbasi et al. 2023), and develop urban land cover mapping (Tavares et al. 2019). Leveraging information based on remote sensing technology, policymakers can improve the decision-making process.

Phenology, a dynamic feature of vegetation, can help differentiate plants from others (Kustiyo et al. 2024). Remote sensing satellite data can estimate phenology by observing vegetation growth and leaf cross-section (Koschor et al. 2022; Yang et al. 2023). To avoid the complexity of multispectral data, plant greenness indices like Normalized Difference Vegetation Index (NDVI) or Enhanced Vegetation Index (EVI), can be used to analyze phenology (Huang et al. 2021; Jimenez et al. 2022; Suárez et al. 2022). These indices facilitate the classification of landscapes, including agriculture, vegetation, land use, water bodies, and forests (Choudhary et al. 2019; Zuo et al. 2019). This information can also be used in decision-making to determine plant age (Nieto et al. 2021).

The effectiveness of artificial intelligence in object identification using remote sensing data has been demonstrated in numerous studies. Classifying hyperspectral airborne data, Support Vector Machine (SVM) yields better accuracy compared to Random Forest (RF) to identify vegetation species that have similar spectral with their surroundings for heterogeneous areas, but RF yields better accuracy for more homogeneous area (Sabat-Tomala et al. 2020). Qian et al. (2015) stated that SVM and Normal Bayes (NB) are more accurate than CART and KNN for identifying land cover from high-resolution satellite images. An ensemble of CNNs with different architectures applied to various image representations functions as an effective feature extractor used to detect cannabis plantations (Ferreira et al. 2019). Sujud et al. (2021) argue that precision accuracy for classification methods depends on various factors; no one can claim that one classifier performs better than others.

Previous research has detected illegal cannabis plantations carried out in China, Afghanistan, and several South American countries, with one thing in common, namely that the average area is quite large, 3 to 9 ha (Sujud et al. 2021) or even more. Detection of cannabis plantations using Landsat 8 NDVI data (Mattiuzzi et al. 2014), IKONOS high-resolution data and deep learning (Ferreira et al. 2019), optical and SAR satellite data fusion, and machine learning (Sujud et al. 2021), as well as high-resolution data (QuickBird and SPOT 5) and machine learning (Bicakli et al. 2022) produces quite high accuracy values of more than 90%.

Unique features of cannabis plantations in Indonesia, such as small, un-irrigated areas, forested areas, and high cloud coverage, pose challenges for building identification models using medium-resolution optical satellite data. This research aims to develop a cannabis plantation detection system applicable in Indonesia by utilizing multitemporal medium optical data, high-resolution satellite data, and other geographic features. By compiling a valid dataset, a model to detect cannabis plantations can be built by leveraging a fast machine learning classifier. The result of this research will benefit law enforcement for efficient and effective detection of illegal cannabis plantations and provide a cannabis plant dataset in Indonesia for future research.

This research uses adjusted satellite data from the Sentinel 2A and 2B missions, collected between 2021 and 2022. The data comes from different sources, resolutions, and times. High-resolution satellite imagery and a database of cannabis eradication operations provided by law enforcement agencies are also used for validation purposes. Aceh Besar District in Nangroe Aceh Darussalam (NAD) will be the focal point of this research.

MATERIALS AND METHODS

Study Area

Although the cultivation of cannabis is prohibited under Indonesia's Narcotics Law of 2009, the practice persists, particularly in NAD². This has prompted law enforcement agencies to conduct frequent eradication operations aimed at eliminating cannabis plantations³. In 2023, BNN together with BRIN (The National Research and Innovation Agency), BIG (The Indonesian Mapping Agency) and local authorities eradicated cannabis plantation in Aceh Besar District, NAD Province, as shown in Fig. 1a. This area was then selected as a study location due to the availability of field data. Field information, serving as secondary data was made available by law enforcement agencies, containing locations and timestamps of eradication activities in spreadsheet form.

Remote sensing data

Leveraging 5-day temporal resolution, the Sentinel-2 constellation⁴ is used in this research to obtain cloud-free data (Fig. 1b). The Sentinel-2 data, acquired between October 2021 and February 2022, comprise 17 selected dates and were utilized to detect cannabis plantations. Sentinel-2 data from March to October 2022 is used to assess the condition of these plantations. The satellite data used includes three visible light spectrum bands and one near-infrared band, all with a spatial resolution of 10 meters.

The eradication site locations for this research were validated using RGB composite imagery from the WorldView-3 satellite by Maxar Technologies (Fig. 1c), available on Google Earth. Acquired in October 2024, this imagery offers a spatial resolution of 31 cm. It adds to the main dataset, which consists of Sentinel-2 images taken over nine months. These images include data in the red, green, blue, and near-infrared bands (bands 2, 3, 4, and 8).

A total of 284 scenes of data were accessible via the Sentinel portal data hub, part of the Copernicus program⁵. These datasets, which have undergone radiometric and

²Kompas, (2023). Ladang Ganja Masih Ditemukan di Aceh, Kali Ini Seluas 2,5 Hektar. [online] Available at: regional.kompas.com/read/2023/02/23/091659278/ladang-ganja-masih-ditemukan-di-aceh-kali-ini-seluas-25-hektar [Accessed 11 Dec. 2024].

³<https://www.thejakartapost.com/indonesia/2024/05/22/aceh-authorities-to-ban-marijuana-laced-dishes-in-restaurants.html> [Accessed 11 Dec. 2024]

⁴Thales Alenia Space. 2021. Sentinel-2 Products Specification Document (PSD).

⁵<https://dataspace.copernicus.eu/browser/>

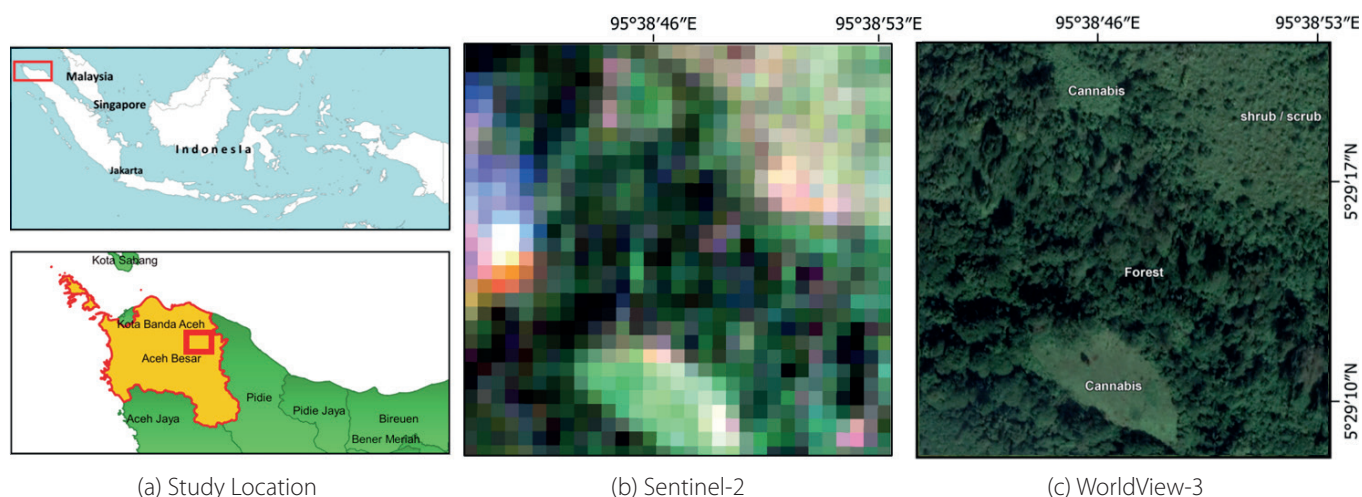


Fig. 1. (a) Study location with (b) input data and (c) reference image

geometric corrections, serve as the primary data for further processing. High-resolution satellite data was provided by BRIN (The National Research and Innovation Agency) and BIN (The National Intelligence Agency), while the base map was provided by BIG (The Indonesian Mapping Agency).

Methodology

The study aimed to develop a cannabis plantation detection system based on digital data processing utilizing remote sensing satellite data and machine learning classifiers. Additionally, the study sought to determine the condition of cannabis plants by analyzing plant growth phenology. The identification of illicit cannabis plantations within forested regions can be effectively achieved through a supervised classification approach employing machine learning classifiers. This method leverages the statistical features of plant growth phenology derived from multi-temporal optical satellite imagery, addressing challenges associated with high cloud cover and varying phenological stages of cannabis plants. Furthermore, the condition of cannabis plants was determined by analyzing their growth phenology based on vegetation index values from multi-temporal remote sensing satellite data.

Cannabis cultivation necessitates direct sunlight (Morello et al. 2022) and adequate water supply (Dillis et al.

2020) for optimal growth. This dependency makes cannabis plantations visible from an aerial perspective and often results in their location near water sources. Consequently, medium-resolution satellite data serves as an ideal tool for locating cannabis plantations, as remote sensing satellites periodically pass over and collect data from areas on the Earth's surface.

Fig. 2 illustrates the flow diagram of the proposed data processing model for utilizing remote sensing to detect cannabis plantations and assess their conditions. The model utilized medium-resolution optical remote sensing data from the Sentinel-2 constellation, covering the period from 2019 to 2022.

The model development involved the following stages:

1. **Data Preparation:** This involves data correction for the satellite data, ensuring it has undergone necessary level corrections. Commonly used geometric and radiometric correction methods are applied. This research used Level-2A, radiometrically and geometrically corrected image products provided by the Sentinel Hub. The Level-2A data is an ortho-image product that is projected using a Digital Elevation Model (DEM) to correct geometric distortions. Bottom-Of-Atmosphere (BOA) radiometric correction was applied to the data, followed by basic pixel features classification (including cloud types identification)⁶. A manual selection process was employed to identify cloud-

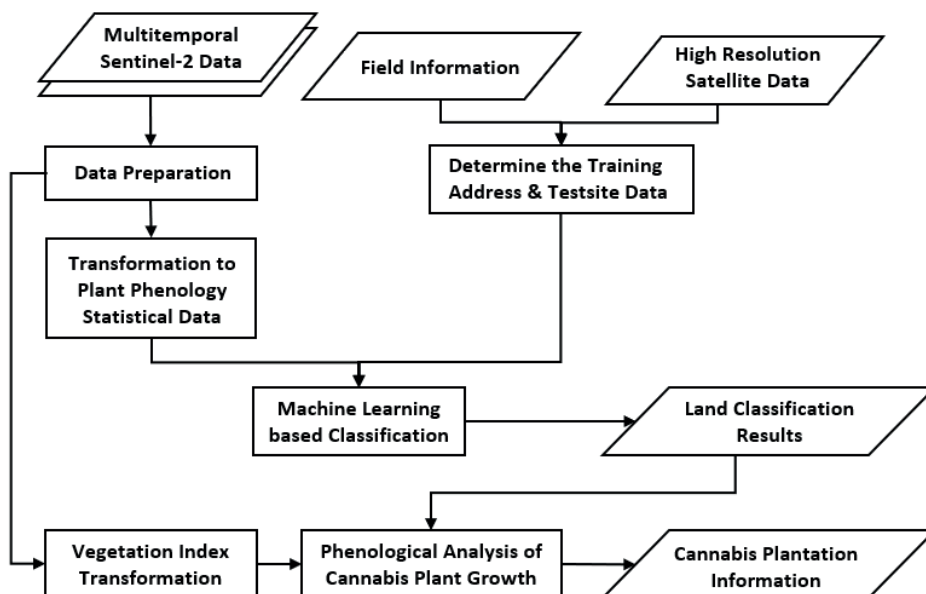


Fig. 2. Proposed model of smart cannabis plantations detection

⁶ Thales Alenia Space. 2021. Sentinel-2 Products Specification Document (PSD).

free, usable data from the four-band multi-temporal Sentinel-2 satellite datasets spanning from 2021 to 2022. This process resulted in the identification of 17 usable datasets for the designated research area.

2. Transformation of Multitemporal Satellite Data:

Data transformation aims to extract statistical parameters that consist of the minimum, maximum, average, and standard deviation of each pixel position as new datasets. Statistical parameters reflect the plant growth phenology and other land characteristics over a period of time (6 months before and 3 months after the plant destruction). NDVI was calculated from the red and NIR bands, and then NDVI along with the red, green, blue, and NIR bands is transformed into statistical parameters.

3. Determination of Training and Test Data: Cannabis dataset, derived from eradication activities provided by Indonesian law enforcement agencies, was validated by high-resolution remote sensing data. The locations (longitude and latitude) of all eradication activities were selected as the centers of spatial datasets. Data from the available multi-temporal Sentinel-2 constellation data were cropped into 32×32 pixels of the dataset. A manual selection was employed to choose cloud-free, usable data. Statistical features (minimum, maximum, median, mean, and standard deviation) were extracted from pixels that contained cannabis information. This dataset was subsequently used to train and test the proposed model's accuracy. Training sample data for machine learning and test site data for accuracy assessments were determined based on field data or location points where authorities have eradicated cannabis plantations. These points were verified or interpreted using high-resolution satellite imagery. Various land classes, such as cannabis plantations, forests, and bush areas, were identified based on satellite data interpretation and field data.

4. Machine Learning based Classification for Cannabis Detection: Machine learning-based detection of cannabis plantation was conducted using statistical features of growth phenology and other objects from multitemporal satellite data, along with the training data. The neural network architecture follows the design proposed by Kushardono et al. (1995a) illustrated in Fig. 3, consisting of three layers: an input layer, a hidden layer, and an output layer. This three-layer configuration offers faster learning rates and higher classification accuracy compared to four-layer architectures.

Input layer contains neurons corresponding to the input data volume, which in this research involves 16 neurons (calculated from 4 statistical features × 4 spectral bands). The hidden layer, based on the optimal configuration identified by Kushardono et al. (1995a), contains twice the number of neurons in the output layer. Deviations from this optimal configuration can prolong the learning process, increase the risk of convergence failure, and reduce classification accuracy. The output layer's neuron count equals the number of class categories. Optimum training parameters for backpropagation, as suggested by Kushardono et al. (1995a), include a learning rate of 0.9 and a momentum rate of 0.1. Non-optimal parameter combinations may result in a higher number of iterations or difficulties in achieving convergence to a target error rate below 0.1.

5. Land Classification Results: The target area was classified into four land classes using the trained neural networks, with input feature data representing land phenology statistical values derived from the optical satellite data. The classification accuracy was then evaluated using a confusion matrix through overlapping analysis with test site data. The overall accuracy was found by dividing the number of correct classifications (shown on the main diagonal of the confusion matrix) by the total number of data points in the matrix. Additionally, the kappa coefficient was used to evaluate the agreement between observed and expected classifications in a confusion matrix, considering chance agreement. This coefficient provides a robust measure of classification performance, particularly useful for imbalanced classes. Kappa is calculated by comparing observed accuracy with expected chance agreement and ranges from -1 (no agreement) to +1 (perfect agreement), with higher values indicating better classifier performance (Congalton and Green 2009).

6. Cannabis Plantation Information: To identify illegal cannabis plantations in forested areas, particularly in the context of extensive satellite image coverage, classification results were filtered using a forest area map. The assessment of cannabis growth stages—ranging from vegetative growth, flowering, and nearing harvest to fallow fields—was conducted through phenological analysis of vegetation index values derived from multispectral optical satellite data.

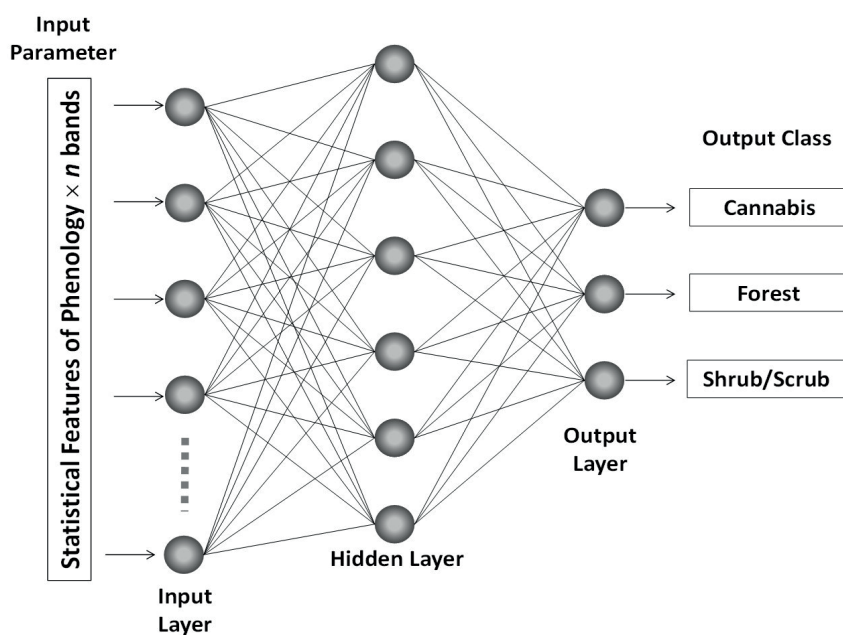


Fig. 3. Neural network architecture

RESULTS

The use of statistical features on plant growth phenology, such as minimum, maximum, average, and standard deviation from each band of multitemporal satellite data, shows good results for training classifiers. Using 3 types of training samples for 8 training areas for the cannabis plantation class, 11 training areas for the forest class, and 12 training areas for the shrub class yields the fast-decreasing tendency of the root mean square (RMS) values in the training process of a backpropagation neural network, indicating fast convergence. It shows that the RMS values decrease to less than 0.1 or 10% after 100 iterations and 0.01 or 1% after 776 iterations, as illustrated in Fig. 4.

Using the backpropagation neural network method, the classification of statistical parameters capturing growth phenology from multi-temporal Sentinel-2 data bands yields de-limitation results for three distinct classes: cannabis plantations (represented in red), forests (green), and shrubs (yellow), as illustrated in Fig. 5a.

A comparative analysis between classification results derived from 10-meter spatial resolution Sentinel-2 data and higher spatial resolution satellite imagery from October 2022, illustrated in Fig. 5, reveals substantial similarity in the spatial distribution and characteristics of land features,

encompassing 2 cannabis plantations, forest vegetation, and bush vegetation. Accuracy tests using data from 254 sample points (see Table 1) show a high accuracy rate of 95% and a kappa score of 0.92.

In a comparative analysis, the same training samples and input features utilized in the back-propagation neural network are applied to an SVM (Support Vector Machine) classifier, following the same settings mentioned in Park et al. (2018). The classification results in Fig. 4b show that the SVM classifier has an accuracy of 94% and a kappa coefficient of 0.91, as seen in Table 2. However, the accuracy results obtained from this classification process are not statistically significant. While the SVM classifier demonstrates a comparable accuracy level, Fig.5b indicates the presence of noise, particularly along the boundaries. This suggests that the SVM classifier does not perform well with training samples that contain noise, such as overlaps between the cannabis class and the bush/scrub class, as well as between the shrub class and the forest class. Conversely, the backpropagation neural network, functioning as a non-parametric classifier, can iteratively refine the training process until convergence, thereby minimizing errors and determining the class based on the highest neuron output value. Consequently, due to the encountered classification errors, particularly noise-related issues, the SVM classifier is not recommended for accurately determining the location of cannabis plantations.

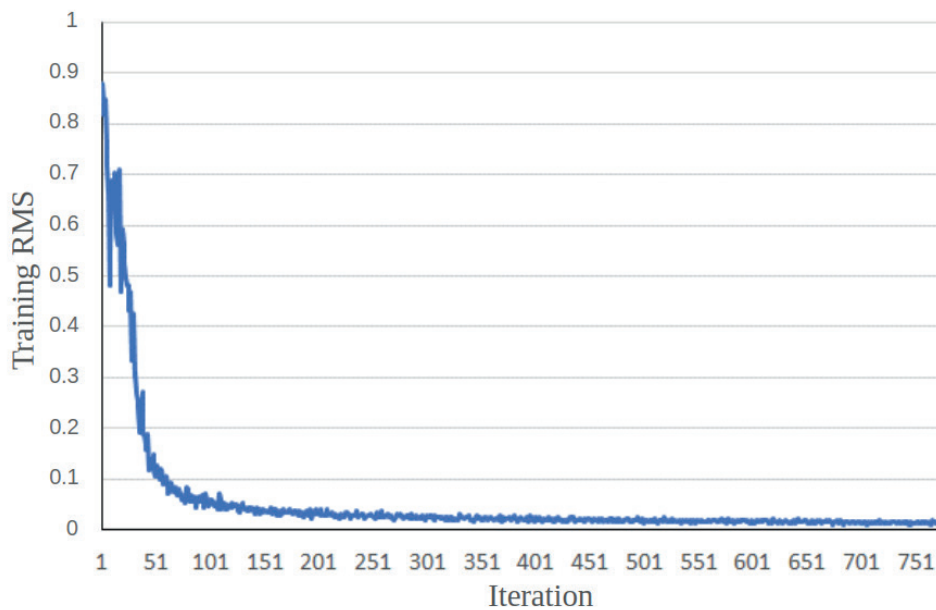


Fig. 4. RMS training reduction in backpropagation neural network learning iterations

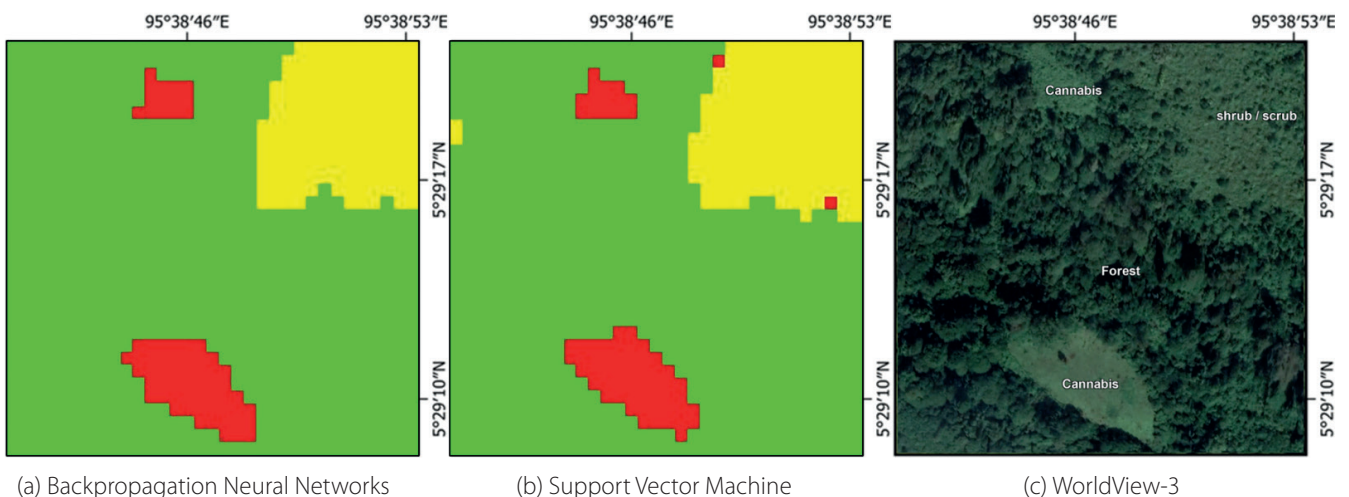


Fig. 5. Classification result (red: cannabis; green: forest; yellow: shrub) based on (a) backpropagation Neural Networks and (b) Support Vector Machine, compared with (c) WorldView-3 data October 2022

Table 1. Accuracy of Neural Network-based classification results for cannabis and non-cannabis (Overall Accuracy = 94.88%; Kappa Coefficient = 0.92)

Class	Ground Truth (Pixels)			Total
	Cannabis Plantations	Forest	Shrub / Scrub	
Unclassified	0	0	0	0
Cannabis Plantations	74	0	0	74
Forest	13	90	0	103
Shrub / Scrub	0	0	77	77
Total	87	90	77	254

Table 2. Accuracy of SVM-based classification results for cannabis and non-cannabis (Overall Accuracy = 94.09%; Kappa Coefficient = 0.91)

Class	Ground Truth (Pixels)			Total
	Cannabis Plantations	Forest	Shrub/ Scrub	
Unclassified	0	0	0	0
Cannabis Plantations	74	0	0	74
Forest	13	88	0	101
Shrub/ Scrub	0	2	77	79
Total	87	90	77	254

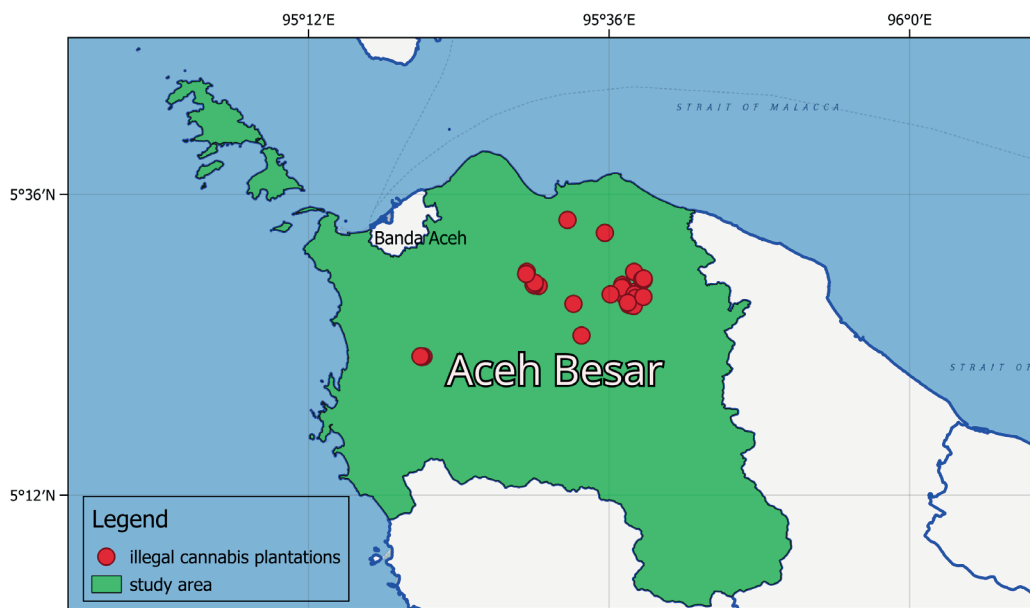


Fig. 6. Distribution of illegal cannabis plantations in Aceh Besar District

Fig. 6 illustrates several identified locations of illegal cannabis plantations in Aceh Besar District, NAD. All identified locations are situated in remote, mountainous, and forested areas. This study demonstrates that the integration of machine learning with medium-resolution remote sensing data is a reliable and effective approach for identifying cannabis plantations with high accuracy (>90%). It provides significant and effective support to law enforcement efforts in Indonesia in combating drug distribution.

Following the identification of cannabis plantation locations in the aforementioned classification results, an assessment of cannabis plantation conditions is conducted based on the vegetation index (NDVI) values derived from

multi-temporal Sentinel-2 satellite data collected between March and October 2022. A phenology graph illustrating the growth stages of the cannabis plants is generated, as illustrated in Fig. 7 According to Desjardins (2018)⁷, cannabis typically undergoes an initial vegetative growth phase lasting up to 8 weeks, followed by a flowering phase lasting 6-8 weeks and culminating in a harvesting phase. The NDVI values graph reveals a discernible pattern that correlates with the predicted age of cannabis plants, as depicted in Fig. 7. Understanding the NDVI pattern graph enables law enforcement agencies to estimate the condition and growth stage of cannabis within plantations, thereby enhancing the capacity to detect and eradicate illegal cannabis cultivation activities.

⁷Desjardins, Jeff. (2018). The Anatomy of a Cannabis Plant, and Its Lifecycle. 1-9. Retrieved December 20, 2023 (<https://www.visualcapitalist.com/anatomy-cannabis-plant/>).

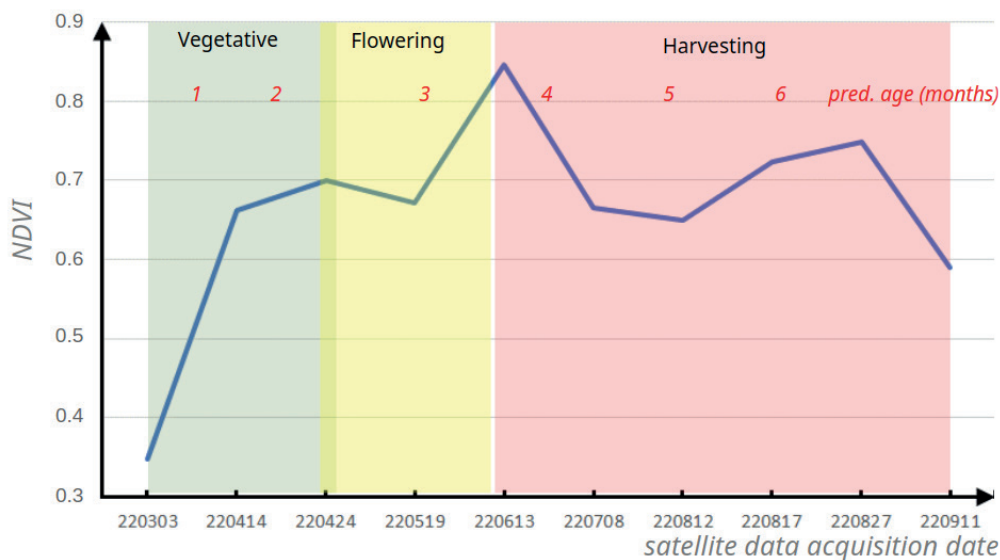


Fig. 7. Graph of NDVI values in cannabis plantation and prediction of the age of cannabis plants

DISCUSSION

The suggested model, which uses medium-resolution Sentinel-2 data, demonstrates high overall accuracy and kappa values by applying two different classifiers to distinguish between three categories: cannabis, forest, and shrub. Specifically, neural network-based classification achieves an accuracy of 94.88% and a kappa value of 0.92, while SVM-based classification yields an accuracy of 94.09% and a kappa value of 0.91. These results are comparable to prior findings. For example, Ferreira et al. (2019) found that high-resolution IKONOS images could help identify cannabis farms using a CNN classifier with an accuracy of 92.16%. Similarly, Sujud et al. (2021) found that an SVM classifier provided the best overall accuracy of more than 90%, compared to RF, GB, and CART, when using a combination of medium-resolution Sentinel-1, Sentinel-2, and Landsat-8 data for detecting cannabis plantations. Bicakli et al. (2022) argued that an RF classifier with high-resolution Planet data yielded a better accuracy of 93% compared to Decision Tree (75.2%), Random Tree (87.1%), KStar (91.0%), and IDK (92.1%).

Previous research identified backpropagation neural networks as a preferred non-parametric classification method over conventional parametric approaches like Maximum Likelihood and Dempster-Shafer's (Kushardono et al. 1995b). Backpropagation is one of the best algorithms for training multilayer perceptron networks due to its ability to minimize errors and efficiency in pattern classification (Suliman and Zhang 2015). Neural networks excel in capturing complex non-linear relationships, handling spectral variations, mixed pixels, radiometric inconsistencies, and limited training data—challenges common in cannabis fields located on tropical hillsides with high cloud cover and small spatial extent. Guo et al. (2012) found that Support Vector Machines (SVMs) achieve slightly higher classification accuracy than neural networks but face limitations, including reliance on kernel selection, difficulty with minimal training data, and challenges in finding an optimal separating hyperplane. Future research should explore spatio-temporal features using Convolutional Neural Networks (CNNs) to better process multitemporal, high-resolution satellite remote sensing data.

Furthermore, this research found that SVM-based classification exhibits higher levels of noise compared to neural network-based classification. SVM appears to struggle with noisy training samples, such as pixels

containing two classes. In contrast, the backpropagation neural network, works as a non-parametric classifier by repeatedly improving its training to reduce mistakes. This research demonstrates that free-access satellite data, specifically from the Sentinel-2 constellation, can be effectively utilized to detect the potential location of illicit crops, such as cannabis, with high accuracy over small areas. This approach reduces reliance on high-resolution commercial satellite data. The results indicate that with an appropriate model, it is possible to extract challenging and sensitive information from freely available satellite data.

The availability of cloud-free Sentinel-2 data over NAD is limited, with only 198 out of 1708 Sentinel-2 observations between 2016 and 2022 having less than 20% cloud cover. Despite this limitation, this research successfully utilized low-cloud-cover data with usable information from locations documented in a law enforcement eradication database, focusing on the cannabis growth period. NDVI analysis revealed distinct patterns compared to surrounding vegetation (Desjardins 2018). Key statistical features (minimum, maximum, median, mean, and standard deviation) were extracted to enhance machine learning classification. Areas obscured by clouds could not be analyzed, but future studies may address this limitation using SAR data.

Cannabis plants undergo distinct growth phases: fallow, seedling, vegetative, flowering, and harvest. Temporal satellite data captures these phases as changes in vegetation greenness, with digital values starting low before planting, rising during the vegetative phase, and falling at harvest. These patterns differ from other land cover types around them. Phenological changes are analyzed using statistical features for each land type, including cannabis, to account for planting time variations. Illegal cannabis, an annual crop grown in remote areas, exhibits phenological statistics that contrast sharply with surrounding land types—for instance, consistently high greenness in forests and shrubs versus frequently low greenness in open land and water bodies.

Illegal cannabis plantations in Aceh (NAD) and other regions are typically found in remote hilly areas. Growth phenology statistics for the same cannabis species show little variation across locations. Differences in soil fertility and rainfall have minimal impact on these features when plantation management is similar. Neural network classifiers effectively mitigate such variations due to their robustness to satellite data noise. This model will work for homogenous cannabis plantations. Field report show that

homogeneous cannabis plantations can be found other districts in NAD, such as: North Aceh District, South Aceh District, Gayo Lues District, etc. Mandailing Natal District in North Sumatera also exhibits this phenomenon.

This research demonstrates that with good data sampling, a combination of optical medium-resolution remote sensing data and machine learning classifiers can be effectively utilized to detect potential locations of illicit crops such as *Cannabis sativa L.* The conditions of cannabis plants from potential locations determined from the proposed method can be determined using vegetation indices such as NDVI or EVI. This model offers a rapid, efficient, and low-cost approach to combating illegal cannabis cultivation. This model might be unsuitable for intercropping plantations, as it was developed using datasets from monoculture cannabis plantations.

CONCLUSION

This research presents a method for processing digital data to find and evaluate illegal cannabis plantations. It uses statistical analysis of the growth pattern of cannabis plants, which are obtained from satellite images taken over time. Additionally, this research has been successful in substantially enhancing the efficiency and speed of detecting illegal cannabis cultivation, thereby strengthening law enforcement efforts in Indonesia. Illegal cannabis plantations in forests can be spotted by classifying data based on the growth patterns of plants, using information gathered from Sentinel-2 satellite images taken at different times. The classification results have an accuracy of about 95%, and the backpropagation

neural network classifier can accurately locate cannabis farms. Assessment of cannabis plantation conditions, including estimation of plant age, is enabled through phenological analysis of cannabis growth patterns using vegetation index values derived from multi-temporal Sentinel-2 satellite data, aligned with established growth stages of cannabis plants.

Our research shows that using statistical data from multi-temporal remote sensing data in a machine learning classifier is the most effective method for detecting illegal cannabis crops in Indonesia, especially in mitigating cloud cover. Using medium-resolution satellite data to detect potential illegal cannabis plantations reduces reliance on costly high-resolution commercial data.

High cloud cover in Indonesia limits this research, despite its numerous successes. This can hinder the use of optical remote sensing satellites for detecting illegal cannabis plantations, as it can obscure the study area. However, under conditions of thin cloud cover, we can still identify the land cover changes and predict the cannabis growth stages. Other machine learning classifiers can extend the model and apply it to regions with similar geographical characteristics. And to enhance the accuracy of identifying land suitable for the cultivation of cannabis plants, the use of multi-temporal Synthetic Aperture Radar (SAR) data texture features, which are unaffected by cloud cover, can be implemented. Additionally, the application of cross-validation techniques can improve the stability and reliability of the accuracy assessment model. Future research could focus on the fusion of data and/or information to enrich feature sets and further enhance predictive accuracy. ■

REFERENCES

- Andre, C. M., Hausman, J. F., and Guerriero, G. (2016). Cannabis Sativa: The Plant of the Thousand and One Molecules. *Frontiers in Plant Science* 7:1–17. doi: 10.3389/fpls.2016.00019.
- Armenteras, D., Cabrera, E., Rodríguez, N., and Retana, J. (2013). National and Regional Determinants of Tropical Deforestation in Colombia. *Regional Environmental Change* 13(6):1181–93. doi: 10.1007/s10113-013-0433-7.
- Bicakli, F., Kaplan, G., and Alqasemi, A. S. (2022). Cannabis Sativa L. Spectral Discrimination and Classification Using Satellite Imagery and Machine Learning. *Agriculture (Switzerland)* 12(6). doi: 10.3390/agriculture12060842.
- Chen, F., and Tsou, J. Y. (2021). DRSNet: Novel Architecture for Small Patch and Low-Resolution Remote Sensing Image Scene Classification. *International Journal of Applied Earth Observation and Geoinformation* 104:102577. doi: 10.1016/j.jag.2021.102577.
- Choudhary, K., Shi, W., Boori, M. S., and Corgne, S. (2019). Agriculture Phenology Monitoring Using NDVI Time Series Based on Remote Sensing Satellites: A Case Study of Guangdong, China. *Optical Memory and Neural Networks (Information Optics)* 28(3):204–14. doi: 10.3103/S1060992X19030093.
- Congalton, R. G., and Green, K. (2009). *Assessing the Accuracy of Remotely Sensed Data: Principles and Practices*. Vol. 25. Second. Florida: CRC Press.
- Dahal, D., Wylie, B., and Howard, D. (2018). Rapid Crop Cover Mapping for the Conterminous United States. *Scientific Reports* 8(1):1–13. doi: 10.1038/s41598-018-26284-w.
- Dillis, C., McIntee, C., Butsic, V., Le, L., Grady, K., and Grantham, T. (2020). Water Storage and Irrigation Practices for Cannabis Drive Seasonal Patterns of Water Extraction and Use in Northern California. *Journal of Environmental Management* 272:110955. doi: 10.1016/j.jenvman.2020.110955.
- Diwediga, B., Agodzo, S., Wala, K., and Le, Q. B. (2017). Assessment of Multifunctional Landscapes Dynamics in the Mountainous Basin of the Mo River (Togo, West Africa). *Journal of Geographical Sciences* 27(5):579–605. doi: 10.1007/s11442-017-1394-4.
- Duraisamy, V., Bendapudi, R., and Jadhav, A. (2018). Identifying Hotspots in Land Use Land Cover Change and the Drivers in a Semi-Arid Region of India. *Environmental Monitoring and Assessment* 190(9). doi: 10.1007/s10661-018-6919-5.
- Elbasi, E., Zaki, C., Topcu, A. E., Abdelbaki, W., Zreikat, A. I., Cina, E., Shdefat, A., and Saker, L. (2023). Crop Prediction Model Using Machine Learning Algorithms. *Applied Sciences (Switzerland)* 13(16). doi: 10.3390/app13169288.
- Ferreira, A., Felipussi, S. C., Pires, R., Avila, S., Santos, G., Lambert, J., Huang, J., and Rocha, A. (2019). Eyes in the Skies: A Data-Driven Fusion Approach to Identifying Drug Crops from Remote Sensing Images. *IEEE Journal of Selected Topics in Applied Earth Observations and Remote Sensing* 12(12):4773–86. doi: 10.1109/JSTARS.2019.2917024.
- Guo, Y., De Jong, K., Liu, F., Wang, X., and Li, C. (2012). A Comparison of Artificial Neural Networks and Support Vector Machines on Land Cover Classification. In Z. Li, X. Li, Y. Liu, and Z. Cai (Eds.), *Computational Intelligence and Intelligent Systems* 316:531–539. ISICA. doi: 10.1007/978-3-642-34289-9_59.
- Huang, S., Tang, L., Hupy, J. P., Wang, Y., and Shao, G. (2021). A Commentary Review on the Use of Normalized Difference Vegetation Index (NDVI) in the Era of Popular Remote Sensing. *Journal of Forestry Research* 32(1):1–6. doi: 10.1007/s11676-020-01155-1.
- Jimenez, R. B., Lane, K. J., Hutrya, L. R., and Fabian, M. P. (2022). Spatial Resolution of Normalized Difference Vegetation Index and Greenness Exposure Misclassification in an Urban Cohort. *Journal of Exposure Science and Environmental Epidemiology* 32(2):213–22. doi: 10.1038/s41370-022-00409-w.

- Karst, A. 2018. Weighing the Benefits and Risks of Medical Marijuana Use: A Brief Review. *Pharmacy* 6(4):128. doi: 10.3390/pharmacy6040128.
- Koscior, E., Forkel, M., Hernández, J., Kinalczyk, D., Pirotti, F., and Kutchartt, E. (2022). Assessing Land Surface Phenology in Araucaria-*Nothofagus* Forests in Chile with Landsat 8/Sentinel-2 Time Series. *International Journal of Applied Earth Observation and Geoinformation* 112. doi: 10.1016/j.jag.2022.102862.
- Kushardono, D., Fukue, K., Shimoda, H., and Sakata, T. (1995a). Optimized Neural Network for Spatial Land Cover Classification with the Aid of Co Occurrence Matrix. *Journal of the Japan Society of Photogrammetry and Remote Sensing* 34(4):22–35. doi: 10.4287/jsprs.34.4_22.
- Kushardono, D., Fukue, K., Shimoda, H., and Sakata, T. (1995b). Comparison of multi-temporal image classification methods. 1995 International Geoscience and Remote Sensing Symposium, IGARSS '95. Quantitative Remote Sensing for Science and Applications, 1282–1284. doi: 10.1109/IGARSS.1995.521726
- Kustiyo, K., Rokhmatuloh, R., Saputro, A. H., and Kushardono, D. (2024). Rice Fields Classification through Spectral-Temporal Data Fusion during the Rainy and Dry Seasons Using Sentinel-2 Optical Images in Subang Regency, West Java, Indonesia. *Paddy and Water Environment* 22(3):375–385. doi: 10.1007/s10333-024-00972-y.
- Lim, K., See, Y. M., and Lee, J. (2017). A Systematic Review of the Effectiveness of Medical Cannabis for Psychiatric, Movement and Neurodegenerative Disorders. *Clinical Psychopharmacology and Neuroscience* 15(4):301–312. doi: 10.9758/cpn.2017.15.4.301.
- Mattiuzi, M., Bussink, C., and Bauer, T. (2014). Analysing Phenological Characteristics Extracted from Landsat NDVI Time Series to Identify Suitable Image Acquisition Dates for Cannabis Mapping in Afghanistan. *Photogrammetrie, Fernerkundung, Geoinformation* 2014(5):383–392. doi: 10.1127/1432-8364/2014/0231.
- Morello, V., Brousseau, v. D., Wu, N., Wu, B. S., MacPherson, S., and Lefsrud, M. (2022). Light Quality Impacts Vertical Growth Rate, Phytochemical Yield and Cannabinoid Production Efficiency in Cannabis Sativa. *Plants* 11(21). doi: 10.3390/plants11212982.
- Nieto, L., Schwalbert, R., Prasad, P. V. V., Olson, B. J. S. C., and Ciampitti, I. A. (2021). An Integrated Approach of Field, Weather, and Satellite Data for Monitoring Maize Phenology. *Scientific Reports* 11(1):1–10. doi: 10.1038/s41598-021-95253-7.
- Park, S., Im, J., Park, S., Yoo, C., Han, H., and Rhee, J. (2018). Classification and Mapping of Paddy Rice by Combining Landsat and SAR Time Series Data. *Remote Sensing* 10(3):1–22. doi: 10.3390/rs10030447.
- Qian, Y., Zhou, W., Yan, J., Li, W., and Han, L. (2015). Comparing Machine Learning Classifiers for Object-Based Land Cover Classification Using Very High Resolution Imagery. *Remote Sensing* 7(1):153–168. doi: 10.3390/rs70100153.
- Sabat-Tomala, A., Raczko, E., and Zagajewski, B. (2020). Comparison of Support Vector Machine and Random Forest Algorithms for Invasive and Expansive Species Classification Using Airborne Hyperspectral Data. *Remote Sensing* 12(3). doi: 10.3390/rs12030516.
- Sirro, L., Häme, T., Rauste, Y., Kilpi, J., Hämäläinen, J., Gunia, K., de Jong, B., and Pellat, F. P. (2018). Potential of Different Optical and SAR Data in Forest and Land Cover Classification to Support REDD+ MRV. *Remote Sensing* 10(6). doi: 10.3390/rs10060942.
- Suárez, H. L. A., Angarita, G. P. G., Castañeda, L. N. R., and Castro, P. P. C. (2022). Illicit Crops, Planning of Substitution with Sustainable Crops Based on Remote Sensing: Application in the Sierra Nevada of Santa Marta, Colombia. *Climate Emergency – Managing, Building , and Delivering the Sustainable Development Goals* 483–494. doi: 10.1007/978-3-030-79450-7_36.
- Sujud, L., Jaafar, H., Hassan, M. A. H., and Zurayk, R. (2021). Cannabis Detection from Optical and RADAR Data Fusion: A Comparative Analysis of the SMILE Machine Learning Algorithms in Google Earth Engine. *Remote Sensing Applications: Society and Environment* 24. doi: 10.1016/j.rsase.2021.100639.
- Suliman, A., and Zhang, Y. (2015). A Review on Back-Propagation Neural Networks in the Application of Remote Sensing Image Classification. *Journal of Earth Science and Engineering* 5:52–65. doi: 10.17265/2159-581X/2015.
- Tavares, P. A., Beltrão, N. E. S., Guimarães, U. S., and Teodoro, A. C. 2019. Integration of Sentinel-1 and Sentinel-2 for Classification and LULC Mapping in the Urban Area of Belém, Eastern Brazilian Amazon. *Sensors (Switzerland)* 19(5). doi: 10.3390/s19051140.
- Wilkinson, S. T., Yarnell, S., Radhakrishnan, R., Ball, S. A., and D'souza, D. C. (2016). Marijuana Legalization: Impact on Physicians and Public Health. *Annual Review of Medicine* 67:453–466. doi: 10.1146/annurev-med-050214-013454.
- Yang, J., Dong, J., Liu, L., Zhao, M., Zhang, X., Li, X., Dai, J., Wang, H., Wu, C., You, N., Fang, S., Pang, Y., He, Y., Zhao, G., Xiao, X., and Ge, Q. (2023). A Robust and Unified Land Surface Phenology Algorithm for Diverse Biomes and Growth Cycles in China by Using Harmonized Landsat and Sentinel-2 Imagery. *ISPRS Journal of Photogrammetry and Remote Sensing* 202:610–636. doi: 10.1016/j.isprsjprs.2023.07.017.
- Zuo, L., Liu, R., Liu, Y., and Shang, R. (2019). Effect of Mathematical Expression of Vegetation Indices on the Estimation of Phenology Trends from Satellite Data. *Chinese Geographical Science* 29(5):756–767. doi: 10.1007/s11769-019-1070-y.

IMPACT OF COAL-BASED ELECTRICITY GENERATION, LAND USE CHANGE, STEEL AND CEMENT PRODUCTION ON CO₂ EMISSIONS: EVIDENCE FROM EASTERN EUROPEAN AND CENTRAL ASIAN COUNTRIES

Mikhail M. Lobanov¹, Jelena Zvezdanović Lobanova^{2*}, Miroljub Milinčić³, Milan Zvezdanović⁴

¹ Institute of Economics of the Russian Academy of Sciences, Nakhimovskiy Prospekt 32, Moscow, 117218 Russian Federation

² Institute of Social Sciences, Kraljice Natalije 45, Belgrade, 11000 Serbia

³ Faculty of Geography, University of Belgrade, Studentski trg 3, Belgrade, 11000 Serbia

⁴ Academy for National Security, Kraljice Ane bb, Belgrade, 11000 Serbia

*Corresponding author: jzvezdanovic@idn.org.rs

Received: December 2nd 2024 / Accepted: February 6th 2025 / Published: March 31st 2025

<https://doi.org/10.24057/2071-9388-2025-3754>

ABSTRACT. The problem of studying carbon footprint factors is one of the key ones for understanding the relationship between socio-economic development and atmospheric pollution. We employ a panel quantile regression approach to reveal the impact of the energy sector (namely, coal-based electricity and hydropower generation), manufacturing (steel and cement production), and agriculture (cropland area change) on CO₂ emissions in 16 Eastern European and 4 Central Asian countries for the period from 2000 to 2020. We provide evidence for a U-shaped environmental Kuznets curve for countries with a lower carbon footprint, while the countries with the highest emissions are found to have an inverted U-shaped relationship between them and GDP per capita. The relationship between electricity production from coal and emissions is positive and significant at all quantiles (except the 30th quantile), and for hydropower, it is negative and significant from the 20th to 70th quantile: a 1% increase in generation leads to CO₂ emissions increase by 0.08-0.20% and a decrease by 0.04-0.07%, respectively. Crude steel production positively influences emissions (from the 10th to 80th quantile levels): a 1% increase in the output of steel products results in carbon emissions increase by 0.05-0.07%. The relationship between cropland expansion and emissions is positive from the 40th quantile, but the coefficient shows high significance only at the 80th quantile. These findings allow us to conclude that CO₂ emissions reduction in Eastern European and Central Asian countries could be achieved by the replacement of coal in the electricity generation structure by renewables (including hydropower), the introduction of sustainable land use practices to preserve carbon sinks, and technological modernization of crude steel production.

KEYWORDS: CO₂ emissions, coal-based electricity generation, hydropower generation, land use change, steel production, cement production

CITATION: Lobanov M. M., Zvezdanović Lobanova J., Milinčić M., Zvezdanović M. (2025). Impact Of Coal-Based Electricity Generation, Land Use Change, Steel And Cement Production On CO₂ Emissions: Evidence From Eastern European And Central Asian Countries. *Geography, Environment, Sustainability*, 139-151

<https://doi.org/10.24057/2071-9388-2025-3754>

ACKNOWLEDGEMENTS: This paper was written as part of the 2025 Research Program of the Institute of Social Sciences with the support of the Ministry of Science, Technological Development, and Innovation of the Republic of Serbia.

Conflict of interests: The authors reported no potential conflict of interest.

INTRODUCTION

Climate change is increasingly affecting global economic growth. More extreme weather events due to rising surface air temperatures make it harder for economies to grow. This means that international organizations and national governments need to create strong climate policies to address these issues. Numerous studies confirm hypotheses about such consequences of global warming as an increase in extreme weather events, melting glaciers and rising sea levels, ocean acidification,

and a decrease in biodiversity. It is obvious that humanity will increasingly experience the consequences of climate change – the main threats include deteriorating human health, declining crop yields, and a sharp growth in the number of environmental migrants.

UN expert bodies and international organizations uniting economically developed countries play a coordinating role in developing measures to mitigate the consequences of climate change and adapt humanity to them. Regular international events within the framework of the United Nations Framework Convention on Climate

Change (UNFCCC) play an important role in uniting efforts in the field of regulating anthropogenic influence on the climate. However, a number of environmental organizations consider the decisions made to be half-hearted and not revolutionary enough. The Paris Agreement, signed at the 21st UN Climate Change Conference, stands out in the list of recent climatic treaties. It aims to limit surface temperature increase compared to pre-industrial times to 2°C by 2100. The signatories also set themselves a more ambitious goal: to strive to keep global warming within 1.5°C by the end of the century. As of the end of 2022, of the 194 countries that have signed up to the Paris Agreement, 136 countries have set a target date for achieving carbon neutrality (usually 2050). However, the number of signatories that have become involved in the decarbonization process remains small: fewer than 30 countries have launched programs to reduce CO₂ emissions.

Carbon dioxide emissions are a key dependent variable in econometric studies of anthropogenic pressure on the atmosphere. Several factors explain this fact. First, research on the causes and consequences of carbon dioxide air pollution has been studied to the greatest extent compared to other types of pollutants, including gases and organic and inorganic particulates. The task of constructing hypotheses and explaining the results of mathematical models is greatly simplified if we consider the already studied effects of CO₂ emissions on the environment, described by climatologists, geographers, and ecologists.

Secondly, an important reason for using CO₂ emissions as a proxy to assess the anthropogenic load on the climate system is the availability of statistical data at the national and international levels (World Bank, OECD, IEA, EDGAR, Eurostat, etc.). However, statistics are also collected and processed for other gaseous emissions. For example, Climate Watch platform provides data for methane (CH₄), nitrous oxide (N₂O), fluorinated gases (F-gases), and greenhouse gases in total.

Thirdly, studies of carbon dioxide emission factors have important practical significance since they make it possible to develop recommendations for adjusting the climate policies of developed and developing countries. The results of the analysis in most studies are policy implications for government agencies and businesses to reduce CO₂ emissions, including those related to the implementation of international obligations to achieve carbon neutrality. The need to achieve target CO₂ emissions in a short time frame determines the special interest of researchers in carbon dioxide and not in any other air pollutant.

The main objective of this paper is to investigate the impact of coal-based electricity generation, land use change, steel and cement production on carbon dioxide emissions in 16 Eastern European and 4 Central Asian countries (in 2000-2020)¹. We employed panel quantile regression approach in order to deal with individual and distributional heterogeneity.

Given the high level of elaboration of the topic, it is very difficult for each new study to make a scientific contribution to the problem of understanding the relationship between social development and atmospheric pollution. Typically, the authors proceed by examining a new sample of countries, applying improved econometric models, and incorporating nonobvious explanatory variables. In our case, we focused on studying the countries of Eastern Europe and Central Asia, which are rarely the subject of study, and we chose such independent variables that, to our knowledge, have never been used to estimate

the dynamics of CO₂ emissions in the 21st century (steel production, cement production, electricity production from coal and cropland area). We did not succeed in finding any studies that deal explicitly with the nexus between these variables and CO₂ emissions. Essentially, we are trying to understand which areas of the economy – energy sector, agriculture, or manufacturing – have a decisive influence on the increase of carbon footprints in given countries.

As we already mentioned, the countries of Eastern Europe (EE) and Central Asia (CA) were chosen as the object of study since they are rarely in the focus of attention of researchers as a relatively homogeneous group with a comparable set of development characteristics (like embedded institutions, organization of industrial systems, energy balance structure, etc.). Individual Central-Eastern European (CEE) and South-Eastern European (SEE) countries are often included in samples with other OECD or European Union countries. In general, the geographical scope of studies of CO₂ emissions factors was initially limited to high-income economies due to the greater volume of accumulated knowledge, the maturity of climate policy, and the availability of relevant statistical data. Later, an increasing number of authors focused on studying the causes of air pollution in developing countries and emerging markets.

Among the limited number of papers considered EE countries, one can mention Atici (2009) (3 CEE countries and Turkey), Kasman and Duman (2015) (15 EU new member states and candidate countries), Pejovic et al. (2021) (27 EU and Western Balkan countries), Simionescu (2021) and Simionescu et al. (2022) (7 and 10 CEE and SEE countries, respectively), Ugurlu (2022) (4 CEE countries), Balsalobre-Lorente et al. (2023) (7 CEE countries). Research on greenhouse gas emission factors in Central Asian countries is a recent development. For example, Nguyen (2019) and Zhang (2019) studied 5 CA countries, Li et al. (2020) examined 8 CEE and 2 CA countries, and Salahodjaev et al. (2022) focused on 45 European and CA countries. To our knowledge, we use the biggest sample of countries from Eastern Europe and Central Asia in our research (excluding those studies with multiregional scope).

LITERATURE REVIEW

The first attempts to examine the dynamic relationship between air pollution, energy consumption, and GDP (as a proxy for income) on the example of developed countries date back to the middle of 2000-ies – e.g., Richmond and Kaufmann (2006), Ang (2007), Soytaş et al. (2007). Since that time, the approach to the set of independent variables in econometric models has changed greatly, and research methods have also become more complex.

We carefully studied the conclusions of more than 80 scientific papers (from 1997 to 2023) and carried out a grouping of variables typically used to consider carbon emission factors. The length limitations of scientific publication make it hard to present the differences in conclusions about emission factors in detail, but we can discuss this issue in general. We identified the following groups of independent variables:

Energy system

Indicators of the development of national energy systems are included in models in most studies (about 90%, according to our estimates), which is due, first of all, to the

¹ Albania, Bosnia and Herzegovina, Bulgaria, Croatia, Czech Republic, Estonia, Hungary, Kazakhstan, Kyrgyzstan, Latvia, Lithuania, Montenegro, North Macedonia, Poland, Romania, Serbia, Slovakia, Slovenia, Tajikistan and Uzbekistan.

fact that energy-related greenhouse gas emissions account for the major share of total anthropogenic emissions (energy sector accounts for 1/4 of global greenhouse gas emissions). As for carbon dioxide, electricity generation is responsible for 43% of global CO₂ emissions (15.1 Gt, according to Climate Watch). In the top CO₂ emitters – China, the USA and India – this share reaches 55, 43 and 52%, respectively.

Researchers have reached a consensus regarding the role of *energy consumption* in expanding the volume of anthropogenic emissions: almost all studies using this dependent variable indicate a statistically significant positive impact of energy use on CO₂ emissions. Likewise, most models show a significant negative impact on emissions from *renewable energy consumption (generation)*, while non-renewables' influence is usually significant and positive. However, the situation becomes more complicated if we consider not aggregate data but more precise data on individual energy generation sources. If, in relation to fossil fuel energy use, coal or hydrocarbon consumption, the model results coincide with generally accepted hypotheses, in the case of *hydroelectricity and nuclear energy consumption (generation)*, researchers' conclusions are often ambiguous and lead to completely different policy recommendations. Regarding *wind, solar, and biomass energy*, the authors do not provide a clear answer to the question about the role of these types of renewable energy in reducing atmospheric emissions (insignificant relationship, negative or even positive effects are identified with approximately the same frequency).

Economy

Independent variables related to economic development are present in almost all models explaining air pollution. This is especially true for economic performance and welfare indicators – GDP and GDP per capita, used as a proxy for national income. It is well known that Grossman and Krueger (1991) first found the inverted U-shaped relationship between income and pollution, which was named the Environmental Kuznets Curve (EKC). The inverted U-shaped EKC hypothesis means that pollution initially increases with income growth, then stabilizes, and finally declines. Quite quickly the validity of the original EKC hypothesis in the long run was called into question: after passing a certain income level, an increase in income might result in the expanding of environmental degradation once again (N-shaped EKC). This can be explained by the idea that the scale effect is more important than the composition and technical effects when the benefits from green innovation decrease (de Bruyn et al. 1998; Torras and Boyce 1998).

The numerous empirical studies testing the validity of the EKC hypothesis show various forms of relationship between income and air pollution. In the frames of our literature review, we identified 73 papers that used GDP or income as an independent variable. Half of the authors made a conclusion about the connection between these variables and CO₂ emissions. Most found an inverted U-shaped EKC (20 papers) or said there is no evidence for the existence of EKC at all (10 papers). A few researchers discovered U-shaped EKC (3), N-shaped EKC (3), and inverted N-shaped EKC (2).

A number of researchers are studying the influence of the *economic structure* on carbon footprint, primarily the relationship between the volume (or share in GDP) of agricultural or industrial production and CO₂ emissions. In almost all cases, industry increases the level of air pollution, and the results for agriculture are ambiguous (Li et al. 2020, Simionescu 2021, Raihan 2023). Gross fixed *capital formation* is also included in the models, but the connection with carbon

emissions most often turns out to be insignificant. A fruitful area of research is studying foreign economic activity (through components of the *balance of payments*). The impact of FDI inflows on emissions is ambiguous, as well as the influence of trade in goods (total trade usually affects negatively, but trade openness (trade to GDP), export and import, on the contrary, affect positively). The relationship between the indicators of labor market development (labor force, labor productivity) and environmental degradation is insignificant in most cases. The most frequently used dependent variable in the field of *financial systems* is domestic credit to the private sector (% of GDP). However, the number of authors proving its positive impact on carbon dioxide emissions is approximately the same as those with the opposite viewpoint.

Population

A study of the influence of indicators related to *population dynamics and settlement patterns* began in the 2000s: the hypothesis was tested that the growth in the number of residents, especially their concentration in cities, inevitably leads to negative environmental consequences. As for demographic indicators (population, population density, population growth), only 3 of the 14 studies we analyzed with these variables showed a significant impact on emissions, both negative and positive (Salman et al. 2019). In contrast, most authors claim that *urbanization* growth leads to higher CO₂ emissions – a direct relationship between these indicators was found in 13 out of 22 studies (Voumik et al. 2023).

Living standards

According to theoretical assumptions, *living standards* indirectly affect greenhouse gas emissions, since societies with higher welfare and quality of life should contribute to reducing the ecological footprint. However, proxies of living standards (poverty, health expenditure, life expectancy, Human Development Index, etc.) are rarely used in the models, and the available results are ambiguous (Li et al. 2020, Simionescu 2021).

Institutional setting

As in other areas of econometric model application, the proxies of the *institutional setting* are increasingly used when studying the causes of atmospheric pollution – for example, the Institutional Quality Index (Worldwide Governance Indicators), Index of Economic Freedom, Political Rights and Civil Liberties Index, Environmental Policy Stringency Index (by OECD), Economic Complexity Index, and Globalization Index (by KOF). It is assumed that a developed institutional environment contributes to the implementation of international ecological obligations, including efforts to achieve climate neutrality. As a rule, the calculation results confirm the hypothesis about the negative impact of institutions on emissions. However, the long-term relationship between indices and emissions does not always remain linear but has a U-shape or N-shape (Apergis and Ozturk 2015, Shahnazi and Dehghan Shabani 2021).

Technology and innovation

Following many researchers, we believe that indicators of *technological development* are one of the key determinants of environmental pressure. However, an important problem is raised: the vast majority of technological development indicators can lead to a false interpretation of the impact of innovation on the carbon

footprint. For example, a country may have a high level of R&D expenditure or a number of patent applications, which are in no way related to environmental issues, and the reduction of emissions within its borders can be entirely related to the import of green technologies and know-how. Most often, works examine the impact of patent applications (ambiguous results), less often – the impact of R&D expenditure, research intensity (R&D expenditure to GDP), number of researchers, high-technology exports, etc. (Allard et al. 2018, Cheng et al. 2021, Petrović and Lobanov 2020).

Other independent variables

The process of studying the factors that influence CO₂ emissions is developing towards the inclusion of more independent variables, the connection of which with the carbon footprint at first glance seems illusory. The authors of such works often make a lot of effort to substantiate the results of their calculations. Examples of non-obvious variables include such proxies for economic development as market capitalization of listed companies, interest rates, consumer price indicators, personal remittances, or mobile cellular subscriptions (Attílio et al. 2023, Paramati et al. 2017). Social development and institutional maturity indicators are also widespread (e.g. the share of women in parliament, the tenure of regional and municipal officials, etc.).

MATERIALS AND METHODS

The aim of this work is to study the impact of the energy sector (coal-based electricity and hydroelectricity generation), the manufacturing industry (steel and cement production) and agriculture (cropland area change) on carbon dioxide emissions in 16 Eastern European and 4 Central Asian countries for the period from 2000 to 2020. An explanation of the selection of appropriate countries for the sample is contained in the Introduction section. In this part of the article, we would like to briefly dwell on the presentation of explanatory and dependent variables (Table 1).

We chose carbon dioxide emissions (in Mt) as the dependent variable. An analysis of more than 80 scientific papers on the factors determining greenhouse gas emissions dynamics shows that authors often use CO₂ emissions as a dependent variable. The Introduction section describes three reasons for the popularity of this

type of greenhouse gas. Absolute values (in t, kt or Mt) are used in 2/5 of the works we analyzed, and the rest of them consider relative values (CO₂ emissions per GDP or per capita). Many authors believe that absolute measures provide a more accurate picture of the cause-and-effect relationship of air pollution and are more meaningful from a practical point of view since countries' international commitments to reduce emissions are determined in absolute figures (e.g. see Friedl and Getzner (2003), Zhang and Cheng (2009), Pao and Tsai (2011)).

As for income data, we used GDP per capita PPP measured in USD at 2017 prices. The authors of other papers considering EE and CA countries also use GDP per capita as a proxy for income (Atici (2009), Kasman and Duman (2015), Li et al. (2020), Simionescu et al. (2022)).

In addition, we examine the impact of technological development on CO₂ emissions using the indicator of research intensity – R&D expenditure to GDP (%). For example, Ang (2009) and Ganda (2019) use the same variable. As we wrote earlier (see the Literature review section), there is no adequate indicator to prove the given relationship: R&D expenditure and patent applications in a particular country are not necessarily aimed at reduction in air pollution, which can be entirely achieved through the import of green technologies. Data on R&D could also be noisy because of the differences in national methodology in statistics collection (Allard et al. 2018).

To analyze the impact of industry and agriculture on CO₂ emissions, we chose crude steel and cement production and change in cropland area. To our knowledge, no studies have yet explored this connection. A serious omission of other works is that almost all researchers use aggregated data (agriculture or industry value-added/value-added per capita/share in GDP). However, almost all carbon dioxide emissions in the industry are associated with the activities of 3-4 branches (cast iron and steel, aluminium, cement, ammonia) and in agriculture – only with land-use change in favor of croplands. The search for a relationship between agriculture/industry value-added with CO₂ emissions has no theoretical or practical significance: according to the data by IPCC and Climate Watch, global greenhouse gas emissions in the 21st century are the result of activities in the energy sector (25%), agriculture (24%) and industry (21%), but CO₂ emissions are connected to the energy sector (92%), industry (5%) and land-use change (3%).

In order to find the extent of influence of renewable and non-renewable energy on carbon emissions, we use such proxies as electricity production from coal and hydropower generation (% of total). The coal-fired thermal

Table 1. Description of variables

Variables	Definition and measurement	Source
EM	CO ₂ emissions, Mt	CO ₂ emissions of all world countries – 2022 Report, Publications Office of the European Union
GDP	GDP per capita PPP, constant USD 2017	WDI database, World Bank
RD	R&D expenditure, % of GDP	WDI database, World Bank
CR	Cropland, thous. ha	FAOSTAT
CO	Electricity production from coal, % of total	Ember Electricity Data Explorer
HY	Hydroelectricity production, % of total	Ember Electricity Data Explorer
CE	Cement production, thous. t	USGS Minerals yearbook
ST	Crude steel production, thous. t	USGS Minerals yearbook

power stations have the highest carbon footprint among power plants using fossil fuels, and hydropower remains a key type of renewable energy. In many EE and CA countries, both types are widely represented in the structure of electricity output and the installed capacity of power plants. Fossil fuel energy use or production is referenced by Al-Mulali (2014), Güney (2022), Raihan and Tuspekova (2022). Meanwhile, hydroelectric energy use or production is included in the model by Al-Mulali et al. (2015), Solarin et al. (2017), and Bilgili et al. (2021).

Following the approach of Cheng et al. (2021), Akram et al. (2020) and Allard et al. (2018), we estimated the effect of the above-mentioned variables on CO₂ emissions with this panel quantile regression model (Eq. 1):

$$\begin{aligned} QEM_{i,t}(\tau/\cdot) = & a_{1,\tau}GDP_{i,t} + a_{2,\tau}GDP^2_{i,t} + \\ & + a_{3,\tau}RD_{i,t} + a_{4,\tau}CO_{i,t} + a_{5,\tau}CR_{i,t} + \\ & + a_{6,\tau}CE_{i,t} + a_{7,\tau}ST_{i,t} + a_{8,\tau}HY_{i,t} + \\ & + \beta_i + \mu_t \end{aligned} \quad (1)$$

$$i = 1, \dots, N, t = 1, \dots, T$$

where β_i and μ_t are the country and time fixed effects, respectively, while $a_{1,\tau}$ to $a_{8,\tau}$ are coefficients. EM_{it} represents CO₂ emissions; GDP_{it} is the GDP per capita; GDP^2_{it} stands for the square of GDP per capita; RD denotes research and development expenditures as a share of GDP ; CO is electricity generated by coal (% of total); CR denotes cropland area; CE and ST are cement and crude steel production, respectively; and HY stands for electricity generated by hydropower plants (% of total). All variables are expressed in natural logarithms.

If the coefficients $a_{1,\tau}$ and $a_{2,\tau}$ are positive and negative, respectively, this will indicate that there is the classical inverted U-shaped curve of the relationship between GDP per capita and CO₂ emissions. However, in case the coefficients $a_{1,\tau}$ and $a_{2,\tau}$ are negative and positive, respectively, there is a U-shaped relationship between CO₂ emissions and income. The dependent variable is EM emissions, while our main variables of interest are CO , CR , ST , and CE .

We applied the panel quantile regression approach in order to examine the determinants of air pollution caused by carbon dioxide. This statistical method, created by Koenker and Bassett (1978), fits the linear function of CO₂ emissions based on the conditional distribution of the explained variable (Zheng et al. 2021). Contrary to the least square estimation method, its main econometric advantage is that it is robust to outliers and heavy distributions, and we are able to analyze potential heterogeneity and asymmetry (Akram et al. 2020). Ordinary Least Squares (OLS) estimators measure the average impact of independent variables on a dependent variable. In contrast, panel quantile regression estimates the effect of the explanatory variables on the explained variables at different quantile points (Xu and Lin 2020). Cade and Noon (2003) state that quantile regression provides a more complete view of possible causal functional relationships between variables for all portions of probability in ecological processes. Since the statistical distribution of ecological data is characterized by unequal variation, the authors pointed out that this method "estimates multiple rates of change from the minimum to maximum response, providing a more complete picture of the relationships between variables missed by other regression methods". The conditional quantile of y_i given x_i can be expressed as (Eq. 2):

$$Q_{y_{it}}(\tau|x_{it}) = x_{it}^T \beta_\tau \quad (2)$$

where $Q_{y_{it}}(\tau|x_{it})$ represents the τ_{th} quantile of the dependent variable, x_{it}^T stands for the vector of independent variables (i and t denoting country and time) for quantile τ , while β_τ is the slope of the independent variable for quantile τ (Allard et al. 2018).

Based on this approach, it is possible to achieve detailed analysis across quantiles since it provides estimates of the dependent variables at each specific point of the conditional distribution, as pointed out by Allard et al. (2018). The importance of the panel quantile approach is particularly evident in cases when the error term is characterized by heteroskedasticity and does not have a normal distribution (Xu and Lin 2016). In order to provide a detailed analysis of the relationship between different conditional distributions of environmental degradation and the explanatory variables, we chose nine quantile points (0.10, 0.20, 0.30, 0.40, 0.50, 0.60, 0.70, 0.80, and 0.90), whereas the 50th quantile denoted the median. In this study, we employed STATA 14 to calculate the panel quantile regression.

RESULTS AND DISCUSSION

In this section, we present the main results of our calculations. In Table 2, we reported descriptive statistics for each variable, which include mean, standard deviation, minimum and maximum values, skewness, kurtosis, and the number of observations. We also provide the correlation matrix for EM regression variables. The correlation of EM and HY is negative, while it is positive for all other variables.

The correlation coefficients between EM and the explanatory variables like CR, ST, and CE had a value higher than 0.7, which might indicate the presence of multicollinearity problems. Therefore, we performed additional tests to confirm that there was no harmful multicollinearity, which occurs if a variance inflation factor (VIF) is in excess of 5. Since none of the variables had a VIF over 5, as can be seen from Table 4, we concluded that the results were suitable for further analysis.

The panel unit root tests are conducted to check whether the variables are stationary. We applied the Levin-Lin-Chu, Im, Pesaran, Shin, and Fisher ADF tests. According to the results (see Table 5), the test results of the variable's level data have not passed the significance test, meaning that these variables are not stationary at level I(0). We took the first difference since some of our variables contain a unit root at a level. This results in all variables becoming stationary at the 1% significance level, leading us to conclude that each variable has an integration of order one. Since the first-difference sequence is stationary for all variables included in our empirical analysis, we will use the first difference of our data.

Based on the Q-Q, which represents the probability graph (Fig. 1), it is possible to determine whether the data distribution is normal. As it can be seen from the graphs, the linear diagonal line denotes normal distributions, while the dotted line shows the deviation from the previously mentioned line. For instance, the economic data is normally distributed in the case when the Q-Q plot coincides with the X₁Y line, and vice versa. Fig. 1 shows that all economic variables do not follow a normal distribution, which has also been confirmed by the Jarque-Bera probability test (see Table 2).

In Table 6, we reported the estimated results of the panel quantile regression approach. The signs of the coefficients of the explanatory variables are as expected.

Table 2. Descriptive statistics

Variables	Mean	Median	Std. dev.	Min	Max	Skewness	Kurtosis	Pr. (J-B test)	N
EM	3.292	3.078	1.283	1.03	5.80	0.205	2.036	0.00	420
GDP	9.639	9.837	0.737	7.17	10.62	-1.204	3.799	0.00	420
RD	-0.831	-0.607	1.043	-4.605	0.941	-0.895	3.816	0.00	420
CO	3.437	3.662	0.992	-2.525	4.552	-2.603	14.406	0.00	325
CR	7.462	7.220	1.263	4.82	10.31	0.266	2.777	0.05	420
CE	7.547	7.600	1.075	4.60	9.85	0.012	2.461	0.08	399
HY	2.644	3.131	1.683	-2.52	4.605	-1.008	3.261	0.00	419
ST	6.839	6.621	1.571	1.79	9.27	-0.463	2.557	0.00	313

Table 3. Correlation matrix

Variable	EM	GDP	RD	CR	CO	ST	CE	HY
EM	1.00							
GDP	0.10	1.00						
RD	0.03	0.68	1.00					
CR	0.88	-0.08	-0.18	1.00				
CO	0.22	-0.08	-0.24	0.22	1.00			
ST	0.75	0.31	0.20	0.63	0.20	1.00		
CE	0.86	0.08	0.08	0.75	-0.02	0.62	1.00	
HY	-0.53	-0.28	-0.34	-0.44	-0.07	-0.57	-0.39	1.00

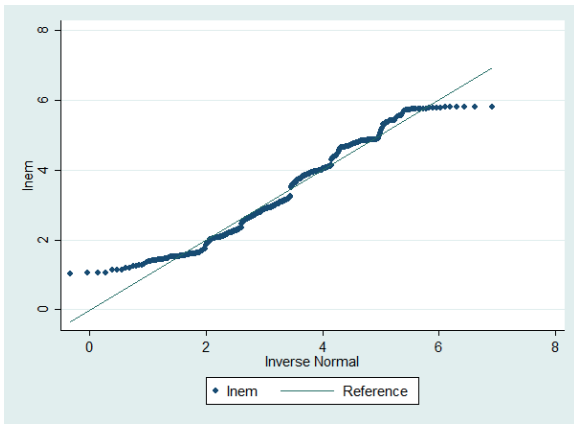
Table 4. VIF test

Variables	VIF	1/VIF
CR	3.87	0.258
CE	3.04	0.328
ST	2.65	0.377
RD	2.42	0.412
GDP	2.07	0.482
HY	1.79	0.559
CO	1.26	0.795
Mean VIF	2.44	

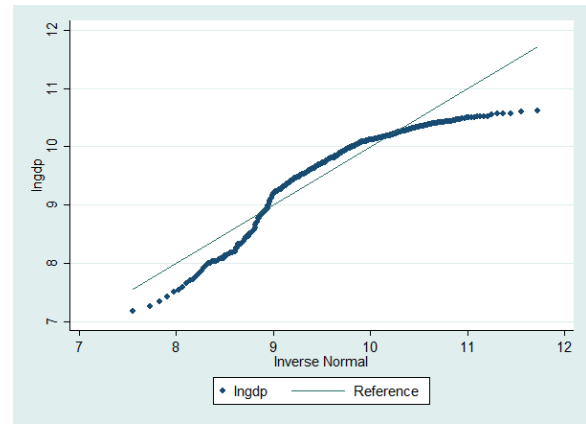
Table 5. Panel data unit root test results

Variables	Levin-Lin-Chu test		Im, Pesaran, Shin		Fisher-ADF test	
	Level	1 st difference	Level	1 st difference	Level	1 st difference
EM	-0.456	-3.874***	-0.234	-6.089***	41.243	108.401***
GDP	-0.335	-2.364***	1.499	-2.303***	30.618	57.869***
RD	-2.586***	-6.813***	-1.240	-5.627***	50.350	102.079***
CO	-1.630**	-7.711***	-0.860	-8.039***	48.986**	117.539***
CR	-8.158***	-14.949	-4.581***	-9.589***	97.039***	129.337***
CE	-3.564	-5.679***	-1.965**	-4.866***	57.395**	87.737***
HY	-5.816***	-12.314***	-6.206***	-12.655***	116.344***	206.307***
ST	-0.718	-7.239***	-0.478	-5.363***	29.950	81.449***

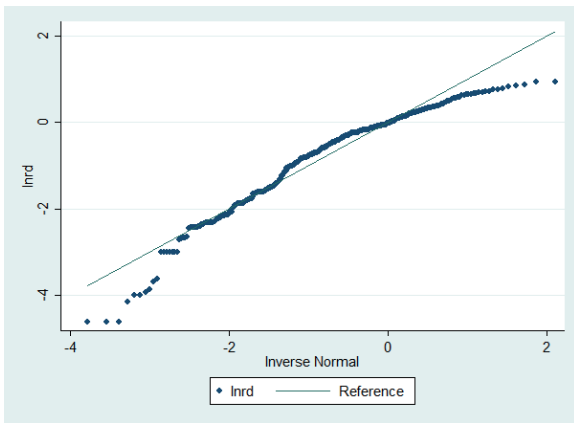
Note: ***, **, and * indicate significant p-values at the 1, 5, and 10% levels. Both a constant and a trend were used in the test.



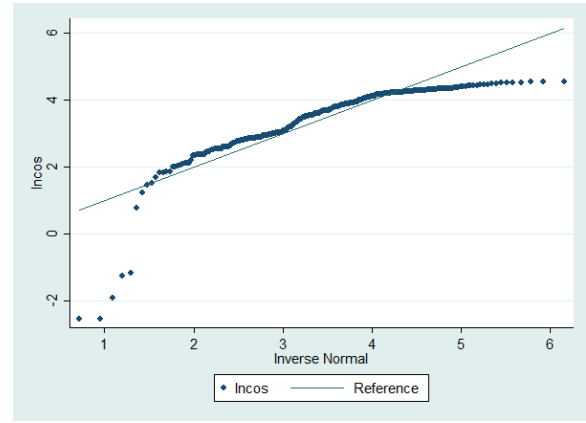
(a) EM



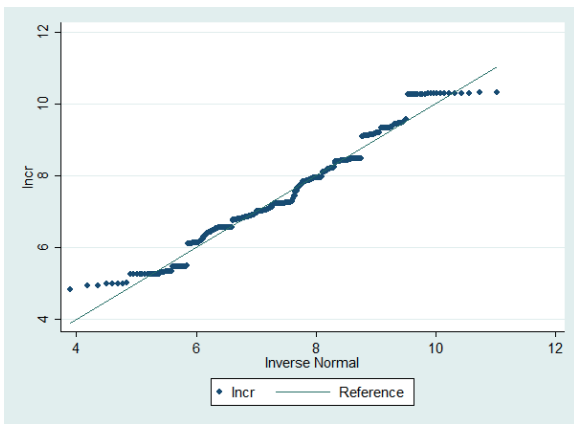
(b) GDP



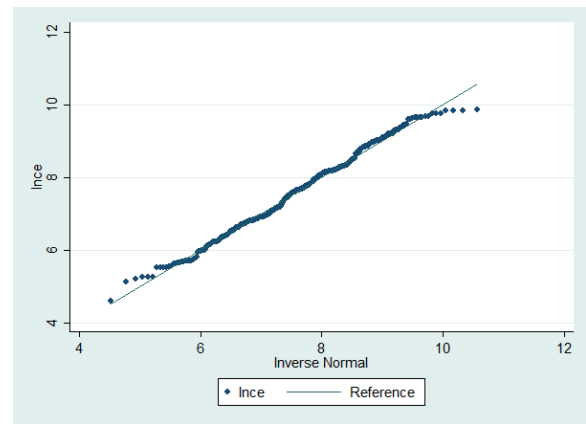
(c) RD



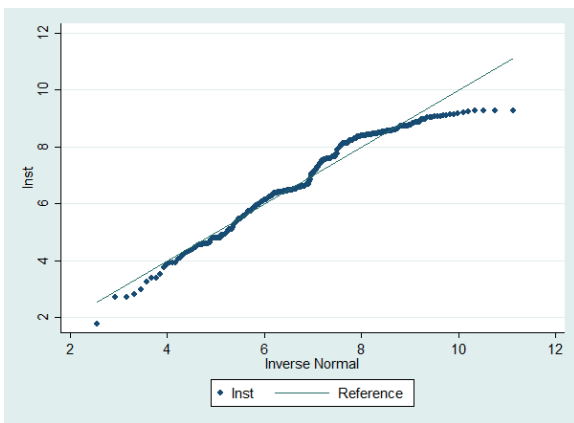
(d) CO



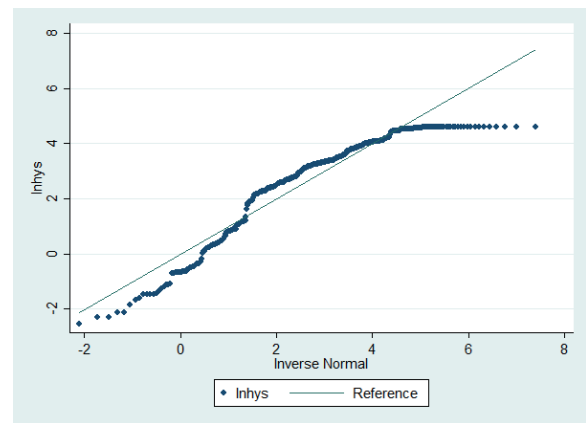
(e) CR



(f) CE



(g) ST



(h) HY

Fig. 1. The normal Q-Q plot for variables transformed by natural logarithm

The coefficients of GDP per capita on CO₂ emissions are negative from the 10th to the 30th quantile but significant only at the 10th quantile. This coefficient became positive and significant at the 70th, 80th, and 90th quantiles. Notably, the impact of GDP per capita on carbon emissions shows an increasing trend from the 50th to the 80th quantile. On the other hand, the impact of square GDP per capita on CO₂ is also heterogeneous, while the positive effect on carbon emissions is greater at the lower quantiles. The negative coefficient is recorded between the 50th and the 90th quantiles but is only statistically significant at the 70th and 80th quantile levels.

Thus, we provide evidence for the U-shaped environmental Kuznets curve for EE and CA countries with the lowest carbon footprint (related to the 10th quantile): a 1% increase in GDP per capita leads to a decrease of 4.34% in CO₂ emissions, while square GDP per capita records an increase of 0.26%. Our findings are in line with Wang et al. (2011) (for Chinese provinces), Destek and Sarkodie (2019) (for China, India, the Republic of Korea, Thailand and Turkey), Sarkodie and Strezov (2019) (for India and South Africa) and Simionescu et al. (2022) (for ten CEE and SEE countries).

In contrast, the countries with the highest emissions (the 70th and the 80th quantile of our sample) are characterized by the 'classical' inverted U-shaped relationship between GDP per capita and CO₂ emissions. For example, in the case of the 80th quantile, an increase of 1% in income results in carbon dioxide emissions increasing by 4.75%, while square GDP per capita records a decrease of 0.21%. So, for such countries, air pollution initially increases with income growth and then declines due to composition and technological effects. There are a lot of studies proving the validity of the inverted U-shaped EKC hypothesis for developed countries, including those from Europe, e.g. Atici (2009) (for Turkey and 3 CEE countries), Kasman and Duman (2015) (for 15 EU NMS and CC), Dogan and Seker (2016) (for EU-15), Shahnazi and Dehghan Shabani (2021) (for EU-28), Salahodjaev et al. (2022) (for 45 European and CA countries).

According to the IPCC classification, land use categories include cropland, grassland, wetland, forest land, and

settlements. The change from one category to another refers to land-use change (LUC). Organic soils emit CO₂ when they are drained to be converted to cropland or grassland; the emissions of carbon dioxide, methane (CH₄) and nitrous oxide (N₂O) also happen as a result of human-induced fires. It is believed that soil contains twice as much carbon as the atmosphere. Conversion of forest land and grassland to cropland can lead to a 20-40% loss of the original soil carbon stocks because of CO₂ sinking.

Many authors use data on agriculture value-added, which cannot be applied to carbon dioxide emissions: while crop and livestock production is responsible for direct emissions of CH₄ and N₂O, they do not contribute to CO₂ emissions. For example, N₂O emissions come from using fertilizers, the cultivation of organic soils, and the decomposition of crop residues, while CH₄ is emitted due to enteric fermentation in ruminants and anaerobic digestion of manure. In general, direct emissions of greenhouse gases from agricultural production were estimated to be 5.0-5.8 GtCO₂e per year in 2000-10, whereas indirect emissions from land use and land-use change were 4.3-5.5 GtCO₂e per year (IPCC 2014).

The total cropland area of our sample countries exceeds 82 million ha (they would only be ahead of India, USA, China and Russia on a global scale). According to our calculations, the coefficients of cropland expansion are negative and non-significant from the 10th to the 30th quantile. Subsequently, this coefficient becomes positive, showing high statistical significance only at the 80th quantile (a 1% increase in cropland use leads to CO₂ emissions increase by 0.28%). This variable has a heterogeneous impact on emissions across different quantiles (it is higher at lower quantiles). Our findings are in line with Zaman and Abd-el Moemen (2017), Spawn et al. (2019) and Magazzino et al. (2023).

The energy system of the vast majority of sample countries is largely based on the extraction and consumption of bituminous coal and lignite. As of 2022, EE countries (especially Poland, Czech Republic, Serbia and Bulgaria) produced 55 million tons of hard coal and 185 million tons of lignite – 99% and 63% of total European extraction. The biggest coal producer in CA is Kazakhstan

Table 6. Panel quantile regression results

Variable	10 th	20 th	30 th	40 th	50 th	60 th	70 th	80 th	90 th
GDP	-4.340** (2.140)	-1.515 (1.845)	-2.280 (1.657)	0.194 (1.714)	1.005 (1.302)	2.248 (2.165)	4.337** (1.991)	4.745*** (1.815)	3.628* (2.189)
GDP2	0.258** (0.107)	0.106 (0.093)	0.141* (0.082)	0.019 (0.085)	-0.021 (0.064)	-0.082 (0.106)	-0.185* (0.098)	-0.210** (0.092)	-0.159 (0.112)
CR	-0.212 (0.184)	-0.120 (0.155)	-0.038 (0.151)	0.023 (0.177)	0.067 (0.195)	0.129 (0.198)	0.106 (0.171)	0.283*** (0.102)	0.175 (0.142)
CO	0.110** (0.048)	0.119* (0.069)	0.083 (0.059)	0.108** (0.045)	0.097** (0.041)	0.127*** (0.044)	0.096* (0.053)	0.144*** (0.055)	0.204*** (0.056)
CE	0.004 (0.049)	0.019 (0.052)	0.016 (0.042)	0.00003 (0.033)	0.029 (0.029)	0.032 (0.031)	0.038 (0.030)	0.032 (0.028)	0.019 (0.047)
ST	0.060** (0.030)	0.053* (0.029)	0.065*** (0.020)	0.069*** (0.016)	0.064*** (0.015)	0.057*** (0.017)	0.058*** (0.021)	0.072** (0.032)	0.045 (0.033)
HY	-0.051 (0.032)	-0.060* (0.035)	-0.072*** (0.023)	-0.062*** (0.014)	-0.052*** (0.013)	-0.035** (0.017)	-0.040** (0.017)	-0.027 (0.020)	-0.014 (0.021)
Intercept	-0.084*** (0.007)	-0.056*** (0.007)	-0.038*** (0.007)	-0.029*** (0.005)	-0.022*** (0.003)	-0.012** (0.005)	-0.004 (0.007)	0.015* (0.009)	0.038*** (0.009)

Note: Bootstrapped standard errors are in parentheses. ***, **, and * indicate significance at the 1%, 5%, and 10%, respectively.

Source: authors' calculations

(90 million tons annually). The share of coal-fired electricity generation is usually decreasing but still significant in the energy balance of many countries: the maximum values during the study period (2000-20) reached 95% in Poland, 87% in North Macedonia, 80% in Kazakhstan, 75% in Serbia and Bosnia and Herzegovina, 72% in the Czech Republic, and 55% in Bulgaria and Montenegro. As we expected, the relationship between electricity production from coal and carbon footprint is positive and significant at all quantiles (with the exception of the 30th quantile); a 1% increase leads to CO₂ emissions increasing by 0.08-0.20%. These findings are consistent with the conclusions about environmental degradation due to the burning of fossil fuels by Al-Mulali (2014), Güney (2022), Raihan and Tuspekova (2022).

The process of substitution of non-renewable energy sources by wind, solar, or biomass is in its initial stages in most of the selected countries. The share of them up to the mid-2010s is too insignificant for a relevant assessment of the impact on emissions in the 21st century. In this regard, we use data on hydropower as a traditional type of renewable energy for EE and CA: in 2022 its share in total energy production was 90-99% in Albania, Kyrgyzstan, and Tajikistan; 55% in Latvia; 40-45% in Croatia and Montenegro; and circa 25-30% in Romania, Bosnia and Herzegovina, North Macedonia, Serbia, and Slovenia. According to our calculations, the impact of hydroelectricity on CO₂ emissions is negative and significant at conventional levels from the 20th to the 70th quantile (a 1% increase in hydropower generation results in a decrease of emissions by 0.04-0.07%). Our findings are also confirmed by Al-Mulali et al. (2015), Solarin et al. (2017) and Bilgili et al. (2021).

Using aggregate data on industrial value-added to assess the industry's carbon footprint is simpler in terms of data searching, but methodologically it is not entirely correct. Products with the maximum carbon footprint are produced by only a few industries (cast iron and steel, aluminium, cement, ammonia), the share of which in the structure of industrial value-added may be quite small. Our analysis of UNFCCC data shows that the share of the steel and cement industries in the structure of industrial CO₂

emissions in 2021 in Poland was 8% and 63%, respectively; in the Czech Republic – 54% and 29%, in Romania – 37% and 46%, in Kazakhstan – 44% and 36%. Thus, using these two variables as proxies of industrial development could provide interesting conclusions. To our knowledge, earlier papers have not proposed such a combination of dependent variables.

The coefficient of steel production is positive and significant in all quantile levels except the 90th quantile (highly significant from the 30th to the 70th quantile); a 1% increase in the output of steel products results in a growth in carbon emissions of 0.05-0.07%. The coefficients for cement production on emissions tend to be notably higher at elevated quantiles, even though this relationship is not statistically significant.

In order to test the robustness, we conducted the quantile regression analysis by including the RD variable. The effect of R&D on carbon emissions is negative, and only at the 40th and the 50th quantile levels has low statistical significance. EE and CA countries adhere to an imitation model of technological development, particularly relying on importing know-how to reduce anthropogenic emissions into the atmosphere. With this approach, the level of R&D expenditures (like any other indicator of technological development) cannot be sensitive to the dynamics of greenhouse gas emissions. Petrović and Lobanov (2020) find that the effect of R&D expenditure growth rates on CO₂ emissions in OECD countries could be positive, negative, and neutral (insignificant) for many years – the relationship between these two variables is country-specific. The coefficients of other regression variables do not change notably, so we conclude that our panel quantile model is robust.

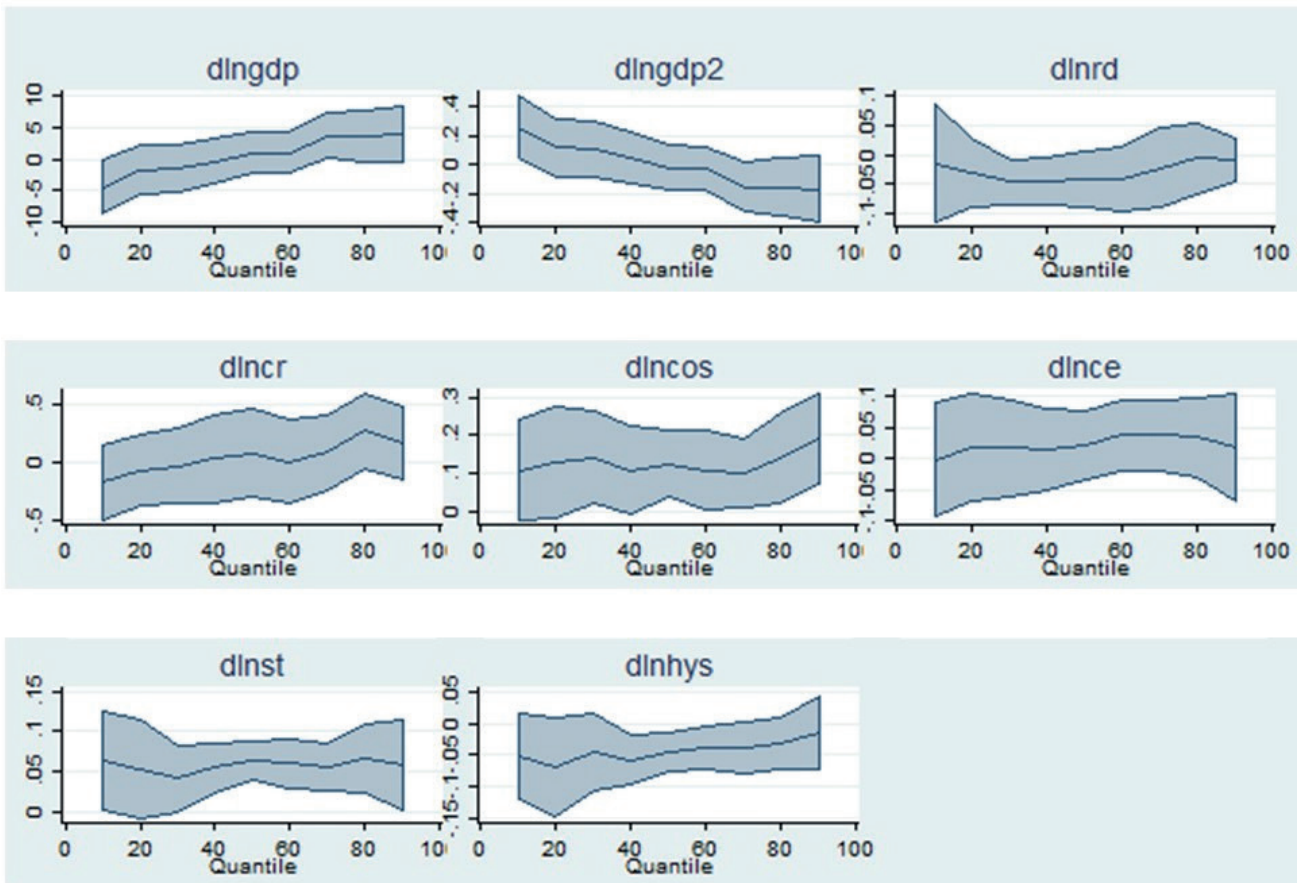
Additionally, we present the quantile regression results in Fig. 2. The effect of GDP per capita has an increasing trend at all selected quantiles, while the square of GDP per capita has a diminishing effect on ecological deterioration. All of our key independent variables have a heterogeneous impact on CO₂ in its condition distribution.

Table 7. Panel quantile regression results (robustness check – with RD)

Variable	10 th	20 th	30 th	40 th	50 th	60 th	70 th	80 th	90 th
GDP	-4.353** (2.169)	-1.687 (1.524)	-1.510 (1.571)	-0.342 (1.681)	0.989 (1.739)	1.051 (2.073)	3.666* (1.929)	3.603* (2.029)	3.849* (2.229)
GDP2	0.259** (0.109)	0.113 (0.079)	0.103 (0.080)	0.046 (0.083)	-0.023 (0.084)	-0.024 (0.101)	-0.154* (0.093)	-0.153 (0.102)	-0.172 (0.117)
RD	-0.015 (0.054)	-0.029 (0.044)	-0.046 (0.029)	-0.044* (0.024)	-0.041* (0.257)	-0.042 (0.032)	-0.022 (0.034)	-0.006 (0.032)	-0.008 (0.015)
CR	-0.177 (0.235)	-0.069 (0.136)	-0.029 (0.161)	0.032 (0.174)	0.079 (0.185)	0.003 (0.174)	0.085 (0.172)	0.277 (0.179)	0.167 (0.201)
CO	0.108 (0.086)	0.129** (0.064)	0.142** (0.058)	0.108* (0.059)	0.124** (0.056)	0.108** (0.052)	0.099* (0.051)	0.141** (0.058)	0.190*** (0.058)
CE	-0.0008 (0.041)	0.017 (0.040)	0.017 (0.036)	0.014 (0.032)	0.023 (0.028)	0.038* (0.022)	0.037 (0.024)	0.034 (0.029)	0.017 (0.040)
ST	0.063* (0.033)	0.052 (0.032)	0.041* (0.022)	0.055*** (0.018)	0.063*** (0.016)	0.059*** (0.016)	0.054*** (0.016)	0.067*** (0.023)	0.058* (0.031)
HY	-0.052 (0.036)	-0.068** (0.033)	-0.045* (0.024)	-0.057*** (0.019)	-0.043** (0.019)	-0.037* (0.022)	-0.038 (0.024)	-0.031 (0.028)	-0.015 (0.028)
Constant	-0.084*** (0.009)	-0.053*** (0.011)	-0.036*** (0.009)	-0.027*** (0.007)	-0.019*** (0.005)	-0.010* (0.005)	-0.002 (0.006)	0.015* (0.007)	0.040*** (0.011)

Note: Bootstrapped standard errors are in parentheses. ***, **, and * indicate significance at the 1%, 5%, and 10%, respectively.

Source: authors' calculations



Note: The labels represent the first difference of the variables (dlngdp – GDP per capita, dlngdp2 – the square value of GDP per capita, dlncr – the R&D expenditure, dlncr –the cropland, dlncos – the electricity production from coal, dlncce – the cement production, dlncst – the crude steel production, dlncys – hydroelectricity production).

Fig. 2. Change in the panel quantile regression coefficients based on Table 7

CONCLUSIONS

In this paper, we study the impact of the energy sector (coal-based electricity and hydroelectricity generation), the manufacturing industry (steel and cement production) and agriculture (cropland area change) on CO₂ emissions in 16 Eastern European and 4 Central Asian countries for the period from 2000 to 2020. In addition, the relationship between the carbon footprint and income and the level of technological development is considered.

First, the relationship between air pollution and income (using GDP per capita PPP as a proxy) is explored in order to confirm or reject the EKC hypothesis. We find evidence for a U-shaped environmental Kuznets curve for EE and CA countries with the lower carbon footprint: in particular, for the 10th quantile, a 1% increase in GDP results in a 4.34% drop in CO₂ emissions, while square GDP per capita is associated with a 0.26% increase in emissions. Less economically developed countries with low pollution levels (Albania, North Macedonia, Montenegro in the Balkans, Tajikistan and Kyrgyzstan in CA) are before the turning point of the U-curve: implementation of green transition policies is still not dampening economic growth, but later the progress in the economy will lead to increased emissions due to a deficit in technology and a qualified labor force.

It is important to note that some of these energy-intensive economies are based on the use of renewables, so emissions with increasing income are still minimal (non-fossil energy generation makes up 90-99% in Albania, Kyrgyzstan, and Tajikistan). On the other side, economically developed countries with low emissions (three Baltic states – Estonia, Latvia, and Lithuania) may face a slowdown in economic growth as they combat air pollution.

Interestingly, we cannot confirm the pollution haven hypothesis, which is often associated with the U-shaped EKC. None of the countries mentioned are examples of relocation of carbon-intensive industries from developed countries with stringent environmental policies.

In contrast, the countries with the highest emissions (the 70th and 80th quantile) are found to have an inverted U-shaped relationship between GDP per capita and CO₂ emissions (for the 80th quantile, an increase of 1% in income results in emissions increasing by 4.75%, while square GDP per capita records a decrease of 0.21%). Energy-intensive economic growth in high-emitting countries like Kazakhstan or Uzbekistan is directly connected with environmental degradation (fossil energy generation makes up 90% of total, heavy industry is almost not equipped with emission-reducing equipment, etc.). On the other hand, more economically developed large emitters of greenhouse gases (e.g., Poland and the Czech Republic) are beginning to reduce their carbon footprint because of the structural (economic composition) and technological effects linked to the inverted U-shaped EKC, as well as due to the environmental awareness of the wealthier population.

According to popular belief, the level of technological development is inversely correlated with environmental pollution. However, most innovation indicators show a general picture and are not directly related to the spread of green technologies and, therefore, are insensitive to data on greenhouse gas emissions. For instance, less air pollution can be achieved by implementing imported green technologies and know-how, so the national data on R&D expenditure or patent applications is not important in this case. We find that the effect of R&D on carbon

emissions is negative but only statistically significant at the 40th and 50th quantiles. This proves that given countries, firstly, may differ in the method of collecting statistical data, and secondly, import green technologies as part of a more general model of technological imitation.

There is a consensus in the literature on the impact of thermal energy on air pollution, but the use of data on coal-based electricity generation is very rare. We find that the relationship between electricity production from coal and CO₂ emissions is positive and significant at almost all quantiles (a 1% increase leads to CO₂ emissions increasing by 0.08-0.20%). The EE and CA countries are traditionally large producers of coal (together more than 330 million tons in 2022) and still widely use it in power generation, although the share of this non-renewable is declining (65-70% in Poland, Kazakhstan, Serbia, Bosnia and Herzegovina, 45-50% in Czech Republic, North Macedonia, Montenegro, Bulgaria). At the same time, the installed capacity of coal-fired thermal power plants is practically not reduced in some countries (Poland, Bulgaria, and Serbia), and even new power units are being commissioned (Kazakhstan). The persistence of coal generation is primarily due to the affordability of brown and steam hard coal and the lack of political will or finance for the transition to low-carbon (natural gas) or carbon-free energy. The implementation of carbon capture and storage technologies (CCS) is critical to reducing emissions.

We choose hydropower to discover the role of non-fossil electricity generation in EE and CA because, in most of the countries, it remains the key type of renewable energy in conditions of the still limited use of wind, solar, and biomass. In 11 of 20 selected countries, the share of hydropower exceeds ¼ in the energy consumption structure; in Albania, Kyrgyzstan, and Tajikistan, it makes 90-99%. We find that the impact of hydroelectricity on CO₂ emissions is negative and significant from the 20th to the 70th quantile (a 1% increase in hydropower generation results in a decrease of emissions by 0.04-0.07%). In the case of key hydropower producers, one can find that they continue to expand their installed capacity: for example, in Romania in the 21st century, it was increased by 7%, in Tajikistan by 30%, and in Kazakhstan by 24%. A strategy to strengthen the role of hydropower will positively contribute to reducing the carbon footprint (except for emissions due to decomposition of aquatic biomass). However, we should not forget the negative consequences of constructing hydroelectric power stations and damming rivers, such as changing the natural course of rivers and their physical conditions, rising risks for upstream and downstream wildlife habitat, microclimate changing, and flooding of agricultural lands and settlements.

The change in cropland area, crude steel and cement production are chosen to examine the impact of industry and agriculture on CO₂ emissions. As far as we know, this combination of these dependent variables has not previously been considered in studies. The use of aggregated data for this purpose (agriculture or industry value-added / value-added per capita / share in GDP) has no theoretical or practical significance, since almost all carbon dioxide emissions in the industry are associated with the activities of 3-4 branches, and in agriculture – only with land-use change in favor of croplands (organic soils emit CO₂ when they are drained to be converted to cropland). More to say, the data on agriculture value-added used by many authors cannot be used in relation to carbon footprint: crop and livestock production is responsible for direct emissions of CH₄ and N₂O, but not CO₂.

We assumed that cropland area change could be one of the key factors in explaining the dynamics of carbon emissions in EE and CA countries. The total cropland area of our sample countries exceeds 82 million ha (they would only be ahead of India, USA, China, and Russia on a global scale). In 2020, compared to the early 2000s, the cropland area in Kazakhstan, rich in fertile chernozem and kastanozem soils, grew by 4%; in Serbia and Bulgaria – by 6% and 8%, respectively; in Tajikistan – by 19%, in the Baltic States – by 30-45%. Our hypothesis is confirmed, but only for the 80th quantile: a 1% increase in cropland use leads to CO₂ emissions increasing by 0.28%.

Thus, the EE and CA countries need to be attentive to environmental degradation caused by various forms of land-use change. The main goal is to make land serve more as a carbon sink, not a carbon source, which is achievable when the storage capacity of carbon in soil and biomass exceeds the emissions from deforestation and organic soil conversion. To preserve carbon sink, the measures of sustainable land use and improved agronomic practices are required: 1) to introduce “carbon farming” (soil carbon sequestration) when CO₂ is removed from the atmosphere and absorbed by the soil (e.g. switching from tillage (including grassland ploughing) by no-till or low-till methods that not disturbing the soil, rotational grazing of livestock, changing planting schedules and using cover crops); 2) to reduce deforestation and promote afforestation and reforestation; 3) to combat wildfires; 4) to develop agroforestry; 5) to rewet drained peatlands. The EE and CA countries can develop appropriate measures within the framework of international agreements, for example, the Glasgow Declaration on Forests (COP26) or the recently revised EU's Regulation on land use, land use change, and forestry.

Enterprises producing cement, cast iron, and steel are the main industrial air pollutants of carbon dioxide (for example, their total share in the Czech Republic, Romania, and Kazakhstan exceeds 80%, in Poland – 70%). Therefore, using aggregate data on industrial value-added to assess the carbon footprint of manufacturing instead of steel and cement industry data is not methodologically correct. We find that the coefficient of steel production is positive and significant from the 10th to 80th quantile levels: a 1% increase in production at the 20th and 80th quantiles leads to 0.05% and 0.07% rise in emissions, respectively. Thus, technological modernization of ferrous metallurgy will be the most important factor in reducing industrial greenhouse gas emissions in EE and CA countries, which together produce 30-35 million tons of crude steel annually (which is comparable to the production of Germany or Brazil).

There are two basic routes to produce steel – by integrated blast furnace-basic oxygen furnace (BF-BOF) and electric arc furnace (EAF). Carbon dioxide emissions are due to the use of BF-BOF: 80-90% of them are associated with the first stage since coal serves as a reducing agent to extract iron from iron ore in a blast furnace (in the second stage the basic oxygen converter turns carbon-rich pig iron, with some scrap added, into crude steel). Depending on the quality of carbon-containing reducing agents (coke), CO₂ emissions from BF-BOF may account for 1.4-1.9 tCO₂/t steel (estimates of World Steel Association and IEA). In contrast, the carbon footprint of EAF route, mostly using scrap, is about 0.3-0.4 tCO₂/t steel, so these furnaces need to be introduced more actively. Generally, the use of secondary metallurgy will reduce the need for primary metals and lead to a reduction in emissions. It is also possible to develop direct reduction of iron (DRI) from ore

or ore concentrate without melting by using solid carbon or a reducing gas, for example, hydrogen.

We prove that cement production positively influences CO₂ emissions, though this relationship is not statistically significant. Interestingly, quantile regression analysis that takes into account the R&D variable shows that for the 60th quantile, the coefficient of cement production is not just positive but also statistically significant. The countries of EE and CA are dynamically expanding cement production: in 2000-2020, it increased by almost 80% – from 48 to 86 million tons (for comparison, the USA, which is in 4th place in the world, produces 95 million tons). There are wet and dry processes of cement production – the first of them is more energy- and source-intensive. In the first stage of the wet method, limestone, clay, and other raw materials are

mixed with water in a ball mill, making slurry. After adding various compounds in storage tanks, the slurry goes to a rotary kiln and then transforms into cement clinker – the process is energy-intensive and links to high emissions of CO₂. Depending on the fuels used and clinker/cement ratio the carbon footprint of wet and dry methods is about 0.7-1.0 and 0.5-0.7 tCO₂/t cement, respectively. In order to reduce the carbon footprint of cement production, the following measures can be taken: to capture CO₂ emissions from the calcination of limestone in clinker production (carbon capture and storage, CCS), to reduce clinker-to-cement ratio (via adoption of supplementary cement materials, SCMs), to use more low-carbon fuels (like bioenergy and waste) instead of fossil fuels, and to develop innovative electric kilns. ■

REFERENCES

- Akram R., Chen F., Khalid F., Ye Z. and Majeed M. T. (2020). Heterogeneous effects of energy efficiency and renewable energy on carbon emissions: Evidence from developing countries. *Journal of Cleaner Production*, 247, 119122, DOI:10.1016/j.jclepro.2019.119122.
- Allard A., Takman J., Uddin G. S. and Ahmed A. (2018). The N-shaped environmental Kuznets curve: an empirical evaluation using a panel quantile regression approach. *Environmental Science and Pollution Research*, 25, 5848–5861, DOI: 10.1007/s11356-017-0907-0.
- Al-Mulali U. (2014). Investigating the impact of nuclear energy consumption on GDP growth and CO₂ emission: A panel data analysis. *Progress in Nuclear Energy*, 73, 172–178, DOI: 10.1016/j.pnucene.2014.02.002.
- Al-Mulali U., Ozturk I. and Lean H.H. (2015). The influence of economic growth, urbanization, trade openness, financial development, and renewable energy on pollution in Europe. *Natural Hazards*, 79, 621–644, DOI: 10.1007/s11069-015-1865-9.
- Ang J.B. (2007). CO₂ emissions, energy consumption, and output in France. *Energy Policy*, 35(10), 4772–4778, DOI: 10.1016/j.enpol.2007.03.032.
- Ang J.B. (2009). CO₂ emissions, research and technology transfer in China. *Ecological Economics*, 68(10), 2658–2665, DOI: 10.1016/j.ecolecon.2009.05.002.
- Apergis N. and Ozturk I. (2015). Testing Environmental Kuznets Curve hypothesis in Asian countries. *Ecological Indicators*, 52, 16–22. DOI: 10.1016/j.ecolind.2014.11.026.
- Atici C. (2009). Carbon emissions in Central and Eastern Europe: environmental Kuznets curve and implications for sustainable development. *Sustainable Development*, 17(3), 155–160, DOI:10.1002/sd.372.
- Attílio L. A., Faria J. R. and Rodrigues M. (2023). Does monetary policy impact CO₂ emissions? A GVAR analysis. *Energy Economics*, 119, p.106559, DOI: 10.1016/j.eneco.2023.106559.
- Balsalobre-Lorente D., Shahbaz M., Murshed M. and Nuta F.M. (2023). Environmental impact of globalization: The case of central and Eastern European emerging economies. *Journal of Environmental Management*, 341, p.118018, DOI: 10.1016/j.jenvman.2023.118018.
- Bilgili F., Balsalobre-Lorente D., Kuşkaya S., Ünlü F., Gençoğlu P. and Rosha P. (2021). The role of hydropower energy in the level of CO₂ emissions: An application of continuous wavelet transform. *Renewable Energy*, 178, 283–294, DOI:10.1016/j.renene.2021.06.015.
- Cade B. and Noon B. (2003). A gentle introduction to quantile regression for ecologists. *Frontiers in Ecology and the Environment*, 1(8), 412–420, DOI: 10.1890/1540-9295(2003)001[0412:AGITQR]2.0.CO;2.
- Cheng C., Ren X., Dong K., Dong X. and Wang Z. (2021). How does technological innovation mitigate CO₂ emissions in OECD countries? Heterogeneous analysis using panel quantile regression. *Journal of Environmental Management*, 280, p.111818, DOI:10.1016/j.jenvman.2020.111818.
- De Bruyn S.M., van den Bergh J.C. and Opschoor J.B. (1998). Economic growth and emissions: reconsidering the empirical basis of environmental Kuznets curves. *Ecological Economics*, 25(2), 161–175, DOI:10.1016/S0921-8009(97)00178-X.
- Destek M.A. and Sarkodie S.A. (2019). Investigation of environmental Kuznets curve for ecological footprint: the role of energy and financial development. *Science of the Total Environment*, 650(2), 2483–2489, DOI:10.1016/j.scitotenv.2018.10.017.
- Dogan E. and Seker F. (2016). Determinants of CO₂ emissions in the European Union: the role of renewable and non-renewable energy. *Renewable Energy*, 94, 429–439, DOI:10.1016/j.renene.2016.03.078.
- Friedl B. and Getzner M. (2003). Determinants of CO₂ emissions in a small open economy. *Ecological Economics*, 45(1), 133–148, DOI:10.1016/S0921-8009(03)00008-9.
- Ganda F. (2019). The impact of innovation and technology investments on carbon emissions in selected organisation for economic co-operation and development countries. *Journal of Cleaner Production*, 217, 469–483, DOI:10.1016/j.jclepro.2019.01.235.
- Güney T. (2022). Solar energy, governance and CO₂ emissions. *Renewable Energy*, 184, 791–798, DOI:10.1016/j.renene.2021.11.124.
- IPCC (2014). *Climate Change 2014: Mitigation of Climate Change*. [online] Available at: https://www.ipcc.ch/site/assets/uploads/2018/02/ipcc_wg3_ar5_full.pdf (accessed 27 August 2024).
- Kasman A. and Duman Y.S. (2015). CO₂ emissions, economic growth, energy consumption, trade and urbanization in new EU member and candidate countries: a panel data analysis. *Economic Modelling*, 44, 97–103, DOI:10.1016/j.econmod.2014.10.022.
- Koenker R. and Bassett Jr G. (1978). Regression quantiles. *Econometrica*, 46(1), 33–50, DOI: 10.2307/1913643.
- Li R., Jiang H., Sotnyk I., Kubatko O. and Almashaqbeh Y.A.I. (2020). The CO₂ emissions drivers of post-communist economies in Eastern Europe and Central Asia. *Atmosphere*, 11(9), p.1019, DOI:10.3390/atmos11091019.
- Magazzino C., Cerulli G., Shahzad U. and Khan S. (2023). The nexus between agricultural land use, urbanization, and greenhouse gas emissions: Novel implications from different stages of income levels. *Atmospheric Pollution Research*, 14(9), p.101846, DOI:10.1016/j.apr.2023.101846.
- Nguyen A.T. (2019). The Relationship between Economic Growth, Energy Consumption and Carbon Dioxide Emissions: Evidence from Central Asia. *Eurasian Journal of Business and Economics*, 12(24), 1–15, DOI:10.17015/ejbe.2019.024.01.
- Pao H.T. and Tsai C.M. (2011). Modeling and forecasting the CO₂ emissions, energy consumption, and economic growth in Brazil. *Energy*, 36(5), 2450–2458, DOI:10.1016/j.energy.2011.01.032.
- Paramati S.R., Mo D. and Gupta R. (2017). The effects of stock market growth and renewable energy use on CO₂ emissions: Evidence from G20 countries. *Energy Economics*, 66, 360–371, DOI: 10.1016/j.eneco.2017.06.025.

- Pejović B., Karadžić V., Dragašević Z. and Backović T. (2021). Economic growth, energy consumption and CO₂ emissions in the countries of the European Union and the Western Balkans. *Energy Reports*, 7, 2775–2783, DOI: 10.1016/j.egy.2021.05.011.
- Petrović P. and Lobanov M.M. (2020). The impact of R&D expenditures on CO₂ emissions: evidence from sixteen OECD countries. *Journal of Cleaner Production*, 248, p.119187, DOI: 10.1016/j.jclepro.2019.119187.
- Raihan A. (2023). The dynamic nexus between economic growth, renewable energy use, urbanization, industrialization, tourism, agricultural productivity, forest area, and carbon dioxide emissions in the Philippines. *Energy Nexus*, 9, p.100180, DOI: 10.1016/j.nexus.2023.100180.
- Raihan A. and Tuspekova A. (2022). Role of economic growth, renewable energy, and technological innovation to achieve environmental sustainability in Kazakhstan. *Current Research in Environmental Sustainability*, 4, p.100165, DOI:10.1016/j.crsust.2022.100165.
- Richmond A.K. and Kaufmann R.K. (2006). Is there a turning point in the relationship between income and energy use and/or carbon emissions? *Ecological Economics*, 56(2), 176–189, DOI:10.1016/j.ecolecon.2005.01.011.
- Salahodjaev R., Sharipov K., Rakhmanov N. and Khabirov D. (2022). Tourism, renewable energy and CO₂ emissions: evidence from Europe and Central Asia. *Environment, Development and Sustainability*, 24(11), 13282–13293, DOI: 10.1007/s10668-021-01993-x.
- Salman M., Long X., Dauda L., Mensah C.N. and Muhammad S. (2019). Different impacts of export and import on carbon emissions across 7 ASEAN countries: A panel quantile regression approach. *Science of The Total Environment*, 686, 1019–1029, DOI: 10.1016/j.scitotenv.2019.06.019
- Sarkodie S.A. and Strezov V. (2019). Effect of foreign direct investments, economic development and energy consumption on greenhouse gas emissions in developing countries. *Science of Total Environment*, 646, 862–871, DOI:10.1016/j.scitotenv.2018.07.365.
- Shahnazi R. and Dehghan Shabani Z. (2021). The effects of renewable energy, spatial spillover of CO₂ emissions and economic freedom on CO₂ emissions in the EU. *Renewable Energy*, 169, 293–307, DOI:10.1016/j.renene.2021.01.016.
- Simionescu M. (2021). The nexus between economic development and pollution in the European Union new member states. The role of renewable energy consumption. *Renewable Energy*, 179, 1767–1780, DOI:10.1016/j.renene.2021.07.142.
- Simionescu M., Strielkowski W. and Gavurova B. (2022). Could quality of governance influence pollution? Evidence from the revised Environmental Kuznets Curve in Central and Eastern European countries. *Energy Reports*, 8, 809–819, DOI:10.1016/j.egy.2021.12.031.
- Solarin S.A., Al-Mulali U. and Ozturk I. (2017). Validating the environmental Kuznets curve hypothesis in India and China: The role of hydroelectricity consumption. *Renewable and Sustainable Energy Reviews*, 80, 1578–1587, DOI: 10.1016/j.rser.2017.07.028.
- Soytas U., Sari R. and Ewing B.T. (2007). Energy consumption, income, and carbon emissions in the United States. *Ecological Economics*, 62(3–4), 482–489, DOI:10.1016/j.ecolecon.2006.07.009.
- Spawn S.A., Lark T.J. and Gibbs H.K. (2019). Carbon emissions from cropland expansion in the United States. *Environmental Research Letters*, 14(4), p.045009, DOI:10.1088/1748-9326/ab0399.
- Torra M. and Boyce J.K. (1998). Income, inequality, and pollution: a reassessment of the environmental Kuznets curve. *Ecological Economics*, 25(2), 147–160, DOI: 10.1016/S0921-8009(97)00177-8.
- Uğurlu E. (2022). Impacts of Renewable Energy on CO₂ Emission: Evidence from the Visegrad Group Countries. *Politics in Central Europe*, 18(2), 295–315, DOI:10.2478/pce-2022-0013.
- Voumik L. C., Mimi M.B. and Raihan A. (2023). Nexus between urbanization, industrialization, natural resources rent, and anthropogenic carbon emissions in South Asia: CS-ARDL approach. *Anthropocene Science*, 2(1), 48–61, DOI: 10.1007/s44177-023-00047-3
- Wang S.S., Zhou D.Q., Zhou P. and Wang Q.W. (2011). CO₂ emissions, energy consumption and economic growth in China: A panel data analysis. *Energy Policy*, 39(9), 4870–4875, DOI:10.1016/j.enpol.2011.06.032.
- Xu B. and Lin B. (2016). A quantile regression analysis of China's provincial CO₂ emissions: where does the difference lie? *Energy Policy*, 98, 328–342, DOI: 10.1016/j.enpol.2016.09.003.
- Xu B. and Lin B. (2020). Investigating drivers of CO₂ emission in China's heavy industry: A quantile regression analysis. *Energy*, 206, 118159, DOI:10.1016/j.energy.2020.118159.
- Zaman K. and Abd-el Moemen M. (2017). The influence of electricity production, permanent cropland, high technology exports, and health expenditures on air pollution in Latin America and the Caribbean Countries. *Renewable and Sustainable Energy Reviews*, 76, 1004–1010, DOI:10.1016/j.rser.2017.03.103.
- Zhang S. (2019). Environmental Kuznets curve revisit in Central Asia: the roles of urbanization and renewable energy. *Environmental Science and Pollution Research*, 26(23), 23386–23398, DOI: 10.1007/s11356-019-05600-5.
- Zhang X.P. and Cheng X.M. (2009). Energy consumption, carbon emissions, and economic growth in China. *Ecological Economics*, 68(10), 2706–2712, DOI:10.1016/j.ecolecon.2009.05.011.
- Zheng H., Song M. and Shen Z. (2021). The evolution of renewable energy and its impact on carbon reduction in China. *Energy*, 237, 121639, DOI: 10.1016/j.energy.2021.121639.



ges.rgo.ru/jour/

ISSN 2542-1565 (Online)